

Program: NSF Frontiers in Earth System Dynamics

Project: Sun to Ice-Impacts on Earth of Extreme Solar Events, NSF Grant No.
AGS-1135432

Principal Investigator: Harlan Spence, University of New Hampshire

Sub-Award Agreement: 12-032, University of New Hampshire to Predictive Science Inc.

Sub-Award Principal Investigators: Jon Linker and Pete Riley, Predictive Science Inc., San
Diego

Report Type: Annual

Reporting Period: October 1, 2012 - September 30, 2013

1. Overview

This report summarizes the technical progress made during the second year of the sub-contract “Sun to Ice-Impacts on Earth of Extreme Solar Events,” (Grant No. AGS-1135432) between NASA and Predictive Science, and covers the period from October 1, 2012 to September 30, 2013. Under this contract, Predictive Science Inc. (PSI) has conducted numerical and data analysis related to issues concerning the eruption and evolution of fast coronal mass ejections (CMEs) and investigated the factors leading to, and the properties of extreme solar events. Our investigation has focused on developing several robust CME generators, and coupling our global MHD results with UNH’s particle acceleration and transport codes. Additionally, we collaborated with a number of other research teams on a range of problems related to CME initiation and evolution.

In the sections that follow, we highlight some of this work, summarize the presentations that were made, and, in Appendix A, provide copies of a selection of peer-reviewed publications that resulted from this work.

2. Summary of Work

2.1. Development of a robust semi-empirical model for generating fast CMEs

Building on the promising initial work during the first year of this program, during the past year, we continued to refine the Titov-Demoullin (TDm) flux rope model and incorporated it into our global MHD code. Our technique differs from other approaches in that the flux rope is allowed to relax to an equilibrium prior to eruption. Thus, the initial conditions are considerably more self-consistent than earlier “superposition” models, which produce ejecta simply by being out of equilibrium from the outset.

We also developed new version of our heliospheric MHD code, which, together with our coronal model, allows us to propagate a CME directly from the surface of the Sun to 1 AU or beyond. Our initial tests have been encouraging: We were able to propagate CMEs seamlessly across the boundary between the coronal and heliospheric models.

Details of the code development effort are provided in the previous eleven monthly reports.

2.2. Development of a global heliospheric model for propagating disturbances through the solar wind

We also completed the development and testing of a new version of our heliospheric MHD code, which, together with our coronal model, allows us to propagate a CME directly from the surface of the Sun to 1 AU. We have used it to: (1) propagate solutions of TDM flux ropes into and through the solar wind; and (2) to initiate generalized cone-model ICMEs. Most recently, we incorporated a spheromak-type magnetic structure within the cone-model ejecta, the results of which are under study.

The details of the algorithm development and testing were written up, submitted and published in *Astrophysical Journal*. The paper is included in Appendix A.

2.3. Coupling the global MHD heliospheric results with UNH's particle code

As a first step towards ultimately coupling our global MHD model with an energetic particle code, we developed a heliospheric solution for the July 23, 2012 extreme CME event. The particle code necessitated that we output the model results at such high time cadence that we had to mail the solution to Matt Gorby at UNH (because data transfer rates across the internet would have been prohibitively slow). Initial results from the particle code are very promising and will be included at a presentation at the Fall AGU (San Francisco, December, 2013). Future collaborations may require that we house the two codes on the same computing system to avoid the need to transfer such large amounts of data, or, additionally, that we couple the two codes together.

2.4. Miscellaneous other studies related to modeling CMEs

We conducted several other studies with colleagues from other institutions, the details of which can be found in Appendix A.

2.5. Presentations and Publications

The work performed as part of this investigation were presented at a number of conferences and workshops. These included:

1. Torok, T., Mikic, Z., Titov, V., Linker, J.A., Downs, C., Lionello, R., Riley, P. (2012).

Constraining CME Modeling With Observations: The Sympathetic Eruptions on 2010 August 1-2. AGU Fall meeting, San Francisco. Invited talk.

2. Torok, T., Downs, C., Lionello, R., Linker, J. A., Titov, V. S., Mikic, Z., and Riley, P. (2013). Numerical modeling of fast CMEs from Sun to Earth. In EGU General Assembly Conference Abstracts, volume 15 of EGU General Assembly Conference Abstracts, page 12485.
3. Torok, T. (2013a). Modeling Solar Eruptions: Where Do We stand? In AAS/Solar Physics Division Meeting, volume 44 of AAS/Solar Physics Division Meeting, page 301.01.
4. Torok, T. (2013b). Modeling Solar Eruptions: Where Do We Stand? In American Astronomical Society Meeting Abstracts, volume 222 of American Astronomical Society Meeting Abstracts, page 200.01.
5. Riley, P., Linker, J. A., and Torok, T., Multiple presentations at the FESD Workshop at LASP, CU, Boulder, Colorado, August, 2013.

The following manuscripts were published during the previous 12 months:

1. Riley, P. and Richardson, I. G. (2013). Using Statistical Multivariable Models to Understand the Relationship Between Interplanetary Coronal Mass Ejecta and Magnetic Flux Ropes. *Sol. Phys.*, 284:217-233.
2. Török, T., Temmer, M., Valori, G., Veronig, A. M., van Driel-Gesztelyi, L., and Vr?nak, B. (2013). Initiation of Coronal Mass Ejections by Sunspot Rotation. *Sol. Phys.*, 286:453-477.
3. Lionello, R., Downs, C., Linker, J. A., Török, T., Riley, P., and Mikic, Z. (2013). Magnetohydrodynamic Simulations of Interplanetary Coronal Mass Ejections. *ApJ*, 777:76.
4. Mikic, Z., Török, T., Titov, V., Linker, J. A., Lionello, R., Downs, C., and Riley, P. (2013). The challenge in making models of fast CMEs. In Zank, G. P., Borovsky, J., Bruno, R., Cirtain, J., Cranmer, S., Elliott, H., Giacalone, J., Gonzalez, W., Li, G., Marsch, E., Moebius, E., Pogorelov, N., Spann, J., and Verkhoglyadova, O., editors, American Institute of Physics Conference Series, volume 1539 of American Institute of Physics Conference Series, pages 42-45.

5. Titov, V. S., Mikic, Z., Török, T., Linker, J. A., and Panasenco, O. (2012). 2010 August 1-2 Sympathetic Eruptions. I. Magnetic Topology of the Source-surface Background Field. *ApJ*, 759:70.
6. Liu, R., Liu, C., Török, T., Wang, Y., and Wang, H. (2012). Contracting and Erupting Components of Sigmoidal Active Regions. *ApJ*, 757:150.
7. Kliem, B., Török, T., and Thompson, W. T. (2012). A Parametric Study of Erupting Flux Rope Rotation. Modeling the "Cartwheel CME" on 9 April 2008. *Sol. Phys.*, 281:137-166.
8. Gosain, S., Schmieder, B., Artzner, G., Bogachev, S., and Török, T. (2012). A Multi-spacecraft View of a Giant Filament Eruption during 2009 September 26/27. *ApJ*, 761:25.
9. Gopalswamy, N., Nieves-Chinchilla, T., Hidalgo, M., Zhang, J., Riley, P., van Driel-Gesztelyi, L., and Mandrini, C. H. (2013a). Topical Issue in Solar Physics: Flux-rope Structure of Coronal Mass Ejections Preface. *ArXiv e-prints*.
10. Gopalswamy, N., Nieves-Chinchilla, T., Hidalgo, M., Zhang, J., Riley, P., van Driel-Gesztelyi, L., and Mandrini, C. H. (2013b). Preface. *Sol. Phys.*, 284:1-4.
11. Gorby, M. J., Schwadron, N. A., Linker, J. A., Spence, H. E., Townsend, L. W., Cucinotta, F. A., and Wilson, J. K. (2012). From CMEs to Earth/Lunar Radiation Dosages: A First in Heliospheric End-to-End Coupling. *LPI Contributions*, 1685:3043.
12. Leake, J. E., Linton, M. G., and Török, T. (2013). Simulations of Emerging Magnetic Flux. I: The Formation of Stable Coronal Flux Ropes. *ArXiv e-prints*.
13. Shen, C., Reeves, K. K., Raymond, J. C., Murphy, N. A., Ko, Y.-K., Lin, J., Mikic, Z., and Linker, J. A. (2013). Non-equilibrium Ionization Modeling of the Current Sheet in a Simulated Solar Eruption. *ApJ*, 773:110.
14. Georgoulis, M. K., Titov, V. S., and Mikic, Z. (2012). Non-neutralized Electric Current Patterns in Solar Active Regions: Origin of the Shear-generating Lorentz Force. *ApJ*, 761:61.

The following manuscripts were recently submitted for publication:

1. Kliem, B., et al., *ApJ*: "Slow Rise And Partial Eruption Of A Double-Decker Filament. Ii Modeling By A Double Flux Rope Equilibrium.

2. Valori, G., et al., Proceedings IAU Symposium No. 300
3. Van Driel-Gesztelyi, L. et al., Proceedings IAU Symposium No. 300
4. A selection of these papers is reproduced in Appendix A.

Appendix A

A Selection of Papers Resulting from the Work Undertaken as part of this
Study

Using Statistical Multivariable Models to Understand the Relationship Between Interplanetary Coronal Mass Ejecta and Magnetic Flux Ropes

P. Riley · I.G. Richardson

Received: 30 January 2012 / Accepted: 18 April 2012 / Published online: 17 May 2012
© Springer Science+Business Media B.V. 2012

Abstract *In-situ* measurements of interplanetary coronal mass ejections (ICMEs) display a wide range of properties. A distinct subset, “magnetic clouds” (MCs), are readily identifiable by a smooth rotation in an enhanced magnetic field, together with an unusually low solar wind proton temperature. In this study, we analyze *Ulysses* spacecraft measurements to systematically investigate five possible explanations for why some ICMEs are observed to be MCs and others are not: i) An observational selection effect; that is, all ICMEs do in fact contain MCs, but the trajectory of the spacecraft through the ICME determines whether the MC is actually encountered; ii) interactions of an erupting flux rope (FR) with itself or between neighboring FRs, which produce complex structures in which the coherent magnetic structure has been destroyed; iii) an evolutionary process, such as relaxation to a low plasma- β state that leads to the formation of an MC; iv) the existence of two (or more) intrinsic initiation mechanisms, some of which produce MCs and some that do not; or v) MCs are just an easily identifiable limit in an otherwise continuous spectrum of structures. We apply quantitative statistical models to assess these ideas. In particular, we use the Akaike information criterion (AIC) to rank the candidate models and a Gaussian mixture model (GMM) to uncover any intrinsic clustering of the data. Using a logistic regression, we find that plasma- β , CME width, and the ratio O^7/O^6 are the most significant predictor variables for the presence of an MC. Moreover, the propensity for an event to be identified as an MC decreases with heliocentric distance. These results tend to refute ideas ii) and iii). GMM clustering analysis further identifies three distinct groups of ICMEs; two of which match (at

Flux-Rope Structure of Coronal Mass Ejections

Guest Editors: N. Gopalswamy, T. Nieves-Chinchilla, M. Hidalgo, J. Zhang, and P. Riley

P. Riley (✉)

Predictive Science, Inc., 9990 Mesa Rim Road, Suite 170, San Diego, CA, USA

e-mail: pete@predsci.com

I.G. Richardson

Astroparticle Physics Laboratory, Code 661, NASA Goddard Space Flight Center, Greenbelt, MD, USA

e-mail: ian.g.richardson@nasa.gov

I.G. Richardson

CRESST and Department of Astronomy, University of Maryland, College Park, MD, USA

the 86 % level) with events independently identified as MCs, and a third that matches with non-MCs (68 % overlap). Thus, idea v) is not supported. Choosing between ideas i) and iv) is more challenging, since they may effectively be indistinguishable from one another by a single *in-situ* spacecraft. We offer some suggestions on how future studies may address this.

Keywords Coronal mass ejections · Magnetic flux ropes · Magnetic clouds

1. Introduction

Coronal mass ejections (CMEs) produce spectacular visual displays involving the sometimes-explosive release of plasma and magnetic field from the solar corona into interplanetary space. Although they have been studied for many years since their discovery in the early 1970s by *Skylab* (Tousey, 1973) and they have the potential to wreak substantial damage to our technologically reliant society (Schieb, 2011), many of their basic properties are not well understood.

A CME can be defined as a large-scale, bright (and dark) transient feature observed in white-light (coronagraph) images of the Sun (see, *e.g.*, Hundhausen, 1993). The limitations of this definition are important. It relies only on white-light observations, which trace electron density. Moreover, these observations are integrated along the line of sight, weighted by the ray path's closest distance to the solar surface. CMEs are, of course, known to be violent eruptions of coronal magnetic fields, which, when viewed in the plane of the sky give rise to “bulb-like” structures or, on the disk, to “halo” structures. The classic three-part structure of a CME consists of a bright front, cavity, and core (see, *e.g.*, Riley *et al.*, 2008). However, we do not observe the magnetic field; we must infer its properties from a combination of numerical models driven by observations of the photospheric field. Clearly, though, the magnetic field must play a central role in the origin and dynamics of the CME, since there are no other sufficient sources of energy to power the eruption. Based on this, we infer that the white-light features we see are the manifestation of a flux rope (FR) structure propagating through the corona.

In the solar wind, interplanetary CMEs (ICMEs) are observed to display a wide range of features in *in-situ* measurements (Zurbuchen and Richardson, 2006). These include: counterstreaming suprathermal electrons, low proton temperature, declining speed profile, enhanced solar wind ion charge states and/or variable composition, and helium abundance enhancements. ICMEs are often (but not always) preceded by interplanetary shock waves (Marubashi, 1997; Bothmer and Schwenn, 1998). We can further distinguish a subset of ICMEs, termed “magnetic clouds” (MCs), that include a coherent structure with a large, smooth rotation of the magnetic field through the event, in concert with an enhanced magnetic field strength and relatively low proton temperature and plasma- β (Burlaga *et al.*, 1981; Klein and Burlaga, 1982). The terms “magnetic cloud” and “flux rope” are often used interchangeably. However, the latter is less rigorously defined, typically requiring only a coherent rotation in the magnetic field. Here, we will reserve FR to describe the magnetic structure near the Sun and MC to describe the relevant *in-situ* measurements.

Few ICMEs display all of these signatures. To compound this, *in-situ* measurements (with the notable exceptions of composition and charge states) are a convolution of intrinsic and evolutionary effects, and disentangling them can be difficult, if not impossible. Clearly, ICMEs are related to CMEs, yet the connection is not always obvious (Riley *et al.*, 2006; Möstl *et al.*, 2009).

ICMEs that are not MCs, or do not obviously contain an MC, need their own moniker. Burlaga *et al.* (2001) suggested the term “complex ejecta” (CE), while others have used the

phrase “non-MC ICME” (e.g., Richardson and Cane, 2004a; Zurbuchen and Richardson, 2006; Gopalswamy, 2010). Since ejecta are observed that could be classified as “simple” but do not contain a clear rotation in the magnetic field, for our purposes the former definition could be misleading (although it could be used for a specific set of events that are complex but do not contain FRs). For clarity, we will refer to the ICMEs with no obvious MC association as non-magnetic clouds, or non-MCs. Thus, $N_{\text{ICME}} = N_{\text{MC}} + N_{\text{non-MC}}$.

A number of studies have investigated the statistical properties of ICMEs and/or MCs. Burlaga *et al.* (2001) studied the properties of fast solar wind ejecta observed by the *Advanced Composition Explorer* (ACE) during 1998–1999 identifying two distinct classes. Although limited to only nine events, they found that, compared to MCs, the CEs had: i) weaker magnetic fields, ii) higher proton temperatures, iii) higher plasma- β , and iv) comparable speeds. Of more significance, the CEs were twice as wide (in the radial direction) as the MCs. Since CMEs near the Sun are inferred to occasionally interact with one another (e.g., Gopalswamy *et al.*, 2001), this led Burlaga *et al.* (2001) to suggest that CEs were the result of the interaction of two or more MCs nearer to the Sun than the point of observation.

The importance of the spacecraft’s trajectory through an event in determining the observed properties has been suspected for a long time. For example, Cane (1988) showed that He abundance enhancements, indicating the presence of ejecta, tended to disappear with increasing angular (longitudinal) distance from the source, suggesting that the flank of the shock, but not the ejecta itself, was being intercepted. Cane, Richardson, and Wibberenz (1997) also concluded that MCs originated, on average, closer to central meridian than non-cloud ICMEs based on *Helios* observations. More recently, Gopalswamy (2006), distinguishing between MCs, non-MCs, and driverless shocks, found that MCs originated close to central meridian longitude ($< 30^\circ$), whereas non-MCs were distributed more broadly across the disk. Most of the driverless shocks originated near the solar limbs (both east and west). These results are consistent with the idea that the observer’s position governs whether one sees an MC. However, some exceptions had to be accounted for; in particular, several driverless shocks, as well as numerous non-MCs that originated from disk center.

Richardson and Cane (2010) updated and expanded their earlier studies (Cane and Richardson, 2003; Richardson and Cane, 2004a) of ICMEs observed near Earth to encompass all events from 1996 through 2009. Of relevance to the present study, they found that solar sources (halo, partial halo, H α , or flare reports) could not be found for 46 % of the ICMEs observed at Earth. For the events for which a source could be found, 95 % lay within 50° of central meridian and 57/43 % of the events lay to the west/east, although the mean location was $W3.2^\circ$. They also extended an earlier analysis of the relative fraction of ICMEs that were magnetic clouds as a function of solar cycle (Cane and Richardson, 2003; Richardson and Cane, 2004b; Riley *et al.*, 2006). Previously, they had shown a tentative result that the MC fraction was larger at solar minimum than at maximum. While the more recent period (2004–2009) was not inconsistent with this, the results (albeit based on a small number of events) did not increase support. They also found a modest correlation (0.6) between the speed and maximum magnetic field strength for those events that were MCs; in contrast, the correlation was weak (0.28) for events that were not MCs. Finally, they noted that, frequently, MC structures were observed to be substructures of larger, more complex ICME regions.

Du, Zuo, and Zhang (2010) developed a comprehensive list of 181 ICMEs observed by the *Ulysses* spacecraft, of which 43 % were identified as MCs. Again, limiting our discussion to relevant points, they found no clear change in the MC fraction with heliolatitude: While there were more MCs than non-MCs in the northern hemisphere (above 50°), the reverse was true in the southern hemisphere.

Most recently, Richardson and Cane (2011) applied the same types of analyses previously performed on near-Earth events to 270 ICMEs they identified in the *Ulysses* measurements. Of these, 125 events overlapped with the events identified by Du, Zuo, and Zhang (2010). Once again, they found a trend for the MC fraction to increase at solar minimum. However, unlike their near-Earth study, the increase was clearer during the most recent minimum (2008). They also concluded that there was a tendency for the MC fraction to increase away from the solar equator, which they argued was consistent with the idea of preferentially intercepting the axis of a flux rope embedded within an ICME when at the latitude of the solar active regions. Additionally, they identified 11 ICMEs that were observed both at *Ulysses* and near Earth when the two spacecraft were separated by less than 30° longitude. Of these, four contained flux rope structure at both locations; five contained flux rope structure at *Ulysses* but not at Earth; one contained flux rope structure at Earth but not at *Ulysses*; and one was devoid of flux rope structure at both locations.

In an attempt to better understand the relationship between MCs and ICMEs, we have identified five possible ideas that might explain why either MCs or non-MCs might appear in *in-situ* measurements. These are described next.

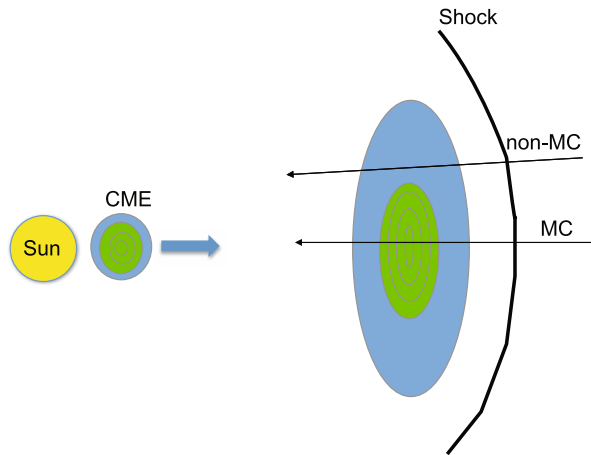
1.1. Is the Presence or Absence of an MC an Observational Selection Effect?

One possible explanation for the relationship between MCs and ICMEs, as discussed above, is that of an “observational selection” effect (*e.g.*, Riley *et al.*, 2003, 2006): Whether one observes an MC depends on the spacecraft’s trajectory through the ejecta (Figure 1). In this scenario, all ICMEs have an MC embedded within a larger ejecta. If MCs are observed only when the spacecraft is fortuitously positioned so that it passes sufficiently close to the flux rope’s axis, then geometrical considerations can be used to assess this hypothesis. For example, consider a flux rope launched with its axis parallel to, and in the heliographic equator. The cross section is shown in Figure 1. We might anticipate intercepting an MC over a broad range of longitudes, but confined to near-equatorial latitudes. At higher latitudes, the spacecraft would likely intercept a shock and sheath region, and then enter an ejecta-like structure, for example, with depressed temperature and compositional anomalies, but without a rotation of the magnetic field. In practice, CMEs are launched from a range of latitudes, which tend to cluster at mid-latitudes where active regions form, and this pattern changes during the course of the solar cycle. Nevertheless, if this picture holds, we might expect the MC fraction to decrease at sufficiently high latitudes.

1.2. Do MC–MC Interactions Destroy Flux Rope Structure?

A second possibility is that two or more MCs interact with one another to produce a CE (or non-MC), destroying the coherent MC structure in the process (Burlaga *et al.*, 2001). Thus, near the Sun the CME contained a FR that was subsequently destroyed prior to being observed at 1 AU or beyond. In this case, we make the explicit association of non-MCs with the “complex ejecta” structures described by Burlaga *et al.* (2001). In their study, they found that the average radial width of such an event was more than twice that for an MC. Thus, hypothesizing that CEs are created by CME–CME interactions suggests that, on average, they should be two or, for three-body interactions, even three times as wide as MCs. Note that the events in the Burlaga *et al.* (2001) study were carefully chosen. The interval was limited to a 1.8-year period in 1998/1999, which coincided with the ascending phase of Solar Cycle 23. Only fast ejecta ($v > 600 \text{ km s}^{-1}$) were considered, which resulted in a total of nine events: four MCs and five CEs, or an MC fraction of $\approx 44 \%$.

Figure 1 Schematic illustrating how the spacecraft's trajectory through an ICME might lead to either the identification of a magnetic cloud or a non-MC (or CE).



Although Burlaga *et al.* (2001) analyzed the duration of the structure as it passed the spacecraft, in view of the hypothesis that aggregations of MCs produce CEs (or non-MCs), the width of the event would appear to be a more appropriate parameter. This is given by: $d \approx \langle v_{\text{CME}} \rangle \times \tau_{\text{CME}}$, where $\langle v_{\text{CME}} \rangle$ is the average speed of the CME and τ_{CME} is the duration of the CME as it passes over the spacecraft. In summary, if MC–MC interactions are a major effect in producing non-MCs, we would expect, on average, that the latter are larger than the former.

1.3. Do Evolutionary Processes in the Solar Wind Produce Flux Ropes?

A third and related possibility is that evolutionary processes within the CME produce a flux rope. In a sense, this reflects the opposite outcome to idea ii). Observations and modeling suggest that CMEs are born as high-pressure structures close to the Sun, due to the large fields and/or densities. As they move farther away and expand, they relax to a more force-free configuration, potentially allowing a complex magnetic field structure to evolve into a more coherent structure (see Figure 2). In this scenario, ICMEs would evolve into MCs with increasing distance from the Sun (J.T. Gosling, personal communication, 1996). In a similar vein, Bellan (2000) argued that a Taylor-like relaxation, whereby the plasma inside a fusion device is driven toward a force-free helical state (Taylor, 1974), might apply to prominences in the corona, in part based on laboratory experiments. If such a scenario holds, we might expect to observe a greater proportion of MCs to ICMEs at larger heliocentric distances; that is, the MC fraction should increase with increasing distance from the Sun. However, Richardson and Cane (2004b), analyzing *Helios* data, did not find a systematic trend in MC fraction and heliocentric distance.

1.4. Are There Two (or More) Intrinsic Mechanisms that Produce Flux-Rope and Non-flux-Rope CMEs?

A superficially obvious explanation for the apparent bimodal presence of MCs and non-MCs is that there are two (or more) distinct mechanisms producing them. A range of self-consistent models of CME initiation and eruption have already been developed, all of which naturally produce FRs in the corona, and, by inference, MCs in the solar wind (see, *e.g.*, Riley *et al.*, 2004). On the other hand, only *ad hoc* schemes, such as pressure pulses, or

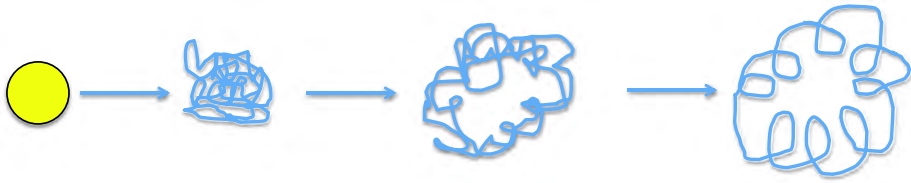


Figure 2 Schematic illustrating how a Taylor relaxation process might produce magnetic clouds from initial non-MCs. For simplicity, the magnetic field is shown as detached from the Sun, but in reality, field lines threading the ejecta would connect back to the Sun. Adapted for ICMEs from a drawing by Bellan (2000).

blast waves (see, *e.g.*, Odstrcil, 2009), can even claim to produce interplanetary transient structures that have no FR component. Thus, as yet there is no self-consistent mechanism starting at or below the photosphere capable of producing a large-scale eruption that does not contain helical fields within it. Therefore, we must appeal to either a new, as yet undiscovered process, or the modification of an existing one that is capable of producing something sufficiently complex. Given the intrinsically more complicated geometry of the “break out” configuration (see, *e.g.*, Lynch *et al.*, 2008), one could posit that it might naturally produce a non-MC, whereas eruption from within a dipolar configuration would be more likely to produce an MC. Of course one could assemble other combinations of “simple” *versus* “complex” scenarios, such as eruptions within active regions *versus* polar crown filaments. However, without a clear set of predictions that can be differentially tested in the data, it would be impossible to confirm or refute a specific pairing.

1.5. Are MCs Merely a Limiting, Easily Identifiable Subset of a Continuum Range of Magnetic Fluctuations Within Ejecta?

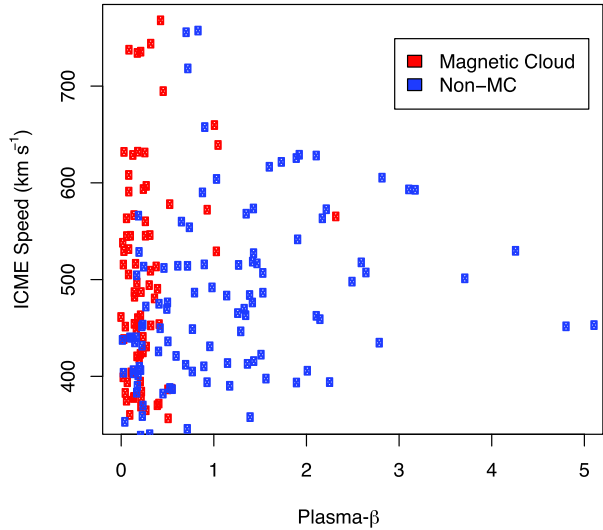
As scientists (or humans), we are driven by a desire to classify objects. MCs represent an obvious coherent structure that can be easily identified in multi-day time series of the interplanetary magnetic field, which makes them an obvious candidate for receiving a name and definition. Since non-MC ICMEs share similar plasma attributes, differing primarily in their magnetic properties, it is natural for us to create two classifications into which all cases neatly fit. But what if the classification is merely threshold based? That is, what if a broad and relatively flat spectrum of event types is produced, but only those that are sufficiently “clear” are identified as MCs? To assess this, we must use a technique that is not “biased” with our tendency to subjectively find patterns in the objects we see.

Thus, in this study we will analyze *Ulysses in-situ* measurements from launch through 2008 to uncover evidence that either supports or refutes one or more of these ideas concerning the relationship between MCs and ICMEs. In particular, we will use a logistic regression analysis to develop a statistical model relating CME properties to the likelihood that an MC is present within the ejecta, using the Akaike information criterion (AIC) to assess which predictor variables best define the model. We will then apply a clustering analysis using a Gaussian mixture model (GMM) to determine whether the data support grouping ICMEs into two or more specific groups, and if so, whether these clusters match the subjective delineation of events into MCs and non-MC ICMEs.

2. Statistical Analysis of *Ulysses* ICMEs

To investigate the relationship between MCs and ICMEs, we use *Ulysses* one-hour averaged data from launch through 2008, obtained from COHWeb at the Space Physics Data Fa-

Figure 3 ICME speed *versus* plasma- β for 181 ICMEs identified by Du, Zuo, and Zhang (2010), color-coded according to whether they were (red) or were not (blue) magnetic clouds.



cility (SPDF) at NASA/GSFC (<http://cohoweb.gsfc.nasa.gov/>). Several comprehensive lists of ICMEs observed by *Ulysses* have been developed in recent years (Ebert *et al.*, 2009; Du, Zuo, and Zhang, 2010; Richardson and Cane, 2011). While there is a significant overlap between these lists (Richardson and Cane, 2011), there are a notable number of differences. Du, Zuo, and Zhang (2010)'s list is the most sparse, containing a total of 181 ICMEs, while Richardson and Cane (2011)'s list is the most extensive, with 270 events. When conducting a statistical analysis, it makes sense to err on the conservative side, provided a sufficiently large number of events are present. Thus, here we restrict our analysis to those events identified by Du, Zuo, and Zhang (2010). Of their identified 181 ICMEs, 77 (or 43 %) were MCs.

In Figure 3 we present all 181 events separated into MCs and non-MCs as a function of solar wind speed and plasma- β , where the plasma- β is defined as $\frac{2n_p k_B T_p}{B^2 / \mu_0}$, where k_B is the Boltzmann constant, and n_p and T_p are the proton density and temperature, respectively. This clearly demonstrates the strong dependence on low values of plasma- β for MCs. This is not surprising, given that MCs are defined by their high magnetic field strength, and, because they are often observed to be expanding, their low density. The figure also hints at a possible dependence on speed, with a tendency for MCs to display a broader range in speed. However, this plot does not separate the two classifications fully: a significant number of the non-MCs are also low- β ($\ll 1$) objects (although there are no low- β , high-speed non-MCs).

In the following sections we apply two statistical analysis techniques to these events: logistic regression and Gaussian mixture models.

2.1. Logistic Regression of the *Ulysses* ICMEs

Logistic regression is a useful technique for predicting a binary outcome from a set of continuous predictor variables (Hosmer and Lemeshow, 2000); that is, it can be used for classification purposes. In our case, the outcome variable is whether the ICME is an MC or not, and the predictor variables are a set of continuous (but averaged for each event) parameters, including plasma- β , speed, width, magnetic field strength, plasma density, α/P ratio, temperature, average charge state of iron (QFe), the ratio of O^7 to O^6 (O^7/O^6), heliocentric

distance, latitude, and sunspot number (SSN). This is not an exhaustive list, but it does include the primary variables used to describe the properties of ICMEs. We note that the last three parameters – distance, latitude, and SSN – are not intrinsic parameters of the event; in fact, distance and latitude are sensitive to the position of the spacecraft. However, they can still be useful for assessing whether the likelihood of identifying an MC, rather than a non-MC, is dependent on the spacecraft’s position in the heliosphere. Similarly, the presence or absence of MCs can be related to the phase of the solar cycle by including SSN as a predictor variable.

We define our binary outcome variable (y) to be 0 or 1, where the latter is the identification of an MC, and write the probability, p , that $y = 1$:

$$\text{logit}(p) = \ln(p/(1 - p)) = \beta_0 + \beta_1 \times x_1 + \dots + \beta_k \times x_k. \quad (1)$$

This represents the logistic regression of y on the predictor variables x_1, \dots, x_k through the estimation of the parameters β_0 through β_k , and, practically speaking, gives the probability that an event described by the observed quantities x_1, \dots, x_k will be an MC. The *logit* function, $\text{logit}(p) = \ln(p/(1 - p))$, is the logarithm of the odds ($p/(1 - p)$), *i.e.*, the chance of a given probability of an outcome occurring. Thus, the logistic regression coefficients give the change in the log odds of the outcome for a unit change in the predictor variable.

In practice, the best estimates of the parameters β_0 through β_k are obtained using the method of maximum likelihood via an interactively reweighted least squares method (Hosmer and Lemeshow, 2000). In contrast to the more familiar least-squares approach, which minimizes variation from the model, maximum likelihood finds the model equation with the highest probability (*i.e.*, likelihood) of explaining the outcome variable, given the predictor variables. In the following analysis, we use the generalized linear model (GLM) implemented in the statistical package R, which includes the logistic regression method described above (Faraway, 2006).

To assess the quality of a particular statistical model, we apply the Akaike Information criterion (AIC), which measures the relative goodness-of-fit (Akaike, 1974). It is based on the idea of minimizing the amount of information lost when a particular model is used to approximate reality. In general, the AIC can be defined as:

$$\text{AIC} = 2K - 2 \ln(L), \quad (2)$$

where K is the number of parameters in the statistical model and L is the maximized likelihood function for the model. The likelihood function expresses the probability of the observed data as a function of the unknown parameters. Thus, the maximized likelihood function involves the selection of those parameters that give the observed data the greatest probability. Practically speaking, the “best” model for a set of predictor variables is the one that minimizes the AIC value. Since AIC includes the number of parameters (*i.e.*, predictor variables), K , the AIC value is penalized for each parameter added; thus, parsimonious models are encouraged. It is important to note that the AIC does not tell us which is the correct model from a physical point of view, only the one that best matches the data. From a different perspective, the AIC score allows us to discount models that perform poorly.

For our purposes, we will treat the AIC score as a defensible method for assessing whether the presence or absence of MCs is dependent on a particular predictor variable, which, in turn, allows us to argue in favor of or against one or more of the ideas that we introduced earlier to explain the MC/ICME relationship.

One final potentially useful statistical tool to apply in our analysis is the variation inflation factor (VIF). It is well known that some solar wind parameters display strong collinearity

with one another, which, if both were included in the statistical model, would be misleading. Plasma- β and magnetic field strength are obvious examples. While we could perform correlation tests for pairs of predictor variables, looking for large positive or negative correlations, this approach has drawbacks. For example, it is possible that a strong linear dependence exists between three or more variables, yet pairwise correlations between them are small. Computing the VIF circumvents this problem by estimating the factor by which the variance increases for each estimated coefficient β_k . We define the VIF for the k th variable to be:

$$\text{VIF}_k = \frac{1}{1 - R_k^2}, \quad (3)$$

where R_k^2 is the multiple correlation between the k th variable and all other variables (Afifi, Clark, and May, 2011). Thus, as R_k approaches 1, signaling the presence of collinearity, the VIF becomes large. Typically, multicollinearity is considered high when $\text{VIF} > 5$.

Table 1 summarizes an initial logistic regression analysis of the *Ulysses* CMEs. The first column lists the 13 predictor variables that were included. We note that two temperatures are computed from the *Ulysses* ion instrument measurements, (T_{\min} and T_{\max}) which are both reported to the SPDF. With no compelling reason to choose one over the other, at least initially, we retain both. The last column ($\text{Pr}(> |z|)$), known as the “ p -value,” gives a measure of the significance of a particular predictor variable. Typically values < 0.01 provide convincing evidence of the significance of a variable. However, we emphasize that this is only statistical evidence and not proof of a causal relationship. Thus, employing a 5% threshold, we infer that plasma- β , width, O^7/O^6 , and heliocentric distance are “parameters of interest,” worthy of further scrutiny. Also note that high p -values do not prove the null hypothesis, *i.e.*, that the variable is not significant, they only tell us that our dataset coupled with the analysis technique was not able to identify such a relationship. Of these, plasma- β , width, and O^7/O^6 are most significant. The second column gives the best-fit coefficient for each predictor variable, $\hat{\beta}_k$ (where the $\hat{}$ denotes the maximum likelihood estimate of the k th variable). Thus, the likelihood of identifying an ICME as an MC depends strongly on it having: i) a low plasma- β , ii) a large width, and iii) high O^7/O^6 . Note that, at least during this initial analysis, speed, density, α/P ratio, QFe, and latitude do not appear to be significant. Although not as important for our study, we note that column three gives the standard error of the estimated coefficients, and column four displays the ratios of the estimated coefficients to their estimated standard error.

Next, we assess the effects on the AIC score of dropping any one predictor variable for the model. Table 2 summarizes this. Again, column one lists each of the predictor variables. The initial AIC score is given in the first cell of column four, with the remaining cells giving the revised AIC score if that variable is dropped. Columns two, three, and five give the degrees of freedom, deviance, and likelihood ratio test (LRT). The deviance is a “quality of fit” statistic and essentially measures the deviation of the reduced model to the full model, while the LRT gives a measure as to the statistical significance of the variable in the multivariate model. For example, we conclude that dropping SSN, that is, the phase of the solar cycle, reduces the AIC score modestly, while dropping the plasma- β raises it dramatically. Since our objective is to lower the AIC score, this suggests that SSN is not a significant variable but that plasma- β and width are.

Before culling parameters from our list of predictor variables based on AIC rankings, as a check for collinearity, we estimated the VIFs for each variable. Not surprisingly, we found $\text{VIF}_{T_{\min}} = 10.3$, since T_{\min} and T_{\max} are highly correlated. However, since neither T_{\min} nor T_{\max} was found to be sufficiently significant, both were removed from the analysis.

Table 1 Results of logistic regression analysis. Column one lists the predictor variables used in the statistical model, column two (Estimate) gives the estimated value of the regression coefficient for each variable, column three (Std. error) gives the standard error for these estimates, column four (z value) gives the results of the z test, and column five ($\text{Pr}(> |z|)$) provides the p -values.

Predictor variable	Estimate	Std. error	z value	$\text{Pr}(> z)$
(Intercept)	0.6030	3.3528	0.180	0.8573
SSN	-0.0046	0.0086	-0.537	0.5910
Plasma- β	-2.9918	0.8938	-3.347	0.0008
Speed	0.0027	0.0043	0.622	0.5337
Width	1.5982	0.4878	3.276	0.0011
Field strength	0.1269	0.0740	1.715	0.0863
Proton density	0.0781	0.0778	1.004	0.3155
α/P ratio	-15.0391	16.9151	-0.889	0.3740
T_{\min}	0.0000	0.0000	1.278	0.2013
T_{\max}	-0.0000	0.0000	-1.694	0.0903
QFe	0.0290	0.1899	0.153	0.8786
O^7/O^6	2.3950	0.8686	2.757	0.0058
Heliocentric distance	-0.8605	0.3765	-2.285	0.0223
Latitude	-0.0173	0.0185	-0.932	0.3512

Table 2 Variation in AIC score when each predictor variable is dropped from the analysis. Column one lists each predictor variable, column two (Df) gives the number of degrees of freedom, column three gives the deviance, column four gives the AIC score, column five gives the results of the likelihood ratio test (*i.e.*, the deviance change), and column six gives the p -value.

Predictor variable	Df	Deviance	AIC	LRT	$\text{Pr}(\text{Chi})$
(none)		117.2	145.2		
SSN	1	117.5	143.5	0.289	0.59059
Plasma- β	1	137.4	163.4	20.182	0.00001
Speed	1	117.6	143.6	0.391	0.53200
Width	1	128.9	154.9	11.642	0.00064
Field strength	1	120.4	146.4	3.138	0.07647
Proton density	1	118.2	144.2	0.987	0.32057
α/P ratio	1	118.1	144.1	0.826	0.36355
T_{\min}	1	118.8	144.8	1.572	0.20992
T_{\max}	1	120.0	146.0	2.716	0.09933
QFe	1	117.3	143.3	0.024	0.87615
O^7/O^6	1	125.8	151.8	8.576	0.00341
Heliocentric distance	1	123.2	149.2	5.971	0.01454
Latitude	1	118.2	144.2	0.911	0.33979

Rerunning the logistic regression with the new subset of predictor variables yielded the results in Table 3: plasma- β , CME width, and O^7/O^6 remain the strongest variables, with heliocentric distance the weakest. Importantly, these results strongly imply that the likeli-

Table 3 Logistic regression analysis for subset of most significant predictor variables. See Table 1 for a description of the column headings.

Predictor variable	Estimate	Std. error	z value	Pr(> z)
(Intercept)	0.4651	0.7744	0.601	0.5481
Plasma- β	-2.9253	0.7473	-3.915	0.0001
Width	1.5000	0.4470	3.356	0.0008
O^7/O^6	2.4366	0.7385	3.299	0.0010
Heliocentric distance	-0.3542	0.1799	-1.969	0.0490

Table 4 Variation in AIC score when each of the most significant predictor variables is dropped from the analysis. See Table 2 for a description of the column headings.

Predictor variable	Df	Deviance	AIC	LRT	Pr(Chi)
(none)		134.8	144.8		
Plasma- β	1	166.4	174.4	31.536	0.00000
Width	1	147.3	155.3	12.505	0.00041
O^7/O^6	1	153.5	161.5	18.678	0.00002
Heliocentric distance	1	138.9	146.9	4.059	0.04395

hood of observing an MC increases with CME width and higher O^7/O^6 , but decreases with heliocentric distance and plasma- β .

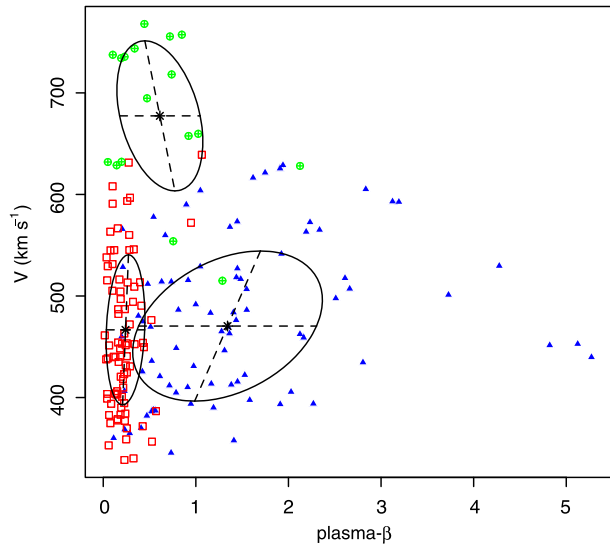
For completeness, and as a complementary check, we repeated the exercise of dropping each predictor variable from the statistical model and recomputed the AIC score. This is shown in Table 4. Focusing on column four, this reinforces the result that, in decreasing order of significance, plasma- β , O^7/O^6 , width, and then heliocentric distance best predict the presence of an MC.

2.2. Gaussian Mixture Model Analysis of *Ulysses* ICMEs

In the previous section we used logistic regression analysis to build a statistical model that related continuous predictor variables to a known (at least subjectively) binary outcome variable (MC or non-MC). However, a complementary question is whether the ICME parameters (*i.e.*, the predictor variables) are clustered into subpopulations. Thus, whereas the logistic regression analysis relied on our identification of the ICME as being either an MC or a non-MC, clustering analysis attempts to find natural groups based only on the predictor variables; *i.e.*, it uses statistical inference derived from the entire population of events without any prior knowledge of the sub-populations. Therefore, to address the question of whether MCs are really a distinct class, we can attempt to identify distinct clusters and see if they match with the events that were identified as either MCs or non-MCs in the *Ulysses* ICME list by Du, Zuo, and Zhang (2010).

The approach we use here is known as the Gaussian mixture model (GMM) (Everitt and Hand, 1981; McLachlan and Peel, 2000). We assume that N observed variables are distributed according to a mixture of K components, where each component belongs to some parametric family, each of which has a different set of parameters. Here, we further assume that the families are Gaussian, being defined by their own mean and variance. That is, each cluster is defined by a Gaussian distribution in the predictor variable parameter space

Figure 4 ICME speed versus plasma- β for *Ulysses*-observed ICMEs. The CMEs are color-coded according to the three components identified by the GMM analysis.



with a unique mean and variance. Computationally, we use the *MCLUST* routine developed for the statistical package *R*, which relies on a Bayesian information criterion (BIC) score to estimate the best clusters. (See also Press *et al.*, 2007 for a discussion on implementing this technique numerically.) BIC and AIC are similar but distinct criteria for model selection, with BIC penalizing free parameters more strongly than AIC. While the number of clusters in GMMs can be specified *a priori*, here, we allow the algorithm to minimize the BIC score by varying the number of components from 1 through 9. For this analysis, we used a subset of parameters listed in Table 1 (plasma- β , speed, width, and O^7/O^6). The results are shown in Figures 4 and 5.

The GMM analysis found that the data were best fit by three components, as identified in Figure 4. Two of the clusters (red and green) tend to have low plasma- β but are separated by speed, whereas the third cluster (blue) has a larger plasma- β and more moderate speed. Comparing these clusters with the events identified subjectively by Du, Zuo, and Zhang (2010) to be either MCs or non-MCs (Figure 3) shows that the red/green clusters overlap well with the MCs, while the blue cluster overlaps with the non-MCs. In fact, the fraction of red/green events that were also MCs was 86 %, while the fraction of the blue events that were also non-MCs was 68 %; both significantly larger than would be expected by chance.

In Figure 5, a scatter-plot matrix is shown, summarizing the relationship between these three clusters and the parameters of the ICMEs. In addition to the relatively obvious clustering in plasma- β – speed space (column 1, row 2) already discussed in relation to Figure 4, the ICMEs are also well separated in width – O^7/O^6 space (column 3, row 4). Specifically, what distinguishes the fast MCs (green) is that they are also wider and have a lower O^7/O^6 ratio than the red component. Finally, we note that the dependence on CME width in the likelihood of an event being an MC rather than a non-MC ICME cannot be discerned in Figure 5. While this relationship is statistically significant, the difference between the mean width of MCs (0.77 AU) and non-MC ICMEs (0.73 AU) is only 0.04 AU, and is clearly not visible between these distributions.

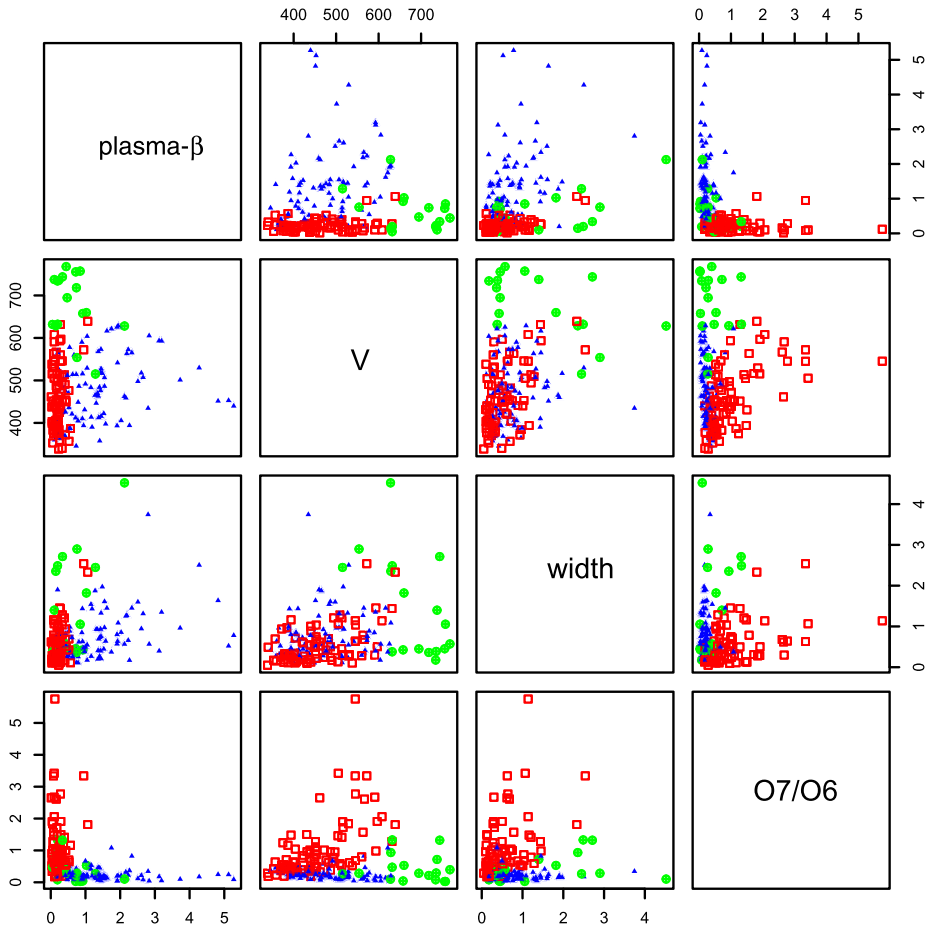


Figure 5 Scatter-plot matrix of plasma- β , speed (V), width, and O^7/O^6 of the ICMEs observed by *Ulysses*. Each panel is color-coded according to the three components identified by the GMM analysis.

3. Summary and Discussion

In this study, we have analyzed the properties of 181 ICMEs observed by the *Ulysses* spacecraft, in an attempt to understand the basic relationship between MCs and non-MCs. We applied two statistical techniques, logistic regression and Gaussian mixture models, to provide a more rigorous assessment of five ideas proposed to resolve the relationship between these two types of ejecta. Our results lead us to the conclusion that only ideas i) and iv) are consistent with the observations. That is, that either (a) an observational selection effect, or (b) the presence of two or more mechanisms is responsible for the MC/ICME relationship.

CME-CME interactions (idea ii)) cannot account for the presence of MCs and non-MCs. Logistic regression analysis strongly suggests that the propensity for an event to be identified as an MC is coupled to the width of the ejecta. Although we found only a modest difference in the size of MCs and non-MCs (0.77 AU versus 0.73 AU, respectively), the result was both statistically significant and in the wrong sense for CME-CME interactions to account for the creation of non-MCs: MCs are likely to be broader than non-MCs. However, a basic

prediction from the Burlaga *et al.* (2001) study was that MCs should be at least half the size of non-MCs, since MC-MC interactions would be unlikely to produce narrower structures. Of course, it is possible that such interactions may account for a small number of cases. In fact, this may explain why our results apparently contradict those of Burlaga *et al.* (2001): In their study, a small number of events (nine) were carefully chosen based on specific criteria.

Evolutionary processes (idea iii)), at least those envisaged through a Taylor-like relaxation process (Bellan, 2000), also cannot explain the relationship between MCs and non-MCs. If it were true, we would expect a trend for more MCs to be identified with increasing distance from the Sun. However, our analysis shows that exactly the opposite effect holds: MCs are less likely to be identified with increasing distance from the Sun.

Finally, we cannot relegate the MC/non-MC relationship to a figment of our imagination (idea v)). Clustering analysis suggests the existence of three distinct classes of ejecta, two of which overlap strongly with the MCs identified by Du, Zuo, and Zhang (2010), and a third which overlaps significantly with non-MCs.

Distinguishing between the remaining two ideas is challenging. First-principle models, which inevitably produce a well-formed flux rope, tend to support the idea that a flux rope is always present, and suggest that an ICME's identification as MC or non-MC in the solar wind must be related to where the observing spacecraft is located and its trajectory with respect to the ICME. However, this can be easily countered by the fact that current global CME models are highly idealized, and, by definition, must produce the simplest of structures. It is conceivable that as the realism of the models improves, they will be able to generate more and more complex structures – to the point that some events may be “complex” while others are “simple.” It is also possible that the degree of complexity might vary spatially within a single event.

An argument for or against a selection effect explanation could be resolved by geometrical arguments. As we have noted, other studies (*e.g.*, Cane, Richardson, and Wibberenz, 1997; Gopalswamy, 2006) suggest that MCs tend to be launched in longitude closer to central meridian (as viewed by the observing spacecraft) than non-MCs. On the other hand, Richardson and Cane (2011) found a weak tendency for the *Ulysses*-observed MC fraction to increase away from the equator, at least up to mid-latitudes. However, the logistic regression analysis described here finds no statistical support for the MC fraction to depend on latitude.

Ultimately, there is little to separate ideas i) and iv) at the location of Earth or *Ulysses*. Like the proverbial blind men feeling different parts of an elephant, relying only on *in-situ* measurements does not afford us the global view that we need to connect everything. Large-scale MHD models should eventually be able to assist us, but, as we have lamented, they are currently too idealized.

An intriguing result from the cluster analysis concerns the presence of three, not two (MC, non-MC) populations of *Ulysses* ICMEs, with MCs being divided into slower events with higher oxygen charge states, and faster, wider events with lower charge states. In particular, the inverse dependence of O^7/O^6 on MC speed appears to be contrary to previous studies based on near-Earth observations (*e.g.*, Richardson and Cane, 2004a) that indicate at least a modest increase in O^7/O^6 with MC speed. We suggest that the two populations of MCs arise principally from i) the *Ulysses* orbit, which extends to high latitudes; ii) the tendency for faster ICMEs to be found at higher latitudes because of the latitude dependence of the solar wind speed, especially around solar minimum when several of the MCs are observed; and iii) the fact that higher charge states in ICMEs are confined to latitudes below $\approx 30 - 40^\circ$. For example, Figure 6(a) shows average O^7/O^6 against ICME speed for the Du *et al.* ICMEs with the symbol type indicating the three groups identified in our study. The

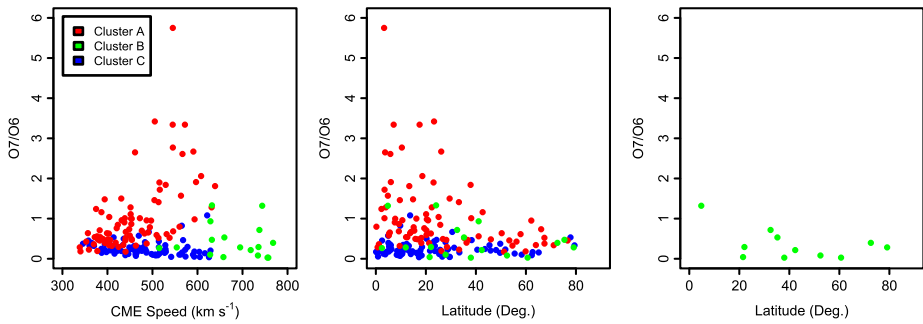


Figure 6 O^7/O^6 versus (a) ICME speed, (b) latitude, and (c) latitude of those “green” ICMEs traveling faster than 650 km s^{-1} .

tendency for the fast (green) MCs to have lower O^7/O^6 than slower MCs is clearly evident. However, the slower, red events do show evidence of an increase in O^7/O^6 with speed to values that exceed those in the green events. Figure 6(b) shows O^7/O^6 versus ICME helio-latitude, indicating that higher values (say > 1) are observed at low latitudes, below $\approx 40^\circ$. A possible interpretation is that the high charge states arising from plasma heating during CME formation and ejection are preferentially observed close to the location of the related solar event and hence are not detected at higher latitudes (see, e.g., Lepri and Zurbuchen, 2004). Figure 6(c) shows only those “green” events with speeds $> 650 \text{ km s}^{-1}$, illustrating that they were predominantly observed at higher latitudes, where higher charge states are more rarely observed. Thus, we suggest that the two populations of MCs indicated by the cluster analysis correspond to lower latitude MCs that typically do not reach high speeds but may have high ion charge states (red events), and a second population of faster ICMEs observed at higher latitudes but which have lower charge states (green events).

This work naturally suggests several possible avenues for future studies. First, it would be interesting to study the properties of the source locations for the “red” (slow and cool) and “green” (fast and hot) types of MCs hinted at by the clustering analysis (Figure 4). Does anything about their origin point to unique properties or processes? Second, how do the *in-situ* composition/charge state properties of the two types of MCs differ? Richardson and Cane (2004a), for example, noted that iron charge states tend to increase with magnetic cloud speed near the Earth, and a similar dependence was found for *Ulysses* events (Richardson and Cane, 2011). This, too, might hint at different origins. Third, do these results hold for ICMEs observed by near-Earth spacecraft? We focused here on ICMEs observed by *Ulysses* so that we could fold both latitude and heliocentric distance into our analysis; however, the database of near-Earth events is considerably larger (Richardson and Cane, 2010). Fourth, can ideas i) and iv) be distinguished from a larger and more systematic study of multi-spacecraft ICMEs? In addition to events observed simultaneously by near-Earth spacecraft (*Geotail*, *Wind*, and *ACE*) and *Ulysses* (see, e.g., Hammond *et al.*, 1995; Riley *et al.*, 2003; Du, Wang, and Hu, 2007; Rodriguez *et al.*, 2008; Richardson and Cane, 2011), events have been measured by *Helios* 1 and 2 (see, e.g., Kallenrode *et al.*, 1993; Cane, Richardson, and Wibberenz, 1997; Burlaga, Behannon, and Klein, 1987) and STEREO A and B (see, e.g., Liu *et al.*, 2008). If combined, these may result in a sufficiently large and statistically significant database from which the final two ideas can be distinguished.

Acknowledgements P.R. gratefully acknowledges the support of NSF’s FESD program as well as NASA SR&T and GI programs, the latter through a subcontract with NRL. We also acknowledge the use of *Ulysses*

observations from NASA/GSFC's Space Physics Data Facility's COHWeb service, and thank the *Ulysses* PIs who have made their observations available via this source.

References

- Afifi, A., Clark, V., May, S.: 2011, *Practical Multivariate Analysis*, 5th edn. *Texts in Statistical Science*, Taylor & Francis, London. ISBN9781439816806.
- Akaike, H.: 1974, A new look at the statistical model identification. *IEEE Trans. Autom. Control* **19**(6), 716–723.
- Bellan, P.M.: 2000, Simulating solar prominences in the laboratory. *Am. Sci.* **88**, 136. doi:[10.1511/2000.2.136](https://doi.org/10.1511/2000.2.136).
- Bothmer, V., Schwenn, R.: 1998, The structure and origin of magnetic clouds in the solar wind. *Ann. Geophys.* **16**, 1–24.
- Burlaga, L.F., Behannon, K.W., Klein, L.W.: 1987, Compound streams, magnetic clouds, and major geomagnetic storms. *J. Geophys. Res.* **92**, 5725–5734. doi:[10.1029/JA092iA06p05725](https://doi.org/10.1029/JA092iA06p05725).
- Burlaga, L.F., Sittler, E.C.J., Mariani, F., Schwenn, R.: 1981, Magnetic loop behind an interplanetary shock – *Voyager*, *Helios*, and IMP-8 observations. *J. Geophys. Res.* **86**, 6673–6684.
- Burlaga, L.F., Skoug, R.M., Smith, C.W., Webb, D.F., Zurbuchen, T.H., Reinard, A.: 2001, Fast ejecta during the ascending phase of solar cycle 23: ACE observations, 1998–1999. *J. Geophys. Res.* **106**(A10), 20957–20978.
- Cane, H.V.: 1988, The large-scale structure of flare-associated interplanetary shocks. *J. Geophys. Res.* **93**, 1–6. doi:[10.1029/JA093iA01p00001](https://doi.org/10.1029/JA093iA01p00001).
- Cane, H.V., Richardson, I.G.: 2003, Interplanetary coronal mass ejections in the near-Earth solar wind during 1996–2002. *J. Geophys. Res.* **108**, 1156. doi:[10.1029/2002JA009817](https://doi.org/10.1029/2002JA009817).
- Cane, H.V., Richardson, I.G., Wibberenz, G.: 1997, Helios 1 and 2 observations of particle decreases, ejecta, and magnetic clouds. *J. Geophys. Res.* **102**, 7075–7086. doi:[10.1029/97JA00149](https://doi.org/10.1029/97JA00149).
- Du, D., Wang, C., Hu, Q.: 2007, Propagation and evolution of a magnetic cloud from ACE to *Ulysses*. *J. Geophys. Res.* **112**, 9101. doi:[10.1029/2007JA012482](https://doi.org/10.1029/2007JA012482).
- Du, D., Zuo, P.B., Zhang, X.X.: 2010, Interplanetary coronal mass ejections observed by *Ulysses* through its three solar orbits. *Solar Phys.* **262**, 171–190. doi:[10.1007/s11207-009-9505-8](https://doi.org/10.1007/s11207-009-9505-8).
- Ebert, R.W., McComas, D.J., Elliott, H.A., Forsyth, R.J., Gosling, J.T.: 2009, Bulk properties of the slow and fast solar wind and interplanetary coronal mass ejections measured by *Ulysses*: Three polar orbits of observations. *J. Geophys. Res.* **114**, 1109. doi:[10.1029/2008JA013631](https://doi.org/10.1029/2008JA013631).
- Everitt, B.S., Hand, D.J.: 1981, *Finite Mixture Distributions*, Chapman & Hall, London, 652–658.
- Faraway, J.J.: 2006, *Extending Linear Models with r: Generalized Linear, Mixed Effects and Nonparametric Regression Models*, Chapman & Hall/CRC, London. ISBN1-584-88424-X. <http://www.maths.bath.ac.uk/~jff23/ELM/>.
- Gopalswamy, N.: 2006, Properties of interplanetary coronal mass ejections. *Space Sci. Rev.* **124**, 145–168. doi:[10.1007/s11214-006-9102-1](https://doi.org/10.1007/s11214-006-9102-1).
- Gopalswamy, N.: 2010, Corona mass ejections: A summary of recent results. In: Dorotovic, I. (ed.) *20th National Solar Physics Meeting*, 108–130.
- Gopalswamy, N., Yashiro, S., Kaiser, M.L., Howard, R.A., Boueret, J.L.: 2001, Radio signatures of coronal mass ejection interaction: Coronal mass ejection cannibalism? *Astrophys. J. Lett.* **548**(1), L91–L94.
- Hammond, C.M., Crawford, G.K., Gosling, J.T., Kojima, H., Phillips, J.L., Matsumoto, H., Balogh, A., Frank, L.A., Kokubun, S., Yamamoto, T.: 1995, Latitudinal structure of a coronal mass ejection inferred from *Ulysses* and Geotail observations. *Geophys. Res. Lett.* **22**(10), 1169–1172.
- Hosmer, D., Lemeshow, S.: 2000, *Applied Logistic Regression*, *Wiley Series in Probability and Statistics: Texts and References Section*, Wiley, New York. ISBN9780471356325.
- Hundhausen, A.J.: 1993, Sizes and locations of coronal mass ejections – SMM observations from 1980 and 1984–1989. *J. Geophys. Res.* **98**, 13177–13200.
- Kallenrode, M.B., Wibberenz, G., Kunow, H., Müller-Mellin, R., Stolpovskii, V., Kontor, N.: 1993, Multi-spacecraft observations of particle events and interplanetary shocks during November/December 1982. *Solar Phys.* **147**, 377–410. doi:[10.1007/BF00690726](https://doi.org/10.1007/BF00690726).
- Klein, L.W., Burlaga, L.F.: 1982, Interplanetary magnetic clouds at 1 AU. *J. Geophys. Res.* **87**, 613–624.
- Lepri, S.T., Zurbuchen, T.H.: 2004, Iron charge state distributions as an indicator of hot ICMEs: Possible sources and temporal and spatial variations during solar maximum. *J. Geophys. Res.* **109**, 6101. doi:[10.1029/2003JA009954](https://doi.org/10.1029/2003JA009954).
- Liu, Y., Luhmann, J.G., Huttunen, K.E.J., Lin, R.P., Bale, S.D., Russell, C.T., Galvin, A.B.: 2008, Reconstruction of the 2007 May 22 magnetic cloud: How much can we trust the flux-rope geometry of CMEs? *Astrophys. J. Lett.* **677**, L133–L136. doi:[10.1086/587839](https://doi.org/10.1086/587839).

- Lynch, B.J., Antiochos, S.K., DeVore, C.R., Luhmann, J.G., Zurbuchen, T.H.: 2008, Topological evolution of a fast magnetic breakout CME in three dimensions. *Astrophys. J.* **683**, 1192–1206. doi:[10.1086/589738](https://doi.org/10.1086/589738).
- Marubashi, K.: 1997, Interplanetary magnetic flux ropes and solar filaments, in coronal mass ejections. In: Crooker, N.U., Joselyn, J.A., Feynman, J. (eds.) *Coronal Mass Ejections*, *Geophys. Monogr. Ser.* **99**, AGU, Washington, 147.
- McLachlan, G., Peel, D.: 2000, *Finite Mixture Models* **44**, Wiley-Interscience, New York, 82. <http://pubs.amstat.org/doi/abs/10.1198/tech.2002.s651>.
- Möstl, C., Farrugia, C.J., Temmer, M., Miklenic, C., Veronig, A.M., Galvin, A.B., Leitner, M., Biernat, H.K.: 2009, Linking remote imagery of a coronal mass ejection to its *in situ* signatures at 1 AU. *Astrophys. J. Lett.* **705**, L180–L185. doi:[10.1088/0004-637X/705/2/L180](https://doi.org/10.1088/0004-637X/705/2/L180).
- Odstrcil, D.: 2009, Numerical simulation of interplanetary disturbances. In: Pogorelov, N.V., Audit, E., Colella, P., Zank, G.P. (eds.) *Numerical Modeling of Space Plasma Flows* **CS-406**, Astron. Soc. Pac., San Francisco, 141–148.
- Press, W.H., Teukolsky, S.A., Vetterling, W.T., Flannery, B.P.: 2007, *Numerical Recipes: The Art of Scientific Computing* **29**, Cambridge University Press, Cambridge 501. <http://www.jstor.org/stable/1269484?origin=crossref>.
- Richardson, I.G., Cane, H.V.: 2004a, Identification of interplanetary coronal mass ejections at 1 AU using multiple solar wind plasma composition anomalies. *J. Geophys. Res.* **109**, 9104. doi:[10.1029/2004JA010598](https://doi.org/10.1029/2004JA010598).
- Richardson, I.G., Cane, H.V.: 2004b, The fraction of interplanetary coronal mass ejections that are magnetic clouds: Evidence for a solar cycle variation. *Geophys. Res. Lett.* **31**, 18804. doi:[10.1029/2004GL020958](https://doi.org/10.1029/2004GL020958).
- Richardson, I.G., Cane, H.V.: 2010, Near-Earth interplanetary coronal mass ejections during Solar Cycle 23 (1996–2009): Catalog and summary of properties. *Solar Phys.*, 189–237. doi:[10.1007/s11207-010-9568-6](https://doi.org/10.1007/s11207-010-9568-6).
- Richardson, I.G., Cane, H.V.: 2011, Identification of interplanetary coronal mass ejections at *Ulysses* using multiple solar wind signatures, and comparison with ICMEs observed at the Earth and in the inner heliosphere. AGU Fall Meeting Abstracts, SH31B–1979.
- Riley, P., Linker, J.A., Mikić, Z., Odstrcil, D., Zurbuchen, T.H., Lario, D., Lepping, R.P.: 2003, Using an MHD simulation to interpret the global context of a coronal mass ejection observed by two spacecraft. *J. Geophys. Res.* **108**, 1272.
- Riley, P., Linker, J.A., Lionello, R., Mikić, Z., Odstrcil, D., Hidalgo, M.A., Cid, C., Hu, Q., Lepping, R.P., Lynch, B.J., Rees, A.: 2004, Fitting flux ropes to a global MHD solution: A comparison of techniques. *J. Atmos. Solar-Terr. Phys.* **66**, 1321–1331.
- Riley, P., Schatzman, C., Cane, H.V., Richardson, I.G., Gopalswamy, N.: 2006, On the rates of coronal mass ejections: Remote solar and *in situ* observations. *Astrophys. J.* **647**, 648–653. doi:[10.1086/505383](https://doi.org/10.1086/505383).
- Riley, P., Lionello, R., Mikić, Z., Linker, J.: 2008, Using global simulations to relate the three-part structure of coronal mass ejections to *in situ* signatures. *Astrophys. J.* **672**, 1221–1227. doi:[10.1086/523893](https://doi.org/10.1086/523893).
- Rodriguez, L., Zhukov, A.N., Dasso, S., Mandrini, C.H., Cremades, H., Cid, C., Cerrato, Y., Saiz, E., Aran, A., Menvielle, M., Poedts, S., Schmieder, B.: 2008, Magnetic clouds seen at different locations in the heliosphere. *Ann. Geophys.* **26**, 213–229. doi:[10.5194/angeo-26-213-2008](https://doi.org/10.5194/angeo-26-213-2008).
- Schieb, P.A.: 2011, Geomagnetic storms. Technical report. <http://www.oecd.org/dataoecd/57/25/46891645.pdf>.
- Taylor, J.B.: 1974, Relaxation of toroidal plasma and generation of reverse magnetic fields. *Phys. Rev. Lett.* **33**, 1139–1141. doi:[10.1103/PhysRevLett.33.1139](https://doi.org/10.1103/PhysRevLett.33.1139).
- Tousey, R.: 1973, First results from Skylab. *Bull. Am. Astron. Soc.* **5**, 419.
- Zurbuchen, T.H., Richardson, I.G.: 2006, *In-situ* solar wind and magnetic field signatures of interplanetary coronal mass ejections. *Space Sci. Rev.* **123**, 31–43. doi:[10.1007/s11214-006-9010-4](https://doi.org/10.1007/s11214-006-9010-4).

Magnetic reconnection driven by filament eruption in the 7 June 2011 event

L. van Driel-Gesztelyi^{1,2,3}, D. Baker¹, T. Török⁴, E. Pariat², L.M. Green¹, D.R. Williams¹, J. Carlyle¹, G. Valori², P. Démoulin², S.A. Matthews¹, B. Kliem⁵, J.-M. Malherbe²

¹ University College London, Mullard Space Science Laboratory, Holmbury St. Mary, Dorking, Surrey RH5 6NT, UK

² LESIA, Observatoire de Paris, CNRS, UPMC, Université Paris Diderot, 5 place Jules Janssen, 92190 Meudon, France; email: Lidia.vanDriel@obspm.fr

³ Konkoly Observatory, Hungarian Academy of Sciences, Budapest, Hungary

⁴ Predictive Science Inc., 9990 Mesa Rim Rd., Suite 170, San Diego, CA 92121, USA

⁵ Institut für Physik und Astronomie, Universität Potsdam, Karl-Liebknecht-Str. 24-25, 14476 Potsdam, Germany

Abstract. During an unusually massive filament eruption on 7 June 2011, SDO/AIA imaged for the first time significant EUV emission around a magnetic reconnection region in the solar corona. The reconnection occurred between magnetic fields of the laterally expanding CME and a neighbouring active region. A pre-existing quasi-separatrix layer was activated in the process. This scenario is supported by data-constrained numerical simulations of the eruption. Observations show that dense cool filament plasma was re-directed and heated in situ, producing coronal-temperature emission around the reconnection region. These results provide the first direct observational evidence, supported by MHD simulations and magnetic modelling, that a large-scale re-configuration of the coronal magnetic field takes place during solar eruptions via the process of magnetic reconnection.

Keywords. MHD, instabilities, Sun: activity, magnetic fields, coronal mass ejections (CMEs), filaments, methods: numerical, data analysis

A spectacular solar eruption occurred on 7 June 2011 observed by NASA's Solar Dynamic Observatory's Atmospheric Imaging Assembly (SDO/AIA). The CME originated in a complex of three adjacent active regions (ARs, see Figure 1) in the southwestern quadrant and carried an unusually massive erupting filament in its core. We carried out a multiwavelength analysis of the event. Using SDO/HMI data we computed the magnetic topology, determining the locations of quasi separatrix layers in the three-AR complex. We also carried out data-constrained MHD simulations of the eruption.

We found that the strong lateral expansion of the erupting magnetic structure led to flux pile-up, current sheet formation/intensification, and magnetic reconnection along a pre-existing quasi separatrix layer in the three-AR complex. The onset of reconnection first became apparent in the SDO/AIA images when downward flowing dense, cool filament plasma originally contained within the erupting flux rope was re-directed towards a neighbouring active region, tracing the change of large-scale magnetic connectivity. Williams et al. (2013) estimated a lower limit of the electron density of the redirected plasma to be 10^{10} cm^{-3} , at least one order of magnitude larger than the typical coronal density. As a result of this unusually high density around the reconnection region, direct plasma heating took place there. The most prominent brightening was seen in the AIA 171 Å waveband ($6.3 \times 10^5 \text{ K}$).

These SDO observations provide one of the first direct imaging observations of mag-

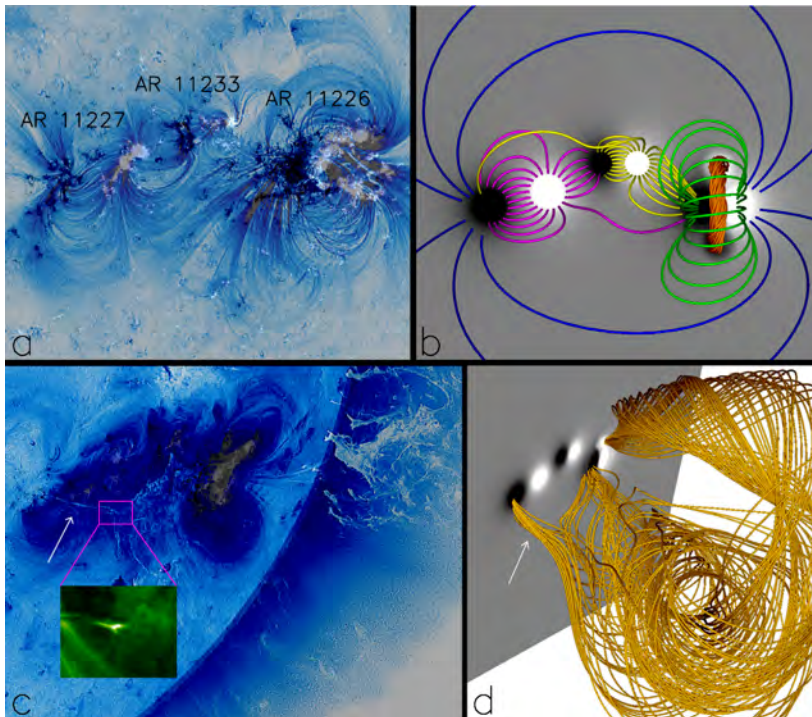


Figure 1. Observations and MHD numerical simulation of the magnetic configuration and the eruption. (a) SDO/AIA 171 Å reverse colour scale image over a co-aligned SDO/HMI magnetic field map of the three neighbouring active regions on 3 June 2011 and (b) corresponding magnetic configuration in the simulation. Black/white indicate negative/positive magnetic polarity, the pre-eruption magnetic flux rope in the rightmost active region is shown in gold. (c) SDO/AIA 171 Å reversed-colour image and (d) a simulation snapshot during the CME eruption on 7 June, by when the active regions have rotated close to the solar limb. The new connections, formed by magnetic reconnection between the magnetic flux rope erupting from AR 11226 and magnetic field lines of AR 11227, are indicated by white arrows. The inset in (c) is a magnification of the in-situ heated bright reconnection region.

netic reconnection in the solar atmosphere. Furthermore, a combination of observations, magnetic modelling, and MHD simulations (Figure 1) provide evidence that during the expansion of a CME’s magnetic structure, instantaneous magnetic reconnection can occur with ambient magnetic field leading to large-scale restructuring. For more details see van Driel-Gesztelyi *et al.* (2013).

Acknowledgements

The authors acknowledge funding from the European Commission’s Seventh Framework Programme under the grant agreement No. 284461 (eHEROES project) and the Hungarian Research grant OTKA K-081421. TT was supported by NASA’s HTP, LWS, and SR&T programs. LMG is grateful for a Royal Society Fellowship, and JC for a joint UCL-MPI Impact PhD Studentship. BK acknowledges support by the DFG.

References

- van Driel-Gesztelyi, L., Baker, D., Török, T., Pariat, E., Green, L.M., Williams, D.R., Carlyle, J., Valori, G., Matthews, S.A., Kliem, B., Malherbe, J.-M.: 2013, *ApJ*, submitted.
 Williams, D.R., Baker, D., & van Driel-Gesztelyi, L.: 2013, *ApJ*, 764, 165

Initiation of Coronal Mass Ejections by Sunspot Rotation

G. Valori¹, T. Török², M. Temmer^{3,4}, A. M. Veronig³, L. van Driel-Gesztelyi^{1,5,6}, B. Vršnak⁷

¹ LESIA, Observatoire de Paris, CNRS, UPMC, Université Paris Diderot, 5 place Jules Janssen, 92190 Meudon, France; email: gherardo.valori@obspm.fr

² Predictive Science Inc., 9990 Mesa Rim Rd., Suite 170, San Diego, CA 92121, USA; email: tibor@predsci.com

³ IGAM/Kanzelhöhe Observatory, Institute of Physics, Universität Graz, Universitätsplatz 5, A-8010 Graz, Austria

⁴ Space Research Institute, Austrian Academy of Sciences, Schmiedlstrasse 6, A-8042 Graz, Austria

⁵ University College London, Mullard Space Science Laboratory, Holmbury St. Mary, Dorking, Surrey RH5 6NT, UK

⁶ Konkoly Observatory, Hungarian Academy of Sciences, Budapest, Hungary

⁷ Hvar Observatory, Faculty of Geodesy, University of Zagreb, Kačićeva 26, HR-10000 Zagreb, Croatia

Abstract. We report observations of a filament eruption, two-ribbon flare, and coronal mass ejection (CME) that occurred in Active Region NOAA 10898 on 6 July 2006. The filament was located South of a strong sunspot that dominated the region. In the evolution leading up to the eruption, and for some time after it, a counter-clockwise rotation of the sunspot of about 30 degrees was observed. We suggest that the rotation triggered the eruption by progressively expanding the magnetic field above the filament. To test this scenario, we study the effect of twisting the initially potential field overlying a pre-existing flux rope, using three-dimensional zero- β MHD simulations. We consider a magnetic configuration whose photospheric flux distribution and coronal structure is guided by the observations and a potential field extrapolation. We find that the twisting leads to the expansion of the overlying field. As a consequence of the progressively reduced magnetic tension, the flux rope quasi-statically adapts to the changed environmental field, rising slowly. Once the tension is sufficiently reduced, a distinct second phase of evolution occurs where the flux rope enters an unstable regime characterized by a strong acceleration. Our simulation thus suggests a new mechanism for the triggering of eruptions in the vicinity of rotating sunspots.

Keywords. MHD, instabilities, Sun: activity, magnetic fields, sunspots, coronal mass ejections (CMEs), filaments, methods: numerical, data analysis

1. Introduction

The eruption on 6 July 2006 in active region NOAA 10898 was a two-ribbon flare accompanied by a filament eruption and a halo CME, the latter being most prominent in the southwest quadrant and reaching a linear plane-of-sky velocity of $\approx 900 \text{ km s}^{-1}$ (Temmer *et al.* 2008). The event was associated with an EIT wave, a type II burst, and very distinct coronal dimming regions. The flare was of class M2.5/2N, located at the heliographic position S9°, W34°. It was observed in soft X-rays (SXR) by GOES (peak time at $\approx 08:37$ UT) as well as in hard-X rays (HXR) with RHESSI, with the two highest peaks of nonthermal HXR emission occurring during 08:20–08:24 UT.

The morphology and evolution of the bipolar active region in the days preceding the eruption were studied using photospheric line-of-sight magnetograms obtained by the

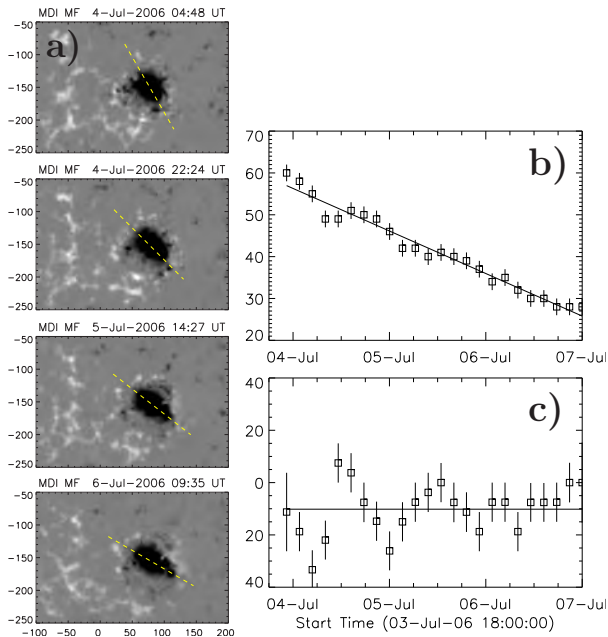


Figure 1. (a) Representative MDI longitudinal magnetic-field maps of the sunspot evolution during 4–6 July 2006: The dashed yellow line outlines the major axis of the sunspot that was used to measure the sunspot rotation. The images are all differentially rotated to the first image of the series, when the sunspot was closer to disk centre. (b) Sunspot rotation determined from the MDI magnetic-field maps over the period 3 July 2006, 22:00 UT, to 7 July 2006, 8:00 UT, showing the orientation of the sunspot’s major axis, measured clockwise from solar East. (c) Sunspot rotation rate in degrees per day, determined as the temporal derivative of the rotation measurements.

MDI instrument (Scherrer *et al.* 1995). The region consisted of a compact negative polarity (the sunspot) surrounded by a dispersed positive polarity, most of which was extending eastwards (Fig. 1a). The two polarities were surrounded by a large, “inverse C-shaped” area of dispersed negative flux to the west of the region (Fig. 2a). The magnetic-flux measurements indicate a mere 5% negative surplus flux in this major bipolar active region of 2.1×10^{22} Mx total flux and maximum-field strengths (negative:positive) in a roughly 10:1 ratio. The sequence in Fig. 1a shows that the sunspot is rotating counter-clockwise during the considered period. The total rotation observed over the three days preceding the eruption is about 30° , with sunspot’s rotation rate of about $10^\circ \text{ day}^{-1}$ (Fig. 1b,c).

The flare and the filament eruption were observed in full-disk $H\alpha$ filtergrams by the Kanzelhöhe Observatory and, over a smaller field-of-view around the active region, by the Hvar Observatory. These observations reveal that the filament consisted of a double structure before and during the eruption. Significant rising motions of the filament could be seen from about 08:23 UT on. The $H\alpha$ flare started by the appearance of very weak double-footpoint brightening at 08:15 UT. We also estimated the kinematics of the filament and the CME front from a time sequence of running-difference images obtained from TRACE, EIT, and LASCO C2/C3 observations. We obtain that the coronal loops overlying the filament started their slow rising phase at 08:15 UT, i.e., about five–ten minutes before the filament. Similarly, the CME front reached its final, almost constant velocity a few minutes before the filament. More details about the methods employed to obtain the above results can be found in Török *et al.* (2013), hereafter Paper I. We refer to that article and to the references therein for further details on the eruption.

Guo *et al.* (2010) suggested that the eruption was triggered by recurrent chromospheric mass injection in the form of surges or jets into the filament channel. Here we propose a different mechanism: Assuming that the filament was suspended in the corona by a magnetic flux rope, we suggest that the continuous rotation of the sunspot led to a slow expansion of the arcade-like magnetic field overlying the filament, i.e., to a continuous weakening of its stabilizing tension, until a critical point was reached at which equilibrium

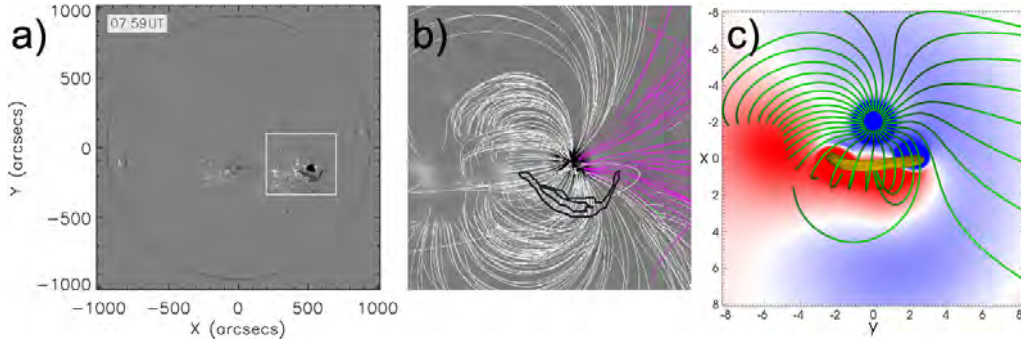


Figure 2. (a) Full-disk MDI magnetogram on 6 July 2006, 07:59 UT. AR10898 is marked by the white box. (b) PFSS magnetic field lines in the AR calculated for 6 July 2006, 06:04 UT, overlaid on a synoptic MDI magnetogram. Pink (white) field lines depict open (closed) fields. The outer contours of the filament, based on $H\alpha$ data taken at 07:59 UT on 6 July 2006, are outlined with black lines. (c) Magnetic configuration used in the simulation, after the initial relaxation of the system, showing the core of the TD flux rope (orange field lines) and the ambient potential field (green field lines). $B_z(z = 0)$ is shown, with red (blue) corresponding to positive (negative) values, and is saturated at 4% $\max(B_z)$ to depict weaker flux distributions.

could not be maintained and the flux rope erupted. We note that we do not claim that the eruption was triggered *exclusively* by this mechanism. Filaments are often observed to spiral into the periphery of sunspots (see, e.g., Green *et al.* 2007), and also in our case an inspection of the TRACE and $H\alpha$ images during the early phase of the eruption suggests a possible magnetic connection between the western extension of the filament-carrying core field and the sunspot area. Thus, the sunspot rotation may have added stress to this field, thereby possibly contributing to drive it towards eruption. On the other hand, for an injection of twist to occur, the core field must be rooted in the centre of the sunspot, not just in its periphery, which is difficult to establish from observations. It appears reasonable to assume that a clear connection between core field and sunspot centre is not always present, and that the stressing of the overlying ambient field by sunspot rotation may be more relevant for the destabilization of the system in such cases. In order to test this scenario, we perform a three-dimensional (3D) MHD simulation in which we twist the stabilizing potential field overlying a stable coronal flux rope. Differently from previous works (e.g., Amari *et al.* 1996), the photospheric vortex motions we use do not directly affect the flux rope, but solely the field surrounding it.

2. Numerical simulation setup

As in previously published simulations (e.g., Török, Kliem, and Titov 2004; Kliem, Titov, and Török 2004), we integrate the $\beta = 0$ compressible ideal MHD equations, ignoring the effects of thermal pressure and gravity, and we employ the coronal flux rope model of Titov and Démoulin (1999), hereafter TD, to construct the initial magnetic field. The main ingredient of the TD model is a current ring of major radius $[R]$ and minor radius $[a]$ that is placed such that its symmetry axis is located at a depth $[d]$ below a photospheric plane. The outwardly directed Lorentz self-force (or “hoop force”) of the ring is balanced by a potential field created by a pair of sub-photospheric point sources $\pm q$ that are placed at the symmetry axis, at distances $\pm L$ from the ring centre. The resulting coronal field consists of an arched and line-tied flux rope embedded in an arcade-like potential field.

We normalize lengths by $l = R - d$ and use a Cartesian grid discretizing the volume

$[-40, 40] \times [-30, 30] \times [0, 60]$, resolved by $307 \times 257 \times 156$ points. The grid is nonuniform in all directions, with an almost uniform resolution $\Delta = 0.05$ in the area mimicking the active region. The top and lateral boundaries are closed, which is justified given the large size of the simulation box. Below the photospheric plane, the tangential components of the magnetic field $[B_{x,y}]$ are extrapolated from the integration domain, and the normal component $[B_z]$ is set such that $\nabla \cdot \mathbf{B} = \mathbf{0}$ in $z = 0$ at all times. The vertical velocities are zero there at all times, and the mass density is fixed at its initial values.

Fig. 2b shows a coronal potential-field source-surface model (Schatten, Wilcox, and Ness 1969, PFSS), obtained from a synoptic MDI magnetogram for Carrington Rotation 2045. It can be seen that the field lines rooted in the main polarity (the sunspot) form a fan-like structure, which partly overlies the pre-eruption filament. In order to build an initial magnetic configuration that resembles this coronal field and the underlying highly asymmetric magnetic flux distribution (Sect. 1), we modify the standard TD model by replacing the pair of sub-photospheric point charges by an ensemble of ten sub-photospheric sources. These are adjusted in order to mimic: the approximate flux balance between the concentrated leading negative polarity and the dispersed following positive polarity; the ratio of approximately 10:1 between the peak field strengths in the leading polarity and the following polarity; the size ratio between these polarities; the presence of an “inverse C-shaped” area of dispersed negative flux to the West of the leading polarity; the fan-like shape of the coronal field rooted in the leading polarity. Since the model is still relatively idealized, all these features can be matched only approximately. We then add a TD flux rope, setting $R = 2.75$, $a = 0.8$, and $d = 1.75$. The position of the rope within the ambient field is guided by the observed location of the filament (Fig. 2b), and its magnetic field strength is chosen such that it is in approximate equilibrium with the ambient potential field. We use an initial density distribution $\rho_0(\mathbf{x}) = |\mathbf{B}_0(\mathbf{x})|^2$, corresponding to a uniform initial Alfvén velocity. In order to obtain a numerical equilibrium as a starting point, we first perform a numerical relaxation for $75 \tau_a$, after which the time is reset to zero.

In order to mimic the observed sunspot rotation, we then twist the main negative flux concentration by imposing tangential velocities at the bottom boundary. They produce a horizontal counterclockwise rotation, chosen such that the velocity vectors always point along the contours of $B_z(x, y, 0, t = 0)$, which assures that the distribution of $B_z(x, y, 0, t)$ is conserved to a very good approximation. The velocities are zero at the polarity centre, located at $(x, y, z) = (-2, 0, 0)$, and decrease towards its edge from their maximum value, equal to 0.005 times the initial Alfvén velocity $[v_{a0}]$. The equations and parameters used to compute the tangential velocities at each time are given in Paper I. The twist injected by such motions is nearly uniform close to the polarity centre and decreases monotonically towards its edge, such that it does not directly affect the flux rope field.

3. Results

The magnetic configuration resulting after the initial numerical relaxation is shown in Fig. 2c and in Fig. 4a. The fan-structure inferred from the PFSS extrapolation is qualitatively well reproduced. The TD flux rope is stabilized by flux rooted towards the southern edge of the main polarity, and the rope is inclined with respect to the vertical, which is due to the asymmetry of the potential field surrounding it.

Figure 4a shows that electric currents are present in the ambient field volume. The strongest current concentrations are located in the front of the flux rope and exhibit an X-shaped pattern in the vertical cut shown. This pattern outlines the locations of quasi-separatrix layers (QSL, see, e.g., Démoulin *et al.* 1996) that separate different connectivity domains. The QSLs are present in the configuration from the very beginning and arise

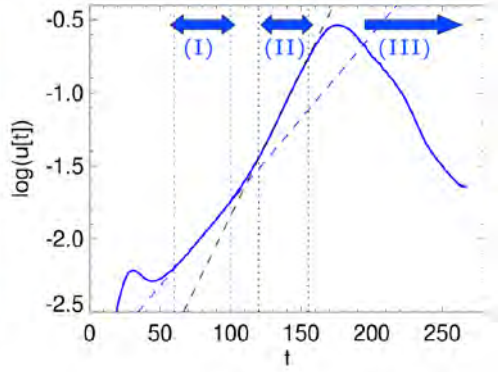


Figure 3. Logarithmic presentation of the velocity of the axis apex of the TD flux rope during the twisting phase, as a function of time. The dashed lines show linear fits, obtained within the time periods marked by the vertical dotted lines of the same color. Thick arrows mark different evolution phases described in the text.

from the complexity of the potential field. Their presence is evident also in the left panel of Fig. 4a: the green field lines show strong connectivity gradients in the northern part of the main polarity and in the vicinity of the western flux rope footpoint. It has been demonstrated that current concentrations form preferably at the locations of QSLs as a system containing such structures is dynamically perturbed (see, e.g., Aulanier, Pariat, and Démoulin 2005). In our case the perturbation results from the – relatively modest – dynamics during the initial relaxation of the system.

After the relaxation, at $t = 0$, we start twisting the main negative polarity, and we quantify the evolution of the TD flux rope by monitoring the velocity at the axis apex of the rope (Fig. 3). Due to the pronounced fan-structure of the field rooted in the main polarity, the photospheric twisting does not lead to the formation of a single twisted flux tube that rises exactly in vertical direction above the TD rope, as it was the case earlier studies (Amari *et al.* 1996; Török and Kliem 2003; Aulanier, Démoulin, and Grappin 2005). Rather, the twisting leads to a slow, global expansion of the fan-shaped field lines, as shown in Fig. 4. Since we are mainly interested in the destabilization of the flux rope, we did not study the detailed evolution of the large-scale field. We expect it to be very similar to the one described in Santos, Büchner, and Otto (2011), since the active region those authors simulated was also dominated by one main polarity, and the field rooted therein had a very similar fan-shaped structure (cf. our Fig. 4 with their Fig. 1).

Important for our purpose is the evolution of the arcade-like part of the initial potential field that directly overlies the TD flux rope. Those field lines are directly affected only by a fraction of the boundary flows and therefore get merely sheared (rather than twisted), which still leads to their slow expansion. As a result, the TD rope starts to rise, adapting to the successively decreasing magnetic tension of the overlying field (phase I in Fig. 3). This initial phase of the evolution is depicted in Fig. 4b. Note that some of the flux at the front of the expanding arcade reconnects at the QSL current layer, which can be expected to aid the arcade expansion to some degree. As can be seen in Fig. 3, the TD rope rises, after some initial adjustment, exponentially during this slow initial phase.

As the twisting continues, a transition to a rapid acceleration takes place after $t \approx 100 \tau_a$, when the rise curve leaves the quasi-static regime. After the transition phase, the TD rope again rises exponentially, but now with a significantly larger growth rate than during the slow rise phase (phase II in Fig. 3). Such a slow (quasi-static) rise phase, followed by a rapid acceleration, is a well-observed property of many filament eruptions in the early evolution of CMEs (see, e.g., Schrijver *et al.* 2008, and references therein), and is also seen for the event studied here (see also Paper I). The evolution of the TD rope after $t \approx 100 \tau_a$ can be associated with the development of the torus instability (Kliem and Török 2006; Démoulin and Aulanier 2010), as has been shown under similar

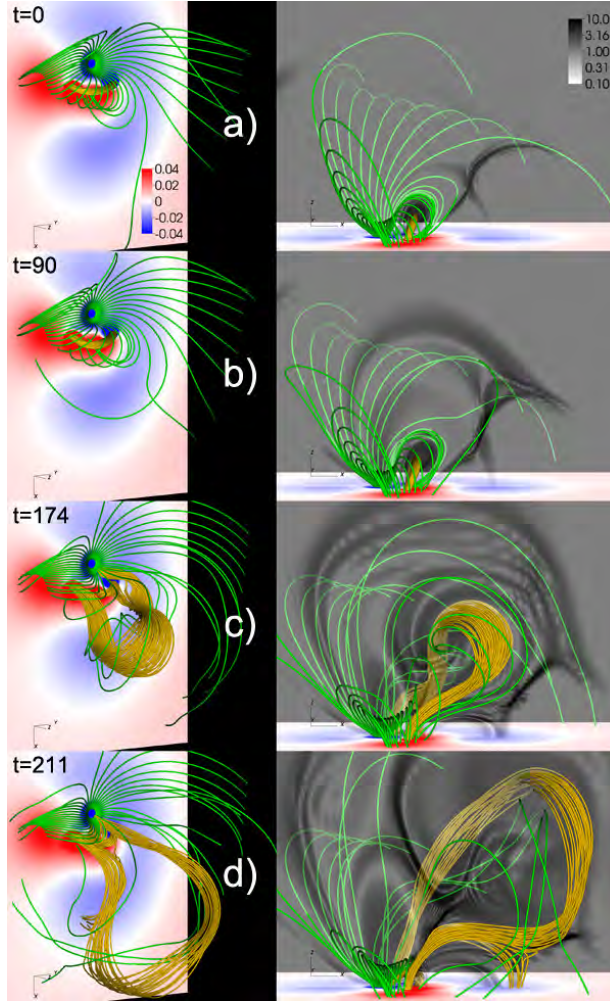


Figure 4. Magnetic configuration after initial relaxation (a), during slow rise phase (b), at time of peak flux rope velocity (c), and during flux rope deceleration (d). The flux rope core is depicted by orange field lines; ambient field lines are green. $B_z(z = 0)$ is shown, with red (blue) corresponding to positive (negative) values. Left panels use a view similar to the observations (see paper I); right panels show a side view. The transparent grey-scales show a logarithmic distribution of $|j|/|B|$ in the plane $x = 0$, outlining the locations of strongest currents. The sub-volume $[-10, 16] \times [-11, 11] \times [0, 18]$ is used for all panels.

conditions in various simulations of erupting flux ropes (Török and Kliem 2007; Fan and Gibson 2007; Schrijver *et al.* 2008; Aulanier *et al.* 2010; Török *et al.* 2011). The right panels in Fig. 4 show that the trajectory of the flux rope is far from being vertical. Such lateral eruptions have been reported frequently in both observations and simulations (see, e.g., Williams *et al.* 2005; Panasenco *et al.* 2011; Yang *et al.* 2012), and are usually attributed to an asymmetric structure of the field overlying the erupting core flux. We believe that this causes the lateral rise also in our case.

As the eruption continues, the trajectory of the flux rope becomes increasingly horizontal, resembling the so-called “roll effect” (Panasenco *et al.* 2011) and indicating that the rope cannot overcome the tension of the large-scale overlying field. Moreover, as a consequence of its increasing expansion, the flux rope strongly pushes against the QSL

current layer, which results in reconnection between the front of the rope and the ambient field. Eventually, the rope splits into two parts, similar to what has been found in simulations of confined eruptions (Amari and Luciani 1999; Török and Kliem 2005). These two effects slow down the rise of the rope after $t \approx 175 \tau_a$ and inhibit its full eruption, i.e., the development of a CME in our simulation (phase III in Fig. 3).

Since QSLs can affect the evolution of an eruption, but are not expected to play a significant role for its initiation, we did not investigate in detail whether or not QSLs were present in the pre-eruption configuration of the 6 July 2006 event. The PFSS extrapolation indicates the presence of a QSL to the North and the West of the main polarity (see the field-line connectivities in Fig. 2b), but less clearly so to its South. Since we merely aim to model the initiation of the eruption rather than its full evolution into a CME, we refrained from further improving our model to obtain a configuration without a strong QSL in front of the flux rope.

4. Summary and Conclusions

We presented a 3D MHD simulation that was designed to test a possible scenario for the initiation and early evolution of the filament eruption and CME that occurred on 6 July 2006 in active region NOAA 10898. Our conjecture was that the slow rotation of the sunspot that dominated the active region progressively reduced the tension of the magnetic field overlying the pre-eruption filament, until the latter could not be stabilized anymore and erupted, resulting in the CME. Using the TD coronal flux rope model as a starting point, we constructed an initial magnetic field that resembles the photospheric flux distribution and coronal magnetic field structure of the active region around the time of the event. In particular, the highly asymmetric flux density and the resulting overall fan-shape of the coronal magnetic field are well captured by the model, while the approximative flux balance of the region is kept. We then mimicked the observed sunspot rotation by imposing photospheric vortex flows localized at the main magnetic polarity of the model. The flows were chosen such that they do not directly affect the flux rope.

As a result of this twisting, the field lines overlying the flux rope start to expand and the rope undergoes a quasi-static adaptation to the changing surrounding field in the simulation, which manifests in a slow rise phase. As the weakening of the overlying field reaches an appropriate level, the torus instability sets in and rapidly accelerates the rope upwards, leading to a second, fast rise phase and eruption. The asymmetry of the ambient field leads to a markedly lateral eruption. This evolution in two phases resembles the often observed slow rise phase and subsequent strong acceleration of filaments in the course of their eruption. However, the presence of a QSL-related current layer in the front of the erupting flux rope in the simulation results in magnetic reconnection which eventually splits the rope before it can evolve into a CME, in contrast to the observations. Although we are not able to follow the expansion of the flux rope beyond this phase, the simulation successfully models the early phases of the eruption (the slow rise and the initial rapid acceleration of the flux rope) in a setting that is qualitatively similar to the observed magnetic configuration around the time of the eruption.

Our simulation thus demonstrates that the continuous expansion due to sunspot rotation of the magnetic field that stabilizes the current-carrying core flux, i.e., the progressive decrease of magnetic tension, can lead to filament eruptions and CMEs.

Acknowledgements

We acknowledge the use of data provided by the SOHO/MDI consortium. SOHO/EIT was funded by CNES, NASA, and the Belgian SPPS. The SOHO/LASCO data used here

are produced by a consortium of the Naval Research Laboratory(USA), Max–Planck–Institut für Aeronomie (Germany), Laboratoire d’Astrophysique de Marseille (France), and the University of Birmingham (UK). SOHO is a mission of international cooperation between ESA and NASA. The *Transition Region and Coronal Explorer* (TRACE) is a mission of the Stanford–Lockheed Institute for Space Research, and part of the NASA Small Explorer program. H α data were provided by the Kanzelhöhe Observatory, University of Graz, Austria, and by the Hvar Observatory, University of Zagreb, Croatia. The research leading to these results has received funding from the European Commission’s Seventh Framework Programme (FP7/2007–2013) under the grant agreements nn^o 218816 (SOTERIA project, www.soteria-space.eu) and n^o 284461 (eHEROES, <http://soteria-space.eu/eheroes/html>). TT was partially supported by NASA’s HTP, LWS, and SR&T programs. LvDG acknowledges funding through the Hungarian Science Foundation grant OTKA K81421.

References

- Amari, T., Luciani, J.F.: 1999, *Astrophys. J. Lett.* **515**, L81.
- Amari, T., Luciani, J.F., Aly, J.J., Tagger, M.: 1996, *Astrophys. J. Lett.* **466**, L39.
- Aulanier, G., Démoulin, P., Grappin, R.: 2005, *Astron. Astrophys.* **430**, 1067.
- Aulanier, G., Pariat, E., Démoulin, P.: 2005, *Astron. Astrophys.* **444**, 961.
- Aulanier, G., Török, T., Démoulin, P., DeLuca, E.E.: 2010, *Astrophys. J.* **708**, 314.
- Démoulin, P., Aulanier, G.: 2010, *Astrophys. J.* **718**, 1388.
- Démoulin, P., Henoux, J.C., Priest, E.R., Mandrini, C.H.: 1996, *Astron. Astrophys.* **308**, 643.
- Fan, Y., Gibson, S.E.: 2007, *Astrophys. J.* **668**, 1232.
- Gopalswamy, N., Yashiro, S., Kaiser, M.L., Howard, R.A., Bougeret, J.L.: 2001, *Astrophys. J. Lett.* **548**, L91.
- Green, L.M., Kliem, B., Török, T., van Driel-Gesztelyi, L., Attrill, G.D.R.: 2007, *Solar Phys.* **246**, 365.
- Guo, J., Liu, Y., Zhang, H., Deng, Y., Lin, J., Su, J.: 2010, *Astrophys. J.* **711**, 1057.
- Kliem, B., Török, T.: 2006, *Phys. Rev. Lett.* **96**(25), 255002.
- Kliem, B., Titov, V.S., Török, T.: 2004, *Astron. Astrophys.* **413**, L23.
- Panasenco, O., Martin, S., Joshi, A.D., Srivastava, N.: 2011, *J. Atmos. Solar-Terr. Phys.* **73**, 1129.
- Santos, J.C., Büchner, J., Otto, A.: 2011, *Astron. Astrophys.* **535**, A111.
- Schatten, K.H., Wilcox, J.M., Ness, N.F.: 1969, *Solar Phys.* **6**, 442.
- Scherrer, P.H., Bogart, R.S., Bush, R.I., Hoeksema, J.T., Kosovichev, A.G., Schou, J., Rosenberg, W., Springer, L., Tarbell, T.D., Title, A., Wolfson, C.J., Zayer, I., MDI Engineering Team: 1995, *Solar Phys.* **162**, 129.
- Schrijver, C.J., Elmore, C., Kliem, B., Török, T., Title, A.M.: 2008, *Astrophys. J.* **674**, 586.
- Temmer, M., Veronig, A.M., Vršnak, B., Rybák, J., Gömöry, P., Stoiser, S., Maričić, D.: 2008, *Astrophys. J. Lett.* **673**, L95.
- Titov, V.S., Démoulin, P.: 1999, *Astron. Astrophys.* **351**, 707.
- Török, T., Kliem, B.: 2003, *Astron. Astrophys.* **406**, 1043.
- Török, T., Kliem, B.: 2005, *Astrophys. J. Lett.* **630**, L97.
- Török, T., Kliem, B.: 2007, *Astronom. Nachr.* **328**, 743.
- Török, T., Kliem, B., Titov, V.S.: 2004, *Astron. Astrophys.* **413**, L27.
- Török, T., Panasenco, O., Titov, V.S., Mikić, Z., Reeves, K.K., Velli, M., Linker, J.A., De Toma, G.: 2011, *Astrophys. J. Lett.* **739**, L63.
- Török, T., Temmer, M., Valori, G., Veronig, A.M., van Driel-Gesztelyi, L., Vršnak, B.: 2013, *Solar Phys.* **286**, 453. referred to as **Paper I**
- Williams, D.R., Török, T., Démoulin, P., van Driel-Gesztelyi, L., Kliem, B.: 2005, *Astrophys. J. Lett.* **628**, L163.
- Yang, J., Jiang, Y., Yang, B., Zheng, R., Yang, D., Hong, J., Li, H., Bi, Y.: 2012, *Solar Phys.* **279**, 115.

Initiation of Coronal Mass Ejections by Sunspot Rotation

T. Török · M. Temmer · G. Valori · A.M. Veronig ·
L. van Driel-Gesztelyi · B. Vršnak

Received: 28 July 2012 / Accepted: 6 March 2013 / Published online: 4 April 2013
© Springer Science+Business Media Dordrecht 2013

Abstract We study a filament eruption, two-ribbon flare, and coronal mass ejection (CME) that occurred in NOAA Active Region 10898 on 6 July 2006. The filament was located South of a strong sunspot that dominated the region. In the evolution leading up to the eruption, and for some time after it, a counter-clockwise rotation of the sunspot of about 30 degrees was observed. We suggest that the rotation triggered the eruption by progressively expanding the magnetic field above the filament. To test this scenario, we study the effect of twisting the initially potential field overlying a pre-existing flux-rope, using three-dimensional zero- β MHD simulations. We first consider a relatively simple and symmetric system, and

Electronic supplementary material The online version of this article (doi:[10.1007/s11207-013-0269-9](https://doi.org/10.1007/s11207-013-0269-9)) contains supplementary material, which is available to authorized users.

T. Török (✉)

Predictive Science, Inc., 9990 Mesa Rim Rd., Suite 170, San Diego, CA 92121, USA
e-mail: tibor@predsci.com

M. Temmer · A.M. Veronig

IGAM/Kanzelhöhe Observatory, Institute of Physics, Universität Graz, Universitätsplatz 5, 8010 Graz, Austria

M. Temmer

Space Research Institute, Austrian Academy of Sciences, Schmiedlstrasse 6, 8042 Graz, Austria

G. Valori · L. van Driel-Gesztelyi

LESIA, Observatoire de Paris, CNRS, UPMC, Université Paris Diderot, 5 place Jules Janssen, 92190 Meudon, France

L. van Driel-Gesztelyi

Mullard Space Science Laboratory, University College London, Holmbury St. Mary, Dorking, Surrey RH5 6NT, UK

L. van Driel-Gesztelyi

Konkoly Observatory, Hungarian Academy of Sciences, Budapest, Hungary

B. Vršnak

Hvar Observatory, Faculty of Geodesy, University of Zagreb, Kačićeva 26, 10000 Zagreb, Croatia

then study a more complex and asymmetric magnetic configuration, whose photospheric-flux distribution and coronal structure are guided by the observations and a potential field extrapolation. In both cases, we find that the twisting leads to the expansion of the overlying field. As a consequence of the progressively reduced magnetic tension, the flux-rope quasi-statically adapts to the changed environmental field, rising slowly. Once the tension is sufficiently reduced, a distinct second phase of evolution occurs where the flux-rope enters an unstable regime characterised by a strong acceleration. Our simulations thus suggest a new mechanism for the triggering of eruptions in the vicinity of rotating sunspots.

Keywords Magnetic fields, corona · Active regions, models · Coronal mass ejections, initiation and propagation · Sunspots, velocity

1. Introduction

Filament (or prominence) eruptions, flares, and coronal mass ejections (CMEs) are the three large-scale eruptive events on the Sun. It has become clear in recent years that they are not independent phenomena, but different observational manifestations of a more general process, namely the sudden and violent disruption and dynamic reconfiguration of a localised volume of the coronal magnetic field (*e.g.* Forbes, 2000). Whether or not all three phenomena occur together appears to depend mainly on the properties of the pre-eruptive configuration. For example, CMEs can occur without a filament eruption (if no filament has formed in the source region of the erupting flux prior to its eruption) and without significant flaring (if the magnetic field in the source region is too weak; *e.g.* Zirin, 1998) or, in extreme cases, even without any low-coronal or chromospheric signature (Robbrecht, Patsourakos, and Vourlidas, 2009). On the other hand, both flares and filament eruptions are not always accompanied by a CME (if, for instance, the magnetic field above the source region is too strong; see, *e.g.*, Moore *et al.*, 2001; Nindos and Andrews, 2004; Török and Kliem, 2005). In large events such as the one studied in this article, however, all three phenomena are observed almost always. Such events typically start with the slow rise of a filament and/or overlying loops (*e.g.* Maričić *et al.*, 2004; Schrijver *et al.*, 2008; Maričić, Vršnak, and Roša, 2009), which is often accompanied by weak pre-flare signatures in EUV or X-rays (*e.g.* Maričić *et al.*, 2004; Chifor *et al.*, 2007). The slow rise is followed by a rapid acceleration and a huge expansion of the eruptive structure, which is then observed as a CME. The rapid acceleration has been found in most cases to be very closely correlated with the flare impulsive phase (*e.g.* Kahler *et al.*, 1988; Zhang *et al.*, 2001; Maričić *et al.*, 2007; Temmer *et al.*, 2008).

Although it is now widely accepted that solar eruptions are magnetically driven, the detailed physical mechanisms that initiate and drive eruptions are still controversial. Accordingly, a large number of theoretical models have been proposed in the past decades (for a recent review see, *e.g.*, Forbes, 2010). Virtually all of these models consider as pre-eruptive configuration a sheared or twisted core field low in the corona, which stores the free magnetic energy required for eruption and is stabilised by the ambient coronal field. The choice of such a configuration is supported by observations of active regions, which often display sheared structures (filaments and soft X-ray sigmoids) surrounded by less sheared, tall loops. An eruption is triggered if the force balance between the core field and the ambient field is destroyed, either by increasing the shear or twist in the core field or by weakening the stabilizing restoring force of the ambient field (see, *e.g.*, Aulanier *et al.*, 2010).

One of the many mechanisms that has been suggested to trigger eruptions is the rotation of sunspots. The idea was put forward by Stenflo (1969), who showed that the order of

magnitude of the energy deposition into coronal structures by sunspot rotations is sufficient to produce flaring activity (see also Kazachenko *et al.*, 2009).

Sunspot rotations have been known for a long time – the first evidence, based on spectral observations, was presented one century ago by Evershed (1910) – and since then they have been the subject of numerous analyses. Still, measurements of sunspot rotation are not straightforward, and, depending on the method employed, can give quite different results (see, *e.g.*, Min and Chae, 2009). Meticulous case studies (*e.g.* Zhang, Li, and Song, 2007; Min and Chae, 2009; Yan *et al.*, 2009), as well as detailed statistical analyses (*e.g.* Brown *et al.*, 2003; Yan and Qu, 2007; Zhang, Liu, and Zhang, 2008; Li and Zhang, 2009; Suryanarayana, 2010) showed that sunspots can rotate significantly, up to several hundreds of degrees over a period of a few days. Interestingly, sunspots do not necessarily rotate as a rigid body: Brown *et al.* (2003) and Yan and Qu (2007) showed that the rotation rate often changes with the distance from the sunspot centre. The rotation of sunspots is commonly interpreted as an observational signature of the emergence of a flux-rope through the photosphere (*e.g.* Gibson *et al.*, 2004) or, more generally, as the transport of helicity from the convection zone into the corona (see, *e.g.*, Longcope and Welsch, 2000; Tian and Alexander, 2006; Tian, Alexander, and Nightingale, 2008; Fan, 2009). On the other hand, observations of strong sunspot rotation without signs of significant flux emergence have been reported (*e.g.* Tian and Alexander, 2006, and references therein), suggesting that intrinsic sunspot rotation of sub-photospheric origin exists. In such cases the rotation rate tends to be smaller than for sunspot rotations associated with flux emergence (*e.g.* Zhu, Alexander, and Tian, 2012).

A number of studies have shown a direct cause–consequence relationship between higher-than-average sunspot rotation and enhanced eruptive activity. For example, Brown *et al.* (2003), Hiremath and Suryanarayana (2003), Hiremath, Lovely, and Kariyappa (2006), Tian and Alexander (2006), Yan and Qu (2007), Zhang, Liu, and Zhang (2008), Li and Zhang (2009), Yan *et al.* (2009, 2012), and Suryanarayana (2010) reported an apparent connection between rotating sunspots (with total rotation angles of up to 200° and more) and eruptive events. In particular, Yan and Qu (2007) attributed eruptive activity in an active region to different rotation speeds in different parts of a sunspot, whereas Yan, Qu, and Kong (2008) found indications that active regions with sunspots rotating opposite to the differential-rotation shear are characterised by high X-class-flare productivity. Romano, Contarino, and Zuccarello (2005) reported a filament eruption that was apparently triggered by photospheric vortex motions at both footpoints of the filament, without any sign of significant flux emergence.

Besides purely observational studies of the relationship between sunspot rotation and eruptive activity, some authors presented a combination of observations and modelling. For example, Régnier and Canfield (2006) utilised multi-wavelength observations and modelling of the coronal magnetic field of the highly flare-productive NOAA Active Region 8210 to show that slow sunspot rotations enabled flaring, whereas fast motions associated with emerging flux did not result in any detectable flaring activity. Moreover, they also showed that the deposition of magnetic energy by photospheric motions is correlated with the energy storage in the corona, which is then released by flaring. Similarly, Kazachenko *et al.* (2009) analysed detailed observations of an M8 flare–CME event and the associated rotating sunspot, and combined them in a minimum-current-corona model. They found that the observed rotation of 34° over 40 hours led to a triplication of the energy content and flux-rope self-helicity, sufficient to power the M8 flare.

Numerical MHD investigations of the relationship between sunspot rotation and eruptive activity started with Barnes and Sturrock (1972), who modelled the coronal magnetic field of

a rotating sunspot surrounded by a region of opposite polarity. They found that the rotation causes an inflation of the magnetic field, and that its energy increases with the rotation angle until, when the rotation angle exceeds $\approx 180^\circ$, it becomes larger than that of the open-field configuration with the same boundary conditions, presumably leading to an eruption.

MHD simulations of the formation and evolution of flux-ropes by twisting line-tied potential fields have been widely performed since then. Calculations were done by either twisting uniform fields in straight, cylindrically symmetric configurations (*e.g.* Mikic, Schnack, and van Hoven, 1990; Galsgaard and Nordlund, 1997; Gerrard, Arber, and Hood, 2002; Gerrard *et al.*, 2003) or by twisting bipolar potential fields; the latter yielding arched flux-ropes anchored at both ends in the same plane (*e.g.* Amari and Luciani, 1999; Gerrard, Hood, and Brown, 2004). Most of these simulations focused on the helical kink instability and its possible role in producing compact flares and confined eruptions. Klimchuk, Antiochos, and Norton (2000) studied the twisting of a bipole with emphasis on the apparently uniform cross-section of coronal loops. Very recently, Santos, Büchner, and Otto (2011) simulated the energy storage for the active region that was studied earlier by Régnier and Canfield (2006). They imposed photospheric flows on an extrapolated potential field and found the formation of pronounced electric currents at the locations of the observed flare sites. The authors concluded that the main flare activity in the active region was caused by the slow rotation of the sunspot that dominated the region.

However, none of the above studies were directly related to CMEs. Amari *et al.* (1996) were the first to show that the formation and continuous twisting of an arched flux-rope in a bipolar potential field can lead to a strong dynamic expansion of the rope, resembling what is observed in CMEs. Later, Török and Kliem (2003) and Aulanier, Démoulin, and Grappin (2005) extended this work by studying in detail the stability properties and dynamic evolution of such a system. The underlying idea of these simulations is that slow photospheric vortex motions can twist the core magnetic field in an active region up to the point where equilibrium cannot be longer maintained, and the twisted core field, *i.e.* a flux-rope, erupts (for the role of increasing twist in triggering a flux-rope eruption see also Chen, 1989; Vršnak, 1990; Fan and Gibson, 2003; Isenberg and Forbes, 2007). What has not been studied yet is whether a twisting of the field *overlying an existing flux-rope* can lead to the eruption of the rope.

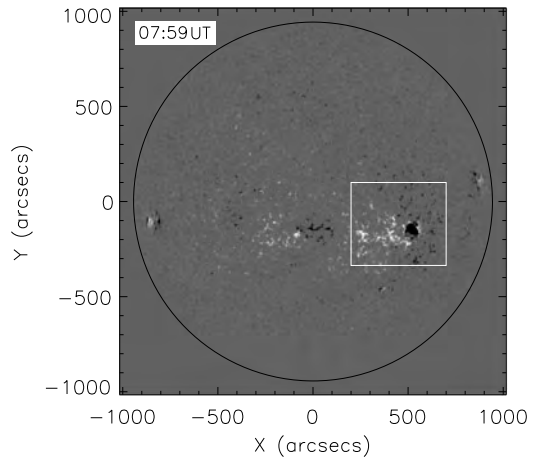
In this article, we present observations of a large solar eruption that took place in the vicinity of a rotating sunspot. We suggest that the continuous rotation of the spot triggered the eruption by successively weakening the stabilizing coronal field until the low-lying core field erupted. We support our suggestion by MHD simulations that qualitatively model this scenario.

The remaining part of this article is organised as follows: In Section 2 we describe the observations, focusing on the initial evolution of the eruption and on the rotation of the sunspot. In Section 3 we describe the numerical simulations, the results of which are presented in Section 4. We finally discuss our results in Section 5.

2. Observations

The eruption on 6 July 2006 in NOAA Active Region 10898 was a textbook two-ribbon flare accompanied by a filament eruption and a halo CME, the latter being most prominent in the southwest quadrant and reaching a linear plane-of-sky velocity of $\approx 900 \text{ km s}^{-1}$ (Temmer *et al.*, 2008). The event was associated with an EIT wave, a type II burst, and very distinct coronal dimming regions. The flare was of class M2.5/2N, located at the heliographic position S9°, W34°. It was observed in soft X-rays (SXR) by GOES (peak time at $\approx 08:37$ UT)

Figure 1 Full-disk line-of-sight SOHO/MDI magnetogram recorded on 6 July 2006, 07:59 UT. The active region under study is marked by the white box.

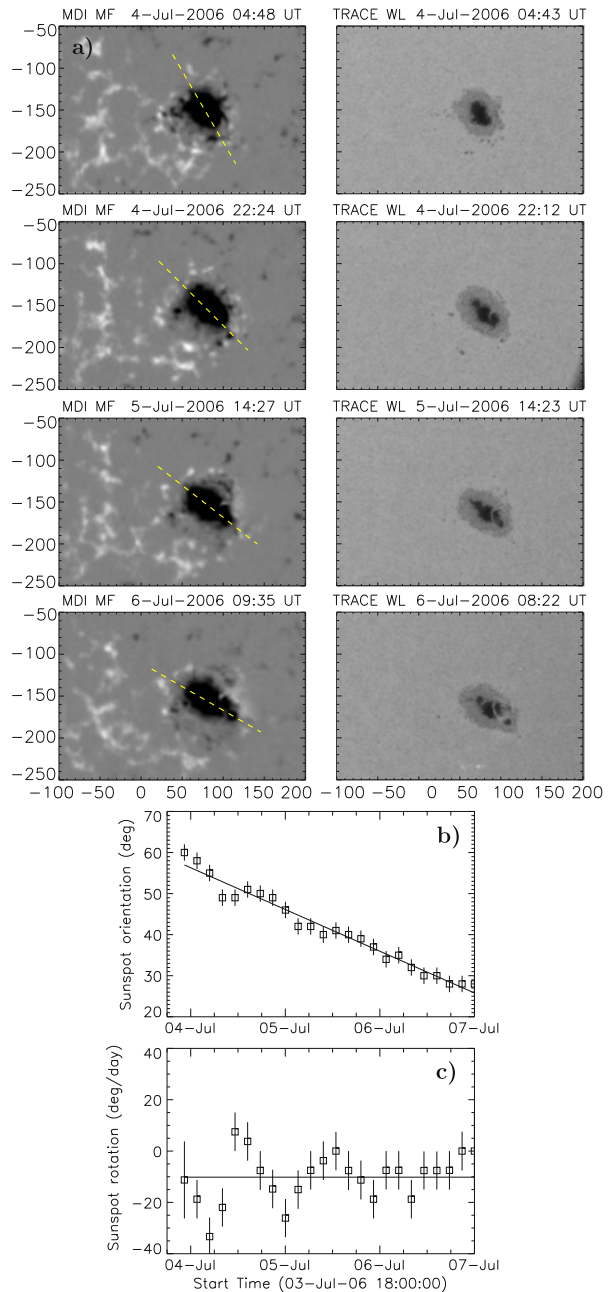


as well as in hard-X rays (HXR) with RHESSI, with the two highest peaks of nonthermal HXR emission occurring during 08:20–08:24 UT.

The evolution of the active region in the days preceding the eruption, and in particular the rotation of the leading sunspot, can be studied using its photospheric signatures. Photospheric line-of-sight magnetograms of the region were obtained by the MDI instrument (Scherrer *et al.*, 1995) onboard the *Solar and Heliospheric Observatory* (SOHO). The active region was a bipolar region of Hale type β , consisting of a compact negative polarity (the sunspot) that was surrounded by a dispersed positive polarity, most of which was extending eastwards (see Figure 1). The maximum of the magnetic-field flux density in the sunspot was about nine times larger than in the dispersed positive polarity. The two polarities were surrounded by a large, “inverse C-shaped” area of dispersed negative flux to the west of the region.

We measured the magnetic flux of the concentrated leading (negative) and dispersed following (positive) polarities using a (re-calibrated) SOHO/MDI synoptic map, which preserves the resolution of the original observation. The map includes magnetic features close to the time of their central meridian passage, when projection effects of the line-of-sight magnetic fields are at minimum. The total magnetic flux (half of the total unsigned flux) was found to be $(2.1 \pm 0.2) \times 10^{22}$ Mx, with the two polarities nearly balanced [$(2.0 \pm 0.2) \times 10^{22}$ and $(-2.2 \pm 0.2) \times 10^{22}$ Mx for the positive and negative flux, respectively]. The error estimates reflect the uncertainty in determining how much of the dispersed positive and negative polarities belonged to the active region. The leading spot, including the penumbral area, had a mean magnetic-field strength (magnetic-flux density over 2340 pixels) of 390 G, reaching 1820 G when a smaller, purely umbral, area was considered (240 pixels). However, since the MDI response becomes non-linear in such a strong, and therefore dark, umbra, the core field strength there was probably higher (≥ 2000 G) (see, *e.g.*, Green *et al.*, 2003). The positive dispersed plage had a much lower mean magnetic-field strength of about 50 ± 10 G, depending on the extent of dispersed positive field measured (magnetic-flux density over 13 060–24 600 pixels). Positive flux concentrations (measured over 600 pixels) within the plage had a characteristic field strength of 220 ± 20 G. In summary, magnetic-flux measurements indicate a mere 5 % negative surplus flux in this major bipolar active region of 2.1×10^{22} Mx total flux and maximum-field strengths (negative : positive) in a roughly 10 : 1 ratio.

Figure 2 (a) Representative images of the sunspot evolution during 4–6 July 2006: MDI longitudinal magnetic-field maps (left column); TRACE white-light images (right column). The TRACE image in the bottom panels corresponds to the time of the M2 flare (starting in soft X-rays at 8:20 UT). The dashed yellow line outlines the major axis of the sunspot that was used to measure the sunspot rotation. The corresponding [SOHO/MDI movie](#) is available in the electronic version of the article. (b) Sunspot rotation determined from the MDI magnetic-field maps over the period 3 July 2006, 22:00 UT, to 7 July 2006, 8:00 UT, showing the orientation of the sunspot's major axis, measured clockwise from solar East. (c) Sunspot rotation rate in degrees per day.



In Figure 2(a) we show snapshots of the sunspot evolution as observed by MDI and the *Transition Region and Coronal Explorer* (TRACE: Handy *et al.*, 1999), ranging from two days before the eruption to one day after it. The images are all differentially rotated to the first image of the series, when the sunspot was closer to disk centre. The sequence shows that the sunspot is rotating counter-clockwise during the considered period (see the

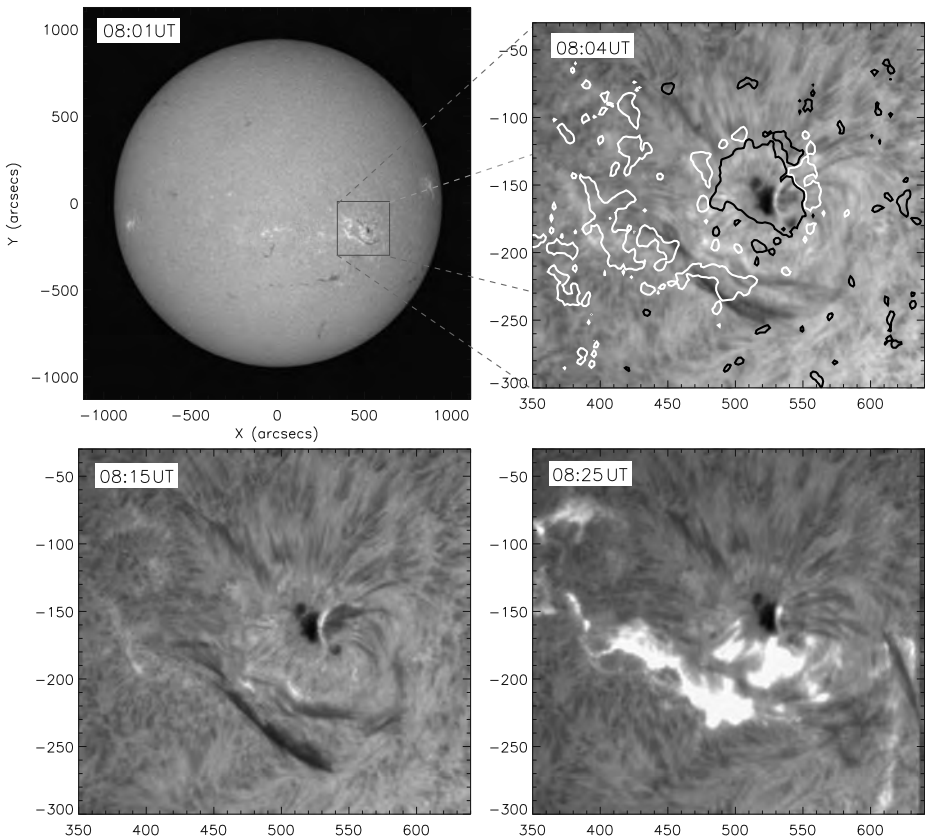


Figure 3 $H\alpha$ filtergram sequence observed before and during the flare on 6 July 2006 by the Kanzelhöhe (full disk) and Hvar (active region area) Observatories. An apparent double structure of the filament is visible South of the sunspot. Contour levels of 100 G from an MDI magnetogram taken at 07:59 UT are added in the top right panel, with white (black) lines corresponding to positive (negative) values.

[Electronic Supplementary Material](#)). From the evolution of the MDI magnetic-field maps, we geometrically determined the major axis of the sunspot and followed its evolution in time. In Figure 2(b) we plot the sunspot's rotation angle over the period 3 July 2006, 22:00 UT, to 7 July 2006, 8:00 UT. The total rotation observed over these three days is about 30° . The sunspot's rotation rate, determined as the temporal derivative of the rotation measurements, yields a mean value of about $10^\circ \text{ day}^{-1}$ during the considered time span (Figure 2(c)). For comparison, we determined the rotation also from the TRACE white-light images and found no significant differences.

The flare and the filament eruption were observed in full-disk $H\alpha$ filtergrams by the Kanzelhöhe Observatory and, over a smaller field-of-view around the active region, by the Hvar Observatory (Figure 3). These observations reveal that the filament consisted of a double structure before and during the eruption (for a similar case of such a double-structured filament, see Liu *et al.*, 2012). Significant rising motions of the filament could be seen from about 08:23 UT on. The $H\alpha$ flare started by the appearance of very weak double-footpoint brightening at 08:15 UT.

Figure 4 (a) TRACE 171 Å running-difference image showing the erupting filament and the overlying CME front. Distances are measured at crossings of the respective leading edges (red solid lines) with the dashed line, starting from the point marked by [x]. (b) Distance–time plot showing the kinematics of the filament and the CME front for the entire distance range. (c) Distance–time plot for the distance range up to $1.8 R_{\odot}$. The distance between [x] and the disk centre is added to all TRACE and EIT data points. (d) Velocity–time plot over the distance range up to $1.8 R_{\odot}$. See text for further details.

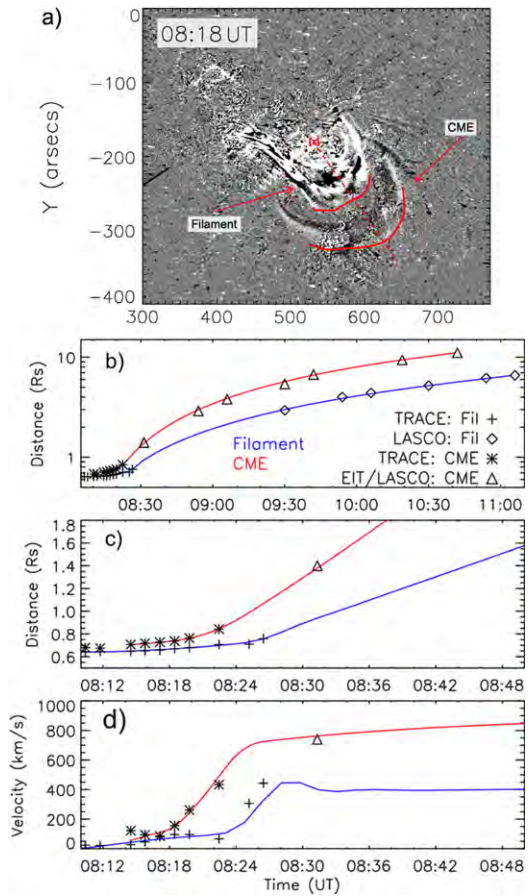


Figure 4(a) shows a running-difference image from TRACE 171 Å in which the erupting filament (the CME core) and the preceding CME front can be identified. From a time sequence of similar images by TRACE, EIT, and LASCO C2/C3 we estimated the kinematics of the filament and the CME front, which are shown in Figure 4(b), (c). The distances were measured in the plane of the sky, from disk centre in the LASCO images and from the midpoint of the line connecting the pre-eruption filament footpoints in the TRACE and EIT images. In order to approximately compensate for this discrepancy, we added to the TRACE and EIT measurements the distance between this point and the disk centre, which corresponds to ≈ 400 Mm. The resulting distances are plotted in Figure 4(b), (c), together with spline-smoothed curves. We did not correct for foreshortening effects, as projection effects only result in a multiplication factor and do not alter the profile of the derived kinematical curves (see, *e.g.*, Vršnak *et al.*, 2007). Additionally, Figure 4(d) gives the velocity profiles for the filament and the CME front, as derived from the first derivative of the distance–time measurements and spline-smoothed curves. From these plots we obtain the result that the coronal loops overlying the filament started their slow rising phase at 08:15 UT, *i.e.* about five–ten minutes before the filament. Similarly, the CME front reached its final, almost constant, velocity a few minutes before the filament.

Various other aspects of the event (flare, CME, EIT wave, dimming) were studied by Jiang *et al.* (2007), McIntosh *et al.* (2007), Attrill *et al.* (2008), Temmer *et al.* (2008), Miklenic, Veronig, and Vršnak (2009), Veronig *et al.* (2010), and Guo *et al.* (2010a). We refer to this work for further details as regards the eruption. Guo *et al.* (2010a) suggested that the eruption was triggered by recurrent chromospheric mass injection in the form of surges or jets into the filament channel. Here we propose a different mechanism, assuming that the filament was suspended in the corona by a magnetic flux-rope, a picture that is supported by various magnetic-field models of active regions containing filaments (*e.g.* Lionello *et al.*, 2002; van Ballegoijen, 2004; Guo *et al.*, 2010b; Canou and Amari, 2010). We suggest that the continuous rotation of the sunspot led to a slow expansion of the arcade-like magnetic field overlying the filament (*i.e.* to a continuous weakening of its stabilizing tension), until a critical point was reached at which equilibrium could not be maintained and the flux-rope erupted. We note that we do not claim that the eruption was triggered *exclusively* by this mechanism. Filaments are often observed to spiral into the periphery of sunspots (*e.g.* Green *et al.*, 2007), and also in our case an inspection of the TRACE and H α images during the early phase of the eruption suggests a possible magnetic connection between the western extension of the filament-carrying core field and the sunspot area. Thus, the sunspot rotation may have added stress to this field, thereby possibly contributing to drive it towards eruption. On the other hand, for an injection of twist as suggested by the simulations mentioned above to occur, the core field must be rooted in the centre of the sunspot, not just in its periphery, which is difficult to establish from observations. It appears reasonable to assume that a clear connection between core field and sunspot centre is not always present, and that the stressing of the overlying ambient field by sunspot rotation may be more relevant for the destabilisation of the system in such cases. In order to test this scenario, we perform a series of three-dimensional (3D) MHD simulations, which are described in the following sections.

3. Numerical Simulations

The purpose of the numerical simulations presented in this article is to show that the rotation of photospheric-flux concentrations can trigger the eruption of an initially stable flux-rope that is embedded in their fields. Differently from previous work (*e.g.* Amari *et al.*, 1996; Török and Kliem, 2003; Aulanier, Démoulin, and Grappin, 2005), the photospheric vortex motions do not directly affect the flux-rope in our simulations, but solely the field surrounding it.

The first simulation (hereafter run 1) involves a relatively simple magnetic configuration, consisting of a flux-rope embedded in a bipolar potential field (see Figure 5(c)). The initially potential field gets twisted at its photospheric-flux concentrations on both sides of the flux-rope in the same manner. This simulation is very idealised with respect to the observations presented in Section 2, in particular because both the initial magnetic configuration and the imposed driving possess a high degree of symmetry.

We then consider a more complex initial magnetic field (hereafter run 2), which is chosen such that it resembles the magnetic-field structure prior to the eruption described in Section 2 (see Figure 5(d)). As in run 1, this configuration contains a flux-rope embedded in a potential field, but the latter is now constructed by a significantly larger number of sub-photospheric sources, in order to mimic the main features of the observed photospheric flux distribution and the extrapolated coronal magnetic field (see Figure 5(c)). Differently from run 1, only one flux concentration is twisted in this case, as suggested by the observations. The purpose of run 2 is to verify that the mechanism studied in run 1 also works in a highly asymmetric

configuration. We do not attempt here to model the full eruption and evolution of the CME, for reasons that are specified below.

To construct our magnetic configurations, we employ the coronal flux-rope model of Titov and Démoulin (1999, hereafter TD). Its main ingredient is a current ring of major radius $[R]$ and minor radius $[a]$ that is placed such that its symmetry axis is located at a depth $[d]$ below a photospheric plane. The outward-directed Lorentz self-force (or “hoop force”) of the ring is balanced by a potential field created by a pair of sub-photospheric point sources $[\pm q]$ that are placed at the symmetry axis, at distances $\pm L$ from the ring centre. The resulting coronal field consists of an arched and line-tied flux-rope embedded in an arcade-like potential field. In order to create a shear component of the ambient field, TD added a sub-photospheric line current to the system. Since the latter is not required for equilibrium, we do not use it for our configurations (see also Rousev *et al.*, 2003; Török and Kliem, 2007).

Previous simulations (*e.g.* Török and Kliem, 2005; Schrijver *et al.*, 2008) and analytical calculations (Isenberg and Forbes, 2007) have shown that the TD flux-rope can be subject to the ideal-MHD helical kink and torus instabilities. Therefore, we adjust the model parameters such that the flux-rope twist stays below the typical threshold of the kink instability for the TD flux-rope (see Török, Kliem, and Titov, 2004). To inhibit the occurrence of the torus instability in the initial configurations, we further adjust the locations and magnitude of the potential field sources such that the field drops sufficiently slowly with height above the flux-rope (see Kliem and Török, 2006; Török and Kliem, 2007; Fan and Gibson, 2007; Aulanier *et al.*, 2010). While this is a relatively easy task for the standard TD configuration used in run 1, an extended parameter search was required for the complex configuration used in run 2, until an appropriate numerical equilibrium to start with could be found.

3.1. Numerical Setup

As in our previous simulations of the TD model (*e.g.* Török, Kliem, and Titov, 2004; Kliem, Titov, and Török, 2004), we integrate the $\beta = 0$ compressible ideal-MHD equations:

$$\partial_t \rho = -\nabla \cdot (\rho \mathbf{u}), \quad (1)$$

$$\rho \partial_t \mathbf{u} = -\rho (\mathbf{u} \cdot \nabla) \mathbf{u} + \mathbf{j} \times \mathbf{B} + \nabla \cdot \mathcal{T}, \quad (2)$$

$$\partial_t \mathbf{B} = \nabla \times (\mathbf{u} \times \mathbf{B}), \quad (3)$$

where \mathbf{B} , \mathbf{u} , and ρ are the magnetic field, velocity, and mass density, respectively. The current density is given by $\mathbf{j} = \mu_0^{-1} \nabla \times \mathbf{B}$. \mathcal{T} denotes the viscous stress tensor, included to improve numerical stability (Török and Kliem, 2003). We neglect thermal pressure and gravity, which is justified for the low corona where the Lorentz force dominates.

The MHD equations are normalised by quantities derived from a characteristic length $[l]$ taken here to be the initial apex height of the axis of the TD current ring above the photospheric plane $[l = R - d]$, the maximum magnetic-field strength in the domain $[B_{0\max}]$, and the Alfvén velocity $[v_{a0}]$. The Alfvén time is given by $[\tau_a = l/v_{a0}]$. We use a Cartesian grid of size $[-40, 40] \times [-40, 40] \times [0, 80]$ for run 1 and $[-40, 40] \times [-30, 30] \times [0, 60]$ for run 2, resolved by $247 \times 247 \times 146$ and $307 \times 257 \times 156$ grid points, respectively. The grids are non-uniform in all directions, with an almost uniform resolution $\Delta = 0.04$ (run 1) and $\Delta = 0.05$ (run 2) in the box centre, where the TD flux-rope and the main polarities are located. The plane $z = 0$ corresponds to the photosphere. The TD flux-rope is oriented along the y -direction in all runs, with its positive-polarity footpoint rooted in the half-plane $y < 0$. We employ a modified two-step Lax–Wendroff method for the integration, and we

additionally stabilise the calculation by artificial smoothing of all integration variables (Sato and Hayashi, 1979; Török and Kliem, 2003).

The boundary conditions are implemented in the ghost layers. The top and lateral boundaries are closed, which is justified given the large size of the simulation box. Below the photospheric plane, the tangential velocities are imposed as described in Section 3.3. The vertical velocities are zero there at all times, and the mass density is fixed at its initial values. The latter condition is not consistent with the imposed vortex flows, but is chosen to ensure numerical stability (see Török and Kliem, 2003). Since we use the $\beta = 0$ approximation, and since the evolution is driven quasi-statically at the bottom plane, fixing the density in $z = -\Delta z$ is tolerable. The tangential components of the magnetic field $[B_{x,y}]$ are extrapolated from the integration domain, and the normal component $[B_z]$ is set such that $\nabla \cdot \mathbf{B} = 0$ in $z = 0$ at all times (see Török and Kliem, 2003). Since our code does not ensure $\nabla \cdot \mathbf{B} = 0$ to rounding error in the rest of the domain, we use a diffusive $\nabla \cdot \mathbf{B}$ cleaner (Keppens *et al.*, 2003), as well as Powell's source-term method (Gombosi, Powell, and de Zeeuw, 1994), to minimise unphysical effects resulting from $\nabla \cdot \mathbf{B}$ errors.

3.2. Initial Conditions

The parameters of the TD equilibrium employed in run 1 are (in normalised units): $R = 2.2$, $a = 0.7$, $d = 1.2$, $L = 1.2$, and $q = 1.27$. The magnetic axis of the TD flux-rope (which is located above the geometrical axis of the current ring, see Valori *et al.*, 2010) has an apex height $z = 1.09$. The potential field connects two fully symmetric flux concentrations and runs essentially perpendicular above the TD flux-rope. The apex of the central field line, *i.e.* the field line connecting the centres of the potential-field polarities, is located at $z = 3.40$. After the initial relaxation of the system (see below), these heights become $z = 1.22$ and $z = 3.62$, respectively. Figures 5(c) and 6(a) show the configuration after the relaxation.

The magnetic configuration used in run 2 is a step towards a more realistic modelling of the coronal field during the 6 July 2006 eruption. Figure 5(b) shows a coronal potential-field source-surface (PFSS) model (Schatten, Wilcox, and Ness, 1969), obtained from a synoptic MDI magnetogram for Carrington Rotation 2045, using the SolarSoft package pfss provided by LMSAL (<http://www.lmsal.com/~derosa/pfsspack/>). It can be seen that the field lines rooted in the main polarity (the sunspot) form a fan-like structure, which partly overlies the filament. We again consider a standard TD flux-rope, with $R = 2.75$, $a = 0.8$, and $d = 1.75$, but now we use an ensemble of ten sub-photospheric sources (five point sources, and five vertically oriented dipoles like the ones used by Török and Kliem, 2003) for the construction of the ambient field, in order to resemble the main properties of the observed photospheric flux distribution and the corresponding PFSS field. By adjusting the positions and strengths of the sources, we tried to mimic the approximate flux balance between the concentrated leading negative polarity and the dispersed following positive polarity, the ratio of approximately 10:1 between the peak field strengths in the leading polarity and the following polarity, the size ratio between these polarities, the presence of an "inverse C-shaped" area of dispersed negative flux to the West of the leading polarity (see Section 2), as well as the fan-like shape of the coronal field rooted in the leading polarity. The position of the flux-rope within the ambient field is guided by the observed location of the filament (Figure 5(b)). Since the model is still relatively idealised, all of these features can be matched only approximately. The resulting configuration (after initial relaxation) is shown in Figure 5(d) and in Figure 8(a) below. It can be seen that the TD flux-rope is stabilised by flux rooted towards the southern edge of the main polarity. The rope is inclined with respect to the vertical, which is due to the asymmetry of the potential field surrounding it.

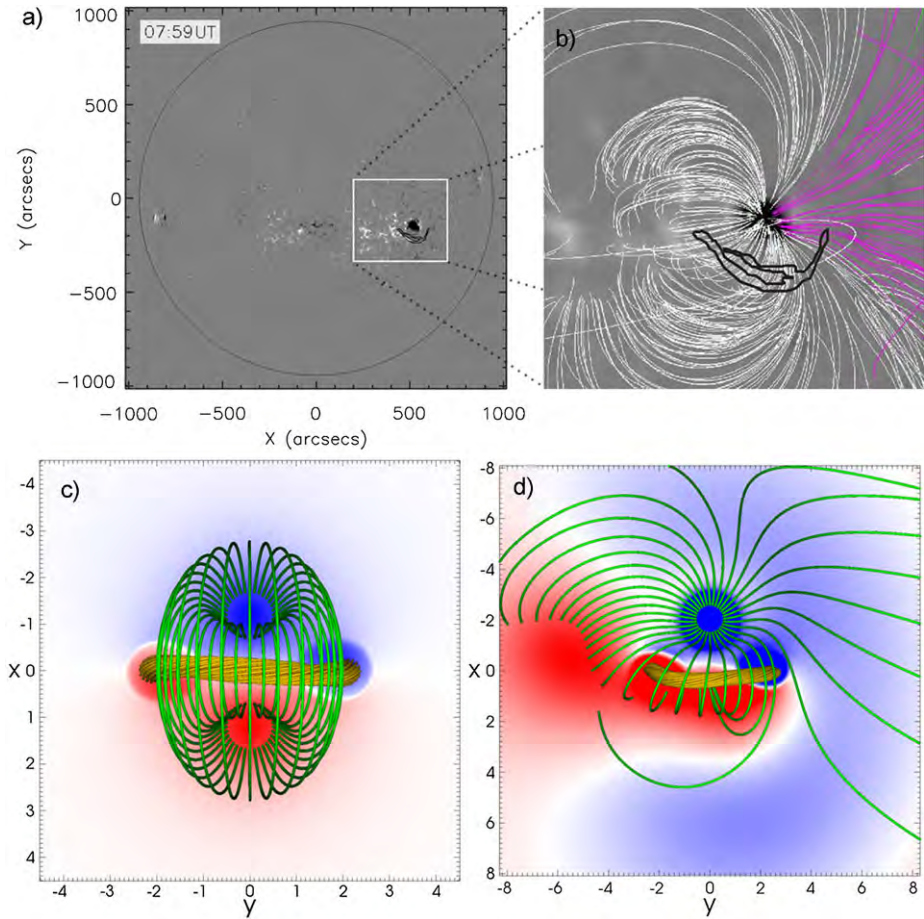


Figure 5 (a) Same as Figure 1. (b) Magnetic-field lines in the active-region area (marked by the white square in panel a) from a potential field source surface (PFSS) model that was calculated for 6 July 2006, 06:04 UT, overlaid on a synoptic MDI magnetogram for the corresponding Carrington Rotation 2045. The model corona is a spherical shell extending from 1.0 to 2.5 R_{\odot} . Pink (white) field lines depict open (closed) fields. The outer contours of the filament, based on $H\alpha$ data taken at 07:59 UT on 6 July 2006, are outlined with black lines. For better illustration, the area is rotated to disk centre. (c), (d): Top view on the magnetic configurations used in runs 1 and 2, respectively, after the initial relaxation of the system (see Section 3 for details). The core of the TD flux-rope is shown by orange field lines, green field lines depict the ambient potential field. B_z is shown in the bottom plane, where red (blue) colours corresponds to positive (negative) values. The colour scale in panel d) is saturated at about 4 % of the maximum B_z , in order to depict also weaker flux distributions.

In contrast to the configuration used in run 1, the magnetic field in run 2 is dominated by one main polarity. Rather than closing down to an equally strong polarity of opposite sign, the flux emanating from the main polarity now spreads out in all directions, resembling a so-called fan–spine configuration (*e.g.* Pariat, Antiochos, and DeVore, 2009; Masson *et al.*, 2009; Török *et al.*, 2009). Note that this flux does not contain fully open field lines, as was presumably the case during the 6 July 2006 eruption (see Figure 5(b)). This is due to the fact that the flux distribution shown in Figure 5(d) is fully surrounded by weak positive flux in the model (imposed to mimic the isolated “inverse C-shaped” weak negative polarity to the

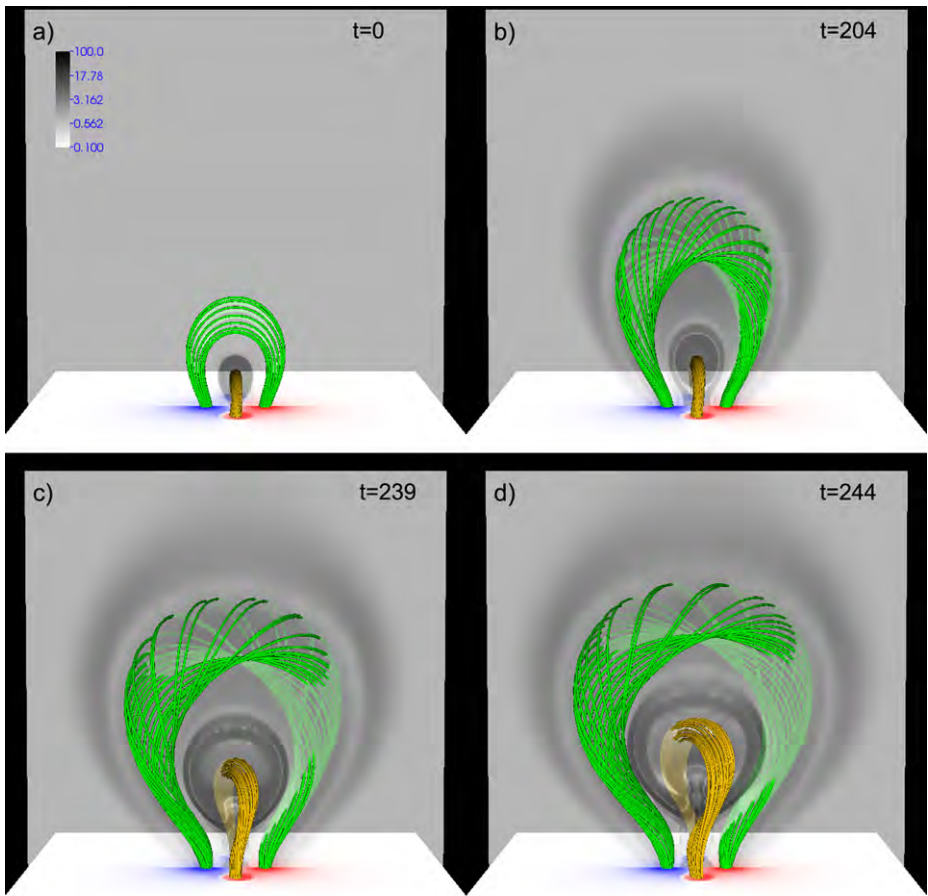


Figure 6 Magnetic-field lines outlining the evolution of the TD flux-rope (orange) and the twisted overlying field (green) for run 1, at $t = 0, 204, 239, 244\tau_A$, respectively; panel (a) shows the system after the initial numerical relaxation. The normal component of the magnetic field $[B_z]$ is shown at the bottom plane $z = 0$, with red (blue) corresponding to positive (negative) values. The transparent grey-scale shows the logarithmic distribution of the current densities divided by the magnetic field strength $[|J|/|B|]$ in the plane $x = 0$. The sub-volume $[-8.5, 8.5] \times [-8, 8] \times [0, 16]$ is shown in all panels. An animation of this figure is available in the [electronic version](#) of this article.

West of the main polarity), so that the positive flux in the total simulation domain exceeds the negative flux shown in Figure 5(b). Note that this “total” flux ratio shall not be confused with the flux ratio between the main polarity and the dispersed positive polarity to its East, which is approximately balanced in the model, in line with the observations.

As in Amari *et al.* (1996), Török and Kliem (2003) and Aulanier, Démoulin, and Grappin (2005), we use an initial density distribution $\rho_0(\mathbf{x}) = |\mathbf{B}_0(\mathbf{x})|^2$ corresponding to a uniform initial Alfvén velocity. For the configuration used in run 2 we also ran a calculation with $\rho_0(\mathbf{x}) = |\mathbf{B}_0(\mathbf{x})|^{3/2}$, *i.e.* with a more realistic Alfvén velocity that decreases with distance from the flux concentrations. We found that the evolution was qualitatively equivalent, but somewhat less dynamic.

In order to obtain a numerical equilibrium as a starting point of the twisting phase, we first performed a numerical relaxation of the two configurations used. This is done for $54\tau_a$ for the system used in run 1, and for $75\tau_a$ for the system used in run 2, after which the time is reset to zero in both cases.

3.3. Photospheric Driving

The velocity field used to twist the potential fields is prescribed in the plane $z = -\Delta z$ and located at their main flux concentrations. It produces a horizontal counter-clockwise rotation, chosen such that the velocity vectors always point along the contours of $B_z(x, y, 0, t = 0)$, which ensures that the distribution of $B_z(x, y, 0, t)$ is conserved to a very good approximation. The flows are given by

$$u_{x,y}(x, y, -\Delta z, t) = v_0 f(t) \nabla^\perp \left\{ \zeta [B_{0z}(x, y, 0, 0)] \right\}, \quad (4)$$

$$u_z(x, y, -\Delta z, t) = 0, \quad (5)$$

with $\nabla^\perp := (\partial_y, -\partial_x)$. A smooth function

$$\zeta = B_z^2 \exp\left(\frac{(B_z^2 - B_{z_{\max}}^2)}{\delta B^2}\right), \quad (6)$$

chosen as by Amari *et al.* (1996), defines the vortex profile. The parameter δB determines the vortex width (see Figure 3 in Aulanier, Démoulin, and Grappin, 2005). We use $\delta B = 0.7$ for run 1 and $\delta B = 2$ for run 2. The parameter v_0 determines the maximum driving velocity. We choose $v_0 = 0.005v_A$ for both runs to ensure that the driving is slow compared to the Alfvén velocity. The velocities are zero at the polarity centre and decrease towards its edge from their maximum value to zero (see Figure 2 in Török and Kliem, 2003). The twist injected by such motions is nearly uniform close to the polarity centre and decreases monotonically towards its edge (see Figure 10 below and Figure 9 in Török and Kliem, 2003). The polarity centres are located at $(\pm 1.2, 0, 0)$ for the configuration used in run 1 and the vortex flows are applied at both flux concentrations. In run 2, we twist the potential field only in the main negative polarity, the centre of which is located at $(-2, 0, 0)$. The function $f(t)$ describes the temporal profile of the imposed twisting. The twisting phase starts with a linear ramp ($0 \leq t \leq t_r$) from $f(0) = 0$ to $f(t_r) = 1$, which is then held fixed. If a final relaxation phase is added, $f(t)$ is analogously linearly reduced to zero and held fixed. In all simulations in this article $t_r = 10\tau_a$.

In contrast to the symmetric configuration used in run 1, where most of the flux emanating from the main polarities arches over the flux-rope, the flux that initially stabilises the rope in run 2 is concentrated towards the southern edge of the polarity, where the imposed vortex velocities are relatively small. In order to obtain the eruption of the TD rope within a reasonable computational time in run 2, we therefore use a δB that is larger than in run 1.

4. Simulation Results

4.1. Run 1

We first consider the more idealised and symmetric case, in which the vortices are applied at both photospheric polarities of the potential field. As a result of the imposed motions, the field lines rooted in the polarities become increasingly twisted and a relatively wide twisted flux-tube is formed, which expands and rises with increasing velocity (Figure 6).

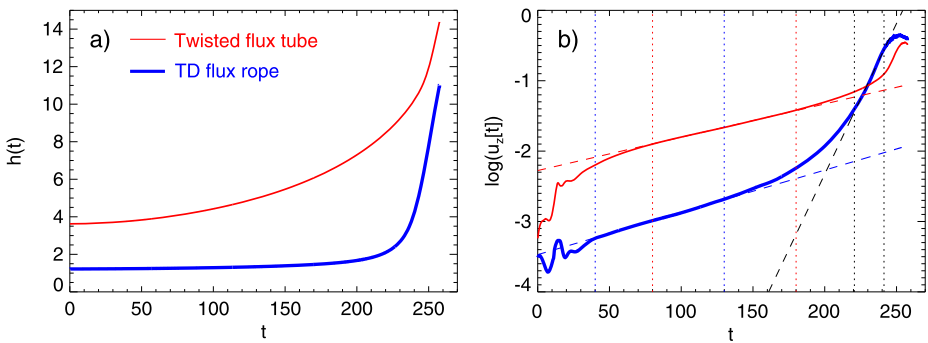


Figure 7 Kinematics of the TD flux-rope (thick blue lines) and of the overlying twisted flux-tube (solid red lines) during the twisting phase in run 1. (a) Height of the axis apex as a function of time. The initial heights are 1.22 for the TD rope and 3.62 for the twisted flux-tube. (b) Logarithmic presentation of the corresponding vertical velocities. The dashed lines show linear fits, obtained within the time periods marked by the vertical dotted lines of the same colour.

Detailed descriptions on the evolution of such twisted fields have been given by Amari *et al.* (1996), Török and Kliem (2003), and Aulanier, Démoulin, and Grappin (2005). Since here we are merely interested in how the rising flux affects the stability of the TD flux-rope, we only note that the rise follows the exponential behaviour found in this earlier work. This is shown in Figure 7, where the kinematics of the two flux systems (the twisted flux-tube and the TD flux-rope) are followed in time by tracking the position of the respective central field-line apex. The exponential rise phase of the twisted flux-tube, preceded by a slower transition, can be clearly seen between $t \approx 80\tau_a$ and $t \approx 180\tau_a$.

The slow rise of the flux-tube successively weakens the stabilizing magnetic tension on the TD rope, so that the latter starts to ascend as well. As can be seen in Figure 7(b), the rise of the TD rope also follows an exponential behaviour up to $t \approx 130\tau_a$. While its growth rate is slightly larger than for the twisted flux-tube, its velocity remains about one order of magnitude smaller. In order to check that this slow exponential rise of the TD rope is indeed an adaptation to the changing ambient field, rather than a slowly growing instability, we performed a relaxation run by ramping down the photospheric driving velocities to zero between $t = 100\tau_a$ and $t = 110\tau_a$ and following the evolution of the system until $t = 181\tau_a$. Both the twisted flux-tube and the TD rope relax towards a numerical equilibrium in this run, without any indication of instability or eruption. Hence, during its slow rise phase until $t \approx 130\tau_a$, the TD rope experiences a quasi-static evolution along a sequence of approximately force-free equilibria, generated by the slowly changing boundary conditions (in particular, the changing tangential components of the magnetic field at the bottom plane).

Starting at $t \approx 130\tau_a$, the TD rope undergoes a successively growing acceleration which ends in a rapid exponential acceleration phase between $t \approx 220\tau_a$ and $t \approx 250\tau_a$ that is characterised by a growth rate significantly larger than during the quasi-static phase (see also the bottom panels of Figure 6). The rope finally reaches a maximum velocity of $0.45v_{a0}$ at $t = 252\tau_a$, after which it starts to decelerate. Such a slow rise phase, followed by a rapid acceleration, is a well-observed property of many filament eruptions in the early evolution of CMEs (see, *e.g.*, Schrijver *et al.*, 2008, and references therein), and is also seen for the event studied in this article (see Figure 4(d)). The evolution of the TD rope after $t \approx 130\tau_a$ can be associated with the development of the torus instability (Bateman, 1978; Kliem and Török, 2006; Démoulin and Aulanier, 2010), as has been shown under similar conditions in

various simulations of erupting flux-ropes (Török and Kliem, 2007; Fan and Gibson, 2007; Schrijver *et al.*, 2008; Aulanier *et al.*, 2010; Török *et al.*, 2011).

During the transition of the TD rope to the torus-unstable regime, the overlying twisted flux-tube continues its slow exponential rise at almost the same growth rate for about 100 Alfvén times, which excludes the possibility that the additional acceleration of the TD rope after $t \approx 130\tau_a$ is due to an adaptation to the evolving environment field. At $t \approx 230\tau_a$, however, the rise speed of the TD rope begins to exceed the rise speed of the flux-tube, and the latter gets significantly accelerated from below by the strongly expanding rope. The overtaking of the twisted flux-tube by the faster TD rope, and the resulting interaction between the two, is reminiscent of the so-called CME cannibalism phenomenon (*e.g.* Gopalswamy *et al.*, 2001; Lugaz, Manchester, and Gombosi, 2005). The investigation of this interaction is, however, beyond the scope of the present article, so that we stopped the simulation at this point.

Run 1 shows that the rotation of the footpoints of a flux system overlying a stable flux-rope can lead to the eruption of the rope, by progressively lowering the threshold for the torus instability. We suggest that this mechanism may have been at the origin of the CME event described in Section 2.

The numerical experiment presented here has a high degree of symmetry, with respect to both the initial magnetic-field configuration and the driving photospheric motions. A practically identical result is obtained if only one of the polarities of the overlying field is twisted, as long as the driving velocity is clearly sub-Alfvénic. In particular, we found that twisting only one flux concentration does not significantly affect the rise direction of the TD rope, indicating that slow asymmetric twisting does not necessarily lead to a non-radial rise of the erupting flux-rope if the overlying field is symmetric. A more general case, which exhibits a strongly non-radial rise, is presented in the following section.

4.2. Run 2

We now consider a much less symmetric initial condition for the magnetic field, together with a driving that is applied to one polarity only. The configuration is still idealised, but closer to the observations (see Sections 2 and 3.2). The purpose of run 2 is to verify that the CME initiation mechanism suggested in Section 4.1 can work also in a more realistic and general setting.

The fan-like structure of the ambient field makes it difficult to follow its evolution during the twisting phase using a single point as a tracer of the whole three-dimensional structure, as was done for run 1. We therefore follow here only the apex of the TD rope axis in time. The inclination of the rope makes it complicated to find the exact position of the axis apex, so we determined it only approximately. Consequently, the trajectories presented in Figure 9 below are somewhat less precise than for run 1.

Figure 8(a) shows that electric currents are formed in the ambient field volume during the initial relaxation of the system. The strongest current concentrations are located in the front of the flux-rope and exhibit an X-shaped pattern in the vertical cut shown. This pattern outlines the locations of quasi-separatrix layers (QSLs: *e.g.* Priest and Forbes, 1992; Démoulin *et al.*, 1996) that separate different flux systems. The QSLs are present in the configuration from the very beginning and arise from the complexity of the potential field (see Section 3.2). Their presence is evident also in the left panel of Figure 8(a): the green field lines show strong connectivity gradients in the northern part of the main polarity and in the vicinity of the western flux-rope footpoint. It has been demonstrated that current concentrations form preferably at the locations of QSLs and other structural

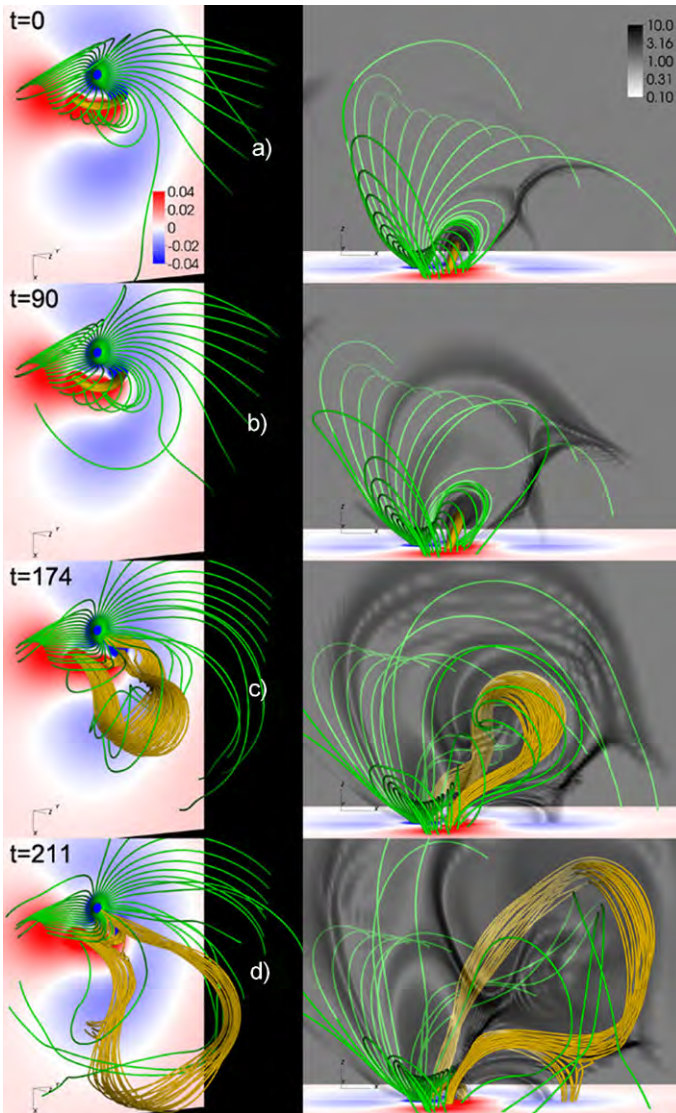


Figure 8 Snapshots of run 2 at times $t = 0, 90, 174, 211\tau_a$, respectively, showing the same features as in Figure 5(d). The system is shown after the initial relaxation (a), during the slow rise phase (b), at the time of the peak flux-rope velocity (c), and during the deceleration of the flux-rope (d). The left panels use a view similar to the observations presented in Section 2, the right panels show a side view. The transparent grey-scale in the right panels depicts the logarithmic distribution of $|j|/|B|$ in the plane $x = 0$, outlining the locations of strong current concentrations. The sub-volume $[-10, 16] \times [-11, 11] \times [0, 18]$ is used for all panels. An animation of this figure is available in the [electronic version](#) of this article.

features like null points, separatrix surfaces, and separators, if a system containing such structures is dynamically perturbed (e.g. Baum and Bratenahl, 1980; Lau and Finn, 1990; Aulanier, Pariat, and Démoulin, 2005). In our case the perturbation results from the – relatively modest – dynamics during the initial relaxation of the system.

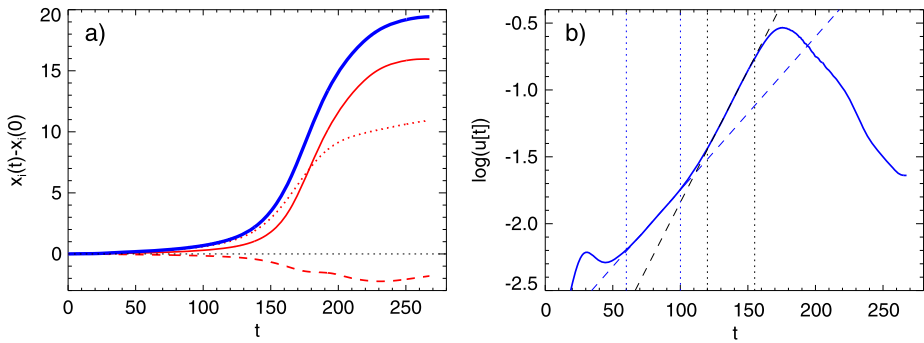


Figure 9 Kinematics of the TD flux-rope in run 2. (a) Red lines show the distances of the axis apex from its initial position, $(x_0, y_0, z_0) = (0.075, 0, 1.076)$, for all three spatial dimensions as a function of time. The solid line shows $x - x_0$, the dashed one $y - y_0$, and the dotted one $z - z_0$. The thick blue line shows the total deviation from the initial position. (b) Logarithmic presentation of the total velocity of the axis apex as a function of time (solid blue line). As in Figure 7, the dashed lines show linear fits obtained for the time periods marked by dotted lines of the same colour.

After the relaxation, at $t = 0$, we start twisting the main negative polarity. Due to the pronounced fan-structure of the field rooted in the main polarity, the photospheric twisting does not lead to the formation of a single twisted flux tube that rises exactly in vertical direction above the TD rope, as was the case in run 1. Rather, the twisting leads to a slow, global expansion of the fan-shaped field lines (see Figure 8 and the corresponding online animations). Since we are mainly interested in the destabilisation of the flux-rope, we did not study the detailed evolution of the large-scale field. We expect it to be very similar to the one described by Santos, Büchner, and Otto (2011), since the active region those authors simulated was also dominated by one main polarity (sunspot), and the field rooted therein had a very similar fan-shaped structure (compare, for example, our Figure 8 with their Figure 1).

Important for our purpose is the evolution of the arcade-like part of the initial potential field that directly overlies the TD flux-rope. Those field lines are directly affected only by a fraction of the boundary flows and therefore get merely sheared (rather than twisted), which still leads to their slow expansion. As was the case for run 1, the TD rope starts to expand as well, adapting to the successively decreasing magnetic tension of the overlying field. This initial phase of the evolution is depicted in Figure 8b. Note that some of the flux at the front of the expanding arcade reconnects at the QSL current layer (see the online animation), which can be expected to aid the arcade expansion to some degree. As in run 1, the TD rope rises, after some initial adjustment, exponentially during this slow initial phase (Figure 9).

As the twisting continues, a transition to a rapid acceleration takes place, which can be seen in Figure 9b after $t \approx 100\tau_a$, when the rise curve leaves the quasi-static regime. After the transition phase, the TD rope again rises exponentially, but now with a significantly larger growth rate than during the slow rise phase. As for run 1, we attribute this transition and rapid acceleration to the occurrence of the torus instability.

The right panels in Figure 8 show that the trajectory of the flux-rope is far from being vertical. As can be seen in Figure 9, the rope axis has reached an inclination of about 45 degrees at the time of its peak rise velocity. Such lateral eruptions have been reported frequently in both observations and simulations (Williams *et al.*, 2005; Aulanier *et al.*, 2010; Bi *et al.*, 2011; Panasenco *et al.*, 2011; Zuccarello *et al.*, 2012; Yang *et al.*, 2012, and references therein), and are usually attributed to an asymmetric

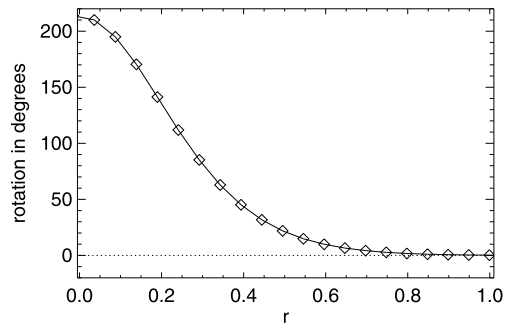
structure of the field overlying the erupting core flux. We believe that this causes the lateral rise also in our case, in particular since we found that asymmetric twisting of a symmetric configuration does not lead to a non-vertical trajectory of the flux-rope (see Section 4.1). We note that such a lateral rise during the very early phase of a CME is different from the often observed deflection of CMEs at coronal holes, where the ejecta is channelled by the structure of the coronal field at larger heights (Kahler, Akiyama, and Gopalswamy, 2012, and references therein). As the eruption continues, the trajectory of the flux-rope becomes increasingly horizontal, resembling the so-called “roll effect” (e.g. Panasenco *et al.*, 2011) and indicating that the rope cannot overcome the tension of the large-scale overlying field. Moreover, as a consequence of its increasing expansion, the flux-rope strongly pushes against the QSL current layer, which results in reconnection between the front of the rope and the ambient field. Eventually, the rope splits into two parts, similar to what has been found in simulations of confined eruptions (Amari and Luciani, 1999; Török and Kliem, 2005). These two effects – which both are not present in run 1 – slow down the rise of the rope after $t \approx 175\tau_a$ and inhibit its full eruption (*i.e.* the development of a CME) in our simulation.

Since QSLs can affect the evolution of an eruption, but are not expected to play a significant role for its initiation, we did not investigate in detail whether or not QSLs were present in the pre-eruption configuration of the 6 July 2006 event. The PFSS extrapolation indicates their presence to the North and the West of the main polarity (see the field-line connectivities in Figure 5(b), but less clearly so to its South. The possible absence of a QSL in front of the erupting core field in the real event is in line with the “smooth” evolution of the observed CME, while in our simulation the coherence of the flux-rope is destroyed before it can evolve into a full eruption. Also, the real large-scale field was probably less confining than our model field: the PFSS extrapolation indicates the presence of open field lines, which are fully absent in our simulation. Since, as stated earlier, we merely aim to model the initiation of the eruption rather than its full evolution into a CME, we refrained from further improving our model to obtain a configuration without a strong QSL in front of the flux-rope and with more open flux.

As for run 1, we check how the system evolves when the twisting is stopped before the flux-rope erupts. When the vortex flows are ramped down to zero during $t = (35-45)\tau_a$ – corresponding to an effective twisting time of $35\tau_a$ – no eruptive behaviour is seen in the subsequent evolution for almost $300\tau_a$, after which we stopped the calculation. However, the system does not fully relax to a numerical equilibrium as it was the case for the simpler configuration (see Section 4.1). Rather, the flux-rope continues to rise very slowly, with velocities smaller than $10^{-3}v_{a0}$. This indicates that the system has entered a meta-stable state, which is possibly supported by continuous slow reconnection at the QSL current layer due to numerical diffusion, so that it can be expected that the rope would finally erupt if the integration were continued sufficiently long. When somewhat more twisting is applied, the system behaves as in the continuously driven configuration, *i.e.* a phase of slow rise is followed by a transition to rapid acceleration and the final eruption of the flux-rope, except that the evolution leading up to the eruption takes the longer the less twist is imposed. For example, for an effective twisting period of $45\tau_a$, the rapid acceleration of the rope sets in at $\approx 265\tau_a$, significantly later than in the continuously driven system.

While it is tempting to quantitatively compare the amount of rotation in the simulation with the observed sunspot rotation, we think that such a comparison can be misleading, since the amount of rotation required for eruption will depend on parameters that have not been studied here and are not available from the observations (see Section 5: Summary and Discussion). Moreover, a quantitative comparison is not straightforward, since the model

Figure 10 Rotation profile for run 2 as a function of distance from the vortex centre; shown at $t = 100\tau_a$, approximately when the transition from slow to fast rise sets in (see Figure 9(b)).



rotation is highly non-uniform (Figure 10), while in the observed case a rigid rotation of the spot was measured (Figure 2). For example, at $t \approx 100\tau_a$, when the transition from slow to fast rise starts in the continuously driven simulation, the field lines rooted very close to the main polarity centre have rotated by about 200° . However, those field lines do not overlie the TD flux-rope directly, rather they connect to the positive polarity region located to the East of the rope (see Figures 5d and 8) and should therefore not significantly influence the rope's stability. On the other hand, the arcade-like field lines that are located directly above the rope are rooted at a distance of $r \approx 0.4$ from the polarity centre, towards its southern edge. As can be seen in Figure 10, the flux surface containing these field lines is rotated by a much smaller amount, about 40° at $t = 100\tau_a$. For the run with an effective twisting time of $t = 45\tau_a$ mentioned above, the imposed total rotation at this flux surface is even smaller, slightly below 20° . These values are similar to the observed sunspot rotation, but, in addition to the reasons given above, such a comparison should be taken with care. While the expansion of the field lines located directly above the TD flux-rope presumably depends mainly on the driving imposed at their footpoints, it is also influenced to some degree by the expansion of higher-lying fields which, in turn, depends on the (significantly larger) amount of rotation closer to the polarity centre. Moreover, the values obtained from the model refer to an overlying field that is initially potential (except for the QSL-related current layers), while the real overlying field may have already contained some stress at the onset of detectable rotational motions. Finally, as discussed at the end of the Introduction, the sunspot rotation may have injected stress also directly into the filament. In both cases, presumably less rotation as suggested by the model would have been required to trigger the eruption.

In summary, the simulation successfully models the early phases of the eruption (the slow rise and the initial rapid acceleration of the flux-rope) in a setting that is qualitatively similar to the observed configuration of the active region around the time of the CME described in Section 2. Hence, the CME-initiation mechanism described in run 1 can work also in more complex and less symmetric configurations.

5. Summary and Discussion

We analyse a filament eruption, two-ribbon flare, and CME that occurred in NOAA Active Region 10898 on 6 July 2006. The filament was located South of a strong sunspot that dominated the region. In the evolution leading up to the eruption, and for some time after it, a counter-clockwise rotation of the sunspot of about 30° was observed. Similar events, which occurred close to a dominant rotating sunspot, were presented by, *e.g.*, Tian and Alexander (2006) and Régnier and Canfield (2006). The triggering of such eruptions is commonly

attributed to the injection of twist (or helicity) beyond a certain threshold by the sunspot rotation (e.g. Török and Kliem, 2003). However, while filaments are frequently observed to spiral into the periphery of main sunspots, the erupting core flux may not always be rooted in the spot itself. Here we suggest that the continuous expansion due to sunspot rotation of the magnetic field that stabilises the current-carrying core flux, *i.e.* the successive decrease of magnetic tension, can also lead to filament eruptions and CMEs in such configurations.

We support this scenario by MHD simulations, in which a potential field overlying and stabilizing a pre-existing flux-rope is slowly twisted at its photospheric-flux concentration(s). The flux-rope is not anchored in these concentrations and is therefore not twisted. In a first configuration, the rope is initially kept in equilibrium by a field rooted in two “sunspots” of opposite polarity that are located at opposite sides of the rope. The twisting of the flux concentrations reproduces the known behaviour of twisted bipolar fields (see, e.g., Amari *et al.*, 1996): a twisted flux tube is generated that expands and rises at an exponentially increasing rate. As a consequence, the magnetic tension of the field above the pre-existing flux-rope is successively weakened. The rope undergoes a quasi-static adaptation to the changing surrounding field, which is manifested in a slow rise phase. As the weakening of the overlying field reaches an appropriate level, the torus instability sets in and rapidly accelerates the rope upwards, leading to a second, fast rise phase and eruption. This evolution in two phases resembles the often-observed slow rise phase and subsequent strong acceleration of filaments in the course of their eruption (see Figure 4, as well as Schrijver *et al.*, 2008, and references therein). Eventually, since the flux-rope erupts faster than the twisted flux-tube rises, the rope catches up and starts to interact with the flux-tube, at which point we stop the simulation.

As a step towards more realistic configurations, we consider a second setup in which the initial ambient field surrounding the flux-rope is created by an ensemble of sub-photospheric sources that qualitatively reproduce the photospheric flux distribution and magnetic-field structure of the active region around the time of the 6 July 2006 event. In particular, the highly asymmetric flux density and the resulting overall fan shape of the active-region field are recovered, while the approximative flux balance of the region is kept. The rotation of the dominant negative polarity (mimicking the observed sunspot rotation) leads to the same qualitative behaviour as in the much more symmetric configuration: after a slow rise phase resembling the quasi-static adaptation of the flux-rope to the expanding ambient field, the rope undergoes a second, strong acceleration phase. In this case, the asymmetry of the ambient field leads to a markedly lateral eruption. However, in contrast to the first configuration, the presence of a QSL-related current layer in the front of the erupting flux-rope leads to reconnection which eventually splits the rope before it can evolve into a CME. Although we are not able to follow the expansion of the flux-rope beyond this phase, we can assert the effectiveness of the proposed mechanism in triggering an eruption also in this more realistic case.

The proposed mechanism requires the presence of a flux-rope in the corona prior to the onset of the twisting motions, which is in line with the relatively small observed rotation of about 30° in our event. Far larger rotations appear to be required to produce a flux-rope that can be driven beyond the threshold of instability by such small additional rotation (e.g. Török and Kliem, 2003; Aulanier, Démoulin, and Grappin, 2005; Yan *et al.*, 2012). It can be expected that the amount of rotation required to initiate the eruption of a pre-existing flux-rope by rotating its overlying field depends on two main parameters: i) the “distance” of the flux-rope from an unstable state and ii) the “effectiveness” of the rotation in reducing the stabilisation by the overlying field. For example, it will take a longer time for a low-lying flux-rope to slowly rise to the critical height required for the onset of the torus instability

than it does for a rope that is already close to this height. Also, the required rotation will be larger if mostly high-arching field lines, rather than field lines located directly above the rope, are twisted. Thus, the amount of rotation required for eruption appears to depend strongly on the details of the configuration. A proper assessment of this question demands an extensive parametric study that is beyond the scope of this article. Here we merely aim to provide proof-of-concept simulations that illustrate the physical mechanism.

In summary, the main result of our study is that the rotation of sunspots can substantially weaken the magnetic tension of the field in active regions, in particular in cases where the sunspot dominates the region. This can lead to the triggering of eruptions in the vicinity of the spot, even if the erupting core flux (the filament) is not anchored in it. The mechanism that we suggest provides an alternative to the common scenario in which eruptions in the vicinity of rotating sunspots are triggered by the direct injection of twist into the erupting core flux.

Acknowledgements We thank the anonymous referee for constructive comments that helped to improve the content of the article. We acknowledge the use of data provided by the SOHO/MDI consortium. SOHO/EIT was funded by CNES, NASA, and the Belgian SPPS. The SOHO/LASCO data used here are produced by a consortium of the Naval Research Laboratory(USA), Max-Planck-Institut für Aeronomie (Germany), Laboratoire d'Astrophysique de Marseille (France), and the University of Birmingham (UK). SOHO is a mission of international cooperation between ESA and NASA. The *Transition Region and Coronal Explorer* (TRACE) is a mission of the Stanford-Lockheed Institute for Space Research, and part of the NASA Small Explorer program. H α data were provided by the Kanzelhöhe Observatory, University of Graz, Austria, and by the Hvar Observatory, University of Zagreb, Croatia. The research leading to these results has received funding from the European Commission's Seventh Framework Programme (FP7/2007–2013) under the grant agreements No. 218816 (SOTERIA project, www.soteria-space.eu) and No. 284461 (eHEROES, <http://soteria-space.eu/eheroes/html>). TT was partially supported by NASA's HTP, LWS, and SR&T programs. LvDG acknowledges funding through the Hungarian Science Foundation grant OTKA K81421.

References

- Amari, T., Luciani, J.F.: 1999, *Astrophys. J. Lett.* **515**, L81. doi:[10.1086/311971](https://doi.org/10.1086/311971).
- Amari, T., Luciani, J.F., Aly, J.J., Tagger, M.: 1996, *Astrophys. J. Lett.* **466**, L39. doi:[10.1086/310158](https://doi.org/10.1086/310158).
- Attrill, G.D.R., van Driel-Gesztelyi, L., Démoulin, P., Zhukov, A.N., Steed, K., Harra, L.K., Mandrini, C.H., Linker, J.: 2008, *Solar Phys.* **252**, 349. doi:[10.1007/s11207-008-9255-z](https://doi.org/10.1007/s11207-008-9255-z).
- Aulanier, G., Démoulin, P., Grappin, R.: 2005, *Astron. Astrophys.* **430**, 1067. doi:[10.1051/0004-6361:20041519](https://doi.org/10.1051/0004-6361:20041519).
- Aulanier, G., Pariat, E., Démoulin, P.: 2005, *Astron. Astrophys.* **444**, 961. doi:[10.1051/0004-6361:20053600](https://doi.org/10.1051/0004-6361:20053600).
- Aulanier, G., Török, T., Démoulin, P., DeLuca, E.E.: 2010, *Astrophys. J.* **708**, 314. doi:[10.1088/0004-637X/708/1/314](https://doi.org/10.1088/0004-637X/708/1/314).
- Barnes, C.W., Sturrock, P.A.: 1972, *Astrophys. J.* **174**, 659. doi:[10.1086/151527](https://doi.org/10.1086/151527).
- Bateman, G.: 1978, *MHD Instabilities*, MIT Press, Cambridge.
- Baum, P.J., Bratenahl, A.: 1980, *Solar Phys.* **67**, 245. doi:[10.1007/BF00149805](https://doi.org/10.1007/BF00149805).
- Bi, Y., Jiang, Y.C., Yang, L.H., Zheng, R.S.: 2011, *New Astron.* **16**, 276. doi:[10.1016/j.newast.2010.11.009](https://doi.org/10.1016/j.newast.2010.11.009).
- Brown, D.S., Nightingale, R.W., Alexander, D., Schrijver, C.J., Metcalf, T.R., Shine, R.A., Title, A.M., Wolfson, C.J.: 2003, *Solar Phys.* **216**, 79. doi:[10.1023/A:1026138413791](https://doi.org/10.1023/A:1026138413791).
- Canou, A., Amari, T.: 2010, *Astrophys. J.* **715**, 1566. doi:[10.1088/0004-637X/715/2/1566](https://doi.org/10.1088/0004-637X/715/2/1566).
- Chen, J.: 1989, *Astrophys. J.* **338**, 453. doi:[10.1086/167211](https://doi.org/10.1086/167211).
- Chifor, C., Tripathi, D., Mason, H.E., Dennis, B.R.: 2007, *Astron. Astrophys.* **472**, 967. doi:[10.1051/0004-6361:20077771](https://doi.org/10.1051/0004-6361:20077771).
- Démoulin, P., Aulanier, G.: 2010, *Astrophys. J.* **718**, 1388. doi:[10.1088/0004-637X/718/2/1388](https://doi.org/10.1088/0004-637X/718/2/1388).
- Démoulin, P., Henoux, J.C., Priest, E.R., Mandrini, C.H.: 1996, *Astron. Astrophys.* **308**, 643.
- Evershed, J.: 1910, *Mon. Not. Roy. Astron. Soc.* **70**, 217.
- Fan, Y.: 2009, *Astrophys. J.* **697**, 1529. doi:[10.1088/0004-637X/697/2/1529](https://doi.org/10.1088/0004-637X/697/2/1529).
- Fan, Y., Gibson, S.E.: 2003, *Astrophys. J. Lett.* **589**, L105. doi:[10.1086/375834](https://doi.org/10.1086/375834).
- Fan, Y., Gibson, S.E.: 2007, *Astrophys. J.* **668**, 1232. doi:[10.1086/521335](https://doi.org/10.1086/521335).

- Forbes, T.: 2010, In: Schrijver, C.J., Siscoe, G.L. (eds.) *Heliophysics: Space Storms and Radiation: Causes and Effects*, Cambridge University Press, Cambridge, 159.
- Forbes, T.G.: 2000, *J. Geophys. Res.* **105**, 23153. doi:[10.1029/2000JA000005](https://doi.org/10.1029/2000JA000005).
- Galsgaard, K., Nordlund, Å.: 1997, *J. Geophys. Res.* **102**, 219. doi:[10.1029/96JA01462](https://doi.org/10.1029/96JA01462).
- Gerrard, C.L., Arber, T.D., Hood, A.W.: 2002, *Astron. Astrophys.* **387**, 687. doi:[10.1051/0004-6361:20020491](https://doi.org/10.1051/0004-6361:20020491).
- Gerrard, C.L., Hood, A.W., Brown, D.S.: 2004, *Solar Phys.* **222**, 79. doi:[10.1023/B:SOLA.0000036877.20077.42](https://doi.org/10.1023/B:SOLA.0000036877.20077.42).
- Gerrard, C.L., Brown, D.S., Mellor, C., Arber, T.D., Hood, A.W.: 2003, *Solar Phys.* **213**, 39. doi:[10.1023/A:1023281624037](https://doi.org/10.1023/A:1023281624037).
- Gibson, S.E., Fan, Y., Mandrini, C., Fisher, G., Demoulin, P.: 2004, *Astrophys. J.* **617**, 600. doi:[10.1086/425294](https://doi.org/10.1086/425294).
- Gombosi, T.I., Powell, K.G., de Zeeuw, D.L.: 1994, *J. Geophys. Res.* **99**, 21525.
- Gopalswamy, N., Yashiro, S., Kaiser, M.L., Howard, R.A., Bougeret, J.-L.: 2001, *Astrophys. J. Lett.* **548**, L91. doi:[10.1086/318939](https://doi.org/10.1086/318939).
- Green, L.M., Démoulin, P., Mandrini, C.H., Van Driel-Gesztelyi, L.: 2003, *Solar Phys.* **215**, 307. doi:[10.1023/A:1025678917086](https://doi.org/10.1023/A:1025678917086).
- Green, L.M., Kliem, B., Török, T., van Driel-Gesztelyi, L., Attrill, G.D.R.: 2007, *Solar Phys.* **246**, 365. doi:[10.1007/s11207-007-9061-z](https://doi.org/10.1007/s11207-007-9061-z).
- Guo, J., Liu, Y., Zhang, H., Deng, Y., Lin, J., Su, J.: 2010a, *Astrophys. J.* **711**, 1057. doi:[10.1088/0004-637X/711/2/1057](https://doi.org/10.1088/0004-637X/711/2/1057).
- Guo, Y., Schmieder, B., Démoulin, P., Wiegmann, T., Aulanier, G., Török, T., Bommier, V.: 2010b, *Astrophys. J.* **714**, 343. doi:[10.1088/0004-637X/714/1/343](https://doi.org/10.1088/0004-637X/714/1/343).
- Handy, B.N., Acton, L.W., Kankelborg, C.C., Wolfson, C.J., Akin, D.J., Bruner, M.E., Carvalho, R., Catura, R.C., Chevalier, R., Duncan, D.W., Edwards, C.G., Feinstein, C.N., Freeland, S.L., Friedlaender, F.M., Hoffmann, C.H., Hurlburt, N.E., Jurevich, B.K., Katz, N.L., Kelly, G.A., Lemen, J.R., Levay, M., Lindgren, R.W., Mathur, D.P., Meyer, S.B., Morrison, S.J., Morrison, M.D., Nightingale, R.W., Pope, T.P., Rehse, R.A., Schrijver, C.J., Shine, R.A., Shing, L., Strong, K.T., Tarbell, T.D., Title, A.M., Torgerson, D.D., Golub, L., Bookbinder, J.A., Caldwell, D., Cheimets, P.N., Davis, W.N., Deluca, E.E., McMullen, R.A., Warren, H.P., Amato, D., Fisher, R., Maldonado, H., Parkinson, C.: 1999, *Solar Phys.* **187**, 229. doi:[10.1023/A:1005166902804](https://doi.org/10.1023/A:1005166902804).
- Hiremath, K.M., Suryanarayana, G.S.: 2003, *Astron. Astrophys.* **411**, L497. doi:[10.1051/0004-6361:20031618](https://doi.org/10.1051/0004-6361:20031618).
- Hiremath, K.M., Lovely, M.R., Kariyappa, R.: 2006, *J. Astrophys. Astron.* **27**, 333. doi:[10.1007/BF02702538](https://doi.org/10.1007/BF02702538).
- Isenberg, P.A., Forbes, T.G.: 2007, *Astrophys. J.* **670**, 1453. doi:[10.1086/522025](https://doi.org/10.1086/522025).
- Jiang, Y., Yang, L., Li, K., Ren, D.: 2007, *Astrophys. J. Lett.* **662**, L131. doi:[10.1086/519490](https://doi.org/10.1086/519490).
- Kahler, S.W., Akiyama, S., Gopalswamy, N.: 2012, *Astrophys. J.* **754**, 100. doi:[10.1088/0004-637X/754/2/100](https://doi.org/10.1088/0004-637X/754/2/100).
- Kahler, S.W., Moore, R.L., Kane, S.R., Zirin, H.: 1988, *Astrophys. J.* **328**, 824. doi:[10.1086/166340](https://doi.org/10.1086/166340).
- Kazachenko, M.D., Canfield, R.C., Longcope, D.W., Qiu, J., Des Jardins, A., Nightingale, R.W.: 2009, *Astrophys. J.* **704**, 1146. doi:[10.1088/0004-637X/704/2/1146](https://doi.org/10.1088/0004-637X/704/2/1146).
- Keppens, R., Nool, M., Tóth, G., Goedbloed, J.P.: 2003, *Comput. Phys. Commun.* **153**, 317. doi:[10.1016/S0010-4655\(03\)00139-5](https://doi.org/10.1016/S0010-4655(03)00139-5).
- Kliem, B., Török, T.: 2006, *Phys. Rev. Lett.* **96**(25), 255002. doi:[10.1103/PhysRevLett.96.255002](https://doi.org/10.1103/PhysRevLett.96.255002).
- Kliem, B., Titov, V.S., Török, T.: 2004, *Astron. Astrophys.* **413**, L23. doi:[10.1051/0004-6361:20031690](https://doi.org/10.1051/0004-6361:20031690).
- Klimchuk, J.A., Antiochos, S.K., Norton, D.: 2000, *Astrophys. J.* **542**, 504. doi:[10.1086/309527](https://doi.org/10.1086/309527).
- Lau, Y.-T., Finn, J.M.: 1990, *Astrophys. J.* **350**, 672. doi:[10.1086/168419](https://doi.org/10.1086/168419).
- Li, L., Zhang, J.: 2009, *Astrophys. J. Lett.* **706**, L17. doi:[10.1088/0004-637X/706/1/L17](https://doi.org/10.1088/0004-637X/706/1/L17).
- Lionello, R., Mikić, Z., Linker, J.A., Amari, T.: 2002, *Astrophys. J.* **581**, 718. doi:[10.1086/344222](https://doi.org/10.1086/344222).
- Liu, R., Kliem, B., Török, T., Liu, C., Titov, V.S., Lionello, R., Linker, J.A., Wang, H.: 2012, *Astrophys. J.* **756**, 59. doi:[10.1088/0004-637X/756/1/59](https://doi.org/10.1088/0004-637X/756/1/59).
- Longcope, D.W., Welsch, B.T.: 2000, *Astrophys. J.* **545**, 1089. doi:[10.1086/317846](https://doi.org/10.1086/317846).
- Lugaz, N., Manchester, W.B. IV, Gombosi, T.I.: 2005, *Astrophys. J.* **634**, 651. doi:[10.1086/491782](https://doi.org/10.1086/491782).
- Maričić, D., Vršnak, B., Roša, D.: 2009, *Solar Phys.* **260**, 177. doi:[10.1007/s11207-009-9421-y](https://doi.org/10.1007/s11207-009-9421-y).
- Maričić, D., Vršnak, B., Stanger, A.L., Veronig, A.: 2004, *Solar Phys.* **225**, 337. doi:[10.1007/s11207-004-3748-1](https://doi.org/10.1007/s11207-004-3748-1).
- Maričić, D., Vršnak, B., Stanger, A.L., Veronig, A.M., Temmer, M., Roša, D.: 2007, *Solar Phys.* **241**, 99. doi:[10.1007/s11207-007-0291-x](https://doi.org/10.1007/s11207-007-0291-x).
- Masson, S., Pariat, E., Aulanier, G., Schrijver, C.J.: 2009, *Astrophys. J.* **700**, 559. doi:[10.1088/0004-637X/700/1/559](https://doi.org/10.1088/0004-637X/700/1/559).

- McIntosh, S.W., Leamon, R.J., Davey, A.R., Wills-Davey, M.J.: 2007, *Astrophys. J.* **660**, 1653. doi:[10.1086/512665](https://doi.org/10.1086/512665).
- Mikic, Z., Schnack, D.D., van Hoven, G.: 1990, *Astrophys. J.* **361**, 690. doi:[10.1086/169232](https://doi.org/10.1086/169232).
- Miklenic, C.H., Veronig, A.M., Vršnak, B.: 2009, *Astron. Astrophys.* **499**, 893. doi:[10.1051/0004-6361/200810947](https://doi.org/10.1051/0004-6361/200810947).
- Min, S., Chae, J.: 2009, *Solar Phys.* **258**, 203. doi:[10.1007/s11207-009-9425-7](https://doi.org/10.1007/s11207-009-9425-7).
- Moore, R.L., Sterling, A.C., Hudson, H.S., Lemen, J.R.: 2001, *Astrophys. J.* **552**, 833. doi:[10.1086/320559](https://doi.org/10.1086/320559).
- Nindos, A., Andrews, M.D.: 2004, *Astrophys. J. Lett.* **616**, L175. doi:[10.1086/426861](https://doi.org/10.1086/426861).
- Panasenco, O., Martin, S., Joshi, A.D., Srivastava, N.: 2011, *J. Atmos. Solar-Terr. Phys.* **73**, 1129. doi:[10.1016/j.jastp.2010.09.010](https://doi.org/10.1016/j.jastp.2010.09.010).
- Pariat, E., Antiochos, S.K., DeVore, C.R.: 2009, *Astrophys. J.* **691**, 61. doi:[10.1088/0004-637X/691/1/61](https://doi.org/10.1088/0004-637X/691/1/61).
- Priest, E.R., Forbes, T.G.: 1992, *J. Geophys. Res.* **97**, 1521. doi:[10.1029/91JA02435](https://doi.org/10.1029/91JA02435).
- Régnier, S., Canfield, R.C.: 2006, *Astron. Astrophys.* **451**, 319. doi:[10.1051/0004-6361:20054171](https://doi.org/10.1051/0004-6361:20054171).
- Robbrecht, E., Patsourakos, S., Vourlidias, A.: 2009, *Astrophys. J.* **701**, 283. doi:[10.1088/0004-637X/701/1/283](https://doi.org/10.1088/0004-637X/701/1/283).
- Romano, P., Contarino, L., Zuccarello, F.: 2005, *Astron. Astrophys.* **433**, 683. doi:[10.1051/0004-6361:20041807](https://doi.org/10.1051/0004-6361:20041807).
- Roussev, I.I., Forbes, T.G., Gombosi, T.I., Sokolov, I.V., DeZeeuw, D.L., Birn, J.: 2003, *Astrophys. J. Lett.* **588**, L45. doi:[10.1086/375442](https://doi.org/10.1086/375442).
- Santos, J.C., Büchner, J., Otto, A.: 2011, *Astron. Astrophys.* **535**, A111. doi:[10.1051/0004-6361/201116792](https://doi.org/10.1051/0004-6361/201116792).
- Sato, T., Hayashi, T.: 1979, *Phys. Fluids* **22**, 1189. doi:[10.1063/1.862721](https://doi.org/10.1063/1.862721).
- Schatten, K.H., Wilcox, J.M., Ness, N.F.: 1969, *Solar Phys.* **6**, 442. doi:[10.1007/BF00146478](https://doi.org/10.1007/BF00146478).
- Scherrer, P.H., Bogart, R.S., Bush, R.I., Hoeksema, J.T., Kosovichev, A.G., Schou, J., Rosenberg, W., Springer, L., Tarbell, T.D., Title, A., Wolfson, C.J., Zayer, I., MDI Engineering Team: 1995, *Solar Phys.* **162**, 129. doi:[10.1007/BF00733429](https://doi.org/10.1007/BF00733429).
- Schrijver, C.J., Elmore, C., Kliem, B., Török, T., Title, A.M.: 2008, *Astrophys. J.* **674**, 586. doi:[10.1086/524294](https://doi.org/10.1086/524294).
- Stenflo, J.O.: 1969, *Solar Phys.* **8**, 115. doi:[10.1007/BF00150662](https://doi.org/10.1007/BF00150662).
- Suryanarayana, G.S.: 2010, *New Astron.* **15**, 313. doi:[10.1016/j.newast.2009.09.004](https://doi.org/10.1016/j.newast.2009.09.004).
- Temmer, M., Veronig, A.M., Vršnak, B., Rybák, J., Gömöry, P., Stoiser, S., Maričić, D.: 2008, *Astrophys. J. Lett.* **673**, L95. doi:[10.1086/527414](https://doi.org/10.1086/527414).
- Tian, L., Alexander, D.: 2006, *Solar Phys.* **233**, 29. doi:[10.1007/s11207-006-2505-z](https://doi.org/10.1007/s11207-006-2505-z).
- Tian, L., Alexander, D., Nightingale, R.: 2008, *Astrophys. J.* **684**, 747. doi:[10.1086/589492](https://doi.org/10.1086/589492).
- Titov, V.S., Démoulin, P.: 1999, *Astron. Astrophys.* **351**, 707.
- Török, T., Kliem, B.: 2003, *Astron. Astrophys.* **406**, 1043. doi:[10.1051/0004-6361:20030692](https://doi.org/10.1051/0004-6361:20030692).
- Török, T., Kliem, B.: 2005, *Astrophys. J. Lett.* **630**, L97. doi:[10.1086/462412](https://doi.org/10.1086/462412).
- Török, T., Kliem, B.: 2007, *Astron. Nachr.* **328**, 743. doi:[10.1002/asna.200710795](https://doi.org/10.1002/asna.200710795).
- Török, T., Kliem, B., Titov, V.S.: 2004, *Astron. Astrophys.* **413**, L27. doi:[10.1051/0004-6361:20031691](https://doi.org/10.1051/0004-6361:20031691).
- Török, T., Aulanier, G., Schmieder, B., Reeves, K.K., Golub, L.: 2009, *Astrophys. J.* **704**, 485. doi:[10.1088/0004-637X/704/1/485](https://doi.org/10.1088/0004-637X/704/1/485).
- Török, T., Panasenco, O., Titov, V.S., Mikić, Z., Reeves, K.K., Velli, M., Linker, J.A., De Toma, G.: 2011, *Astrophys. J. Lett.* **739**, L63. doi:[10.1088/2041-8205/739/2/L63](https://doi.org/10.1088/2041-8205/739/2/L63).
- Valori, G., Kliem, B., Török, T., Titov, V.S.: 2010, *Astron. Astrophys.* **519**, A44. doi:[10.1051/0004-6361/201014416](https://doi.org/10.1051/0004-6361/201014416).
- van Ballegoijen, A.A.: 2004, *Astrophys. J.* **612**, 519. doi:[10.1086/422512](https://doi.org/10.1086/422512).
- Veronig, A.M., Rybak, J., Gömöry, P., Berkebile-Stoiser, S., Temmer, M., Otruba, W., Vrsnak, B., Pötzi, W., Baumgartner, D.: 2010, *Astrophys. J.* **719**, 655. doi:[10.1088/0004-637X/719/1/655](https://doi.org/10.1088/0004-637X/719/1/655).
- Vršnak, B.: 1990, *Solar Phys.* **129**, 295. doi:[10.1007/BF00159042](https://doi.org/10.1007/BF00159042).
- Vršnak, B., Sudar, D., Ruždjak, D., Žic, T.: 2007, *Astron. Astrophys.* **469**, 339. doi:[10.1051/0004-6361:20077175](https://doi.org/10.1051/0004-6361:20077175).
- Williams, D.R., Török, T., Démoulin, P., van Driel-Gesztelyi, L., Kliem, B.: 2005, *Astrophys. J. Lett.* **628**, L163. doi:[10.1086/432910](https://doi.org/10.1086/432910).
- Yan, X.L., Qu, Z.Q.: 2007, *Astron. Astrophys.* **468**, 1083. doi:[10.1051/0004-6361:20077064](https://doi.org/10.1051/0004-6361:20077064).
- Yan, X.L., Qu, Z.Q., Kong, D.F.: 2008, *Mon. Not. Roy. Astron. Soc.* **391**, 1887. doi:[10.1111/j.1365-2966.2008.14002.x](https://doi.org/10.1111/j.1365-2966.2008.14002.x).
- Yan, X.L., Qu, Z.Q., Xu, C.L., Xue, Z.K., Kong, D.F.: 2009, *Res. Astron. Astrophys.* **9**, 596. doi:[10.1088/1674-4527/9/5/010](https://doi.org/10.1088/1674-4527/9/5/010).
- Yan, X.L., Qu, Z.Q., Kong, D.-F., Xu, C.L.: 2012, *Astrophys. J.* **754**, 16. doi:[10.1088/0004-637X/754/1/16](https://doi.org/10.1088/0004-637X/754/1/16).
- Yang, J., Jiang, Y., Yang, B., Zheng, R., Yang, D., Hong, J., Li, H., Bi, Y.: 2012, *Solar Phys.* **279**, 115. doi:[10.1007/s11207-012-0002-0](https://doi.org/10.1007/s11207-012-0002-0).
- Zhang, J., Li, L., Song, Q.: 2007, *Astrophys. J. Lett.* **662**, L35. doi:[10.1086/519280](https://doi.org/10.1086/519280).

- Zhang, J., Dere, K.P., Howard, R.A., Kundu, M.R., White, S.M.: 2001, *Astrophys. J.* **559**, 452. doi:[10.1086/322405](https://doi.org/10.1086/322405).
- Zhang, Y., Liu, J., Zhang, H.: 2008, *Solar Phys.* **247**, 39. doi:[10.1007/s11207-007-9089-0](https://doi.org/10.1007/s11207-007-9089-0).
- Zhu, C., Alexander, D., Tian, L.: 2012, *Solar Phys.* **278**, 121. doi:[10.1007/s11207-011-9923-2](https://doi.org/10.1007/s11207-011-9923-2).
- Zirin, H.: 1998, *The Astrophysics of the Sun*, Cambridge University Press, Cambridge.
- Zuccarello, F.P., Bemporad, A., Jacobs, C., Mierla, M., Poedts, S., Zuccarello, F.: 2012, *Astrophys. J.* **744**, 66. doi:[10.1088/0004-637X/744/1/66](https://doi.org/10.1088/0004-637X/744/1/66).

2010 AUGUST 1–2 SYMPATHETIC ERUPTIONS. I. MAGNETIC TOPOLOGY OF THE SOURCE-SURFACE BACKGROUND FIELD

V. S. TITOV¹, Z. MIKIC¹, T. TÖRÖK¹, J. A. LINKER¹, AND O. PANASENCO²

¹ Predictive Science Inc., 9990 Mesa Rim Road, Suite 170, San Diego, CA 92121, USA; titovv@predsci.com

² Helio Research, 5212 Maryland Avenue, La Crescenta, CA 91214, USA

Received 2012 June 18; accepted 2012 September 14; published 2012 October 17

ABSTRACT

A sequence of apparently coupled eruptions was observed on 2010 August 1–2 by *Solar Dynamics Observatory* and *STEREO*. The eruptions were closely synchronized with one another, even though some of them occurred at widely separated locations. In an attempt to identify a plausible reason for such synchronization, we study the large-scale structure of the background magnetic configuration. The coronal field was computed from the photospheric magnetic field observed at the appropriate time period by using the potential field source-surface model. We investigate the resulting field structure by analyzing the so-called squashing factor calculated at the photospheric and source-surface boundaries, as well as at different coronal cross-sections. Using this information as a guide, we determine the underlying structural skeleton of the configuration, including separatrix and quasi-separatrix surfaces. Our analysis reveals, in particular, several pseudo-streamers in the regions where the eruptions occurred. Of special interest to us are the magnetic null points and separators associated with the pseudo-streamers. We propose that magnetic reconnection triggered along these separators by the first eruption likely played a key role in establishing the assumed link between the sequential eruptions. The present work substantiates our recent simplified magnetohydrodynamic model of sympathetic eruptions and provides a guide for further deeper study of these phenomena. Several important implications of our results for the S-web model of the slow solar wind are also addressed.

Key words: magnetic reconnection – solar wind – Sun: coronal mass ejections (CMEs) – Sun: flares – Sun: magnetic topology

Online-only material: color figures

1. INTRODUCTION

Coronal mass ejections (CMEs) are spectacular solar phenomena that have been intensely studied over more than 40 years. Being the main driver of space weather disturbances near the Earth, they are part of a more general eruption process, often including filament eruptions and flares. Although it is now understood that these phenomena are due to a local destabilization of the coronal magnetic field, many basic questions on the physics of CMEs are still under study (e.g., Forbes 2000, 2010). Accordingly, theoretical and numerical investigations of CME initiation and evolution have so far focused mainly on *single* eruptions.

However, there also exist *multiple* eruptions occurring within a relatively short period of time and at different, often widely separated, locations. In the largest events, the respective source regions can cover a full hemisphere (so-called global CMEs; e.g., Zhukov & Veselovsky 2007), so that such events naturally produce large heliospheric disturbances. While it has been argued whether or not the temporal correlation of multiple eruptions is coincidental (e.g., Biesecker & Thompson 2000), both statistical investigations (e.g., Moon et al. 2002; Wheatland & Craig 2006) and detailed case studies (e.g., Wang et al. 2001; Jiang et al. 2011; Yang et al. 2012; Shen et al. 2012) indicate that there are *causal connections* between them.³ We accept this fact as a starting point of our study and will henceforth call such eruptions *sympathetic* or *linked*.

The physical mechanisms of these connections, however, have yet to be unveiled. In earlier works they have been related,

for instance, to destabilization by chromospheric large-scale waves (Ramsey & Smith 1966) or large-scale properties of convective flows (Bumba & Klvana 1993). More recent research suggests that the mechanisms linking sympathetic eruptions act in the corona and involve its magnetic field structure. For example, one proposed mechanism relies on perturbations propagating along field lines between the source regions of eruptions (e.g., Jiang et al. 2008), while another appeals to changes in the background field due to reconnection (Liu et al. 2009; Zuccarello et al. 2009; Jiang et al. 2011; Shen et al. 2012). Yet such explanations were often based on qualitative and sometimes rather speculative considerations.

The high-cadence, full-disk observations by *Solar Dynamics Observatory* (*SDO*), along with studies of the large-scale coronal magnetic field, now provide us the opportunity to substantially increase our understanding of such eruptions. The event under study attracted considerable attention in the solar community and beyond. It involved an entire hemisphere of the Sun, consisted of several flares and six filament eruptions and CMEs, and triggered a geomagnetic storm on August 3 (Harrison et al. 2012). A detailed account of all eruptions and their precursors can be found in Schrijver & Title (2011). Here, we restrict ourselves to the main five eruptions, whose connections we aim to explain in the present study. Using a combination of *SDO* data and analysis of field line connectivity for the 2010 August 1–2 eruptions, Schrijver & Title (2011) found evidence that *all* involved source regions were connected by structural features such as separatrix surfaces, separators, and quasi-separatrix layers (QSLs; Priest & Démoulin 1995; Démoulin et al. 1996; Titov et al. 2002). We have recently performed a simplified magnetohydrodynamic (MHD) simulation of a subset of these eruptions (Török et al. 2011), in which two successive

³ We do not distinguish here between sympathetic flares and sympathetic CMEs, since typically both are part of the same eruption process.

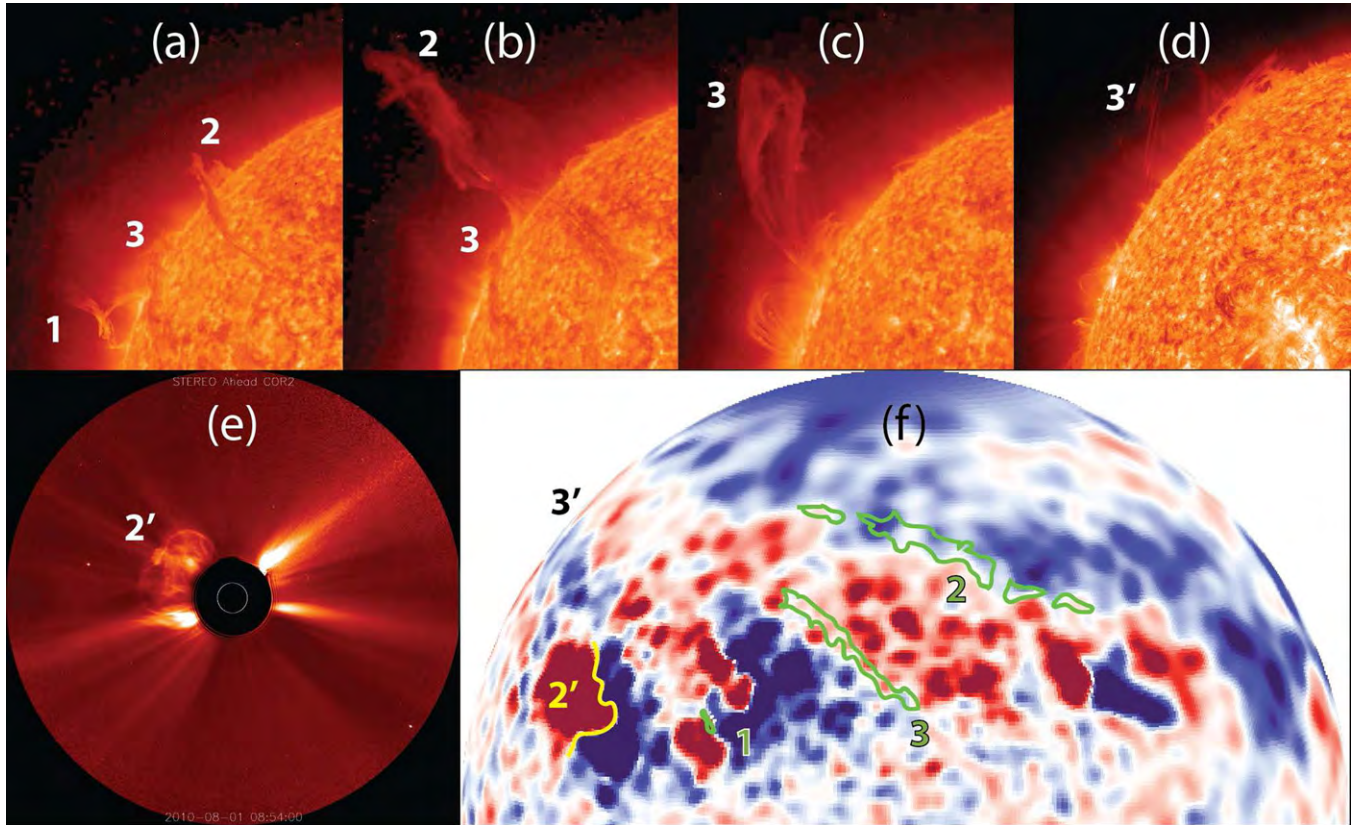


Figure 1. Sympathetic CMEs on 2010 August 1 with the main eruptions numbered in the order of their occurrence, primed numbers indicate near-simultaneous events; (a)–(c) eruptions 1, 2, and 3 as seen by *STEREO-A* 304 Å at 02:56, 09:16, and 22:06 UT (left to right); (d) eruption 3' observed by *SDO/AIA* 304 Å at 21:30 UT; (e) eruption 2' captured by the COR2 coronagraph on board *STEREO-A* at 08:54 UT; (f) synoptic MDI magnetogram and contours (green) of the pre-eruption filaments that were visible in H α , the yellow line indicates the location of the active-region filament 2' prior eruption.

(A color version of this figure is available in the online journal.)

eruptions were initiated by reconnection at a separator high in the corona. Thus, this work strongly supports the idea that the structural features can indeed play a key role in generating linked eruptions.

While these new results are very encouraging, further research is needed. First, our simulation used only a simplified magnetic configuration and addressed just a subset of the complex sequence of CMEs on 2010 August 1–2. Second, the findings by Schrijver & Title (2011), being of a general nature, did not explain the exact role of structural features in connecting individual eruptions. We show here that a comprehensive structural analysis of the magnetic environment in which such eruptions occur allows one to get deeper insights into the relationship between linked eruptions.

Figure 1 shows that the sequence of eruptions started with a CME following the eruption of the small filament 1. About 6 hr later, the large quiescent filament 2 erupted, almost simultaneously with a C-class flare and fast CME originating in active-region NOAA 11092 (whose polarity inversion line is denoted by 2') to the east of filament 1. After another 12 hr, the large quiescent filament 3 erupted, again almost simultaneously with a large filament eruption (denoted by 3') that was observed above the eastern limb. All of the large filament eruptions evolved into separate CMEs. Interestingly, while a filament was present along 2', it did not erupt as part of the CME (Liu et al. 2010).

Our topological analysis of the large-scale background coronal field, which we describe in detail in Section 3, reveals that, first, all of the erupting filaments were located prior to their

eruption below so-called pseudo-streamers (e.g., Hundhausen 1972; Wang et al. 2007). A pseudo-streamer is morphologically similar to a helmet streamer but, in contrast to it, divides coronal holes of the same rather than opposite polarity and contains two lobes of closed magnetic flux below its cusp to produce a ρ -type structure. These structures are quite common in the corona (e.g., Eselevich et al. 1999) and are often observed to harbor filaments in their lobes (Panasenco & Velli 2010). As the latter authors pointed out, an eruption in one lobe of a pseudo-streamer is often followed by an eruption in the other lobe shortly thereafter, indicating that these structures are prone to producing linked eruptions.

Second, as suggested by Török et al. (2011), the eruptions 2 and 3, which originated below one pseudo-streamer, were apparently triggered by eruption 1 that occurred outside the pseudo-streamer. Third, as also suggested in that study, the fact that filament 2 erupted before filament 3, although it was located further from eruption 1 than filament 3, can be explained by the topological properties of the pseudo-streamer.

These three conclusions are strongly supported by our analysis in Sections 3 and 4 and indicate the central role that pseudo-streamers may play in many linked eruptions. We further develop this concept and generalize it in Section 4, arguing that the order of *all* our eruptions, including those of filaments 2' and 3', is not coincidental but causal. It is essentially predetermined by the overall magnetic topology of the ensemble of pseudo-streamers that were involved into the eruptions. We comprehensively investigate this topology in the framework of the potential field source-surface (PFSS; Altschuler & Newkirk 1969;

Schatten et al. 1969) model (Section 2.1), using new techniques for the structural analysis of magnetic fields (Section 2.2).

Being of a general character, our findings on magnetic topology of pseudo-streamers have a broader impact than was initially anticipated for this study. In particular, they also provide important implications for the problem of the origin of the slow solar wind, which was recently addressed in the framework of the so-called S-web model (Antiochos et al. 2007; Antiochos et al. 2011; Linker et al. 2011) and whose aspects have already been discussed in a number of papers (Titov et al. 2011; Wang et al. 2012; Crooker et al. 2012). We address the implications of our new results for the S-web model in Section 5 and summarize our work in Section 6.

Although solar magnetic fields obtained from PFSS and MHD models often qualitatively match each other, at least if the latter are based only on line-of-sight magnetograms (Riley et al. 2006), it remains an open question whether the magnetic field topology, as understood in mathematical terms, is in both cases the same. Section 3.3 makes it clear that this question indeed requires a special study, which is already on the way and will be described in the part II of a series of papers. In that part, we will repeat our analysis of the magnetic structure for the global solar MHD model derived from the same magnetogram as used in the present PFSS model. We will also compare the results of our analysis for both these models and, additionally, extend the discussion of these results, which we start in Section 4, in relation to observations.

2. INVESTIGATION METHODS

2.1. PFSS Model

As a boundary condition for our PFSS model, we used the magnetic data that were derived from a *Solar and Heliospheric Observatory*/MDI synoptic map of the radial field B_r for Carrington rotation 2099 (2010 July 13–August 9) using the Level 1.8.2 calibration. We processed the synoptic map, first, by interpolating it to a uniform latitude–longitude mesh with a resolution of 0.5° . The polar magnetic field was fitted in the new map with a geometrical specification to reduce noise in the poorly observed polar regions. Second, we smoothed the resulting B_r by applying a diffusion operator such that its nonuniform diffusion coefficient was smaller in the active region and larger everywhere else. Finally, we interpolated the obtained B_r distribution from the uniform grid to a nonuniform one that has a higher and lesser resolution, respectively, inside and outside the eruptive region. This region is spread in longitude and latitude approximately from 45° to 180° and from -20° to 65° , respectively, with the resolution ranging from $0.37^\circ \times 0.37^\circ$ in this region to $2.6^\circ \times 1.8^\circ$ outside (see Figure 2(a)).

The spherical source surface, at which the scalar magnetic potential is set to be constant, is chosen at $r = 2.5 R_\odot$, where R_\odot is the solar radius. For such a PFSS model, we have computed the photospheric map of coronal holes on a uniform grid with an angular cell size of 0.125° , which is much smaller than the smallest grid cell for the computed field itself. The result is shown in Figure 2(b) together with the source-surface distribution of the squashing factor Q , which will be discussed below. The three coronal holes of negative polarity that are located in the eruptive region are distinctly disconnected from each other and from the negative northern polar coronal hole. As will become clear later, the presence of these coronal holes in the eruptive region is crucial for understanding both the

underlying magnetic topology and the plausible casual link that this topology sets up between the erupting filaments.

2.2. Techniques for Analyzing Magnetic Structure

Magnetic configurations can generally have both *separatrix surfaces* and *QSLs*. To comprehensively analyze the structure of our configuration, it is necessary to determine all such structural features, whose complete set we call the *structural skeleton* of the configuration. We fulfill this task in two steps: first, we identify the footprints of the corresponding (quasi-)separatrix surfaces at the photosphere and source surface by calculating the distributions of the *squashing factor* Q of elemental magnetic flux tubes (Titov et al. 2002; Titov 2007); these footprints are simply high- Q lines of the calculated distributions. Second, using the found footprints as a guide, we trace a number of field lines that best represent these surfaces.

For the calculation of Q we use its definition in spherical coordinates (Titov 2007; Titov et al. 2008). By construction, the Q factor has the *same* value at the conjugate footprints, so it can be used as a marker for field lines. In other words, despite being originally defined at the boundary surfaces only, the Q factor can be extended into the volume by simply transporting its defined values along the field lines according to the equation

$$\mathbf{B} \cdot \nabla Q = 0,$$

where \mathbf{B} is a given coronal magnetic field and Q is an unknown function of space coordinates. This equation can be solved in many different ways depending on the desirable accuracy and efficiency of the computation. We will describe our methods for extending Q in the volume in a future article together with other techniques for investigating (quasi-)separatrix surfaces, while here we would like to outline a few relevant considerations.

The extension of Q in the volume makes it possible to determine the structural skeleton as a set of high- Q layers. They can intersect each other in a rather complicated way, especially low in the corona. With increasing height, however, the intersections become simpler, which particularly helps our goal of studying the large-scale structure. Determining the Q distribution at a given cut plane, similar as done before in other works (Aulanier et al. 2005; Titov et al. 2008; Pariat & Démoulin 2012; Savcheva et al. 2012a, 2012b), is also helpful for analyzing complex structures. We calculate Q distributions at cut planes, extending the method that Pariat & Démoulin (2012) described for configurations with plane boundaries to the case of spherical boundaries. The high- Q lines in such distributions visualize the cuts of the structural skeleton by those planes. As will be shown below (Figure 9), this kind of visualization becomes particularly useful if the colors corresponding to low values of Q ($\lesssim 10^2$) are chosen to be transparent.

We also find it useful to apply this transparency technique to the photospheric and source-surface Q distributions, particularly if one uses in addition a special color coding that takes into account the local sign of the normal field B_r at the boundary. The function that facilitates this color coding is called *signed log Q* or simply *slog Q* and defined as (Titov et al. 2011)

$$\text{slog } Q \equiv \text{sign}(B_r) \log[Q/2 + (Q^2/4 - 1)^{1/2}]. \quad (1)$$

Using a symmetric blue–white–red palette in combination with the above transparency mask, we make visible in *slog Q* distributions only high- Q lines, colored either in blue or red in negative or positive polarities, respectively. The resulting maps

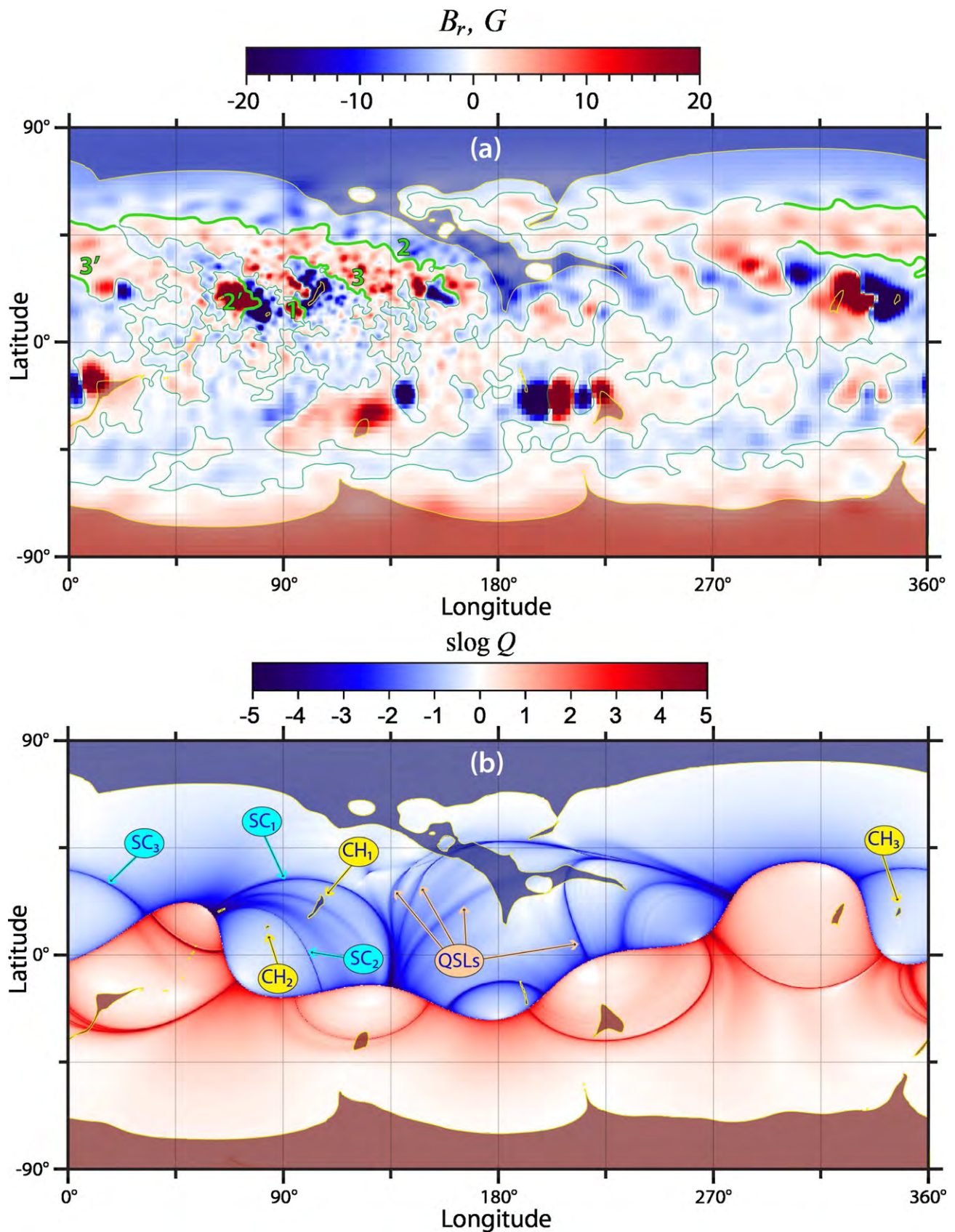


Figure 2. Map of B_r (a) used as a photospheric boundary condition for our PFSS model of the 2010 August 1–2 magnetic field and map of $\text{slog } Q$ for this model at the source surface (b) with superimposed (semi-transparent) photospheric map of coronal holes (shaded either in dark red ($B_r > 0$) or dark blue ($B_r < 0$) and outlined in yellow). Thin (green) lines represent the photospheric polarity inversion line, whose thick segments designate the location of the filaments, part of which are numbered in the order they erupted. Yellow balloons indicate the coronal holes involved in the eruptions; cyan balloons indicate source-surface footprints of the separatrix curtains of these pseudo-streamers.

(A color version of this figure is available in the online journal.)

provide a compact and powerful representation of the structural skeleton at the boundaries, as evident from our illustrations below.

Since our magnetic field is potential, Q acquires high values only in three cases: either the corresponding field lines scatter from localized inhomogeneities of the field nearby its null points or minimum points (Titov et al. 2009) or touch the so-called bald patches (BPs), which are certain segments of the photospheric polarity inversion line (Seehafer 1986; Titov et al. 1993). To make the whole analysis comprehensive, we separately determine the location of all such relevant features and then relate them to the high- Q lines at the boundaries by tracing a number of field lines that pass through these features. The pattern of high- Q lines determined at spherical surfaces of different radii provides us with estimates of the regions in which the magnetic nulls and minima can be present. Using then standard numeric algorithms (see, e.g., Press et al. 2007), both these features are found as local minima of B^2 that is defined between the grid points in these regions by cubic spline interpolation. Calculation of the matrix of magnetic field gradients $[\nabla\mathbf{B}]$ and its eigenvectors at the found nulls and minima allows us to determine the local (quasi-)separatrix structure, which is further used to initialize tracing of the respective (quasi-)separatrix field lines. For tracing generalized (quasi-)separators (see Section 3), which connect a pair of any of the above three features (i.e., nulls, minima, or BP points), we use a technique that is based on similar principles as described earlier for classical null-null separators by Close et al. (2004) and Haynes & Parnell (2010).

3. ANALYSIS OF THE MAGNETIC STRUCTURE

3.1. Coronal Holes versus High- Q Lines at the Boundaries

As mentioned in Section 2.1, the eruptive region contains three coronal holes of negative polarity that are distinctly disconnected at the photospheric level by positive parasitic polarities. With increasing height, however, these coronal holes start to expand and subsequently merge with each other and with the main body of the northern polar coronal hole. Being fully open at the source surface, the magnetic fluxes of these coronal holes still remain separated by the so-called *separatrix curtains* (SCs; Titov et al. 2011). As will become clear below, the SCs are simply vertical separatrix surfaces that originate at null points of the magnetic field low in the corona. At the source surface, their footprints appear as arcs joined at both ends to the null line of the magnetic field, so that the corresponding junction points divide the null line into several segments. Taken in different combinations, such segments and footprints of SCs form several closed contours. The contours encompass the fluxes corresponding to the coronal holes that are disconnected at the photospheric level from each other and from the like-polarity coronal holes at the poles. This fact clearly manifests itself on our source-surface $\text{slog}Q$ map that is superimposed in Figure 2(b) on top of the photospheric coronal holes' map. The figure indicates, in particular, that the high- Q line of the footprint SC_2 (SC_3) and the null-line segment to which the footprint adjoins encompass the CH_2 (CH_3) flux. Similarly, the source-surface footprints SC_1 and SC_2 and two short null-line segments to which the footprints adjoin encompass the CH_1 flux.

It should be noted, however, that some of the source-surface high- Q lines do not represent the footprints of SCs, but rather the footprints of QSLs that stem at the photosphere from narrow open-field corridors connecting spaced parts of otherwise single

coronal holes. The high- Q lines of QSLs usually appear less sharp than those of SC footprints (see Figure 2(b)). The indicated QSL footprints can easily be related to certain open-field corridors in the northern polar coronal hole. If one traces down several field lines from the paths that go across these high- Q lines, the photospheric footprints of these field lines will sweep along the respective open-field corridors, as predicted earlier by Antiochos et al. (2007). However, a similar procedure in the case of the SCs would give a very different result, which becomes clear after analyzing the magnetic topology low in the corona near the indicated coronal holes.

As a first step in this analysis, let us consider the coronal-hole maps and $\text{slog}Q$ distribution, both defined at the photospheric level and superimposed onto each other as shown in Figure 3. The pattern of high- Q lines here is more complicated than at the source surface, as expected. Nevertheless, in the region of interest, it prominently reveals three high- Q lines (red), which are identified after inspection as photospheric footprints of the above-mentioned SCs. They traverse along parasitic polarities and separate the indicated coronal holes in a similar manner as their source-surface counterparts. Note also that these footprints and nearby filaments are locally co-aligned, and at least five of these filaments were eruptive.

Figure 4 shows the described distributions of $\text{slog}Q$ and B_r in three dimensions and a few field lines that produce loop-arcade structures above the filaments. The loops of arcades are rooted with one footpoint at the positive parasitic polarities that disconnect our three coronal holes either from each other (CH_1 from CH_2) or (CH_1 and CH_3) from the northern coronal hole. Thus, these arcades form in pairs the twin magnetic field lobes of the three pseudo-streamers embedded between the indicated coronal holes. We also see here that four of the five filaments (all the numbered ones, except for 2', in Figures 3 and 4) were initially located inside such lobes.

3.2. Separatrix Structure of Pseudo-streamers

Of particular interest to us is the question on how the pseudo-streamer lobes are bounded in our configuration by separatrix surfaces of the magnetic field. It turns out that these surfaces originate either at the null points or at the BPs, both mentioned already in Section 2.2 in connection with high- Q lines. Following Priest & Titov (1996), we will use the terms “fan surface” and “spine line” to designate, respectively, two-dimensional and one-dimensional separatrix structures that are related to a null point. They are defined through the eigenvectors of the matrix of magnetic field gradients at this point in the following way. The fan separatrix surface is woven from the field lines that start at the null point in the plane spanned on the eigenvectors, whose eigenvalues are of the same sign. The spine line is a separatrix field line that reaches the null point along the remaining third eigenvector. For a potential field, the spine line is always perpendicular to the fan surface.

In accordance with the recent analytical model of pseudo-streamers (Titov et al. 2011), the boundaries of our pseudo-streamers are composed of three types of separatrix surfaces, two of which are the fan surfaces of some coronal null points, while the third one is a BP separatrix surface. The fans of the first type have a curtain-like shape, whose field lines emanate from a null point, called henceforth basic one. We have already discussed these surfaces above as SCs in connection with boundary high- Q lines. They contain both closed and open field lines and extend from the photosphere to the source surface, as shown in Figures 5 and 6.

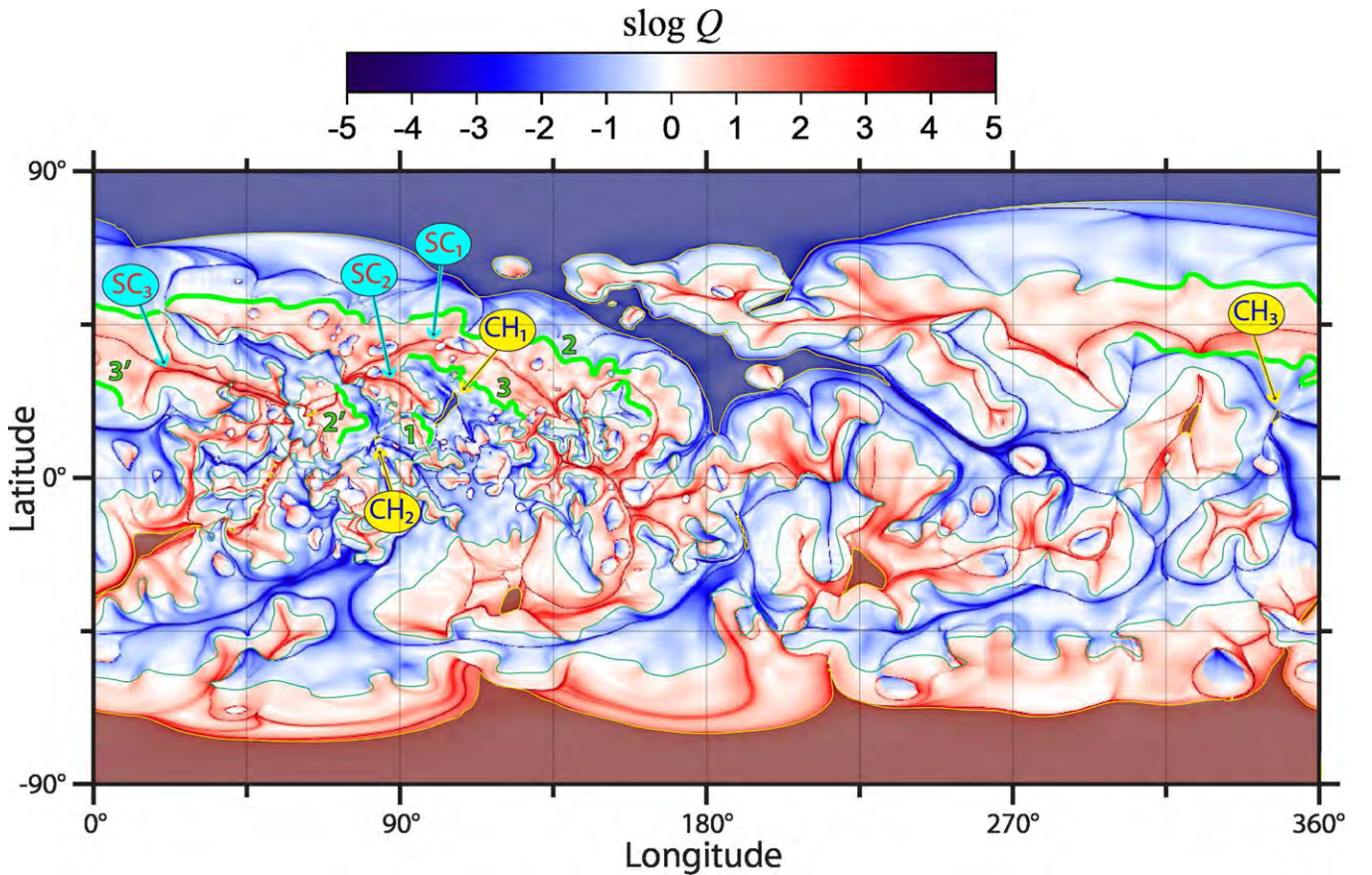


Figure 3. Map of $\text{slog } Q$ for our PFSS model at the photosphere with superimposed (semi-transparent) photospheric map of coronal holes and the photospheric polarity inversion line, both shown in the same way as in Figure 2. Yellow balloons indicate the coronal holes of the pseudo-streamers involved in the eruptions; cyan balloons indicate photospheric footprints of the separatrix curtains of these pseudo-streamers.

(A color version of this figure is available in the online journal.)

The fans of the second type are associated with other nulls and include only closed field lines. Each of these fans bounds the closed flux of the parasitic polarity in a given pseudo-streamer only at one flank and forms a half-dome-like surface, whose edge is located in the middle of the pseudo-streamer and coincides exactly with the spine line of the basic null point (see Figure 7). The second half-dome is formed in all our three pseudo-streamers by the third type of separatrix surfaces that originate in BPs at the opposite flanks of pseudo-streamers. In fact, in our third pseudo-streamer even both separatrix half-domes are due to the presence of BPs (Figure 8).

3.3. Field Line Topology of Separatrix Curtains

Consider now in more detail the field line topology in all our three pseudo-streamers, starting from the two neighboring separatrix curtains SC_1 and SC_2 (see Figures 5 and 6). The field lines in each of these curtains fan out from its own basic null point that is located between two adjacent coronal holes of like polarity and above the respective parasitic polarity. The footprints of SCs, which are discussed in Section 3.1, can be viewed then as photospheric or source-surface images of single null points N_1 and N_2 due to their mapping along closed or open, respectively, field lines.

Within a given SC, such a mapping is continuous everywhere except for few special field lines, called *separators*, where the mapping suffers a jump. This jump takes place whenever a mapping field line hits a null point (like N_{1-2} and N_{1-3} in

Figure 5, or a BP, like BP_1 in both Figures 5 and 6). To distinguish these separators from other field lines, we have plotted them thicker in these and further similar figures.

In addition to the mentioned closed separators, there are also two open ones for each of the curtains. These open separators connect the null N_1 (or N_2) to a pair of null points belonging to the source-surface null line. The latter is simply the helmet streamer cusp, from which the heliospheric current sheet arises. Each of these pairs of nulls also coincides with the end points of the source-surface footprints of SCs.

Note, however, that any null line of the magnetic field is a topologically unstable feature that can exist only under very special conditions. We think, therefore, that the source-surface null line is most likely an artifact inherent only in the employed PFSS model. If passing from PFSS to MHD model, such a null line must turn at radii close to $2.5 R_\odot$ into a feature that has a substantially different magnetic topology. Thus, the indicated topological linkages have yet to be refined, using a more realistic than PFSS model of the solar corona. We will do that in our next paper II, while here we proceed the analysis, assuming that our findings on open separators are approximately correct.

3.4. Field Line Topology of Separatrix Half-domes

Consider now in more detail the topology of separatrix domes (Figure 7), starting from the pseudo-streamers that are embedded between CH_1 , CH_2 , and the northern polar coronal

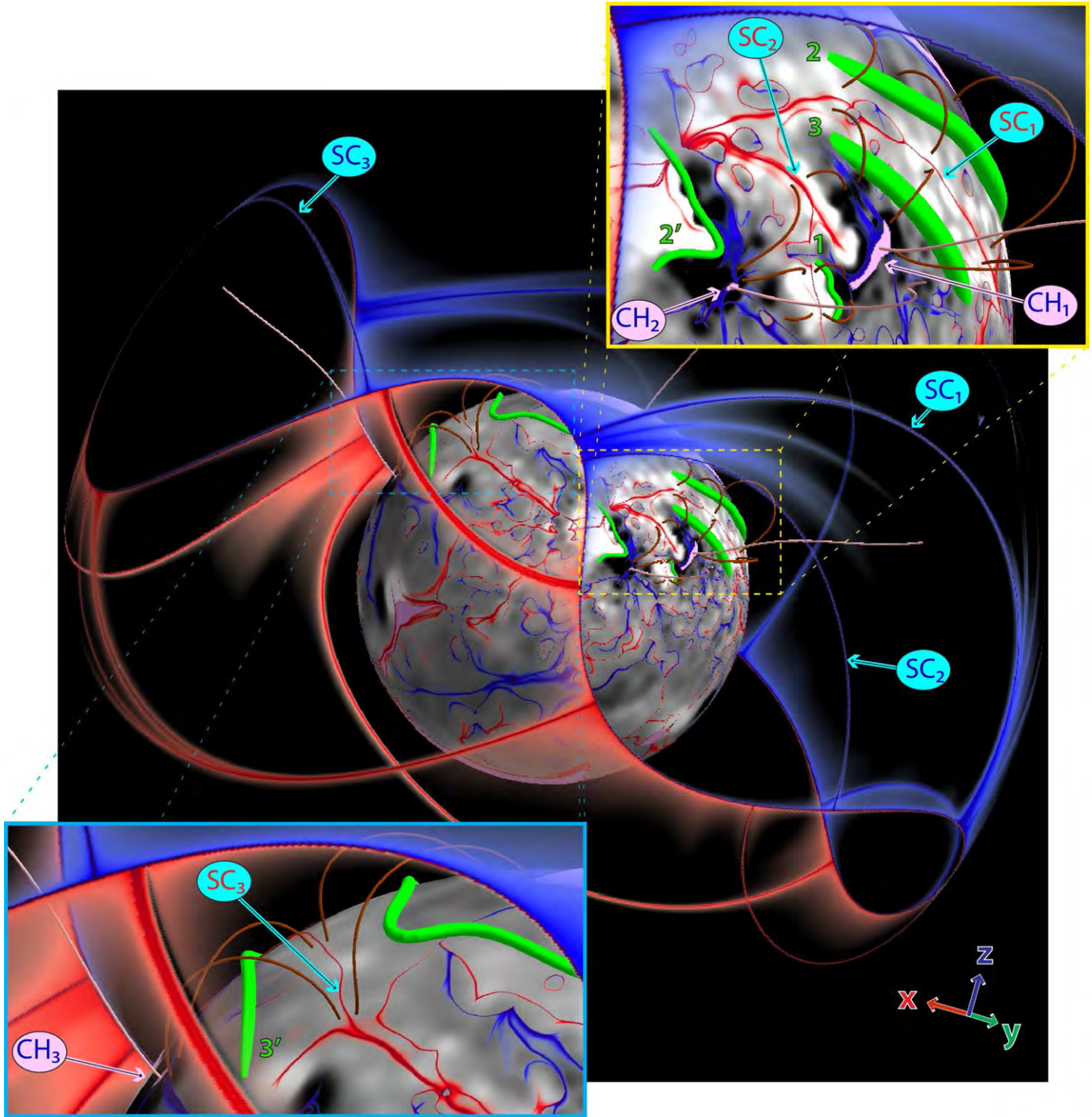


Figure 4. $\text{slog}Q$ distributions are mapped on the photospheric and source-surface globes with a varying opacity such that the low- Q areas ($Q \lesssim 300$) appear to be fully transparent. The photospheric $\text{slog}Q$ map is superimposed on the respective gray-scale B_r distribution with the coronal holes shaded in light magenta. Green tubes depict the major filaments prior to the onset of sympathetic eruptions and several field lines (brown) indicate the pseudo-streamer lobes enclosing these filaments. Open field lines (colored in pink) start in the middle of the coronal holes closest to the pseudo-streamers. The vector triad in the lower right-hand corner indicates the angle orientation of the Cartesian system that is rigidly bound to the Sun center with the z -axis directed to the north pole.

(A color version of this figure is available in the online journal.)

hole. The eastern half-domes (on the left) are combined in one simply connected surface, because they originate in one small bald patch BP_1 located at the border of an active region near the filament $2'$. Spreading out from BP_1 , the field lines extremely diverge within this surface at the nulls N_1 and N_2 and hit the photosphere near the indicated coronal holes. Two of these field lines (red and thick), however, go instead straight to N_1 and N_2 and so, as discussed above, are *generalized separators* belonging to SC_1 and SC_2 , respectively.

In contrast to the eastern half-domes, the western ones (on the right) do not merge with each other and have different originations. The half-dome covering filaments 2 and 3 is simply a fan surface of an extra null point N_{1-2} that is located far to the west from the basic null N_1 . These two nulls are connected by an ordinary separator, which belongs to both this half-dome and the curtain SC_1 .

It is somewhat surprising, but the half-dome covering filament 1 appears to be a quasi-separatrix surface that originates at

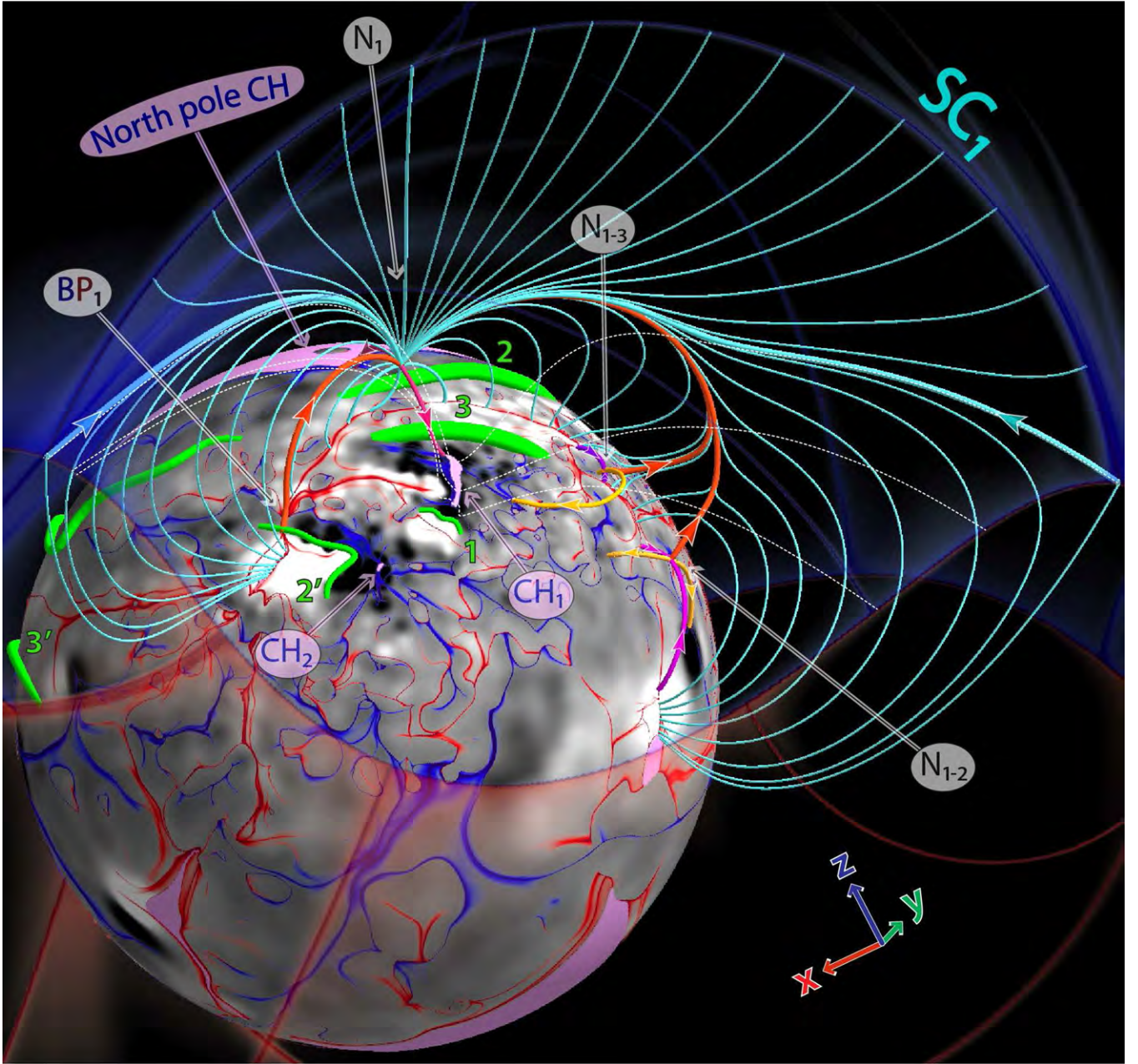


Figure 5. Field line topology of the separatrix curtain SC_1 of pseudo-streamer 1 (embedded between the northern polar coronal hole and CH_1). The thickest lines represent separators, of which the red ones are closed field lines connecting the null point N_1 either to the bald patch BP_1 or another nulls N_{1-2} or N_{1-3} , while the cyan ones are open field lines connecting N_1 to the null line of the source surface. Magenta lines are the spine field lines of the nulls; the yellow lines are the separatrix field lines that emanate from the nulls N_{1-2} and N_{1-3} along the fan eigenvectors that are complementary to the separator ones; several field lines (white dashed) belonging to the boundary of CH_1 are also shown. The maps at the photosphere and source surface and their color coding are the same as in Figure 4.

(A color version of this figure is available in the online journal.)

a magnetic minimum point M_{2-1} lying very close to the photosphere. The field line (red and thick) that passes through and connect M_{2-1} to the basic null N_2 is a *quasi-separator*. The field direction remains unchanged after passing this line through the minimum M_{2-1} , as opposed to a genuine null point, where the field direction would change to the opposite. A similar behavior of the field at M_{2-1} would also occur if it were a degenerate null point, whose one eigenvalue identically equals zero (Titov et al. 2011). We regard this possibility as highly unlikely here, but we cannot fully exclude it, relying only on our numerical study as an approximation of nature.

The existence of the null N_{1-3} in the first of the two discussed pseudo-streamers brings an extra complexity into the structure.

Figures 5 and 7 show that, similarly to N_{1-2} , the null N_{1-3} is connected via an additional separator to the basic null N_1 . This implies that the fan surface of N_{1-3} is also a half-dome such that its edge coincides with the spine line of the null N_1 . We did not plot this half-dome in Figure 7 to avoid cluttering the image with too many lines, but it is very similar to the plotted half-dome that originates in the null N_{1-2} .

The third pseudo-streamer, which is embedded between CH_3 and the northern polar coronal hole, has the topology as analogous as the one of the two others considered above (see Figure 8). The main difference is only that both half-domes originate here at bald patches BP_2 and BP_3 , which are located at the opposite flanks of the pseudo-streamer. In this respect,

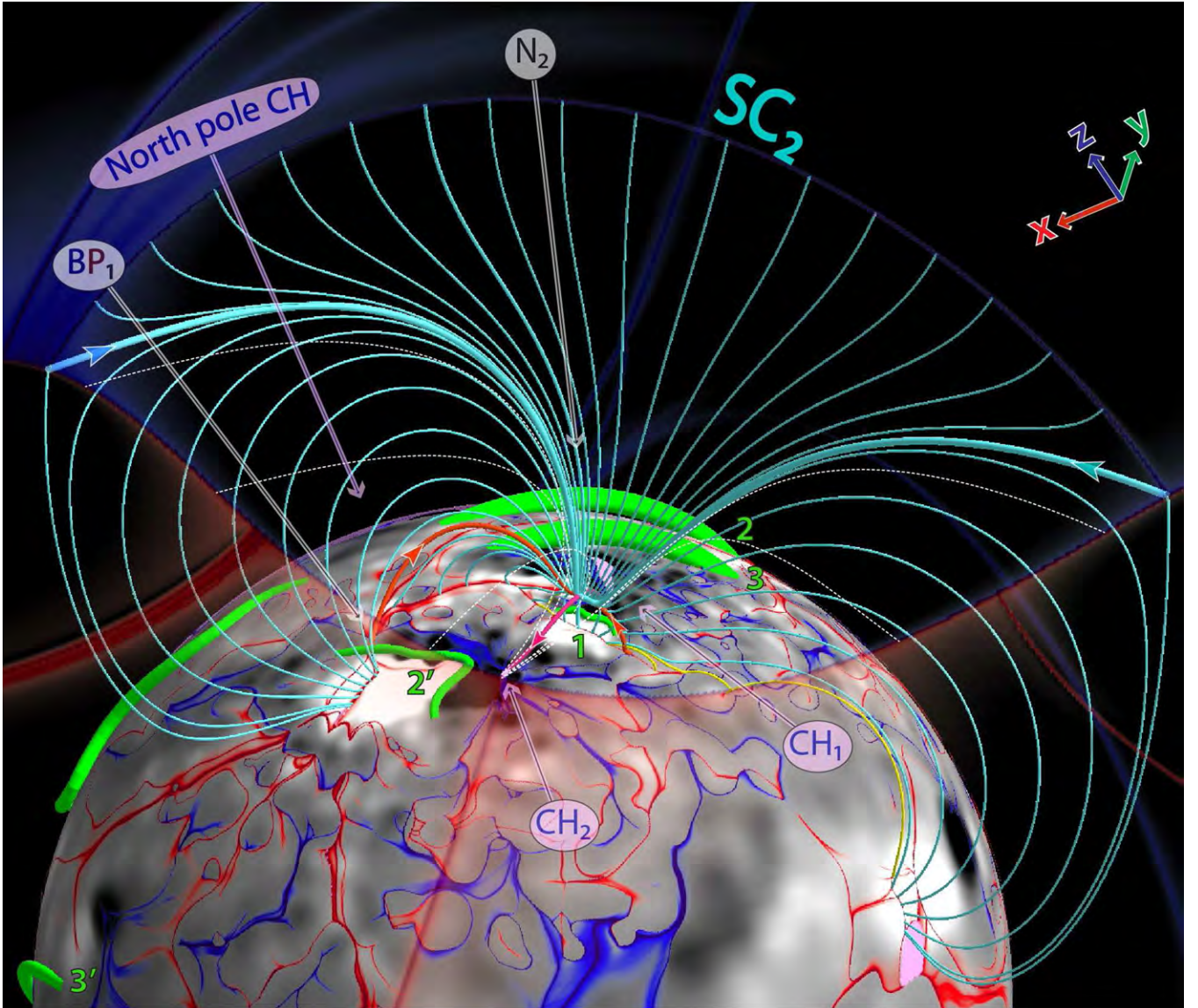


Figure 6. Field line topology of the separatrix curtain SC_2 of pseudo-streamer 2 (embedded between the coronal holes CH_1 and CH_2). The field line styles are the same as in Figure 5, except that the thin yellow lines represent separatrix field lines associated with small-scale photospheric polarity regions. The maps at the photosphere and source surface and their color coding are the same as in Figure 4.

(A color version of this figure is available in the online journal.)

the structure is the same as the one used before for initializing our MHD model of sympathetic eruptions (Török et al. 2011). It is important that these simulations have demonstrated that the generalized separators connecting such BPs and null points are physically similar to the ordinary separators. They both appear to be preferred sites for the formation of current sheets and reconnection of magnetic fluxes.

3.5. Field Line Topology versus High- Q Lines in the Cut Planes

A complementary way to study the structure of a pseudo-streamer is to consider its cross-sectional Q distributions and analyze their variation in response to changing location of the cut plane. As one can anticipate from the above analysis, the simplest pattern of high- Q lines appears to occur in the cut plane across the very middle of pseudo-streamers, where the basic null point is located. The corresponding high- Q lines form there a \cap -type intersection such that the vertical line and arc in the symbol \cap represent, respectively, the discussed SCs and domes.

The shape of separatrix domes at this place essentially follows the path of the spine line associated with the respective basic null point. Above such a dome, the SC separates the open fields of two adjacent coronal holes and observationally corresponds to the stalk of the pseudo-streamer.

However, with shifting the cut plane from the middle to the flanks of pseudo-streamers, the pattern of high- Q lines gets more complicated. In particular, the above high- Q arc can split into several lines, each of which corresponds to a separate half-dome, except for the uppermost line. The latter asymmetrically rises on one side from the curtain up to the source surface and, touching it, forms a cusp. This line determines the border between closed and open fields, since it is nothing else than an intersection line of the cut plane with the separatrix surface of the helmet streamer. Figure 9 illustrates such a structure in a particular cut plane; it also shows schematically how the cross-sectional pattern varies along the pseudo-streamer. Only three cases where the cut plane passes at the photospheric level outside CH_1 and CH_2 are shown in this figure, while the

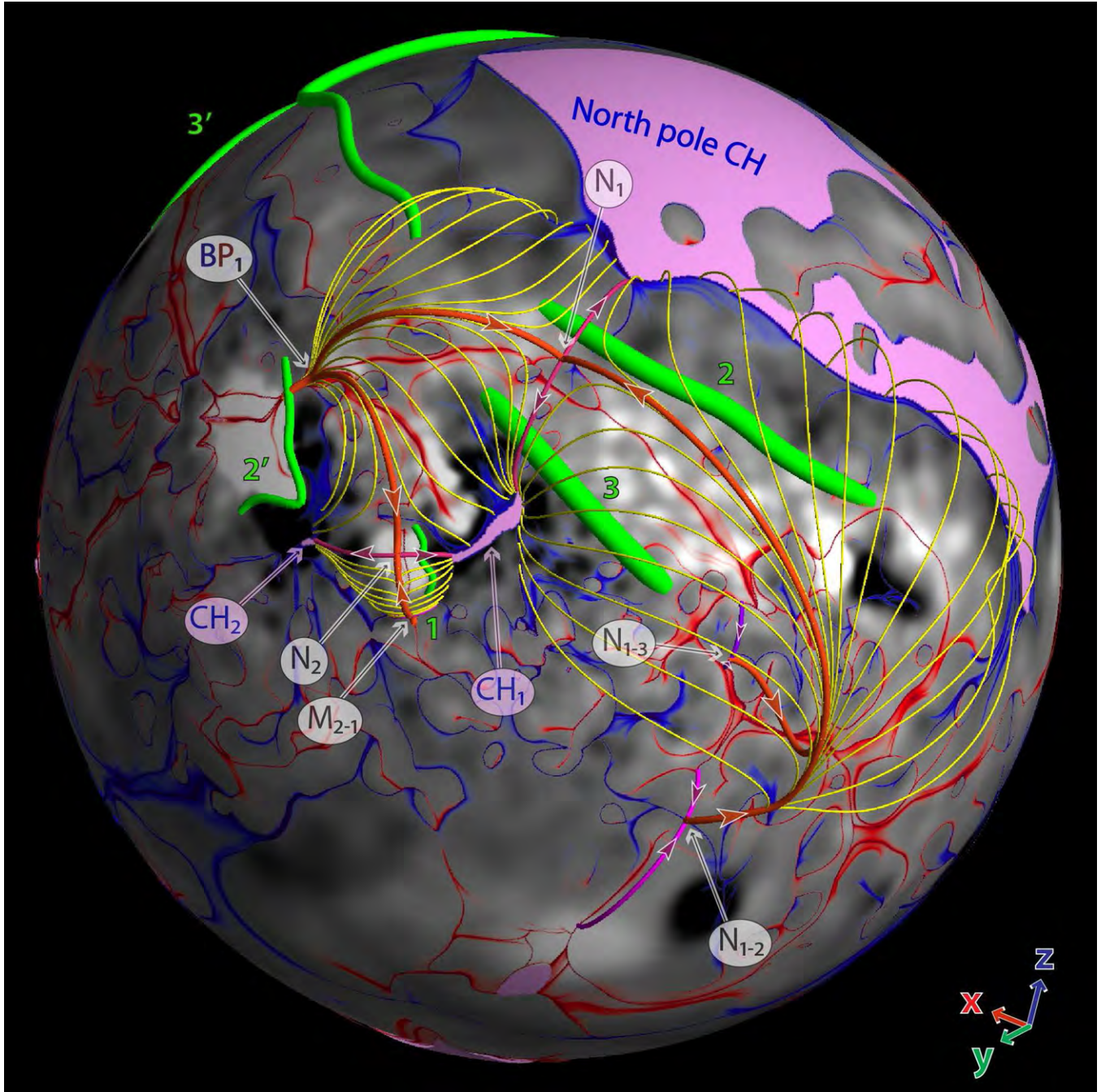


Figure 7. Field line topology of the separatrix domes of pseudo-streamers 1 and 2, one of which is embedded between the northern polar coronal hole and CH_1 and the other between the coronal holes CH_1 and CH_2 . The field line styles are the same as in Figures 5 and 6, except that the thin yellow lines represent separatrix field lines starting either at the bald patch BP_1 or in the fan plane of the null point N_{1-2} ; a similar separatrix dome associated with the null N_{1-3} is not shown. The same style is used for the field lines of the quasi-separatrix surface originated at the magnetic minimum point M_{2-1} . The maps at the photosphere and source surface and their color coding are the same as in Figures 4–6.

(A color version of this figure is available in the online journal.)

remaining cases can be reproduced analogously from the above analysis.

3.6. Concluding Remarks

So far, we have only fully described the structural skeleton of the first pseudo-streamer, including the separatrix curtain SC_1 and respective half-domes with their separators. As concerned with the other two pseudo-streamers, we still have not touched on several separators depicted in Figures 6 and 8 with yellow

and orange thin lines. These separators are due to “scattering” of the SC field lines on small photospheric flux concentrations of negative polarity. Such scattering occurs at BPs or null points to yield additional half-domes, whose edges coincide with the spine lines of the basic nulls N_2 or N_3 . The existence of these features, however, can vary depending on the resolution and smoothing of the used magnetic data, so we ignore them in our study, focusing only on stable structural features that are due to large-scale properties of the configuration.

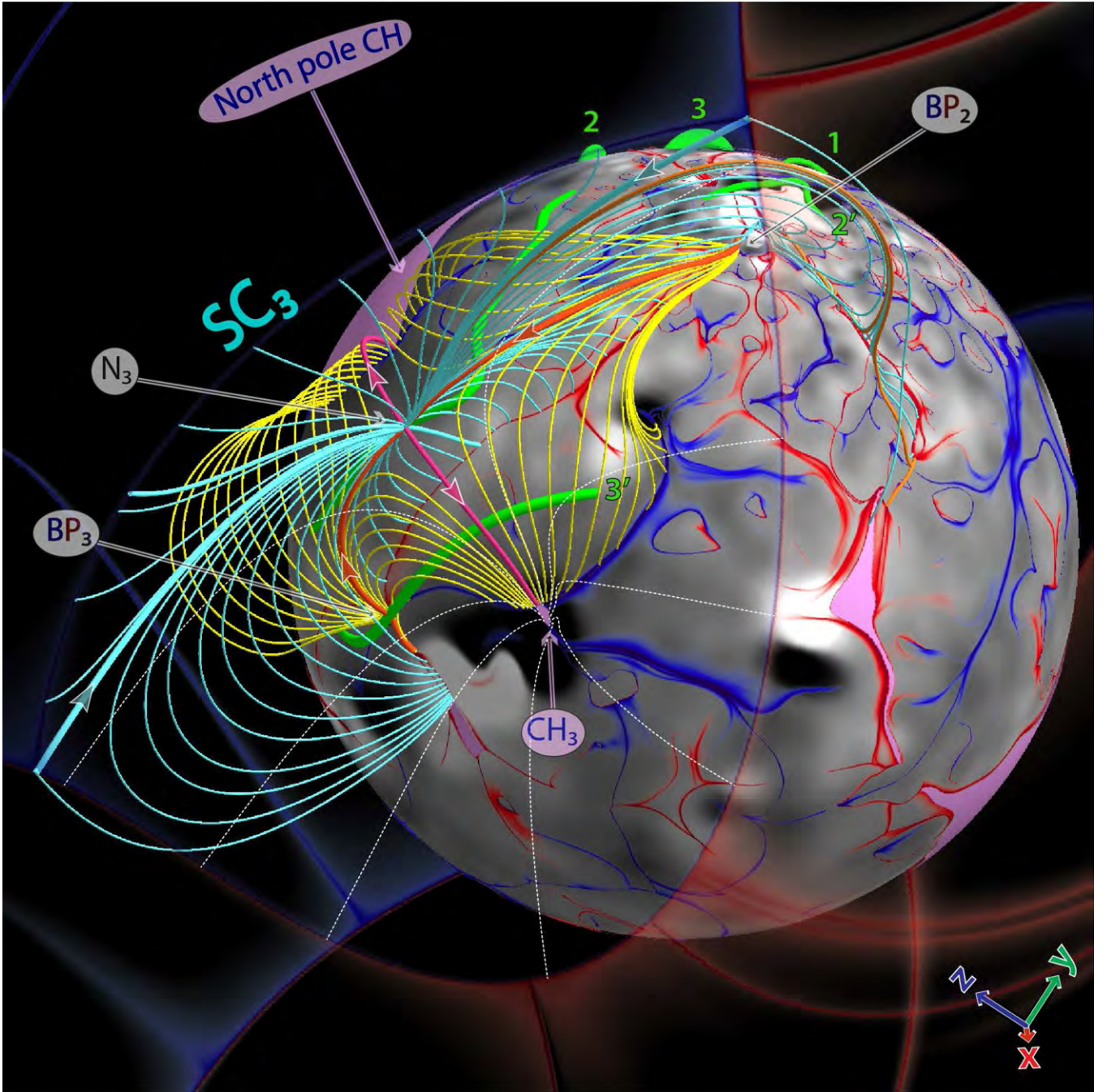


Figure 8. Field line topology of the separatrix curtain (cyan) and dome (yellow) of pseudo-streamer 3 (embedded between the northern polar CH and CH_3). The field line styles are the same as in Figures 5–7, except that the thin orange lines represent the separatrix field lines that are associated with the bald patches and null points of small-scale photospheric polarity regions. The maps at the photosphere and source surface and their color coding are the same as in Figures 4–7.

(A color version of this figure is available in the online journal.)

One also has to remember that the described structure might be distorted in reality by the field of filaments whenever they are present inside pseudo-streamer lobes. Note, however, that such filaments reside prior to eruption in the middle of the lobes along photospheric polarity inversion lines. So possible intense currents of the filaments are located relatively far from the found separatrix domes and curtains and hence the contribution of such currents to the total field must be small at these places compared to the background potential field. Therefore, we think that at large length scales our PFSS model is accurate enough to describe the structure of the real pseudo-streamers with the filaments inside the lobes.

4. MAGNETIC TOPOLOGY AS A CAUSAL LINK IN SYMPATHETIC CMEs

We have studied in Section 3 how SCs and half-domes originate in a given pseudo-streamer at magnetic null points and/or BPs and how they intersect each other along separator field lines. These results are of importance for unveiling a causal link in the sequential eruption of filaments, in which the magnetic topology and reconnection likely played a key role. Indeed, according to the present state of knowledge (Priest & Forbes 2000), a perturbation in the neighborhood of a separator line generally creates along it a current sheet, across which

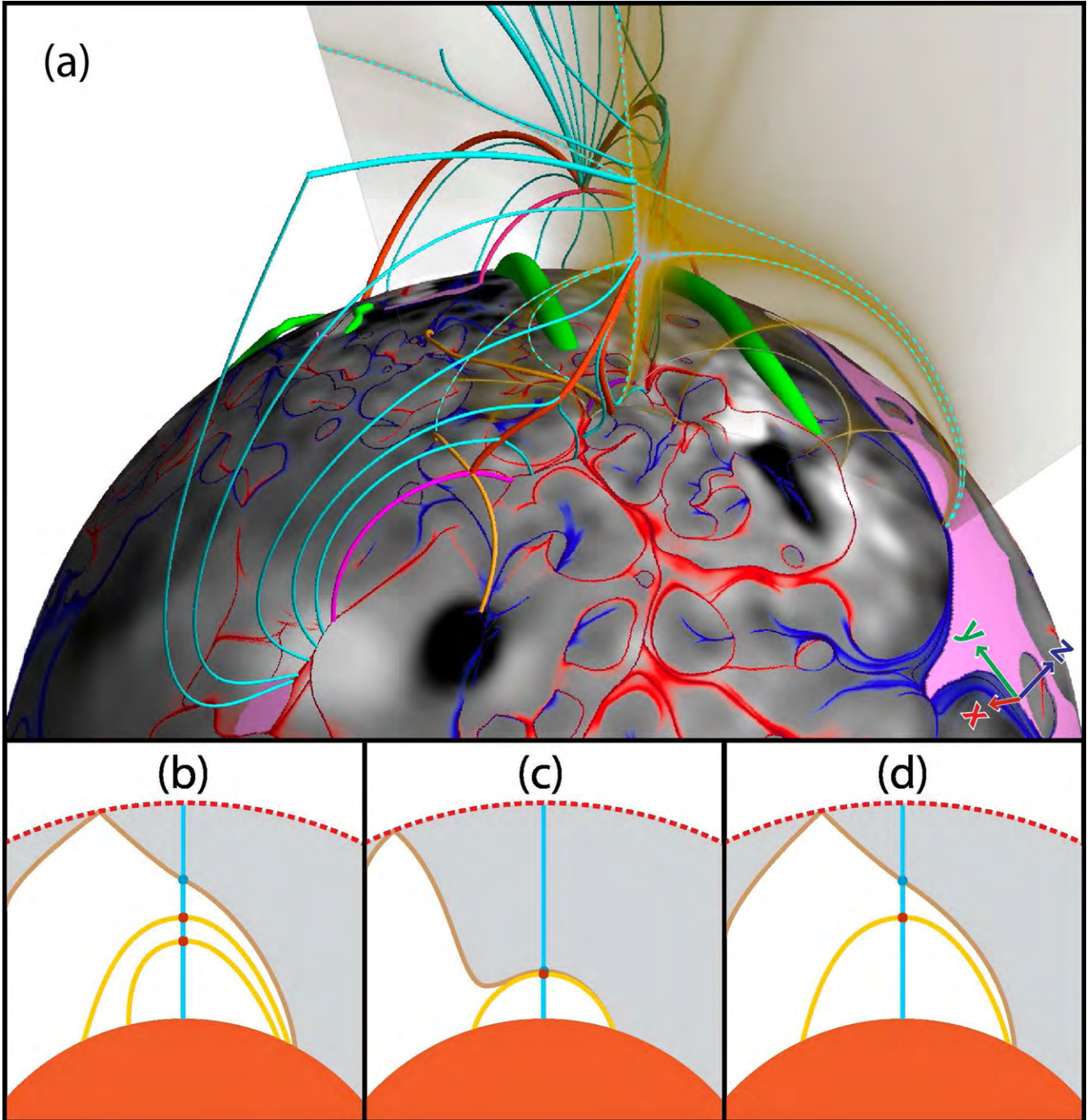


Figure 9. Field line topology of the separatrix curtain SC_1 in relation to the $\log Q$ distribution in a cut plane across the pseudo-streamer 1 (a). This distribution is plotted by using a yellow palette, whose opacity linearly decreases with $\log Q$ in the range from 2.5 to 0.3 down to a complete transparency; the maps at the photosphere, their color coding, and the field line styles are the same as in Figure 5. Dashed (cyan) curves highlight the high- Q lines that represent the intersection lines of the cut plane with SC_1 , helmet-streamer separatrix surface, and two separatrix domes. Such a structure is shown also schematically for this cut and two others in panels (b)–(d), respectively, where the open-field regions are shaded in gray; the extra two cuts are made successively further eastward from the middle of the pseudo-streamer.

(A color version of this figure is available in the online journal.)

magnetic fluxes subsequently reconnect in an amount depending on the form and strength of the perturbation. As demonstrated above, each of our pseudo-streamers contains several separators, all of which are connected to a basic null point. A perturbation in its neighborhood is expected then to cause reconnection along each of these separators, resulting ultimately in a flux redistribution between adjacent topological regions.

It follows from our analysis that these regions are simply the volumes bounded by various parts of the SC, half-domes, and

separatrix surface of the helmet streamer. Unfortunately, such a complex topological partition of the volume makes it difficult to foresee all the details of the response of our pseudo-streamers to different MHD perturbations. It is clear, however, that eventually such perturbations will change the magnetic fluxes in the lobes and consequently the stability conditions for the filaments within them. The latter in turn can influence the order of eruption of the filaments, which was recently demonstrated in our simple MHD model of sympathetic eruptions (Török et al. 2011).

In this model, a pseudo-streamer similar to the one that stems from the basic null N_1 played a key role in guiding the eruptions of the magnetic flux ropes, analogous to our filaments 2 and 3. Thus, our present topological analysis of the potential background field further substantiates the model.

Let us put now the results of that model into the context of our present analysis in order to explain the observed sequence of the 2010 August 1–2 CMEs. For simplicity, we restrict our consideration to the reconnection processes that occur in the vicinity of the basic nulls of the pseudo-streamers, where we expect the greatest perturbation to occur during the onset of eruptions. As shown above, all separatrix half-domes merge there and form together with the SC a simple ρ -type intersection. Such a separatrix structure implies that, irrespective of the form of the external perturbation, the reconnection triggered there will be of the interchange type (e.g., Fisk 2005). It will exchange the fluxes between the lobes and coronal holes in such a way that the sum of the fluxes in both the two lobes and the two coronal holes remains unchanged. In other words, the diagonally opposite lobes and coronal holes form conjugate pairs, so that the flux in one pair increases by the same amount that it decreases in the other pair.

To facilitate further discussion, we label the pseudo-streamers by the numeric label of their basic null; similarly, we label the lobes by the label of their embedded filament. Note, first, that erupting filament 1 resides initially in pseudo-streamer 2, which is located south of pseudo-streamer 1 (see Figure 7). Therefore, the rise of filament 1 perturbs the southern side of pseudo-streamer 1 and eventually triggers interchange reconnection between the fluxes of coronal hole CH_1 and lobe 2. This reconnection reduces the flux in lobe 2, thereby removing the field lines that overlie and stabilize filament 2, eventually causing it to erupt (i.e., the second eruption). On the other hand, this same interchange reconnection causes the flux in lobe 3 to increase, adding field lines that overlie filament 3, thus further stabilizing it. However, later in time, after erupting filament 2 has risen to a sufficient height, a vertical current sheet forms in its wake, providing a site for interchange reconnection between the fluxes of lobe 3 and the northern polar coronal hole. This second reconnection eventually reduces the flux in lobe 3, removing field lines that overlie and stabilize filament 3, eventually causing filament 3 to erupt (i.e., the third eruption).

This scenario is consistent with that proposed for the sequential eruption of filaments 1–3 in our idealized model (Török et al. 2011). There is one difference though: our present PFSS model reveals that filament 1 was also located inside a pseudo-streamer, which is pseudo-streamer 2 in our notation. The presence of this pseudo-streamer, however, merely facilitates the eruption of filament 1, because its overlying field becomes open at a very low height. So this new feature fits nicely with our earlier proposed mechanism.

The present analysis suggests possible explanations also for the eruptions 2' and 3'. According to Figures 5–7, filament 2' passes above bald patch BP_1 , which is connected by two separators to the basic null points N_1 and N_2 . As discussed above, the rise of filaments 1 and 2 is expected to activate these separators, forming current sheets along them, and subsequently triggering reconnection. Around the location of BP_1 , this reconnection may have been of the tether-cutting type (Moore et al. 2001), reducing the confinement of the active-region core field and eventually unleashing its eruption. This explanation is in agreement with the fact that *SDO/AIA* observed several brightenings in the active region before the CME occurred. There was

a particularly strong brightening at $\sim 06:36$ UT below and above filament 2', very close to the bald patch BP_1 (see the inset in Figure 10). This brightening occurred after filament 2 had already started to rise, implying the above activation of the separator and subsequent reconnection in the vicinity of bald patch BP_1 . We note that Liu et al. (2010) also associated the pre-eruption brightening at $\sim 06:36$ UT to tether-cutting reconnection, triggered, however, by photospheric converging flows rather than separator activation. It appears indeed possible that both processes played a role. We will make a more detailed comparison of our topological analysis with observations in Paper II.

The location of pseudo-streamers 1 and 3 indicates that the eruptions 2 and 2' should produce a significant perturbation of the northern side of pseudo-streamer 3. This should lead to interchange reconnection between lobe 3' and the northern polar coronal hole, reducing the magnetic flux in this lobe and eventually causing filament 3' to erupt, in a similar way as described for filament 2. Note also that filament 3' rises above bald patch BP_3 , which is connected by a separator to the basic null N_3 (see Figure 8). As discussed above for eruption 2', resulting tether-cutting reconnection may trigger the destabilization of filament 3', in tandem with the indicated flux reduction in the lobe 3' caused by interchange reconnection.

This concludes the extended scenario for the sympathetic eruptions under study. Figure 10 summarizes it, presenting all the topological features that are relevant for this scenario. In particular, it depicts the closed separators (red thick lines) that form a long chain that traverses through all three pseudo-streamers. As described above, such a separator chain likely sets up a global coupling between eruptions occurring at widely separated locations. Figuratively speaking, this separator chain plays the role of a “safety fuse” in which a single eruption at one end of the chain triggers along it a sequence of the observed electromagnetic explosions.

Additional global coupling between pseudo-streamers and eruptions might also be provided by the open separators (thick cyan lines in Figure 10), which connect the basic nulls of the pseudo-streamers to the cusp of the helmet streamer. This coupling, however, has yet to be verified. It requires a more advanced model than the PFSS model used in the present study. We plan to use an MHD model for this purpose in the next step of our study.

The proposed explanation of the assumed causal link in the observed sympathetic eruptions is of substantial heuristic value. It is particularly useful as a guide for setting up and analyzing further numerical studies of these eruptions. In combination with our structural analysis, more detailed numerical simulations of CMEs in this configuration are needed to prove the existence of such a link and to deepen its understanding.

5. IMPLICATIONS FOR THE S-WEB MODEL

The structural analysis of pseudo-streamers that we have described has important implications not only for sympathetic CMEs but also for the slow solar wind. The recent S-web model (Antiochos et al. 2011; Linker et al. 2011) has sparked substantial interest in the community (Crooker et al. 2012; Wang et al. 2012). Unfortunately, several important issues related to this model are not well understood. Since the results obtained above relate to the S-web model, we will use this opportunity to clarify these issues.

The first issue relates to the concept of coronal-hole connectivity. Some confusion has arisen because the connectivity

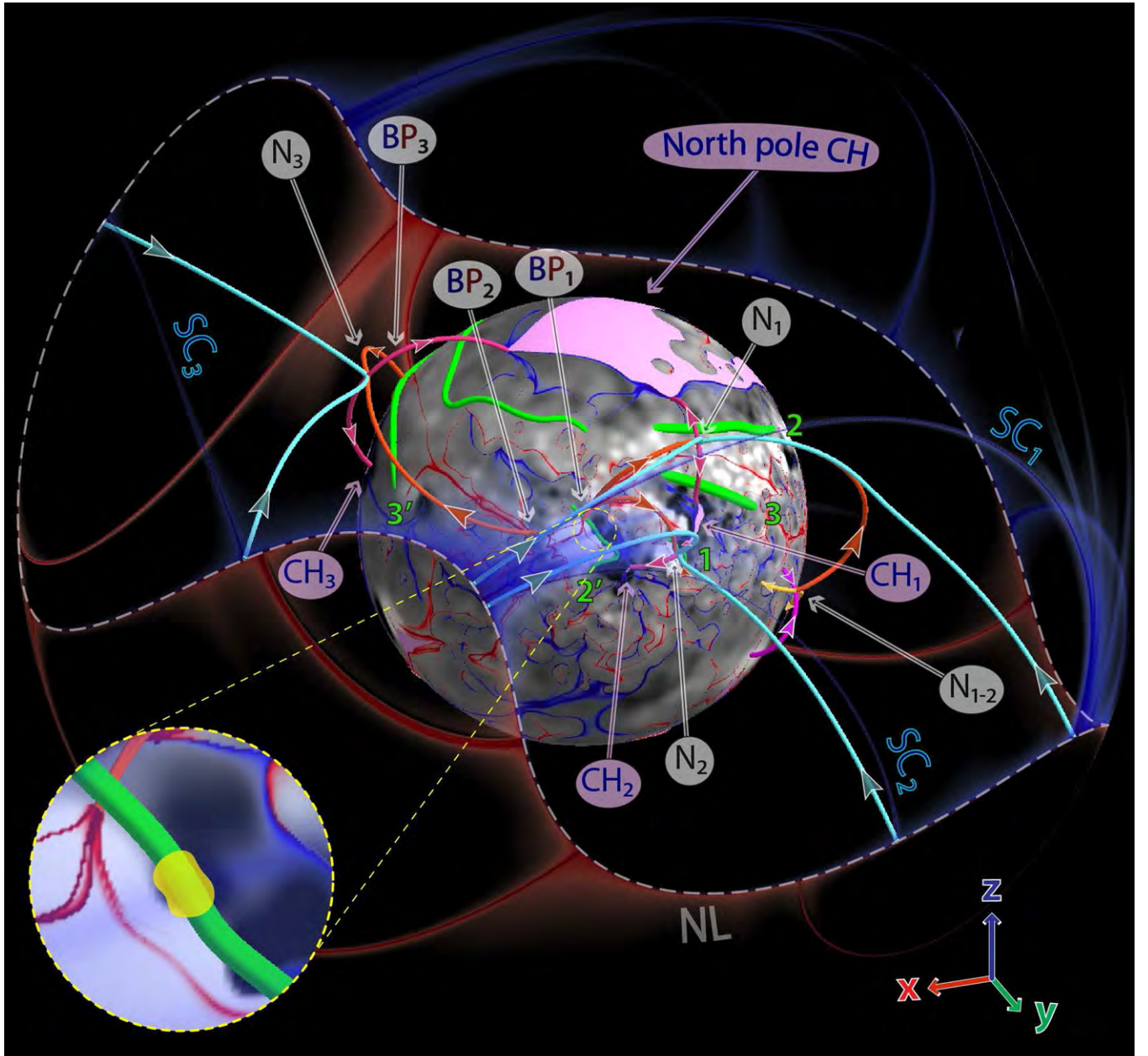


Figure 10. Chain of separators and spine lines in all three pseudo-streamers that were involved in the 2010 August 1–2 sympathetic CMEs. The white dashed line is the null magnetic field line of the source surface—together with the open separator field lines (cyan), it provides a global coupling between all three null points of the pseudo-streamer separatrix curtains. The inset shows a zoomed region near BP_1 , where a strong pre-flare brightening (indicated by yellow blob) was observed by *SDO/AIA* at $\sim 06:36$ UT shortly after which eruption 2' started.

(A color version of this figure is available in the online journal.)

of coronal holes has been interpreted in two different senses. We can consider coronal holes either as two-dimensional regions at the photosphere or as three-dimensional regions in the corona. Though coronal holes of like polarity are always connected when considered as three-dimensional regions, it is important to note that they *can be disconnected* in the photosphere when considered as two-dimensional regions (Titov et al. 2011). In this case, they merge at some height in the corona via a field line separatrix structure that observationally manifests itself as a pseudo-streamer.

The pseudo-streamers we described above (see Figures 5–8) illustrate this fact conclusively. All these cases were characterized by disconnected coronal holes CH_1 , CH_2 , and CH_3 (Figure 2), each of which merges with an adjacent coronal

hole at the height of the basic null point of the corresponding pseudo-streamer. At heights where the magnetic field becomes completely open, the corresponding separatrix curtains SC_1 , SC_2 , and SC_3 serve as interfaces between the holes. Note also that their footprints appear at the source surface as very sharp high- Q lines, whose ends are joined to the null line of the magnetic field (Section 3.1).

Of course, this does not exclude the possibility for different parts of photospheric open-field regions to be connected with each other through narrow corridors. Several examples of such corridors are also seen in our northern polar coronal hole (Figure 2). They imply the appearance of QSLs in the open field, as proposed first by Antiochos et al. (2007), and whose transformation into SCs and back to QSLs has been described

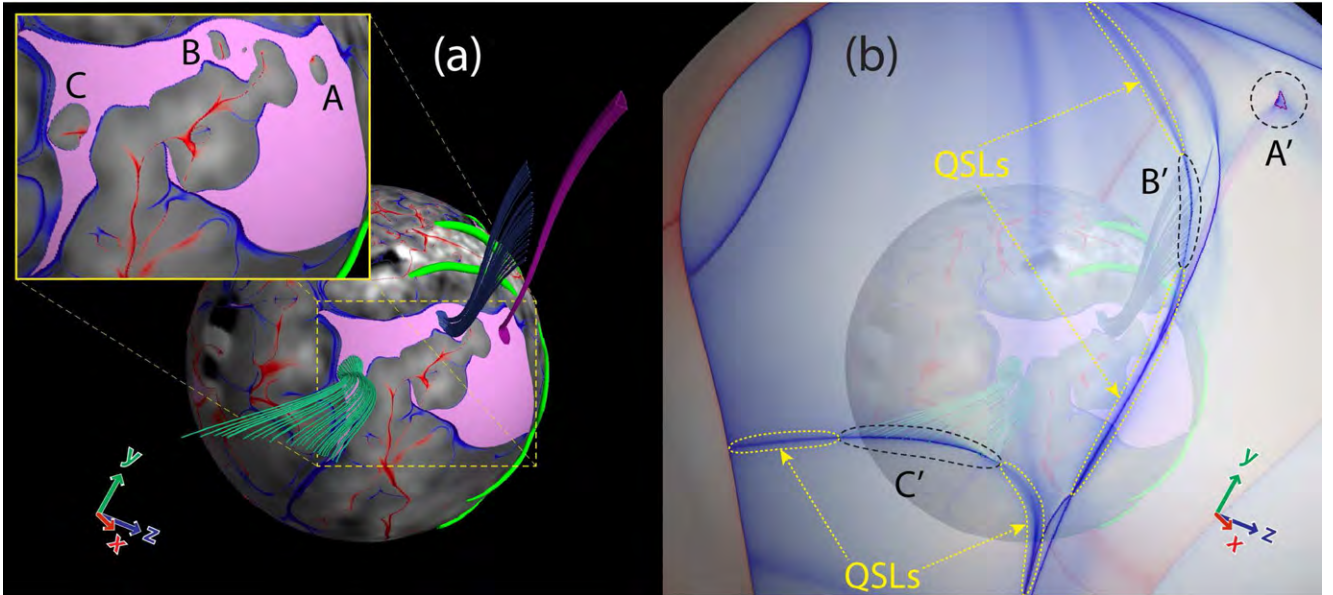


Figure 11. Structure of magnetic field lines near parasitic polarity regions A, B, and C embedded into the northern coronal hole (a) and location of their footprints A', B', and C' at the source surface (b), where a (semi-transparent) $\text{slog} Q$ distribution is also displayed. The high- Q lines encircled by dashed (yellow) lines correspond to the footprints of QSLs that originate in the photospheric open-field corridors adjacent to these polarities.

(A color version of this figure is available in the online journal.)

at length by Titov et al. (2011). As already pointed out in Section 3.1, such QSLs appear at the source surface as high- Q lines with a smooth distribution of Q across their widths (Figure 2(b)). Just as in the case of SCs, these high- Q lines are joined at both ends to the null line of the magnetic field.

Thus, in both the case of truly disconnected and connected coronal holes, interpreted as two-dimensional photospheric regions, their mapping to the source surface connects to the null line of the helmet streamer. This is in contrast to the interpretation of Crooker et al. (2012), who regarded this property of the field line mapping as evidence of the connectivity of coronal holes at the photospheric level. Moreover, we think that the V-shaped coronal hole they interpreted as connected in the photosphere is actually disconnected, as our earlier study of the same case indicates in the framework of the global MHD model (Titov et al. 2011). This particular example shows that when coronal holes are connected in three dimensions it does not necessarily imply that they are connected in the photosphere too.

It remains to be studied how numerous the above open-field QSLs are, compared to SCs, in magnetic configurations with a realistically high resolution. Note that by definition they both belong to the S-web. In the $\text{slog} Q$ -distribution at the source surface, the S-web appears as a network of high- Q arcs connected to the null line of the helmet streamer (Figure 2(b)). The width in latitude of the S-web at this surface is a well-defined quantity, because its value is uniquely related to the open photospheric flux that is (nearly) disconnected from the main bodies of the polar coronal holes. It is unlikely that this flux, and hence the width of the corresponding S-web, will significantly change if one further increases the resolution of the input magnetic data and the corresponding PFSS model.

This conclusion is in contrast with the statement of Wang et al. (2012) that the S-web will extend to the polar region if one resolves its small parasitic polarities. Each such polarity will, indeed, bring additional (quasi-)separatrix structures into the open-field regions. However, in contrast to the SCs of pseudo-streamers, these structures will, first, have a much smaller angular size and, second, will not criss-cross the S-web, but

rather stay mostly isolated from it. Since the quasi-separatrix structures arising from parasitic polarities in polar coronal holes have different geometrical sizes and structural properties, their physical properties are also likely to be different. Therefore, they have not been included into the definition of the S-web (Antiochos et al. 2011), regardless of the fact that the polar plumes associated with these parasitic polarities might appear similar to pseudo-streamers observationally.

To clearly make this point, Figure 11 shows what happens around three small parasitic polarities (A, B, and C) embedded into the northern coronal hole. Panel (a) depicts three sets of open field lines that start very close to the oval high- Q lines bordering the closed magnetic flux of these polarities. Panel (b) shows their source-surface footprints A', B', and C', indicating that such field lines hit the boundary far away from the null line. Thus, their behavior indeed differs from that of the field lines belonging to the SCs we described previously.

In particular, as stated above, for polarities that are far from the main border of their surrounding coronal hole, such as A, their signature at the source surface A' is completely isolated from the S-web. Polarities B and C, however, are much closer to the coronal-hole border; they are detached from it by only a relatively narrow open-field corridor. As expected, the field lines starting in these corridors form QSLs whose footprints at the source surface adjoin on each side of their respective footprints B' and C' (as shown in Figure 2(b)). The high- Q lines resulting from these merged QSLs would appear, at first sight, to form arcs whose ends join the null line of the helmet streamer. However, we would argue that these “arcs” do not genuinely belong to the S-web because these segments have rather low values of $\log Q$ ($\lesssim 1.5$). In summary, we have argued that the addition of small parasitic polarities in polar coronal holes would not contribute to the S-web significantly, if at all. We intend to test this conjecture in future work by explicitly calculating the contribution of parasitic polarities in high-resolution PFSS models.

These considerations help us to predict how our S-web will change with increasing resolution of the input magnetic data

and the corresponding PFSS model. First, increased resolution will cause additional fragmentation of the disconnected coronal holes, while leaving their total magnetic flux approximately unchanged. Our analysis suggests that this will increase the number of cells and high- Q lines in the S-web, but will not substantially increase its width in latitude at the source surface.

Depending on the strength of the parasitic polarities introduced when going to higher resolution, and their positions in coronal holes, the separatrix structure enclosing these polarities can be of two types. First, it can be just a single BP separatrix surface, as in our examples shown in Figure 11. This structure contains no null points in the corona, but nevertheless it completely separates the closed flux of the parasitic polarity from the surrounding magnetic field (Bungey et al. 1996; Müller & Antiochos 2008). Second, it can also be a more familiar structure with a dome-like fan surface and spine line across both coming out from a single null point and surrounded by QSLs (Masson et al. 2009).

These two types of separatrix structures are similar in that their (quasi)-separatrix field lines do not fan out in the open-field region as much as they do in pseudo-streamers. The perturbation of such a structure due to local flux emergence or photospheric motion causes formation of a current sheet and reconnection, both localized in a small region near the corresponding BPs or null points. This process can be considered as a mechanism for producing coronal plumes or “anemone” jets in polar coronal holes (Moreno-Insertis et al. 2008; Müller & Antiochos 2008; Pariat et al. 2010).

The pseudo-streamers are structurally very different. As shown above, they contain several separators, two of which are open, while the others are closed. An emergence, submergence, and/or displacement of photospheric flux concentrations in the lobes of pseudo-streamers, and in their surrounding, must lead to the formation of current sheets along the separators closest to the source of the perturbations. Since current sheets form along the entire length of separators, the related reconnection processes proceed similarly (Parnell et al. 2010). This indicates that reconnection in pseudo-streamers and coronal plumes might have quite different characteristics, which additionally substantiates the original definition of the S-web.

The open separators are lines at which the open and closed magnetic fields become in contact with each other. They appear to be the longest separators in the pseudo-streamers, so most of the interchange reconnection must occur along them. How does it proceed in the presence of multiple closed separators, all connected together with the basic nulls of the pseudo-streamers? This question is of particular importance for understanding the physics of pseudo-streamers and has never been investigated before, because their topological structure was unknown. The answer to this fundamental question is crucial to determine if the S-web model can explain the origin of the slow solar wind. Therefore, it ought to be the focus of the future studies, with special emphasis on the processes that occur both at open separators and the QSLs associated with open-field corridors.

The plasma sheets of pseudo-streamers, as observed in the white-light corona, are composed of fine ray-like structures that are presumed to be formed by interchange reconnection at the streamer cusp (Wang et al. 2012). Such an explanation is consistent with our discussion of open separators, except that in our scenario reconnection occurs along the entire length of these separators rather than just at the mentioned cusp points (which are the footpoints of our open separators at the source surface). In light of our present analysis, the observed ray-like structures are

likely a part of the S-web. For structural features (like separators) to be visible, they have to not only be present, but also perturbed sufficiently (e.g., by waves or photospheric motions). Therefore, at any moment in time, only a small fraction of the S-web might be visible in white light.

It should also be emphasized that the S-web model does not assume a priori that reconnection in pseudo-streamers generates the slow wind in the form of plasma blobs, as it does in helmet streamers (Wang et al. 2012). In fact, we expect that this process must be so different here that it will directly affect the observational properties of the pseudo-streamers. Indeed, in contrast to the helmet streamers, the reconnection in the pseudo-streamers has to occur not in the plasma sheet itself but rather at its edges, where the above open separators are located. Consequently, the pseudo-streamer material must be replenished, at least in part, by the plasma that flows out from those edges. This process has likely to occur in a sporadic fashion, namely, each time when the interchange reconnection takes place between open and closed fields. As a result, the respective reconnection outflows have to be modulated accordingly to produce in the pseudo-streamers the mentioned above ray-like rather than blob-like structures. This consideration shows that, irrespective of its relevance to the problem of the origin of the slow solar wind, the question on how the interchange reconnection modifies the properties of the wind flow in the pseudo-streamers deserves very close attention in the future studies.

6. SUMMARY

We have studied the large-scale topology of the coronal magnetic field determined in the framework of a PFSS model for the time period 2010 August 1–2, when a sequence of sympathetic CMEs occurred. First, this model was computed from the observed data of the photospheric magnetic field. Second, we have calculated high-resolution distributions of the squashing factor Q at the photospheric and source-surface boundaries and at several cut planes across the regions where the CMEs started. Third, we have developed a special technique for tracing (quasi)-separatrix field lines that pass through the high- Q lines of such distributions. These tools allowed us to fulfill a comprehensive analysis of the magnetic field structure.

Of particular interest to us were large-scale separatrix surfaces that divide the coronal volume into topologically distinct regions in which the erupting filaments originated. We have found that four of these five filaments were initially located in the lobes of three pseudo-streamers. Such lobes are obtained as a result of intersection of curtain-like and dome-like separatrix surfaces of the coronal magnetic field. The SC is a fan separatrix surface associated with a null point that is called basic one and located at a certain height in the corona between two adjacent coronal holes of like polarity. Such a curtain is formed by open and closed field lines fanning out from the basic null point. The dome separatrix surfaces are made of two half-domes joined with each other along the spine line of this null point. The half-domes are formed by the field lines that also fan out either from a BP or another null point, which both are located at the flanks of the pseudo-streamer.

In the middle cross-section passing through the basic null of a pseudo-streamer, these separatrix surfaces intersect to produce a \cap -type shape in which the vertical line and arc represent the SC and adjoint half-domes, respectively. Above the half-domes in this cross-section, the curtain separates adjacent coronal holes of like polarity and observationally corresponds to the stalk of

pseudo-streamers. At heights below the basic null of the pseudo-streamer, the coronal holes become disconnected by closed magnetic fields rooted in parasitic polarities and separated by the distance equal to the local width of the separatrix half-domes.

The separatrix surfaces of the pseudo-streamers in the August 1–2 events are located relatively far from the pre-eruption positions of the filaments, so that their contributions to the total field and hence their influence on these surfaces must be small. Therefore, our source-surface model should be sufficiently accurate to reproduce the large-scale structure of real pseudo-streamers with filaments inside.

The indicated SCs intersect half-domes along closed separator field lines, or simply separators, that pass through the null points or BPs at the flanks of the pseudo-streamers. In addition, these curtains intersect the helmet-streamer separatrix surface twice along open separator field lines, which connect the basic nulls of the pseudo-streamers to streamer-cusp points. Invoking our recent MHD model of sympathetic eruptions (Török et al. 2011), we argue that magnetic reconnection at both these types of separators is likely a key process in sympathetic eruptions, because it controls how magnetic fluxes are redistributed between the lobes of pseudo-streamers during eruptions. It has been demonstrated here that the configuration which harbored the first three erupting filaments had a similar magnetic topology as was assumed in that model. Thus, the present topological analysis of the PFSS background field substantiates the previous assumptions on the initial configuration in Török et al. (2011).

Here, we proceeded with a generalization of this earlier proposed scenario, by noticing, first, that the indicated separators in our configuration form a huge chain that traverses through all three pseudo-streamers involved in the eruptions. We have qualitatively explained how a single eruption at one end of such a separator chain can trigger a whole sequence of eruptions.

We have also discussed the implications of our obtained results for the S-web model of the slow solar wind by emphasizing those issues that have not been well understood so far. First, we have demonstrated how the pseudo-streamer structure accommodates disconnection and merging of two coronal holes, respectively, below and above the basic nulls of the pseudo-streamers. Second, we have explained the differences in magnetic topology between pseudo-streamers and separatrix structures enclosing small parasitic polarities in the polar coronal holes and discussed why such structures were not included in the original definition of the S-web. Third, we have emphasized that the sources of the slow solar wind most likely reside both at the separators of pseudo-streamers and QSLs originated in narrow photospheric corridors of the open magnetic field.

The contribution of V.S.T., Z.M., T.T., and J.A.L. was supported by NASA's HTP, LWS, and SR&T programs, SHINE under NSF Grant AGS-1156119, CISM (an NSF Science and Technology Center), and a contract from Lockheed-Martin to Predictive Science, Inc.; O.P. was supported by NSF Grant ATM-0837519 and NASA Grant NNX09AG27G.

REFERENCES

- Altschuler, M. D., & Newkirk, G. 1969, *Sol. Phys.*, **9**, 131
- Antiochos, S. K., DeVore, C. R., Karpen, J. T., & Mikić, Z. 2007, *ApJ*, **671**, 936
- Antiochos, S. K., Mikić, Z., Titov, V. S., Lionello, R., & Linker, J. A. 2011, *ApJ*, **731**, 112
- Aulanier, G., Parlat, E., & Démoulin, P. 2005, *A&A*, **444**, 961
- Biesecker, D. A., & Thompson, B. J. 2000, *J. Atmos. Sol.–Terr. Phys.*, **62**, 1449
- Bumba, V., & Klvana, M. 1993, *Ap&SS*, **199**, 45
- Bungey, T. N., Titov, V. S., & Priest, E. R. 1996, *A&A*, **308**, 233
- Close, R. M., Parnell, C. E., & Priest, E. R. 2004, *Sol. Phys.*, **225**, 21
- Crooker, N. U., Antiochos, S. K., Zhao, X., & Neugebauer, M. 2012, *J. Geophys. Res.*, **117**, 4104
- Démoulin, P., Henoux, J. C., Priest, E. R., & Mandrini, C. H. 1996, *A&A*, **308**, 643
- Eselevich, V. G., Fainshtein, V. G., & Rudenko, G. V. 1999, *Sol. Phys.*, **188**, 277
- Fisk, L. A. 2005, *ApJ*, **626**, 563
- Forbes, T. 2010, in *Models of Coronal Mass Ejections and Flares*, ed. C. J. Schrijver & G. L. Siscoe (Cambridge: Cambridge Univ. Press), 159
- Forbes, T. G. 2000, *J. Geophys. Res.*, **105**, 23153
- Harrison, R. A., Davies, J. A., Möstl, C., et al. 2012, *ApJ*, **750**, 45
- Haynes, A. L., & Parnell, C. E. 2010, *Phys. Plasmas*, **17**, 092903
- Hundhausen, A. J. (ed.) 1972, *Coronal Expansion and Solar Wind* (Berlin: Springer)
- Jiang, Y., Shen, Y., Yi, B., Yang, J., & Wang, J. 2008, *ApJ*, **677**, 699
- Jiang, Y., Yang, J., Hong, J., Bi, Y., & Zheng, R. 2011, *ApJ*, **738**, 179
- Linker, J. A., Lionello, R., Mikić, Z., Titov, V. S., & Antiochos, S. K. 2011, *ApJ*, **731**, 110
- Liu, C., Lee, J., Karlický, M., et al. 2009, *ApJ*, **703**, 757
- Liu, R., Liu, C., Wang, S., Deng, N., & Wang, H. 2010, *ApJ*, **725**, L84
- Masson, S., Parlat, E., Aulanier, G., & Schrijver, C. J. 2009, *ApJ*, **700**, 559
- Moon, Y.-J., Choe, G. S., Park, Y. D., et al. 2002, *ApJ*, **574**, 434
- Moore, R. L., Sterling, A. C., Hudson, H. S., & Lemen, J. R. 2001, *ApJ*, **552**, 833
- Moreno-Insertis, F., Galsgaard, K., & Ugarte-Urra, I. 2008, *ApJ*, **673**, L211
- Müller, D. A. N., & Antiochos, S. K. 2008, *Ann. Geophys.*, **26**, 2967
- Panasenco, O., & Velli, M. M. 2010, *Magnetic Structure of Twin Filaments Inside Pseudostreamers*, AGU Fall Meeting Abstracts, A1663
- Parlat, E., Antiochos, S. K., & DeVore, C. R. 2010, *ApJ*, **714**, 1762
- Parlat, E., & Démoulin, P. 2012, *A&A*, **541**, A78
- Parnell, C. E., Haynes, A. L., & Galsgaard, K. 2010, *J. Geophys. Res.*, **115**, A02102
- Press, W. H., Teukolsky, S. A., Vetterling, W. T., & Flannery, B. P. 2007, *Numerical Recipes: The Art of Scientific Computing* (3rd ed.; Cambridge, NY: Cambridge Univ. Press)
- Priest, E. R., & Démoulin, P. 1995, *J. Geophys. Res.*, **100**, 23443
- Priest, E. R., & Forbes, T. G. 2000, *Magnetic Reconnection: MHD Theory and Applications* (Cambridge: Cambridge Univ. Press), 612
- Priest, E. R., & Titov, V. S. 1996, *Phil. Trans. R. Soc. A*, **354**, 2951
- Ramsey, H. E., & Smith, S. F. 1966, *AJ*, **71**, 197
- Riley, P., Linker, J. A., Mikić, Z., et al. 2006, *ApJ*, **653**, 1510
- Savcheva, A., Parlat, E., van Ballegoijen, A., Aulanier, G., & DeLuca, E. 2012a, *ApJ*, **750**, 15
- Savcheva, A. S., van Ballegoijen, A. A., & DeLuca, E. E. 2012b, *ApJ*, **744**, 78
- Schatten, K. H., Wilcox, J. M., & Ness, N. F. 1969, *Sol. Phys.*, **6**, 442
- Schrijver, C. J., & Title, A. M. 2011, *J. Geophys. Res.*, **116**, A04108
- Seehafer, N. 1986, *Sol. Phys.*, **105**, 223
- Shen, Y., Liu, Y., & Su, J. 2012, *ApJ*, **750**, 12
- Titov, V. S. 2007, *ApJ*, **660**, 863
- Titov, V. S., Forbes, T. G., Priest, E. R., Mikić, Z., & Linker, J. A. 2009, *ApJ*, **693**, 1029
- Titov, V. S., Hornig, G., & Démoulin, P. 2002, *J. Geophys. Res.*, **107**, 1164
- Titov, V. S., Mikić, Z., Linker, J. A., & Lionello, R. 2008, *ApJ*, **675**, 1614
- Titov, V. S., Mikić, Z., Linker, J. A., Lionello, R., & Antiochos, S. K. 2011, *ApJ*, **731**, 111
- Titov, V. S., Priest, E. R., & Démoulin, P. 1993, *A&A*, **276**, 564
- Török, T., Panasenco, O., Titov, V. S., et al. 2011, *ApJ*, **739**, L63
- Wang, H., Chae, J., Yurchyshyn, V., et al. 2001, *ApJ*, **559**, 1171
- Wang, Y.-M., Grappin, R., Robbrecht, E., & Sheeley, N. R., Jr. 2012, *ApJ*, **749**, 182
- Wang, Y.-M., Sheeley, N. R., Jr., & Rich, N. B. 2007, *ApJ*, **658**, 1340
- Wheatland, M. S., & Craig, I. J. D. 2006, *Sol. Phys.*, **238**, 73
- Yang, J., Jiang, Y., Zheng, R., et al. 2012, *ApJ*, **745**, 9
- Zhukov, A. N., & Veselovsky, I. S. 2007, *ApJ*, **664**, L131
- Zuccarello, F., Romano, P., Farnik, F., et al. 2009, *A&A*, **493**, 629

The Challenge in Making Models of Fast CMEs

Zoran Mikić, Tibor Török, Viacheslav Titov, Jon A. Linker, Roberto Lionello,
Cooper Downs and Pete Riley

Predictive Science, Inc., 9990 Mesa Rim Road, San Diego, CA 92121

Abstract. It has been a challenge to explain theoretically how fast CMEs (exceeding $\sim 1,000$ km/s) occur. Our numerical models suggest that it is not easy to release enough magnetic energy impulsively from an active region. We have been studying CME models that are constrained by observed magnetic fields, with realistic coronal plasma density and temperature profiles, as derived from thermodynamic models of the corona. We find that to get fast CMEs, the important parameters are the magnetic energy density, the magnetic field drop-off index, and the Alfvén speed profile in active regions. We describe how we energize active regions, and how we subsequently initiate CMEs via flux cancellation. We contrast CMEs from idealized zero-beta models with more sophisticated models based on thermodynamic solutions.

Keywords: Coronal Mass Ejections, Solar Corona, Magnetohydrodynamics (MHD)

PACS: 96.60.P-, 96.60.ph, 96.60.qf, 95.30.Qd

INTRODUCTION

It has been difficult to develop successful models of fast coronal mass ejections (CMEs). By fast CMEs we mean those whose speed significantly exceeds the ambient solar wind speed (i.e., exceeding $\sim 1,000$ km/s). In order to explain fast CMEs, we need to demonstrate that a significant fraction of the magnetic energy in an active region can be converted into kinetic energy to accelerate the CME, produce a shock wave low in the corona, open overlying closed magnetic field lines, and accelerate energetic particles. Our numerical models suggest that it is not easy to release enough magnetic energy impulsively for these purposes. This has to be done using realistic parameters (magnetic field strength, coronal density, active region size, solar wind, and global field model). It is desirable to use self-consistent CME initiation mechanisms (e.g., photospheric shearing flows, flux cancellation, flux emergence), rather than starting from configurations that are initially out of equilibrium.

To understand CMEs theoretically it is helpful to idealize the problem to the simplest possible configuration that retains the essential characteristics of CMEs. This is a difficult task, since this simplification might compromise the very goal of getting a fast CME. The photospheric magnetic field that is used in models is typically smoothed because simulations with large Alfvén speed and high-resolution meshes are computationally challenging. This smoothing tends to reduce the size of the photospheric field. In our experience, models with overly smoothed fields do not tend to produce fast CMEs. The smoothing process reduces the magnetic energy density in the active region and the magnitude of the Alfvén speed in the corona, and it is likely that these reductions may lower the speed of CMEs.

The plasma density can also affect the speed of CMEs (presumably via the Alfvén speed). Therefore, the models need to have a realistic density profile, requiring an accurate energy equation in the model, and a reasonable coronal heating model. With a sophisticated energy equation [1], we are able to model the cold, dense prominences that frequently erupt together with the CME. As we describe below, the mass trapped in the prominence may affect the speed of the CME, requiring an accurate model of the lower corona and chromosphere.

Finally, the magnetic field overlying the active region may affect how the CME is confined and the nature of the eruption. Since this field arises from distant magnetic field sources, a global model whose scale is much larger than the source active region may be required to properly model the CME.

It is apparent that all these aforementioned considerations make the modeling of fast CMEs difficult. This may be the reason that models have generally not been able to produce fast CMEs.

AN IDEALIZED MODEL

We illustrate our methodology by developing an idealized model of a CME that was observed on 12 May 1997. We have studied this event for many years. Even though this CME occurred in the SOHO era, it is still relevant today, simply because it is not very well understood yet. The halo CME originated in a “simple” small bipolar active region (AR 8038) at $N21^{\circ}W08^{\circ}$, and was accompanied by a C1.3 flare at 04:42 UT. The projected CME speed was ~ 250 km/s; the estimated actual CME speed was ~ 600 km/s. This CME has been described by Plunkett et al. [2] (LASCO); Thompson et al. [3] (EIT waves); Webb et al. [4] (interplanetary magnetic cloud);

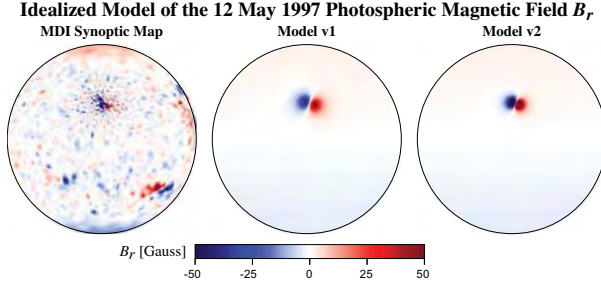


FIGURE 1. The two idealized models of the 12 May 1997 photospheric magnetic field, compared to the SOHO/MDI magnetogram.

Ambastha and Mathew [5] (flux cancellation); Gopalswamy and Kaiser [6] (Type II radio); Attrill et al. [7] (coronal dimmings); and Crooker and Webb [8] (interchange reconnection).

Despite the fact that this was not a fast CME, it is an excellent case to study for the following reason. Our simulations of the pre-eruption corona with a thermodynamic model reproduce several characteristics of the observations, including signatures in EUV and X-ray emission (coronal hole morphology, quiet Sun and active region emission, sigmoid). Furthermore, our simulated eruptions also match the observations, including prominence formation, dimming regions in EUV and X-rays, post-flare loops, and EIT waves. Nevertheless, all our attempts to simulate this CME produce an eruption that is less energetic than the observed CME.

A procedure for developing a simplified model using a global sun-centered dipole and a sub-surface bipole to represent the active region (AR) was described by Titov et al. [9]. We adopt a similar procedure, matching the observed AR flux ($\sim 5 \times 10^{21}$ Mx) and the total global flux ($\sim 4.3 \times 10^{22}$ Mx). The resulting global dipole has $B_r = 2.8$ G at the poles.

We are studying two versions of the model: v1 has a smoother version of the magnetogram with $B_r(\text{max}) = 50$ G in the AR; v2 has less smoothing with $B_r(\text{max}) = 180$ G. The idea is to determine if the reduction of photospheric magnetic field by smoothing reduces the speed of the CME. Both models match the observed AR magnetic flux. Figure 1 shows the models compared to the photospheric field observed with the SOHO/MDI magnetogram.

The simulations are performed with our spherical 3D resistive MHD code, using a semi-implicit technique to overcome the time step limit imposed by the Alfvén speed, and a fully implicit scheme to advance the resistive, viscous, and thermal conduction terms [10, 11]. In the transverse direction, the smallest cells (in the AR) have a size of 2,300 km (690 km) for a medium (high) resolution mesh. In the vertical direction, for the thermodynamic model, the smallest cells have a size of 220 km (60 km) for a medium (high) resolution mesh. The resis-

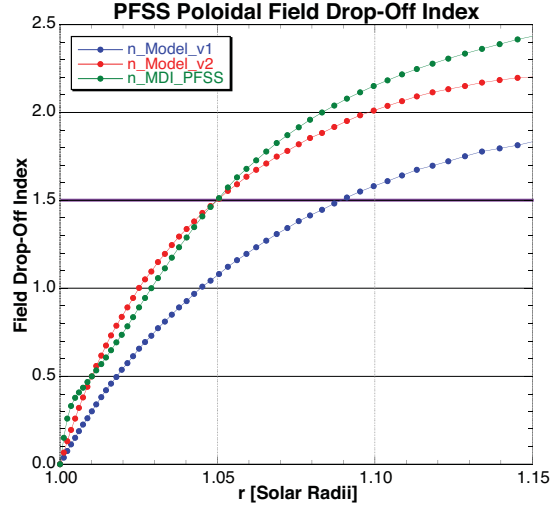


FIGURE 2. The field drop-off index (vertically above the neutral line) for the high-resolution MDI data and for Models v1 and v2.

tivity is chosen to be uniform, with a Lundquist number $S = 10^6$.

Kliem and Török [12] have described how the drop-off of the poloidal component of the potential field that confines a flux rope affects its stability. Assuming that locally $B_{\text{pol}} = B_0(h/h_0)^{-n}$, where $h = r - R_\odot$ is the height above the photosphere, the local drop-off index is $n = -d(\ln B_{\text{pol}})/d(\ln h)$. A heuristic condition for stability is: when $n \gtrsim 1.5$ above the flux rope, the rope erupts more easily; when $n \lesssim 1.5$, the rope tends to be stable [12]. Démoulin and Aulanier [13] consider the critical value to be closer to 1.1–1.3. Török and Kliem [14] have investigated the effect of n on the speed of CMEs. Fields that fall off rapidly with height (larger n) are easier to disrupt, and may produce faster CMEs. An example is a quadrupolar configuration, as exemplified by the Breakout Model [15]. Figure 2 compares n for the high-resolution MDI magnetogram, and for Models v1 and v2 (using a PFSS model). It can be seen that Model v2 matches n of the high-resolution data, whereas Model v1 has a lower n . This is an indication that Model v1 may have been smoothed too much and may have difficulty producing fast CMEs, consistent with our preliminary results. Full confirmation will require a detailed comparison of models v1 and v2 (work in progress).

ACTIVE REGION ENERGIZATION AND CME TRIGGERING

We briefly describe how we typically energize the active region in our model, and how we trigger the eruption. We start with a potential field, and energize the AR by emerging transverse magnetic field along the polarity inversion line (PIL), specified via a boundary condition at $r = R_\odot$ on the transverse electric field, $\mathbf{E}_t = \nabla_t \Phi$.

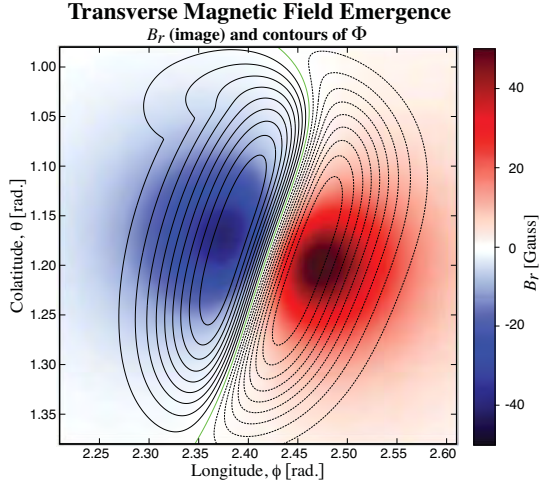


FIGURE 3. The potential Φ used to energize the AR by emerging transverse magnetic field along the PIL (green).

The potential Φ is chosen to change sign across the PIL; see Fig. 3. Since \mathbf{E}_t is the gradient of a scalar, this electric field does not change B_r in the photosphere. We find that the transverse magnetic field emerged by this process introduces shear at the neutral line. The magnetic energy in the active region is raised significantly above the potential field energy.

After the energization is complete, the eruption is triggered by applying flux cancellation at the PIL. There is evidence that flux cancellation preceded the 12 May 1997 CME [5], and may have been its trigger. MDI magnetograms show clear evidence of cancellation of flux at the PIL. This flux cancellation is specified by imposing converging flows at $r = R_\odot$, together with photospheric diffusion [e.g., 16, 17, 18]. Figure 4 shows a typical example of the flow used. In its early stages, flux cancellation converts the highly sheared field along the PIL into a filament. We have found these techniques to be a very flexible way to energize and trigger CMEs.

ZERO BETA AND THERMODYNAMIC MODELS

The full thermodynamic model with an improved energy equation is very costly to run, since it requires high-resolution meshes and small time steps. A “zero-beta” model, in which gravity and pressure forces are neglected, is a useful approximation. In this model, the energy equation is not solved (since $p = 0$). The zero-beta model is numerically more efficient, and is frequently used for the rapid investigation of stability. It is important to note that the coronal density profile $\rho(\mathbf{x})$ can be chosen freely in this model. This choice affects the Alfvén speed profile. In general, it is difficult to choose a realistic ρ profile, especially when the magnetic field varies over a large range (as is the case for global simulations

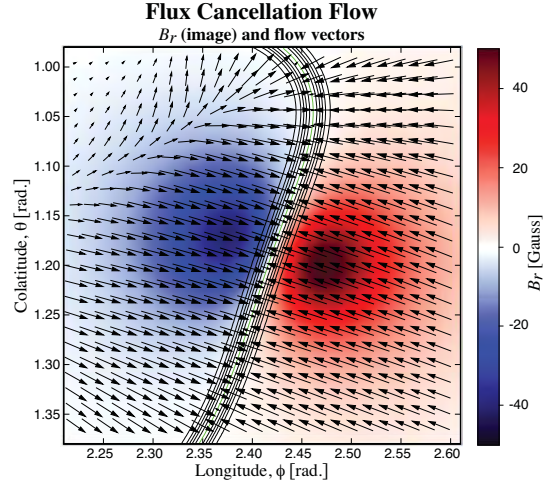


FIGURE 4. Flow applied at $r = R_\odot$ that converges towards the PIL (green), resulting in cancellation of flux. This frequently triggers the initiation of a CME. The contours show the photospheric resistivity.

with high resolution in active regions). That is a primary reason to use a thermodynamic model in which ρ is determined self-consistently. We have found that the choice of $\rho(\mathbf{x})$ can dramatically influence the assessment of a fast CME model.

We studied the energization and eruption of Model v1 using the zero-beta and thermodynamic models. We found that when an arbitrary, though reasonable, density profile was specified in the zero-beta model, the CME reached a certain speed. When we repeated this case using a density profile that was derived from the thermodynamic model (which is more realistic), the CME speed was significantly different. The case with the “fake” density profile was appreciably more energetic. (It turned out to have a higher coronal Alfvén speed.) This ought to be a cautionary tale for users of zero-beta models.

Furthermore, we noticed that the thermodynamic model generally gave less energetic eruptions for the same conditions (energization and flux cancellation), as illustrated in Fig. 5. The thermodynamic model has a smaller burst of kinetic energy, and a correspondingly more gradual release of magnetic energy, than the zero-beta model. (In this case the zero-beta model used the ρ profile from the thermodynamic model to make the comparison as similar as possible.) In the thermodynamic model, the lower field lines in the erupting filament appear to be trapped by the dense plasma in the chromosphere/low corona, in contrast to the zero-beta model, as seen in Figure 6. The thermodynamic model shows the self-consistent formation of a prominence (cool, dense material) in the filament channel, an exciting development in its own right. Since the physics in the thermodynamic model is more accurate, conclusions about the speed of CMEs based on the zero-beta model need to be

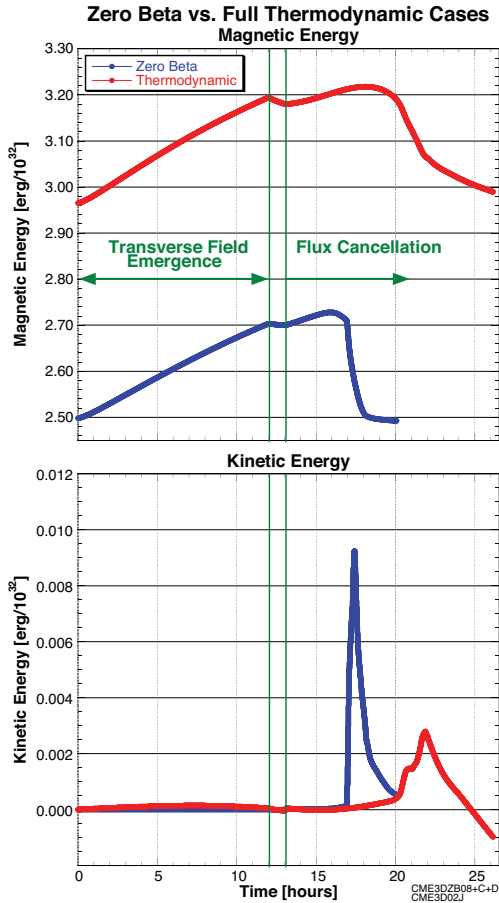


FIGURE 5. The magnetic and kinetic energy for zero-beta and a full thermodynamic simulations. The kinetic energy for the thermodynamic case is that above the initial value.

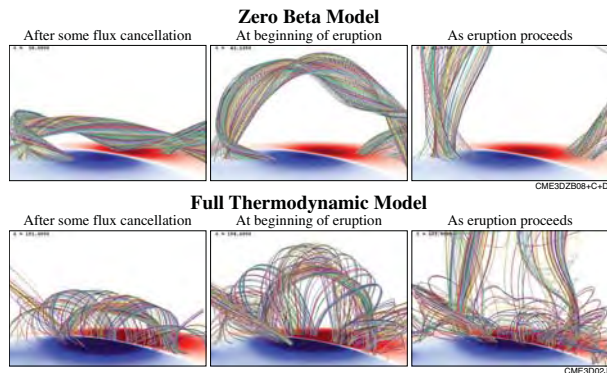


FIGURE 6. The evolution of selected field lines for zero-beta and full thermodynamic simulations.

made carefully.

CONCLUSIONS

It is apparent that models of fast CMEs do not come easily. Although our analysis is not complete, there are strong indications that magnetograms of active regions

used in models must not be smoothed too much, to maximize the chances of getting a fast CME. It appears to be necessary for the models to maintain high Alfvén speeds. The presence of a large field drop-off index low in the corona also helps. Zero-beta models are very useful, but need to be used carefully when making conclusions about the speed of CMEs. Full thermodynamic models offer promise to model the formation of prominences and their eruption within CMEs.

ACKNOWLEDGMENTS

This work was supported by NASA's LWS & Helio-physics Theory Programs, by a subcontract from Lockheed Martin (NASA prime contract NNG04EA00C in support of SDO/AIA), and by NSF via the CISM and FESD Centers.

REFERENCES

1. R. Lionello, J. A. Linker, and Z. Mikić, *ApJ* **690**, 902–912 (2009).
2. S. P. Plunkett, B. J. Thompson, R. A. Howard, D. J. Michels, O. C. St. Cyr, S. J. Tappin, R. Schwenn, and P. L. Lamy, *Geophys. Res. Lett.* **25**, 2477–2480 (1998).
3. B. J. Thompson, S. P. Plunkett, J. B. Gurman, J. S. Newmark, O. C. St. Cyr, and D. J. Michels, *Geophys. Res. Lett.* **25**, 2465–2468 (1998).
4. D. F. Webb, R. P. Lepping, L. F. Burlaga, C. E. DeForest, D. E. Larson, S. F. Martin, S. P. Plunkett, and D. M. Rust, *J. Geophys. Res.* **105**, 27251–27260 (2000).
5. A. Ambastha, and S. K. Mathew, in *Advanced Solar Polarimetry*, edited by M. Sigwarth, 2001, vol. 236 of *ASP Conf. Series*, p. 313.
6. N. Gopalswamy, and M. L. Kaiser, *Adv. Sp. Res.* **29**, 307–312 (2002).
7. G. Attrill, M. S. Nakwacki, L. K. Harra, L. van Driel-Gesztelyi, C. H. Mandrini, S. Dasso, and J. Wang, *Sol. Phys.* **238**, 117–139 (2006).
8. N. U. Crooker, and D. F. Webb, *J. Geophys. Res. (Space Physics)* **111**, 8108 (2006).
9. V. S. Titov, Z. Mikić, J. A. Linker, and R. Lionello, *ApJ* **675**, 1614–1628 (2008).
10. Z. Mikić, D. C. Barnes, and D. D. Schnack, *ApJ* **328**, 830–847 (1988).
11. Z. Mikić, J. A. Linker, D. D. Schnack, R. Lionello, and A. Tarditi, *Physics of Plasmas* **6**, 2217–2224 (1999).
12. B. Kliem, and T. Török, *Phys. Rev. Lett.* **96**, 255002 (2006).
13. P. Démoulin, and G. Aulanier, *ApJ* **718**, 1388–1399 (2010).
14. T. Török, and B. Kliem, *Astron. Nachr.* **328**, 743 (2007).
15. S. K. Antiochos, C. R. DeVore, and J. A. Klimchuk, *ApJ* **510**, 485–493 (1999).
16. T. Amari, J. F. Luciani, J. J. Aly, Z. Mikić, and J. Linker, *ApJ* **585**, 1073–1086 (2003).
17. T. Amari, J.-J. Aly, Z. Mikić, and J. Linker, *ApJ* **717**, L26–L30 (2010).
18. T. Amari, J.-J. Aly, J.-F. Luciani, Z. Mikić, and J. Linker, *ApJ* **742**, L27 (2011).

CONTRACTING AND ERUPTING COMPONENTS OF SIGMOIDAL ACTIVE REGIONS

RUI LIU^{1,2}, CHANG LIU², TIBOR TÖRÖK³, YUMING WANG¹, AND HAIMIN WANG²

¹ CAS Key Lab of Geospace Environment, Department of Geophysics & Planetary Sciences,
University of Science & Technology of China, Hefei 230026, China; rliu@ustc.edu.cn

² Space Weather Research Laboratory, Center for Solar-Terrestrial Research, NJIT, Newark, NJ 07102, USA

³ Predictive Science Inc., 9990 Mesa Rim Road, Suite 170, San Diego, CA 92121, USA

Received 2011 December 29; accepted 2012 August 2; published 2012 September 12

ABSTRACT

It has recently been noted that solar eruptions can be associated with the contraction of coronal loops that are not involved in magnetic reconnection processes. In this paper, we investigate five coronal eruptions originating from four sigmoidal active regions, using high-cadence, high-resolution narrowband EUV images obtained by the *Solar Dynamic Observatory (SDO)*. The magnitudes of the flares associated with the eruptions range from *GOES* class B to class X. Owing to the high-sensitivity and broad temperature coverage of the Atmospheric Imaging Assembly (AIA) on board *SDO*, we are able to identify both the contracting and erupting components of the eruptions: the former is observed in cold AIA channels as the contracting coronal loops overlying the elbows of the sigmoid, and the latter is preferentially observed in warm/hot AIA channels as an expanding bubble originating from the center of the sigmoid. The initiation of eruption always precedes the contraction, and in the energetically mild events (B- and C-flares), it also precedes the increase in *GOES* soft X-ray fluxes. In the more energetic events, the eruption is simultaneous with the impulsive phase of the nonthermal hard X-ray emission. These observations confirm that loop contraction is an integrated process in eruptions with partially opened arcades. The consequence of contraction is a new equilibrium with reduced magnetic energy, as the contracting loops never regain their original positions. The contracting process is a direct consequence of flare energy release, as evidenced by the strong correlation of the maximal contracting speed, and strong anti-correlation of the time delay of contraction relative to expansion, with the peak soft X-ray flux. This is also implied by the relationship between contraction and expansion, i.e., their timing and speed.

Key words: Sun: coronal mass ejections (CMEs) – Sun: flares

Online-only material: animation, color figures

1. INTRODUCTION

It is generally regarded that solar eruptions are due to a disruption of the force balance between the upward magnetic pressure force and the downward magnetic tension force. Since the eruption can only derive its energy from the free energy stored in the coronal magnetic field (Forbes 2000), “the coronal field lines must contract in such a way as to reduce the magnetic energy $\int_V B^2/8\pi$ ” (Hudson 2000, p. L75). The contraction must be associated with the reduction of the magnetic tension force for each individual loop-like field line undergoing contraction, as its footpoints are effectively anchored in the photosphere. Eventually, a new force balance would be achieved between the magnetic pressure and tension force after the energy release. From an alternative viewpoint, the average magnetic pressure $B^2/8\pi$ must decrease over the relevant volume \mathcal{V} across the time duration of the eruption. \mathcal{V} can be roughly regarded as the flaring region, primarily in which magnetic energy is converted into other forms of energies. The contraction process, termed “magnetic implosion” by Hudson (2000), is very similar to the shrinkage of post-flare loops (Forbes & Acton 1996), except that loop shrinkage is driven by temporarily enhanced magnetic tension force at the cusp of the newly reconnected field lines, whereas loop contraction is driven by reduced magnetic pressure in the flaring region. Additionally, with newly reconnected loops piling up above older ones, the post-flare arcade as a whole often expands, rather than shrinks, with time.

Hudson (2000, p. L75) concluded that “a magnetic implosion must occur simultaneously with the energy release,” based on

no assumption about the energy release process itself. However, the detailed timing and location of loop contraction might provide diagnostic information on the eruption mechanism. For example, when the reconnection-favorable flux emerges inside a filament channel (Figure 1(a); adapted from Chen & Shibata 2000), it cancels the small magnetic loops below the flux rope, which results in a decrease of the local magnetic pressure. The whole dipolar magnetic structure must contract correspondingly. Meanwhile, plasmas on both sides of the polarity-inversion line (PIL) would move inward to form a current sheet below the flux rope and the subsequent evolution could follow the paradigm of the standard flare model (e.g., Kopp & Pneuman 1976). In that case, overlying coronal loops could be observed to initially contract and then erupt. In a different scenario, a twisted flux rope confined by potential-like magnetic fields is found to be energetically favorable to “rupture” through the overlying arcade via ideal-MHD processes (Figure 1(b); adapted from Sturrock et al. 2001). This is clearly demonstrated in MHD simulations by Gibson & Fan (2006) and Rachmeler et al. (2009), in which overlying loops can be seen to be pushed upward and aside as the flux rope kinks and expands, and after the rope ruptures through the arcade, overlying loops on both sides quickly contract toward the core region, due to the reduction of the magnetic pressure in the core field with the escape of the flux rope. In particular for this scenario (Figure 1(b)), one would expect to see both the expanding flux rope and the contracting overlying loops during the eruption as long as the arcade is only partially opened. Although both scenarios involve a pre-existing flux rope, they can supposedly

Table 1
List of Events

Date	AR	Location	Hale	GOES	v_c^{\max} (km s^{-1}) ^a	v_e^{\max} (km s^{-1}) ^b	Δt (min) ^c
2010 Aug 1	11092	N13E21	α/β	C3.2	-51	83	9.0
2010 Sep 3	11105	N19W23	$\beta/-$	B2.8	-12	94	34.6
2011 Feb 13	11158	S19W03	β/β	M6.6	-195	538	1.8
2011 Feb 15	11158	S21W21	$\beta\gamma/\beta\gamma$	X2.2	-320	401	2.4
2011 Jun 21	11236	N17W19	$\beta\gamma/\beta\gamma$	C7.7	-57	90	12.4

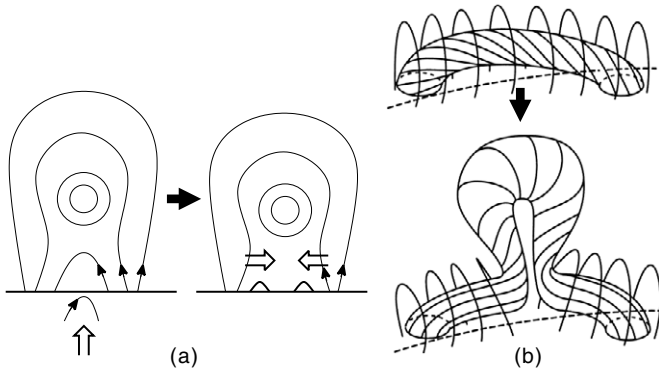
Notes.^a Maximum contracting speed.^b Maximum expanding speed.^c Time delay of contraction relative to expansion.

Figure 1. CME models relevant to magnetic implosion. (a) Schematic diagram of the emerging flux triggering mechanism for CMEs (adapted from Chen & Shibata 2000). The emerging flux inside the filament channel cancels the pre-existing loops, which results in the in situ decrease of the magnetic pressure. Magnetized plasmas are driven inward to form a current sheet beneath the flux rope. (b) Schematic sketch showing that in the three-dimensional space a twisted flux rope can rupture the overlying magnetic arcade and erupt by pushing the magnetic arcade aside (adapted from Sturrock et al. 2001). With the escape of the flux rope, the arcade field undergoes contraction due to the decreased magnetic pressure in the core field.

also accommodate those models in which the flux rope forms immediately prior to (e.g., Moore et al. 2001), or during the course of (e.g., Antiochos et al. 1999), the eruption.

Corresponding to the aforementioned models (Figure 1), our previous observational studies also suggest two different scenarios, i.e., (1) the bunch of coronal loops undergoing contraction later becomes the front of the eruptive structure (Liu et al. 2009b) and (2) the contracting loops are distinct from the eruptive structure (Liu & Wang 2009, 2010). The role of contraction in the eruption, however, has been unclear in both scenarios. For Scenario 1, the event reported by Liu et al. (2009b) remains unique in the literature; as for Scenario 2, the eruptive structure is not easy to detect before its appearance as a coronal mass ejection (CME) in the coronagraph, unless there is dense filament material serving as the tracer (Liu & Wang 2009). In some cases, its slow ascension and expansion during the early stage might manifest as the gradual inflation of overlying coronal loops (Liu et al. 2010b). Only with the advent of the *Solar Dynamic Observatory* (SDO; Pesnell et al. 2012), which provides a continuous and wide temperature coverage, is the eruptive structure itself more frequently identified beneath the coronagraph height as a hot, diffuse plasmoid (e.g., Liu et al. 2010c; Cheng et al. 2011).

Here in a further investigation of Scenario 2, we identify both the erupting and contracting components using SDO data, and hence for the first time we are able to study in detail

their relationship as well as the implication for the eruption mechanism and the associated energy release process. In the rest of this paper, we present in Section 2 the results of our investigation on five flares (Table 1) observed by the Atmospheric Imaging Assembly (AIA; Lemen et al. 2012) on board SDO, and we make concluding statements in Section 3.

2. OBSERVATION

2.1. Overview

In addition to the symbiosis of the erupting and contracting components, the five flares studied here all occurred in sigmoidal active regions (Figure 2), which had a sinusoidal shape in the warm AIA channels such as 211 Å (dominated by Fe XIV, $\log T = 6.3$) and 335 Å (dominated by Fe XVII, $\log T = 6.4$) or hot channels like 94 Å (dominated by Fe XVIII, $\log T = 6.8$). Upon close inspection, one can see that two groups of J-shaped loops, which are oppositely oriented with respect to each other, collectively have a sinusoidal appearance (Figure 2). In cold channels such as 171 Å (dominated by Fe IX and Fe X, $\log T = 5.8$) and 193 Å (dominated by Fe XII, $\log T = 6.1$), these regions were dominated by large-scale loops arched over the elbows of the hot sigmoid, suggesting that the highly sheared core field is restrained by the potential-like overlying field. Since nonpotential (sheared or twisted) fields are reservoirs of magnetic free energy, it is not surprising that sigmoidal regions are significantly more likely to be eruptive than non-sigmoidal regions (Hudson et al. 1998; Canfield et al. 1999; Glover et al. 2000), and are deemed to be one of the most important precursor structures for solar eruptions.

Of the five flares, both the M6.6 flare on 2011 February 13 and the X2.2 flare two days later on February 15 occurred in the same AR 11158. One can see that on February 13, when it was still classified as a β -region, AR 11158 was only a “rudimentary” sigmoid compared with its status on February 15. The hot loops in AIA 94 Å in the center of the active region, however, were already highly sheared, taking the similar east–west orientation as the major PIL along which the two bipolar regions interacted and major flares took place (see Beaufregard et al. 2012 for details).

Utilizing the newly released vector magnetograms with the 0.5 pixel size for AR 11158 (Hoeksema et al. 2012) obtained by the Helioseismic and Magnetic Imager (HMI; Scherrer et al. 2012) on board SDO, we constructed the non-linear force-free field (NLFFF) model using the “weighted optimization” method (Wiegelmann 2004) after preprocessing the photospheric boundary to best suit the force-free condition (Wiegelmann et al. 2006). NLFFF extrapolation using the vector magnetogram at about 16:00 UT on 2011 February 13

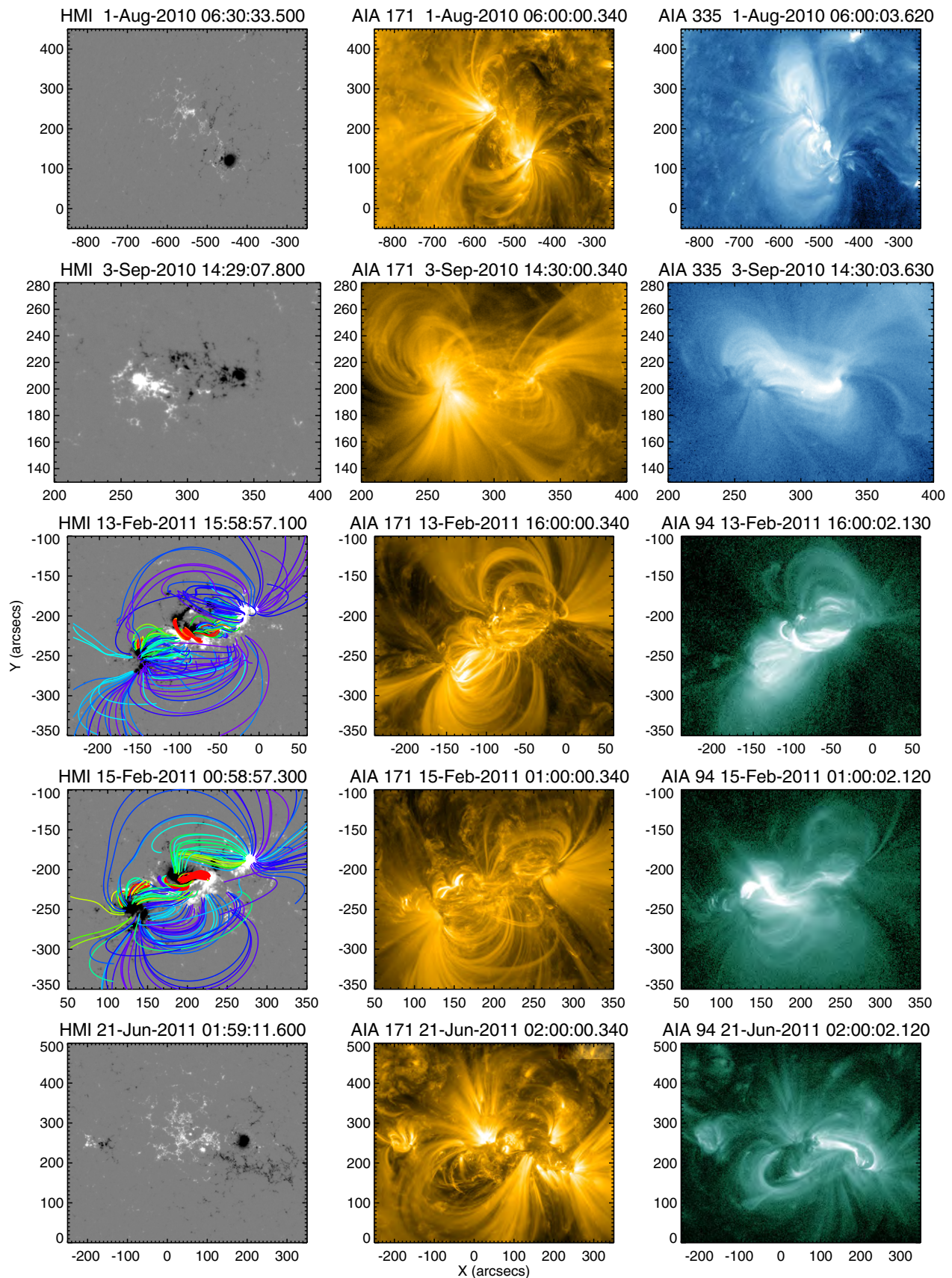


Figure 2. Pre-flare configuration for the five flares studied. Left column: line-of-sight magnetograms obtained by the Helioseismic and Magnetic Imager (HMI) on board *SDO*. Middle and right columns: corresponding EUV images in the cold and warm/hot AIA channels, respectively, showing the sigmoidal morphology and structure. For AR 11158 (third and fourth rows), we use HMI vector magnetograms to construct nonlinear force-free field (NLFFF; see the text for details). The extrapolated field lines are color coded according to the intensity of vertical currents on the surface.

(A color version of this figure is available in the online journal.)

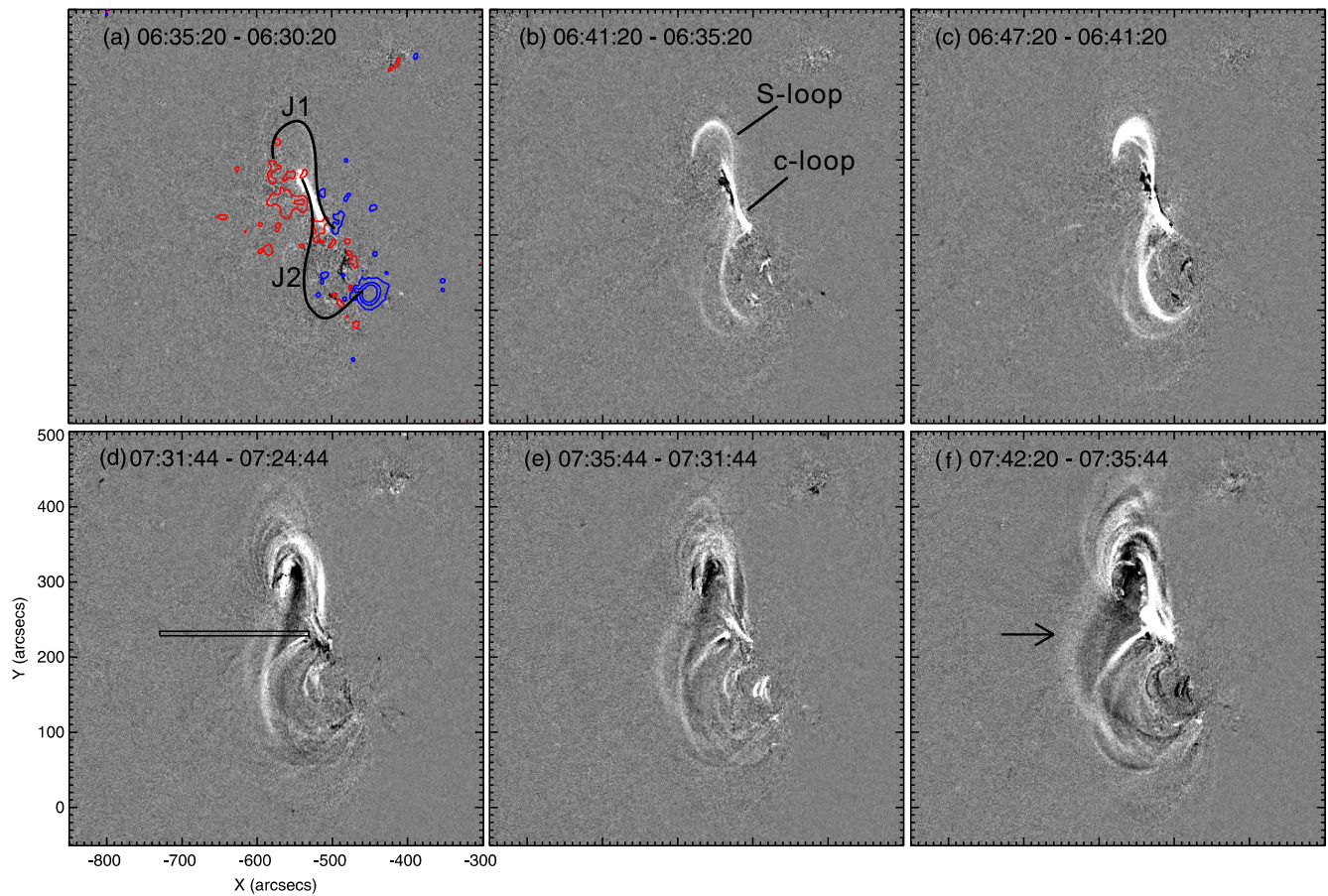


Figure 3. AIA 94 Å difference images, displaying the formation of an S-shaped loop via tether-cutting from two J-shaped loops and its subsequent transformation into a blowing-out bubble marked by an arrow in panel (f). Panel (d) shows the slit through which the space-time diagram in Figure 5(c) is obtained. (A color version of this figure is available in the online journal.)

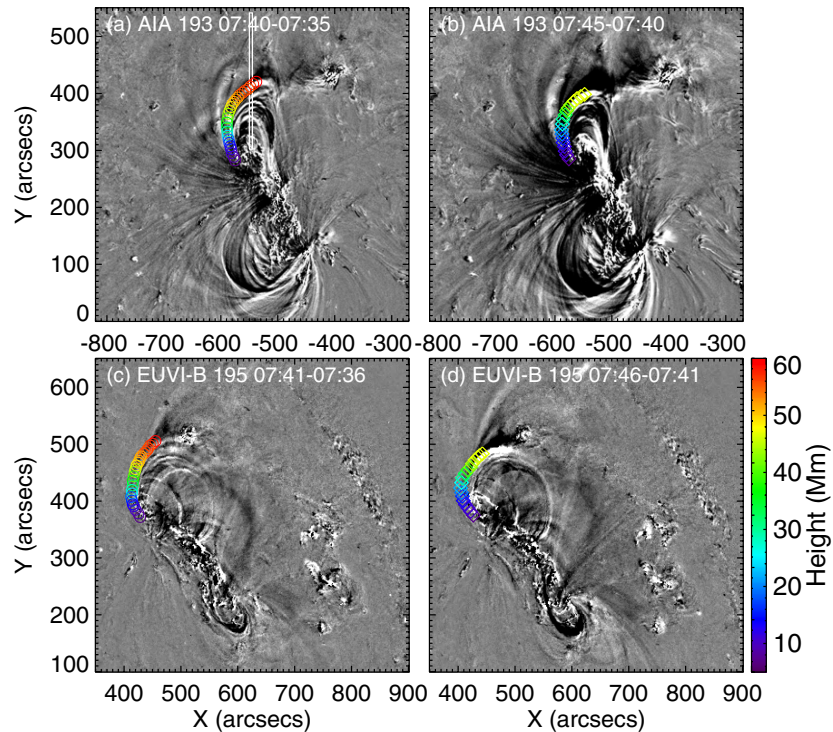


Figure 4. Stereoscopic reconstruction of the contracting loop overlying the northern elbow of the sigmoid. The height information of the loop, which is color coded, is obtained by pairing AIA 193 Å and EUVI-B 195 Å images. Panel (a) shows the slit through which the space-time diagram in Figure 5(b) is obtained. The expanding bubble is also visible in both view points, associated with coronal dimming in AIA 193 Å.

(A color version of this figure is available in the online journal.)

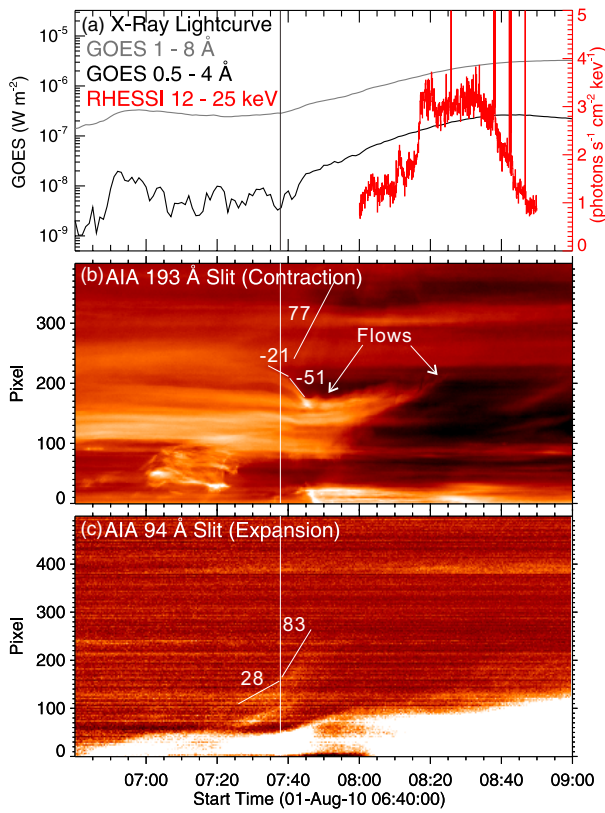


Figure 5. Temporal evolution of the contracting loop and the expanding bubble seen through the slits, in relation to the X-ray emission. Numbers indicate speeds of various features in km s^{-1} . The vertical line marks the transition of the exploding bubble from a slow- to a fast-rise phase.

(A color version of this figure is available in the online journal.)

indeed shows highly sheared field lines near the flaring PIL and potential-like field lines overlying it, similar in morphology to the hot and cold coronal loops, respectively (Figure 2). NLFFF extrapolation using the vector magnetogram at about 01:00 UT on February 15 gives a similar result. The extrapolated field lines are color coded according to the intensity of vertical currents on the surface. Field lines whose footpoints are associated with strong current densities ($>0.02 \text{ A m}^{-2}$) are in red. The footpoints of these red field lines are cospatial with the four footpoint-like flare brightenings in AIA 94 Å images (Liu et al. 2012; Wang et al. 2012).

2.2. 2010 August 1 Event

The eruption in the sigmoidal region NOAA AR 11093 on 2010 August 1 conformed to the classical “sigmoid-to-arcade” transformation (e.g., Moore et al. 2001), i.e., prior to the eruption, the sigmoidal structure consisted of two opposite bundles of J-shaped loops, and after the eruption, it appeared as a conventional post-flare arcade. The evolution in between the two states was revealed in detail for the first time by AIA observations (Liu et al. 2010c). In the AIA 94 Å difference images (Figure 3), one can see that an S-shaped loop started to glow at about 06:40 UT, about 1 hr before the flare onset. As its glowing was preceded by a heating episode in the core region (Figure 3(a)), the topological reconfiguration resulting in the formation of the continuous S-shaped loop was very likely due to the tether-cutting reconnection (Moore et al. 2001). The S-shaped loop remained in quasi-equilibrium in the lower corona for about 50 minutes, with the central dipped portion rising quasi-statically. During this interval, there was a weak enhancement in GOES soft X-rays (SXR), whose source, however, was located at the southeast limb according

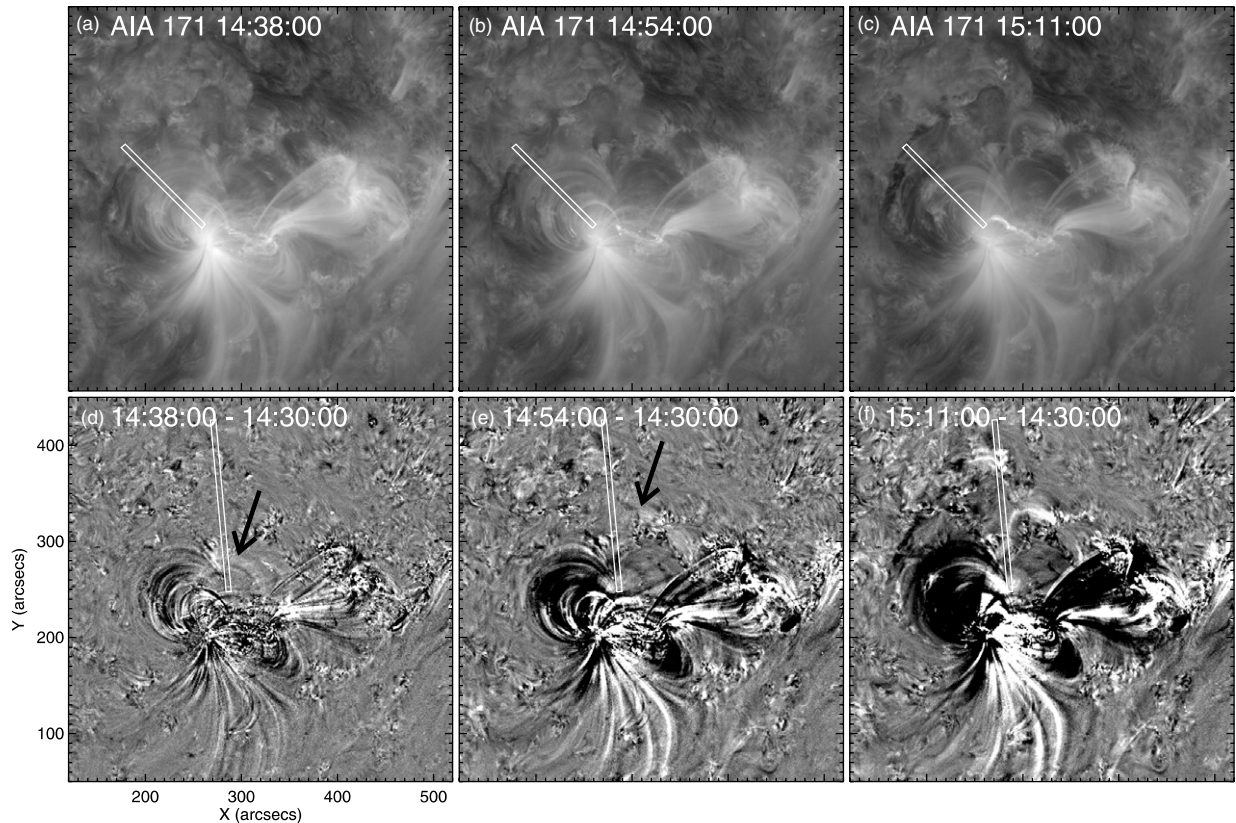


Figure 6. AIA observation of the 2010 September 3 B-flare. Top panels show original 171 Å images and bottom panels show the corresponding difference images. The expanding bubble is indicated by arrows.

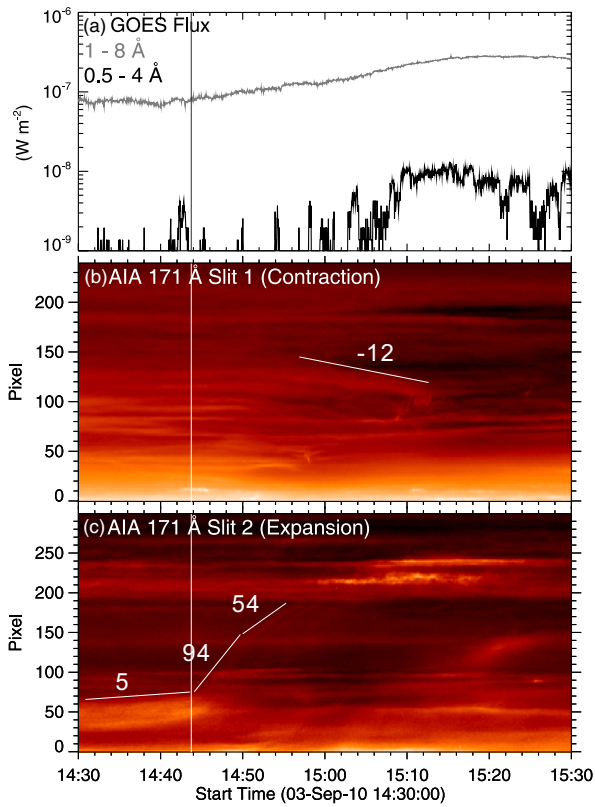


Figure 7. Temporal evolution of the contracting loop and the expanding bubble in relation to the X-ray emission. The space–time diagrams are obtained by stacking image slices cut by the slits shown in Figure 6. The vertical line marks the transition of the exploding bubble from a slow- to a fast-rise phase. (A color version of this figure is available in the online journal.)

to *RHESSI* observations (see Figure 3 in Liu et al. 2010c). At about 07:30 UT, about 10 minutes prior to the onset of the C3.2 flare, the speed increased to tens of kilometers per second, as the S-shaped loop sped up its transformation into an arch-shaped loop, which eventually led to a CME.

During the eruption, a group of coronal loops overlying the northern elbow of the sigmoid was observed to contract in cold AIA channels such as 171 and 193 Å. The contraction was also visible in EUV images taken by the Extreme-Ultraviolet Imager (EUVI; Wuelser et al. 2004) on board the “Behind” satellite of the *Solar Terrestrial Relations Observatory (STEREO-B)*. The viewing angle was separated by about 70° between *SDO* and *STEREO-B*. By pairing EUVI with AIA images, we are able to derive the three-dimensional location of the loop undergoing contraction via a triangulation technique called *tie point* (Inhester 2006), which is implemented in an SSW routine, SCC_MEASURE, by W. Thompson. From the difference images (Figure 4) one can see both the contracting loop, whose height is color coded, and the expanding bubble, which is associated with coronal dimming in AIA 193 Å. With stereoscopic views, it becomes clear that the contraction is not simply a projection effect due to the loops being pushed aside by the expanding bubble.

We place slits across both the contracting loops (Figure 4(a)) and the expanding bubble (Figure 3(d)). By stacking the resultant image cut over time, we obtain space–time diagrams for a series of AIA 193 and 94 Å images at 12 s cadence (Figures 5(b) and (c)). Note that to increase the signal-to-noise ratio, we integrate over the width of the slit (10 pixels), and that to reveal the diffuse, expanding bubble, we carry out base differencing to make the 94 Å space–time diagram, whereas original 193 Å images are used for the contracting loops which are more clearly

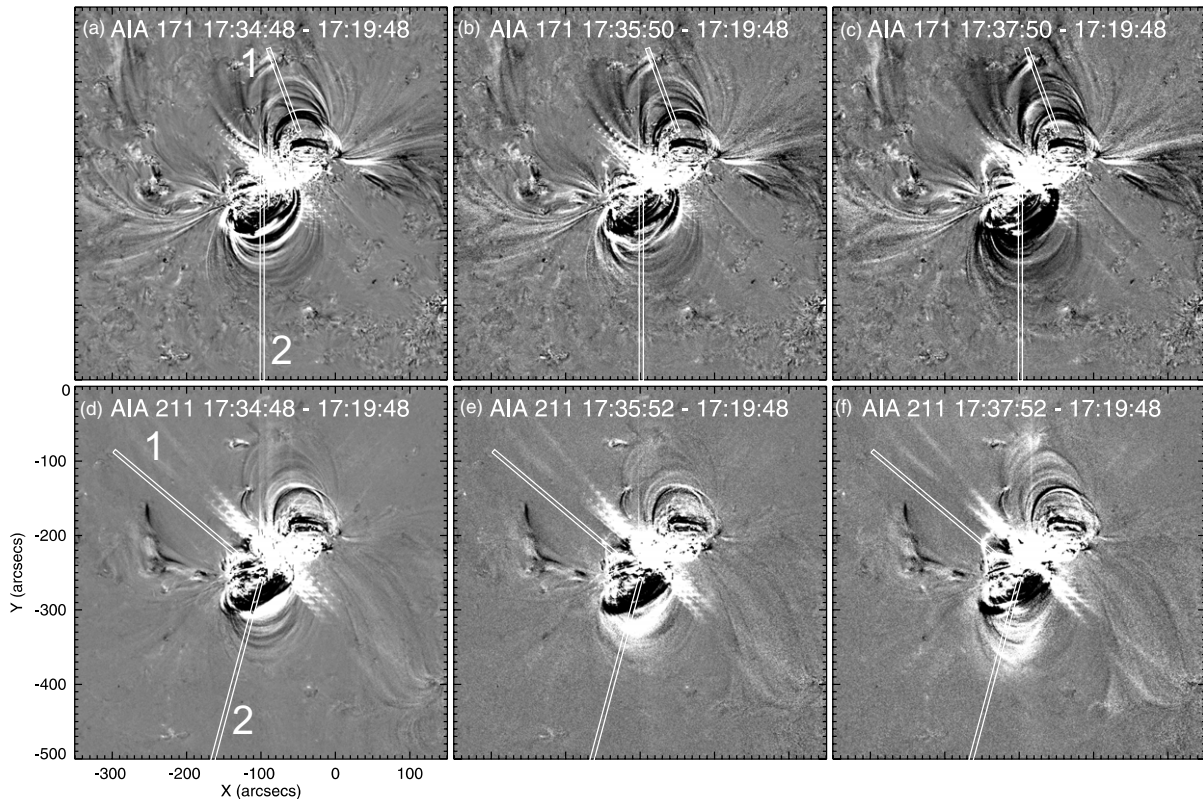


Figure 8. AIA observation of the 2011 February 13 M flare. Top panels show 171 Å difference images and bottom panels 211 Å difference images. An animation of 211 Å images as well as corresponding difference images is available in the online version of the journal. (Animation of this figure is available in the online journal.)

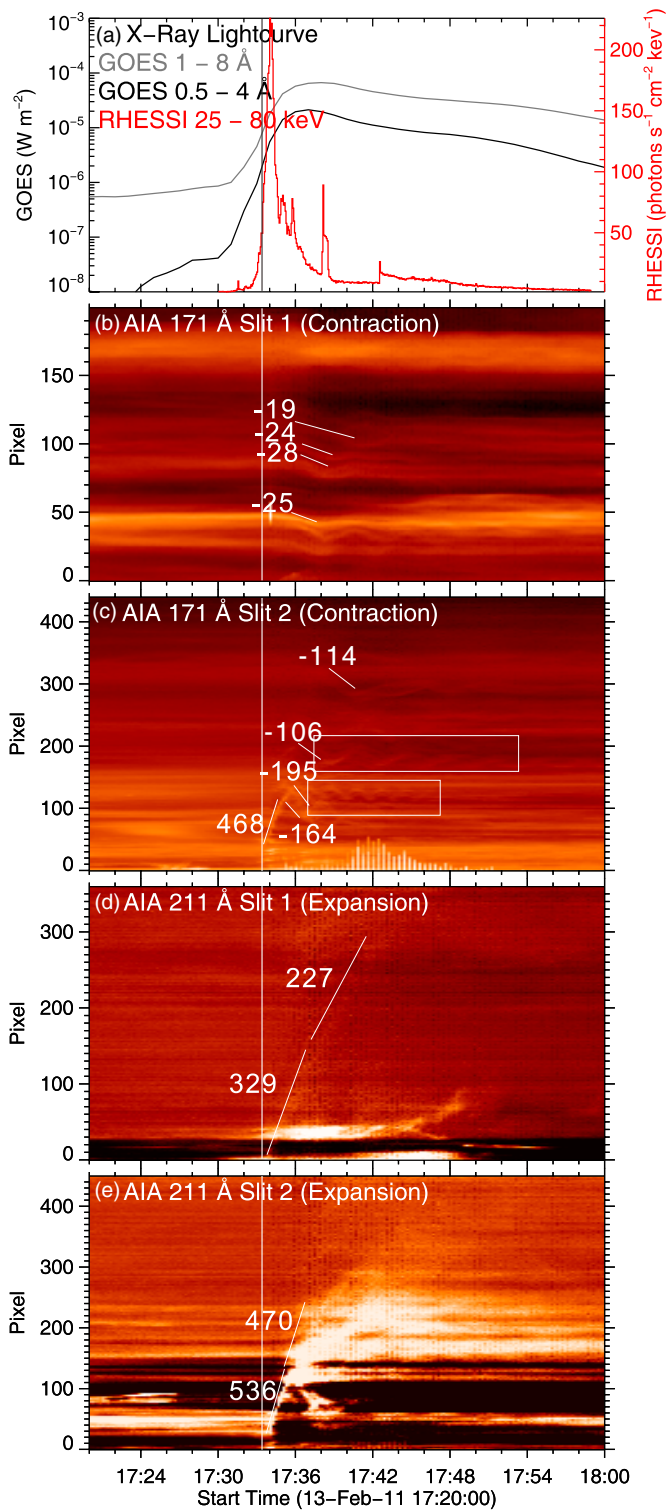


Figure 9. Temporal evolution of the contracting loop and the expanding bubble in relation to the X-ray emission. The space-time diagrams are obtained by stacking image slices cut by the slits as shown in Figure 8. The vertical line marks the beginning of the explosion.

(A color version of this figure is available in the online journal.)

defined in EUV. From Figure 5(c), one can see that the bubble initially rose slowly by $\sim 30 \text{ km s}^{-1}$, and then transitioned into a phase of fast rise by $\sim 80 \text{ km s}^{-1}$ at about 07:38 UT. The height-time profile is piecewise-linear fitted although the transition is smooth and there seems to be continuous acceleration.

The transition time is approximately coincident with the flare onset in terms of the *GOES* 1–8 Å flux. A very diffuse erupting feature can also be marginally seen in the 193 Å space-time diagram, whose speed is similar to the bubble in 94 Å. The contraction of the overlying loops slightly lagged behind the rising of the bubble, and there was a similar transition from slow to fast contraction, slightly lagging behind the speed transition of the bubble by less than three minutes. It is worth noting that the apparently upward-moving feature in the wake of contraction was due to flows along the northern elbow of the sigmoid, not to the recovery of the contracting loops.

2.3. 2010 September 3 Event

In the 2010 September 3 event, both the contracting loops and expanding bubble were visible in the 171 Å channel. But the diffuse bubble can only be seen in the difference images (bottom panels in Figure 6, marked by arrows). The contracting loops were located to the east of the bubble, overlying the eastern elbow of the sigmoid (top panels in Figure 6). Similar to the 2010 August 1 event, in the wake of the bubble erupting, obvious coronal dimming can be seen in the cold AIA channels such as 171 and 193 Å. The dynamics of the bubble can also be characterized by a slow-rise followed by a fast-rise phase, the transition of which coincided with the gradual increase of the *GOES* 1–8 Å flux (Figure 7). The bubble shows a deceleration signature after 14:48 UT. The loop contraction lagged behind the transition time at about 14:44 UT by about 10 minutes.

2.4. 2011 February 13 Event

The 2011 February 13 M6.6 flare was associated with irreversible changes in the photospheric magnetic field (Liu et al. 2012). Using high-resolution and high-precision *Hinode* vector magnetograms and line-of-sight HMI magnetograms, Liu et al. (2012) found that the field change mainly took place in a compact region lying in the center of the sigmoid, where the strength of the horizontal field increased significantly across the time duration of the flare. Moreover, the near-surface field became more stressed and inclined toward the surface while the coronal field became more potential. An intriguing observation is that the current system derived from the extrapolated coronal field above the region with an enhanced horizontal field underwent an apparent downward collapse in the wake of the sigmoid eruption. Liu et al. (2012) concluded that these results are a superimposed effect of both the tether-cutting reconnection producing the flare and the magnetic implosion resulting from the energy release.

Coronal EUV observations agree with the above conclusion drawn from photospheric field measurements regarding magnetic implosion. At the onset of the impulsive phase, two arch-shaped loops originating from the center of the sigmoid were observed to expand outward in 211 Å in different directions (bottom panels of Figure 8) but at similar projected speeds (Figures 9(d) and (e)), while coronal loops overlying both elbows of the sigmoid were observed to contract (top panels of Figure 8), with the loops overlying the eastern elbow contracting much faster (Figures 9(b) and (c)). For this relatively energetic event, the eruption only preceded the contraction by tens of seconds, and the contracting speed becomes as fast as 200 km s^{-1} . In the wake of the contraction, loops overlying the eastern elbow underwent oscillation for several cycles (marked by rectangles in Figure 9), similar to the events studied by Liu & Wang (2010), Gosain (2012), and Kallunki & Pohjolainen (2012). Beyond the

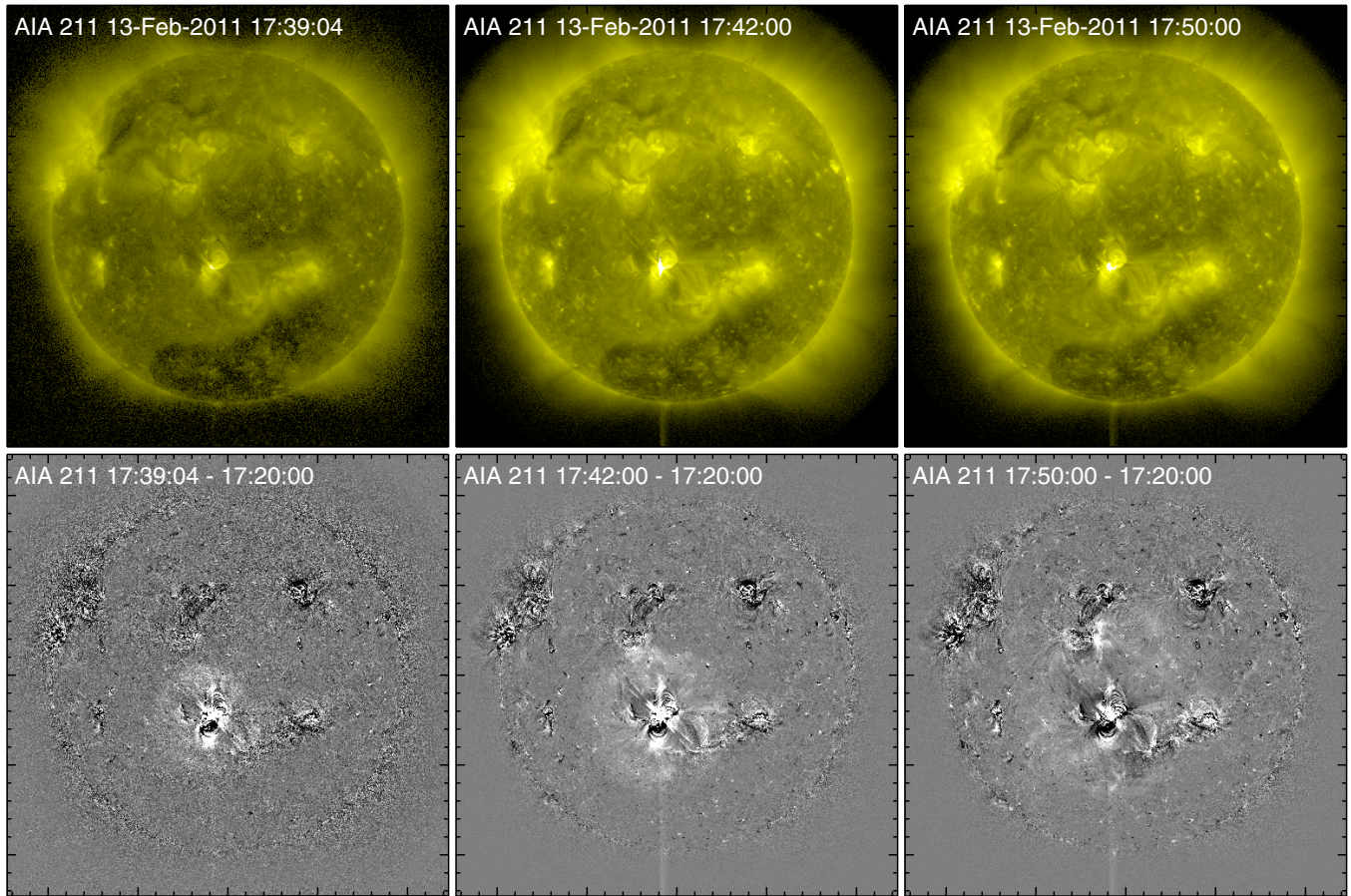


Figure 10. Snapshots of the full-disk AIA 211 Å images (top panels) and the corresponding difference images (bottom panels). In the difference images, a diffuse front can be seen propagating outward from the active region of interest.

(A color version of this figure is available in the online journal.)

expanding loops, one can also see in the animation of the AIA 211 Å difference images (accompanying Figure 8) a diffuse oval front with enhanced intensity propagating outward, well separated from the expanding loops. This oval structure has been identified in MHD simulations as a shell of return currents surrounding the flux rope (Aulanier et al. 2010; Schrijver et al. 2011). From Figure 10 one can see that the front was propagating anisotropically, apparently restrained by nearby active regions and the coronal hole in the southern polar region.

2.5. 2011 February 15 Event

The 2011 February 15 X2.2 flare in AR 11158 is the first X-class flare of the current solar cycle, hence it has generated a lot of interests and has been intensively studied. Kosovichev (2011) reported that the flare produced a powerful “Sunquake” event due to its impact on the photosphere. Wang et al. (2012) reported a rapid, irreversible change of the photospheric magnetic field associated with the flare. Beauger et al. (2012) studied the shear flows along the PIL as well as the white-light flare emission. Schrijver et al. (2011) investigated the coronal transients associated with the flare. In particular, Schrijver et al. (2011, p. 167) observed “expanding loops from a flux-rope-like structure over the shearing PIL between the central δ -spot groups of AR 11158, developing a propagating coronal front (“EIT wave”), and eventually forming the CME moving into the inner heliosphere.” Here the expanding loops are identified as the erupting component.

The active region as seen in the AIA 171 Å channel was dominated by two groups of potential-like loops overlying the elbows of the forward S-shaped sigmoid as seen in the hot AIA channels (Figure 2). Both groups of potential-like loops were observed to contract during the X2.2 flare. In each group, loops underwent contraction successively with those located at lower altitudes starting to contract first, presumably due to the limited propagation speed of the Alfvén wave (see also Liu & Wang 2010; Gosain 2012), whereas loops at higher altitudes had a faster contraction speed (Figures 12(b) and (c)). These contracting/collapsing features were also independently noted by Schrijver et al. (2011), Gosain (2012), and Sun et al. (2012) using different approaches but with similar interpretation, in agreement with Liu & Wang (2009).

Immediately prior to the loop contraction, a bubble (marked by red arcs in the middle panels of Figure 11) can be best seen to originate from the core of the sigmoid and to expand northeastward in the 211 Å channel and southwestward in the 94 Å channel (bottom panels of Figure 11; marked by red arcs). A transition from a slow- to fast-rise phase can still be marginally seen in the 211 Å channel. But the duration of the slow-rise phase was very short, lasting for only about two minutes. The transition time at about 01:50 UT still preceded the loop contraction by about three minutes. The commencement of the bubble expansion at about 01:48 UT was concurrent with the onset of the nonthermal hard X-ray (HXR) emission at 35–100 keV. This expanding bubble was also closely associated with “an expanding intensity front propagating away from the

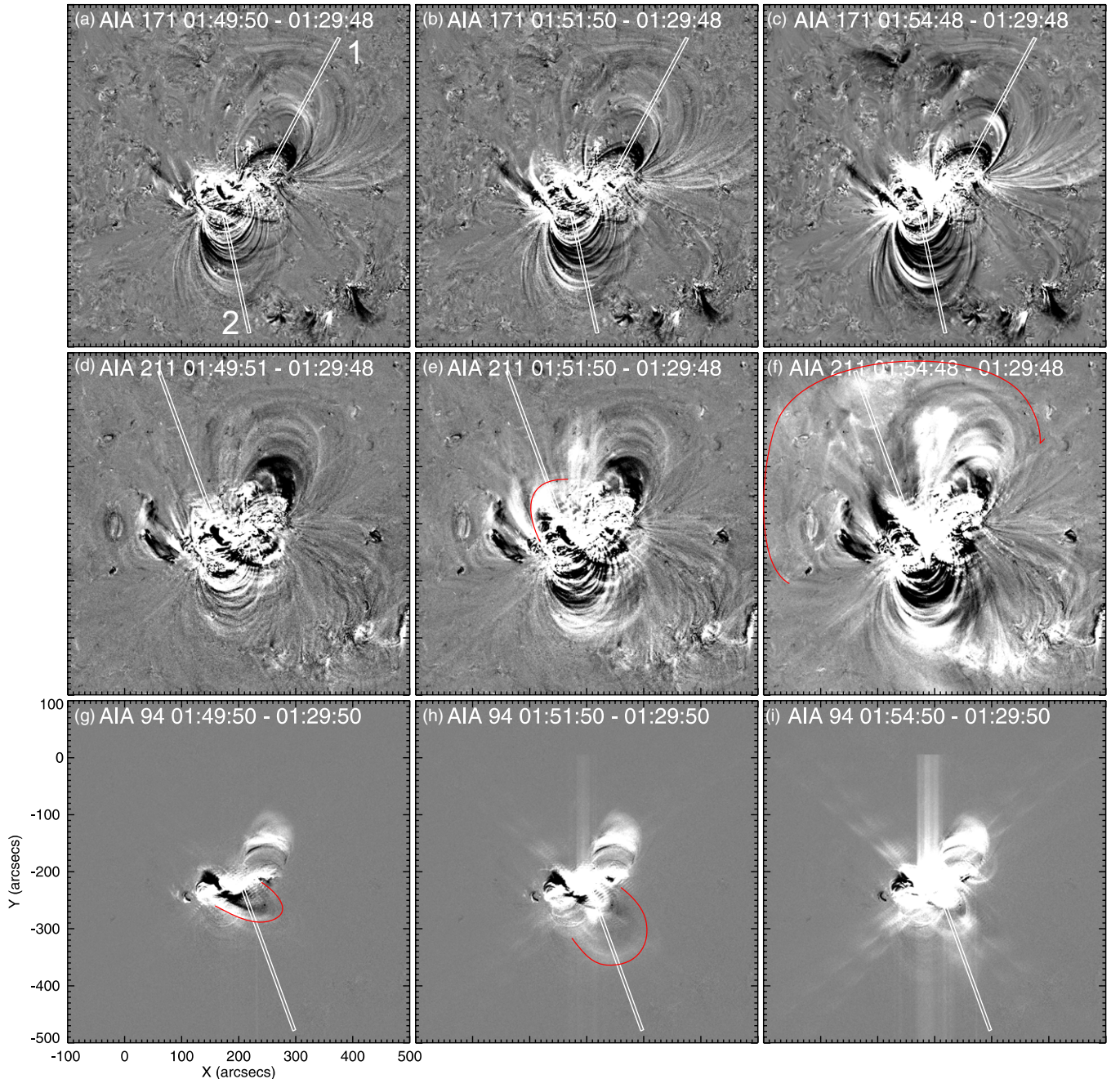


Figure 11. AIA observation of the 2011 February 15 X-flare. From the top, middle, to bottom panels, we show the 171, 211, and 94 difference images, respectively. The expanding bubble is highlighted by red arcs.

(A color version of this figure is available in the online journal.)

flaring region seen on the disk, and the leading edge of the intensity signature of the CME propagating outward from the Sun into the heliosphere,” as identified by Schrijver et al. (2011, p. 181). These three distinct features are suggested to be different observational aspects of the eruption of a flux rope (Schrijver et al. 2011). Similar to the February 13 event, in the wake of the contraction, loops overlying both elbows underwent oscillation (see Figure 12, also see Liu & Wang 2010; Gosain 2012; Kallunki & Pohjolainen 2012).

2.6. 2011 June 21 Event

In the 2011 June 21 event, the group of coronal loops overlying the eastern elbow of the sigmoid was observed to

contract in the 171 Å channel (top panels in Figure 13). At the same time, a bubble originating from the center of the sigmoid was observed to expand eastward in the 94 Å channel (bottom panels in Figure 13). Both the contraction and the expansion occurred prior to the C7.7 flare. The transition time of the bubble from a relatively slow- to a fast-rise phase was roughly coincident with the onset of the flare (Figure 14).

3. DISCUSSION AND CONCLUSION

We have investigated four sigmoidal active regions, in which five eruptions with signatures of magnetic implosion occurred. The magnitudes of the flares associated with the eruptions span almost the whole flare “spectrum,” from *GOES* class B

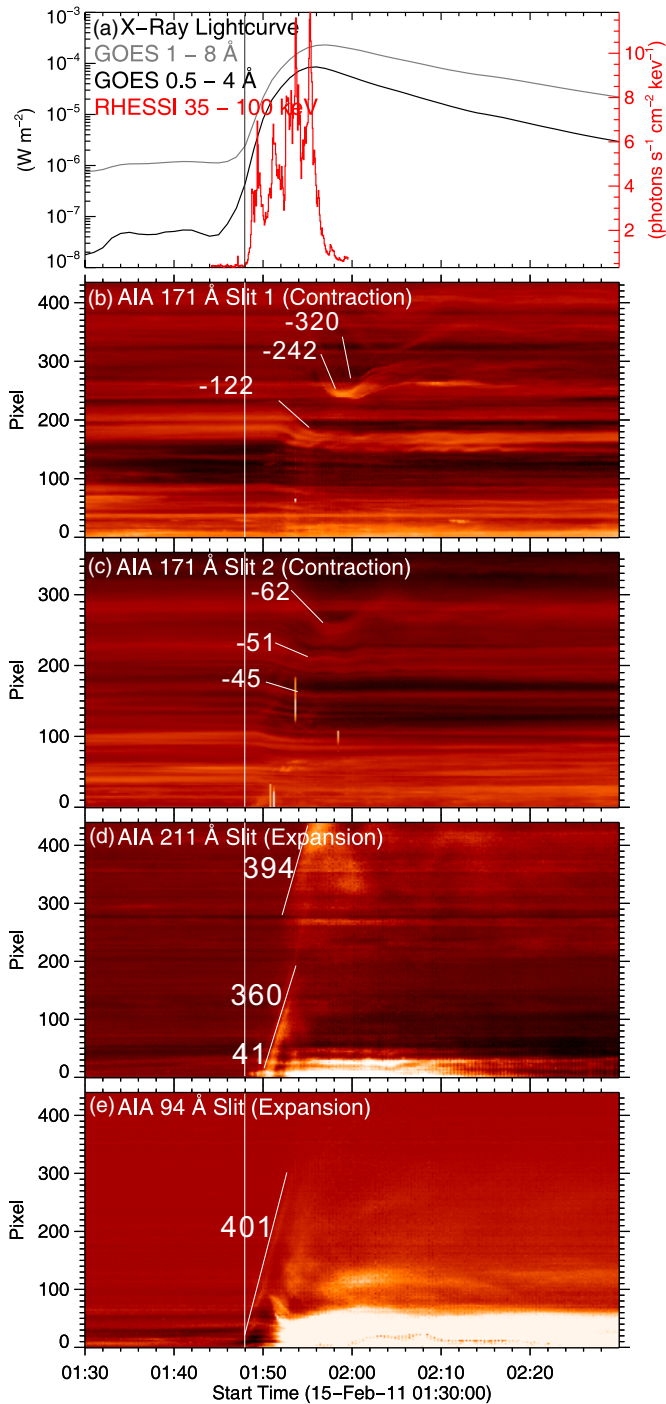


Figure 12. Temporal evolution of the contracting loop and the expanding bubble in relation to the X-ray emission. The space-time diagrams are obtained by stacking image slices cut by the slits as shown in Figure 11. The vertical line marks the beginning of the explosion.

(A color version of this figure is available in the online journal.)

to X. In all of the flares studied, there are both contracting and erupting components: the former is only observed in cold EUV channels and the latter is preferentially visible in warm/hot EUV channels. This is because the contracting component is composed of large-scale, potential-like coronal loops overlying the elbows of the sigmoid, while the erupting component is associated with newly reconnected flux tubes originating from the center of the sigmoid (cf. Liu et al. 2010c; Aulanier et al. 2010; Schrijver et al. 2011). Several important aspects of these observations are discussed as follows.

1. *Consequence of loop contraction.* The overlying loops undergoing contraction never regain their pre-flare positions, which implies a new equilibrium with reduced magnetic energy as the eruption is powered by magnetic energy. One may argue that the apparent contraction of coronal loops could be a projection effect, i.e., the loop plane tilts due to the flare impulse. But in that case, one would expect the restoration of the loops once the flare impulse has passed away. In observations, however, the contracting loops may oscillate about a lower height (e.g., Figure 9; see also Liu & Wang 2010), but never reach the original heights after the eruption. Thus, the contraction within the loop plane must make a significant contribution.
2. *Correlation between contraction and eruption.* The contraction speed seems to depend on the intensity/magnitude of the eruption. From Figure 15, one can see that despite this very small sample size, the peak *GOES* SXR flux as a proxy of the flare magnitude is linearly correlated very well with the measured maximal contraction speed in the log-log plot, although not so well with the maximal erupting speed. Unlike contracting loops which are clearly defined, however, the measurement of the erupting speed involves larger uncertainties as the front of the expanding bubble tends to get more and more diluted and eventually overwhelmed by the background during propagation, thereby leading to underestimation of its speed. One more caveat to keep in mind is that these speeds are not necessarily measured at the time of the peak SXR flux.
3. *Timing.* The eruption precedes the contraction in all of the flares studied, thus establishing loop contraction as a consequence of eruption. There is also a trend that the more energetic the eruption, the smaller the time delay of the loop contraction relative to the onset of the expansion of the erupting component, which is demonstrated in Figure 15 as a strong anti-correlation between the time delay and the peak *GOES* SXR flux in the log-log plot. This time delay is presumably determined by the expansion speed of the erupting component. In addition, in the relatively weak B- and C-flares, the initiation of the erupting component precedes the increase in *GOES* SXR fluxes, but in the stronger M- and X-flares, it is concurrent with the increase in nonthermal HXR fluxes. This may lend support to Lin (2004), who concluded that CMEs are better correlated with flares if there is more free energy available to drive the eruption. However, since the CME progenitor, i.e., the expanding bubble, forms before the flare onset as the weak events clearly demonstrate, the CME must be independent of the conventionally defined flare, or, the flare is only a byproduct of the CME, unless the eruption mechanism for the weak events is different from that for the energetic ones.
4. *Asymmetry of contraction.* The two groups of coronal loops overlying the elbows of the sigmoid often contract asymmetrically, i.e., not only do they contract at different speeds but either group could show little sign of contraction, which depends on the detailed interaction between the core field and the arcade field, including, presumably, their relative strength and the spatial distribution of the decay index of the restraining field (Kliem & Török 2006; Liu et al. 2009a, 2010a). For the 2010 August 1 event in particular, Liu et al. (2010c) concluded that the majority of the flare loops were formed by the reconnection of the stretched legs of the less sheared loops overlying the southern elbow and the center of the sigmoid, based on the reconnection rate

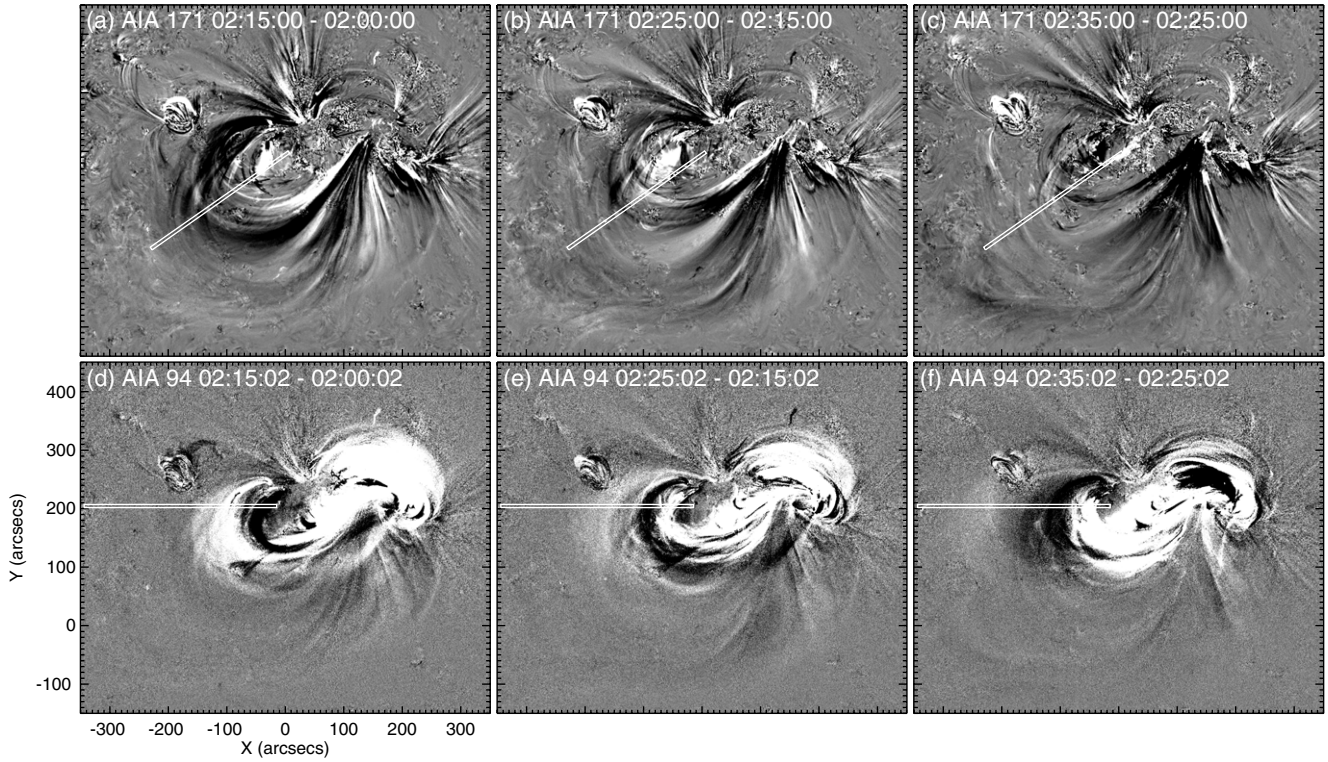


Figure 13. AIA observation of the 2011 June 21 C-flare. The top panels show the 171 Å difference images and the bottom panels the 94 Å difference images.

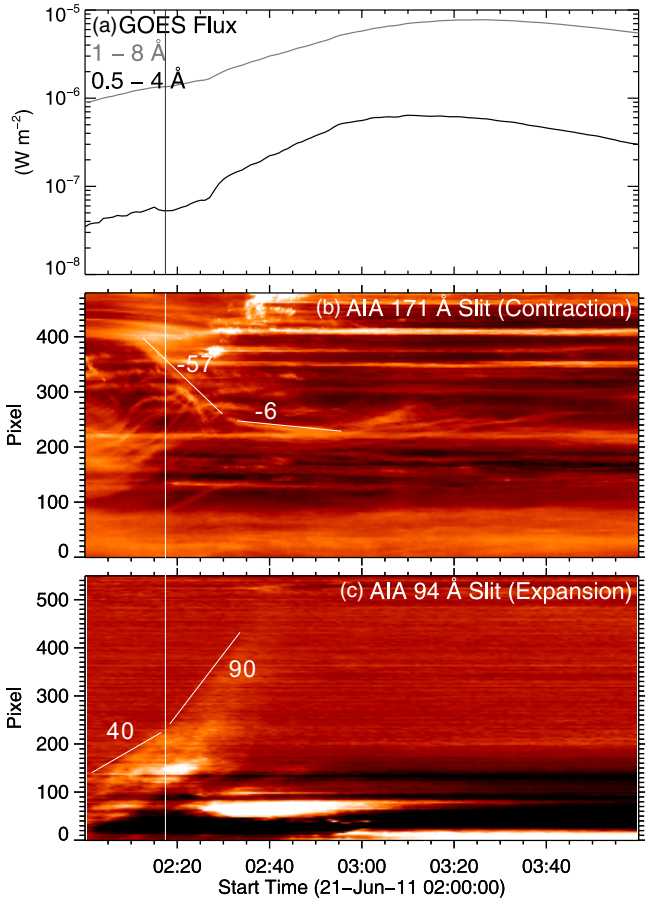


Figure 14. Temporal evolution of the contracting loops and the expanding bubble in relation to the X-ray emission. The space-time diagrams are obtained by stacking image slices cut by the slits as shown in Figure 13. The vertical line marks the transition of the exploding bubble from a slow- to a fast-rise phase. (A color version of this figure is available in the online journal.)

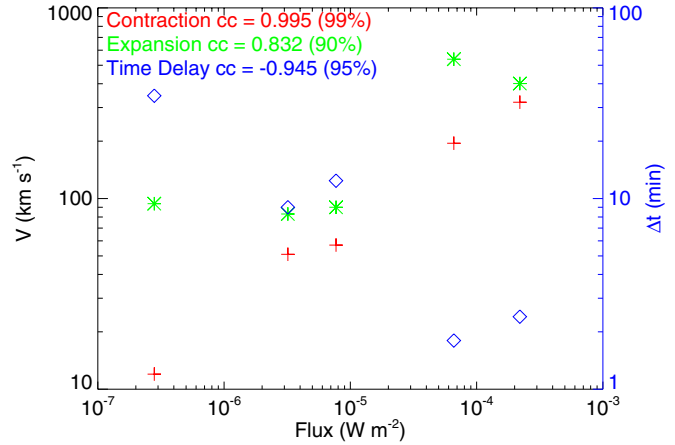


Figure 15. Correlation of the maximal contraction/expansion speed, V , and the time delay of contraction relative to expansion, Δt , with the flare magnitude in terms of the peak *GOES* 1–8 Å flux. The confidence level of the linear correlation coefficient, cc , of $\log(V)$ and $\log(\Delta t)$ with $\log(F)$ is given in the brackets. (A color version of this figure is available in the online journal.)

inferred from the $H\alpha$ ribbon motion. The eruption therefore left most loops overlying the northern elbow unopened. This explains why only these loops underwent obvious contraction. The intensity/magnitude of the eruption could be another relevant factor as among the events studied only those greater than M class show contraction of loops overlying both elbows of the sigmoid.

5. *Implication for eruption mechanism.* As the contracting component is distinct from the erupting component, we conclude that these eruptions conform to the “rupture model” in which the arcade field is partially opened (Sturrock et al. 2001; Figure 1(b)). We can further exclude the breakout model because the coronal loops undergoing

contraction are arched over, rather than located to the side of, the sheared core field. The loop contraction in the latter occasion results from reconnection at the magnetic null above the central lobe in the breakout model.

In conclusion, these observations substantiate that loop contraction is an integrated process in eruptions of sigmoidal active regions in which the restraining arcade field is only partially opened, consistent with theoretical expectations. The consequence of loop contraction is a new equilibrium of the coronal field with reduced magnetic energy, and the process itself is a result of the flare energy release, as evidenced by the strong correlation of the maximal contracting speed, and strong anti-correlation of the time delay of contraction relative to expansion, with the peak SXR flux.

The authors are grateful to the *SDO*, *STEREO*, and *RHESSI* teams for the free access to the data and the development of the data analysis software. R.L. acknowledges the Thousand Young Talents Program of China. R.L. and Y.W. were supported by grants from NSFC 41131065 and 41121003, 973 key project 2011CB811403, CAS Key Research Program KZZD-EW-01-4, and the fundamental research funds for the central universities WK2080000031. R.L., C.L., and H.W. were supported by NSF grants ATM-0849453 and ATM-0819662. The contribution of T.T. was supported by CISM (an NSF Science and Technology Center).

REFERENCES

- Antiochos, S. K., DeVore, C. R., & Klimchuk, J. A. 1999, *ApJ*, 510, 485
- Aulanier, G., Török, T., Démoulin, P., & DeLuca, E. E. 2010, *ApJ*, 708, 314
- Beauregard, L., Verma, M., & Denker, C. 2012, *Astron. Nachr.*, 333, 125
- Canfield, R. C., Hudson, H. S., & McKenzie, D. E. 1999, *Geophys. Res. Lett.*, 26, 627
- Cheng, X., Zhang, J., Liu, Y., & Ding, M. D. 2011, *ApJ*, 732, L25
- Chen, P. F., & Shibata, K. 2000, *ApJ*, 545, 524
- Forbes, T. G. 2000, *J. Geophys. Res.*, 105, 23153
- Forbes, T. G., & Acton, L. W. 1996, *ApJ*, 459, 330
- Gibson, S. E., & Fan, Y. 2006, *ApJ*, 637, L65
- Glover, A., Ranns, N. D. R., Harra, L. K., & Culhane, J. L. 2000, *Geophys. Res. Lett.*, 27, 2161
- Gosain, S. 2012, *ApJ*, 749, 85
- Hoeksema, et al. 2012, *Sol. Phys.*, to be submitted
- Hudson, H. S. 2000, *ApJ*, 531, L75
- Hudson, H. S., Lemen, J. R., St. Cyr, O. C., Sterling, A. C., & Webb, D. F. 1998, *Geophys. Res. Lett.*, 25, 2481
- Inhester, B. 2006, arXiv:astro-ph/0612649
- Kallunki, J., & Pohjolainen, S. 2012, *Sol. Phys.*, 122
- Kliem, B., & Török, T. 2006, *Phys. Rev. Lett.*, 96, 255002
- Kopp, R. A., & Pneuman, G. W. 1976, *Sol. Phys.*, 50, 85
- Kosovichev, A. G. 2011, *ApJ*, 734, L15
- Lemen, J. R., Title, A. M., Akin, D. J., et al. 2012, *Sol. Phys.*, 275, 17
- Lin, J. 2004, *Sol. Phys.*, 219, 169
- Liu, C., Deng, N., Liu, R., et al. 2012, *ApJ*, 745, L4
- Liu, C., Lee, J., Jing, J., et al. 2010a, *ApJ*, 721, L193
- Liu, R., Alexander, D., & Gilbert, H. R. 2009a, *ApJ*, 691, 1079
- Liu, R., Liu, C., Park, S.-H., & Wang, H. 2010b, *ApJ*, 723, 229
- Liu, R., Liu, C., Wang, S., Deng, N., & Wang, H. 2010c, *ApJ*, 725, L84
- Liu, R., & Wang, H. 2009, *ApJ*, 703, L23
- Liu, R., & Wang, H. 2010, *ApJ*, 714, L41
- Liu, R., Wang, H., & Alexander, D. 2009b, *ApJ*, 696, 121
- Moore, R. L., Sterling, A. C., Hudson, H. S., & Lemen, J. R. 2001, *ApJ*, 552, 833
- Pesnell, W. D., Thompson, B. J., & Chamberlin, P. C. 2012, *Sol. Phys.*, 275, 3
- Rachmeler, L. A., DeForest, C. E., & Kankelborg, C. C. 2009, *ApJ*, 693, 1431
- Scherrer, P. H., Schou, J., Bush, R. I., et al. 2012, *Sol. Phys.*, 275, 207
- Schrijver, C. J., Aulanier, G., Title, A. M., Pariat, E., & Delannée, C. 2011, *ApJ*, 738, 167
- Sturrock, P. A., Weber, M., Wheatland, M. S., & Wolfson, R. 2001, *ApJ*, 548, 492
- Sun, X., Hoeksema, J. T., Liu, Y., et al. 2012, *ApJ*, 748, 77
- Wang, S., Liu, C., Liu, R., et al. 2012, *ApJ*, 745, L17
- Wiegmann, T. 2004, *Sol. Phys.*, 219, 87
- Wiegmann, T., Inhester, B., & Sakurai, T. 2006, *Sol. Phys.*, 233, 215
- Wuelser, J.-P., Lemen, J. R., Tarbell, T. D., et al. 2004, *Proc. SPIE*, 5171, 111

MAGNETOHYDRODYNAMIC SIMULATIONS OF INTERPLANETARY CORONAL MASS EJECTIONS

ROBERTO LIONELLO, COOPER DOWNS, JON A. LINKER, TIBOR TÖRÖK, PETE RILEY, AND ZORAN MIKIĆ
Predictive Science, Inc., 9990 Mesa Rim Road, Suite 170, San Diego, CA 92121-2910, USA; lionel@predsci.com, cdowns@predsci.com,
linker@predsci.com, tibor@predsci.com, pete@predsci.com, mikic@predsci.com
Received 2013 July 5; accepted 2013 September 4; published 2013 October 17

ABSTRACT

We describe a new MHD model for the propagation of interplanetary coronal mass ejections (ICMEs) in the solar wind. Accurately following the propagation of ICMEs is important for determining space weather conditions. Our model solves the MHD equations in spherical coordinates from a lower boundary above the critical point to Earth and beyond. On this spherical surface, we prescribe the magnetic field, velocity, density, and temperature calculated typically directly from a coronal MHD model as time-dependent boundary conditions. However, any model that can provide such quantities either in the inertial or rotating frame of the Sun is suitable. We present two validations of the technique employed in our new model and a more realistic simulation of the propagation of an ICME from the Sun to Earth.

Key words: magnetohydrodynamics (MHD) – solar wind – Sun; coronal mass ejections (CMEs)

Online-only material: color figures

1. INTRODUCTION

Interplanetary coronal mass ejections (ICMEs) are the solar-wind counterpart of coronal mass ejections (CMEs), which are huge bursts of solar material released from the corona of the Sun (for a comprehensive review of theory and observations, see Kunow et al. 2006). After approximately one to four days after a CME eruption, an ICME may reach Earth, interact with the geomagnetic field, and cause a geomagnetic storm (Gosling 1990) if the direction of the field in the cloud is opposite (southward) with respect of that of the Earth (Burlaga et al. 1987). Therefore, knowing the structure of the magnetic field of an ICME is of fundamental importance for predicting its geoeffectiveness. CMEs are typically associated with flux ropes, but their magnetic geometry, when they arrive at Earth as ICMEs, is less clear (e.g., Vourlidas et al. 2013). Some ICMEs are observed in situ as so-called magnetic clouds, defined as regions of low proton temperature, enhanced magnetic field strength, and smooth rotation of the magnetic field vector (e.g., Burlaga et al. 1982), the latter indicating flux-rope geometry. Gosling et al. (1991) estimated that about one third of all ICMEs contain a magnetic cloud or flux rope, although this fact may vary systematically with the solar cycle (Riley et al. 2006). Some ICME ejecta have multiple magnetic clouds (i.e., a single structure with multiple subclouds distinguishable, Wang et al. 2002, 2003), the likely result of the interaction of several CMEs.

Given the importance of ICMEs for determining space weather conditions, several computational models have been developed to study their propagation in space. Although a few attempts have been made to simulate the origin of a CME on the Sun and its propagation as an ICME simultaneously (Usmanov & Dryer 1995; Wu et al. 1999; Groth et al. 2000; Manchester et al. 2006; Feng et al. 2010), this approach is very challenging for computational reasons. First, the solar corona and the heliosphere have remarkably different physical properties, resulting in a much smaller integration time step in coronal simulations compared with heliospheric simulations. Hence, a heliospheric computation costs a small fraction of a coronal calculation. Moreover, it is often the case that several coronal simulations are necessary to explore parameter space prior to modeling the full propagation. On the other hand,

boundary conditions for a heliospheric model are relatively straightforward to implement beyond the critical MHD wave points. These boundary conditions can be obtained from the upper boundary of a coronal model extending just above the critical points. Therefore, a two-model integrated approach, where a coronal calculation acts as a driver for the heliospheric evolution, is more widespread. Riley et al. (2001b) integrated three-dimensional (3D) MHD models of the solar corona and heliosphere. They used a line-of-sight magnetogram as input to the coronal model and they first determined the steady-state solar wind at $30 R_{\odot}$ during various solar phases of activity. Then, they used those values to drive the heliospheric model and calculate the structure of the solar wind out to 5 AU. Since the boundary conditions for this model are not time dependent, its applicability to the study of ICMEs is limited. Odstrcil et al. (2002) and Riley et al. (2003) studied the disruption of a sheared helmet streamer, which launches a CME, with a 2D MHD coronal model. Then, they used the time-dependent boundary conditions at the outer surface of the coronal solution to drive a 2D MHD heliospheric calculation of the propagation of the CME in interplanetary space. This model (Enlil) was later extended to 3D and showed how it could accept input data from empirical, observational, and numerical coronal models (Odstrcil et al. 2003, 2008). However, the present version of the model at the Community Coordinated Modeling Center¹ does not accept evolving, time-dependent boundary conditions for the magnetic field at the surface beyond the critical points. Another limitation of the Enlil model is that it does not have 4π spatial coverage (i.e., 4π steradian coverage of the spherical computational domain), an important requirement for the study of ICME propagation according to Kleimann (2012). The model of Usmanov & Goldstein (2006) combines an inner region MHD solution from 1 to $20 R_{\odot}$ with a 3D outer solution, which is constructed by forward integration along the hyperbolic radial coordinate and extends from $20 R_{\odot}$ to 10 AU. This model does not include the capability to evolve the boundary conditions during the simulations. Tóth et al. (2005, 2012) presented the Space Weather Modeling Framework (SWMF), an integrated suite of numerical tools that includes, among others, coupled

¹ <http://ccmc.gsfc.nasa.gov>

models of the solar corona and heliosphere. This framework was used, for example, by Lugaz et al. (2007) to study three CMEs originating from active region 9236 as they propagate from the Sun to the Earth. Notwithstanding the great flexibility of the SWMF, its single components are meant to be used in conjunction with one another and it requires additional software modules to be created for each additional third-party coronal model (Tóth et al. 2005, 2012). Other MHD models of ICME propagation used a steady-state ambient solar wind, which was either derived from an MHD coronal solution (Odstroil et al. 2004) or prescribed (Odstroil et al. 2005; Merkin et al. 2011) from the empirical Wang–Sheeley–Arge Model (WSA) model (Wang & Sheeley 1995; Arge & Pizzo 2000). The so-called cone model (Zhao et al. 2002) can be used to calculate the ICME parameters kinematically, which can be inserted into the precalculated, steady-state background. Although useful and simple to operate, the cone model does not include a flux rope and cannot provide real interplanetary magnetic field predictions for physical quantities inside the ICME. The MHD model of the solar wind presented in Hayashi (2012) does use time-dependent boundary conditions, which are determined from the solar magnetic field and interplanetary scintillation observations as input at the spherical surface beyond the critical points. Although it can also be coupled with cone models of CMEs, it does not accept the output of coronal MHD models of the initiation and early stages of propagation of CMEs as a driver at the lower boundary.

The purpose of this paper is to illustrate the details of an MHD model that provides the evolution of density, temperature, velocity, and magnetic field of ICMEs, to present validation examples of our technique; and to describe a more realistic calculation based on the interplanetary propagation of the coronal model of CME initiation by T. Török et al. (in preparation; see Section 4). Our heliospheric model is derived from the coronal model of Lionello et al. (2009), building on the work of Riley et al. (2001b). It has been designed to include capabilities that are not found together in any other single available model: (1) it is fully 3D MHD and covers the whole 4π (i.e., the polar regions are included); (2) it accepts time-dependent boundary conditions at the lower surface, making it suitable both for studies of solar-wind evolution and ejecta propagation; (3) the driver at the lower surface is flexible enough to use data obtained either from other models (coronal MHD or empirical) or from observations; these data may have been calculated either in the inertial or rotating frame of the Sun; and (4) the computation itself can be implemented either in the inertial or in the rotating frame of reference.

This paper is organized as follows. The equations and the solution technique are described in Section 2. Then, in Section 3, two validation examples are shown, one in the non-rotating frame and one in the rotating frame of reference. The description of the more realistic case is contained in Section 4, which is followed by our conclusions.

2. MODEL

Here we present the equations that are advanced numerically in our model and how the time-dependent boundary conditions are implemented in a flexible way.

2.1. MHD Equations

Our model of ICME propagation is derived from the 3D, time-dependent, MHD model of Lionello et al. (2009), the numerical details of which were presented in Lionello et al. (1998, 1999)

and Mikić et al. (1999). In a computational domain extending between $r_{\min} \leq r \leq r_{\max}$, the following set of partial differential equations in spherical coordinates are solved:

$$\nabla \times \mathbf{B} = \frac{4\pi}{c} \mathbf{J}, \quad (1)$$

$$\nabla \times \mathbf{A} = \mathbf{B}, \quad (2)$$

$$\frac{\partial \mathbf{A}}{\partial t} = \mathbf{v} \times \mathbf{B} - \frac{c^2 \eta}{4\pi} \nabla \times \mathbf{B}, \quad (3)$$

$$\frac{\partial \rho}{\partial t} + \nabla \cdot (\rho \mathbf{v}) = 0, \quad (4)$$

$$\frac{1}{\gamma - 1} \left(\frac{\partial T}{\partial t} + \mathbf{v} \cdot \nabla T \right) = -T \nabla \cdot \mathbf{v} + \frac{m}{k\rho} S, \quad (5)$$

$$\rho \left(\frac{\partial \mathbf{v}}{\partial t} + \mathbf{v} \cdot \nabla \mathbf{v} \right) = \frac{1}{c} \mathbf{J} \times \mathbf{B} - \nabla p + \rho \mathbf{g} + \nabla \cdot (\nu \rho \nabla \mathbf{v}) + \mathbf{F}_{\text{fict}}, \quad (6)$$

where \mathbf{B} is the magnetic field, \mathbf{J} is the electric current density, \mathbf{A} is the vector potential, ρ , \mathbf{v} , p , and T are the plasma mass density, velocity, pressure, and temperature, respectively, $\mathbf{g} = -g_0 R_\odot^2 \hat{\mathbf{r}}/r^2$ is the gravitational acceleration, η the resistivity, and ν is the kinematic viscosity. In the inertial frame of reference, the fictitious force term, \mathbf{F}_{fict} , is absent. In the rotating frame of reference, we have

$$\mathbf{F}_{\text{fict}} = \rho (2\boldsymbol{\Omega} \times \mathbf{v} + \boldsymbol{\Omega} \times (\boldsymbol{\Omega} \times \mathbf{v})). \quad (7)$$

Here, the first term of the right hand side is the Coriolis force, while the second term is the centrifugal force. Both depend on the angular velocity $\boldsymbol{\Omega}$. S in Equation (5) represents the energy source term. Although in future studies we plan to explore the use of the full thermodynamic treatment of Lionello et al. (2009), which includes collisionless thermal conduction, in this work we use the so-called polytropic approximation as in Linker et al. (2003), which prescribes a simple adiabatic energy equation (i.e., $S = 0$, which is appropriate in the heliosphere), and choose a suitable value for γ (generally, 1.5; Totten et al. 1996; Feldman et al. 1998).

2.2. Boundary Conditions

The method used to specify the boundary conditions in the heliospheric model is determined not only by the requirements of the heliospheric calculation itself but also by the characteristics of the coronal model that provides the data. For maximum flexibility, we allow the calculation to be either in the corotating or inertial frame of reference in either model. However, we foresee that our typical coupled calculation will be in the corotating frame for the corona and in the inertial frame for the heliosphere. Moreover, we want to be able to use coronal calculations performed in the corotating frame of reference, without including the contribution of the fictitious forces of Equation (7).

In specifying the boundary conditions in our model, we also need to ensure that the problem is well posed by examining the characteristic curves associated with the system (e.g., Jeffrey 1966, p. 122). At the lower boundary of coronal models, only some of the seven characteristic curves of MHD are outgoing (e.g., Lionello et al. 2009). Hence, there is an upper limit on

how many fields may be prescribed as boundary conditions at the lower spherical surface r_{\min} , while the rest are to be determined by solving the characteristic equations. On the contrary, in a heliospheric model, since the plasma is supersonic and super-Alfvénic, all scalar and vector fields must be specified, provided that the solenoidal property of the magnetic field, $\nabla \cdot \mathbf{B} = 0$, is preserved. To model ejecta propagation and solar wind variations, the values at $r = r_{\min}$ of ρ , T , \mathbf{B} , and \mathbf{v} must be generally specified as functions of latitude, longitude, and time (θ, ϕ, t) . The quantities are either extracted from a spherical shell in a coronal MHD calculation (provided it is chosen beyond the critical points), from an empirical model such as WSA, from a combination of MHD and empirical models (Riley et al. 2001b), or, in principle, from suitable observations. Transformations in coordinates with linear interpolation of all the fields in the three variables (θ, ϕ, t) are needed to account for differences in the structure of the grid and temporal sampling between our heliospheric model and the model from which the boundary values are obtained. Depending on whether the calculation providing the boundary conditions is in the same frame of reference of the heliospheric model or not, an additional interpolation in ϕ may be necessary to account for rotation:

$$f'(\theta, \phi, t) = f(\theta, \phi \pm \Omega t, t), \quad (8)$$

where f is ρ , T , or one of the components of \mathbf{v} and \mathbf{B} at the boundary. The minus sign is used when the boundary conditions are extracted from a corotating frame and are used in an inertial frame; the plus sign is used when the calculation is in the corotating frame and the boundary conditions are provided in an inertial frame. Finally, a frame of reference transformation is applied to v'_ϕ :

$$v_\phi^{(\text{helio})} = v'_\phi \pm \Omega r_{\min} \sin \theta. \quad (9)$$

However, when the boundary conditions are extracted from a corotating model that neglects the effects of fictitious forces, this transformation is applied only when calculating the electric field, as explained below.

Although the transformed ρ , T , and \mathbf{v} may be directly used as time-dependent boundary conditions, the boundary condition for the induction equation, Equation (3), requires knowledge of the electric field, $\mathbf{E} = -\mathbf{v} \times \mathbf{B}$. Hence, we use the following approach, which accurately represents the interpolated \mathbf{E} field on the new grid and automatically preserves the solenoidal properties of \mathbf{B} . The radial component of the electric field, E_r , at the boundary can be readily inserted to calculate the evolution of the radial component of the vector potential, A_r . This is not the case for the tangential components $\mathbf{E}_t = (E_\theta, E_\phi)$, because linear interpolation, when second derivatives are calculated, may introduce strong currents near the poles. To avoid this, we rewrite \mathbf{E}_t as the sum of two arbitrary potentials $\Psi(\theta, \phi)$ and $\Phi(\theta, \phi)$:

$$\mathbf{E}_t = \nabla_t \times \Psi \hat{\mathbf{r}} + \nabla_t \Phi. \quad (10)$$

∇_t indicates tangential derivatives in (θ, ϕ) . The potential Ψ controls the change of the radial component of the magnetic field, $B_r(\theta, \phi, t)$, and can be obtained by inverting

$$\nabla_t^2 \Psi = \frac{\partial B_r}{\partial t}. \quad (11)$$

The second potential Φ controls the shearing of the magnetic field and does not change B_r . It is obtained by solving the following equation:

$$\nabla_t^2 \Phi = -\nabla_t \cdot (\mathbf{v} \times \mathbf{B})_t, \quad (12)$$

where the transformation of Equation (9) is applied to the longitudinal component of \mathbf{v} if the boundary conditions are extracted from a corotating model that neglects the effect of fictitious forces. Since $-\nabla^2$ is a symmetric, positive-definite operator, we discretize the operator on the (θ, ϕ) grid and invert it using a conjugate-gradient algorithm to obtain Ψ and Φ . Once we know the two potentials, we retrieve \mathbf{E}_t and apply it as boundary condition for \mathbf{A}_t , assuming that the contribution of the resistive term in Equation (3) is negligible.

3. VALIDATION OF THE TECHNIQUE

Here, we present two validation examples of our heliospheric model, one computed for the case $\Omega = 0$ and one that accounts for solar rotation. Coronal simulations are first performed to provide the boundary conditions to drive the heliospheric model. These field values are extracted from a spherical surface within the coronal model so that there may be a partial superposition between the coronal and heliospheric computational domains. Thus, a comparison between the coronal and heliospheric calculations is possible. We simulate a CME eruption using the 3D MHD coronal model of Lionello et al. (2009) in the polytropic approximation, as it was employed by Linker et al. (2003). The computational domain extends from 1 to $50 R_\odot$ and is discretized on a non-uniform $200 \times 150 \times 200$ mesh in (r, θ, ϕ) . The radial resolution varies between $0.01 R_\odot$ at the solar surface to $0.9 R_\odot$ at the outer boundary. The minimum and maximum sizes of the longitudinal and latitudinal grids are $0''.7$ and $4''.7$, respectively, with the points concentrated in the area where the CME erupts. We have prescribed a uniform resistivity profile such that the ratio of the resistive dissipation time with the Alfvén wave propagation time is $\tau_R/\tau_A = 10^6$. A typical reference value for $\tau_A = R_\odot/V_A$ is 24 minutes, if we take an Alfvén speed $V_A = 480 \text{ km s}^{-1}$ (e.g., for $|\mathbf{B}| = 2.2 \text{ G}$ and $n_0 = 10^8 \text{ cm}^{-3}$). This low resistivity value is prescribed to ensure that a minimum dissipation is present everywhere in the computational domain and to eliminate structures smaller than the grid resolution. In general, it is smaller than the numerical dissipation introduced by the upwinding treatment of advection, $\tau_U = 2 R_\odot^2/(V \Delta r)$ (Lionello et al. 1999). For example, in the low corona, where $\Delta r = 0.01 R_\odot$, we have $\tau_U \gtrsim \tau_R$ only for flows smaller than 0.1 km s^{-1} . In the higher corona and in the heliosphere, numerical dissipation dominates over the prescribed value. Similarly, we have chosen a uniform viscosity profile such that $\tau_v/\tau_A = 500$. Also, this value of viscosity is necessary to dissipate unresolved scales without substantially affecting the global solution.

3.1. Non-Rotating Case

In the non-rotating case ($\Omega = 0$), we prescribe a global dipole field for \mathbf{B} as the initial condition of the coronal model and a previously calculated solar wind solution for the plasma properties. Figure 1(a) shows a cut of the entire computational domain in the meridional plane showing some magnetic field lines of the initial dipole. We then relax the system for 6.7 days until we obtain a steady state. The configuration of the magnetic field after this relaxation phase is presented in Figure 1(c), where the field appears mostly radial and the current sheet in the equatorial plane is evident. Figure 2(a) shows the configuration closer to the solar surface. Open field regions are visible at the poles, while closed field lines are present at equatorial latitudes, surmounted by the typical cusp-like field lines. On top of the streamer, the current sheet is formed (Figure 2(c)), while

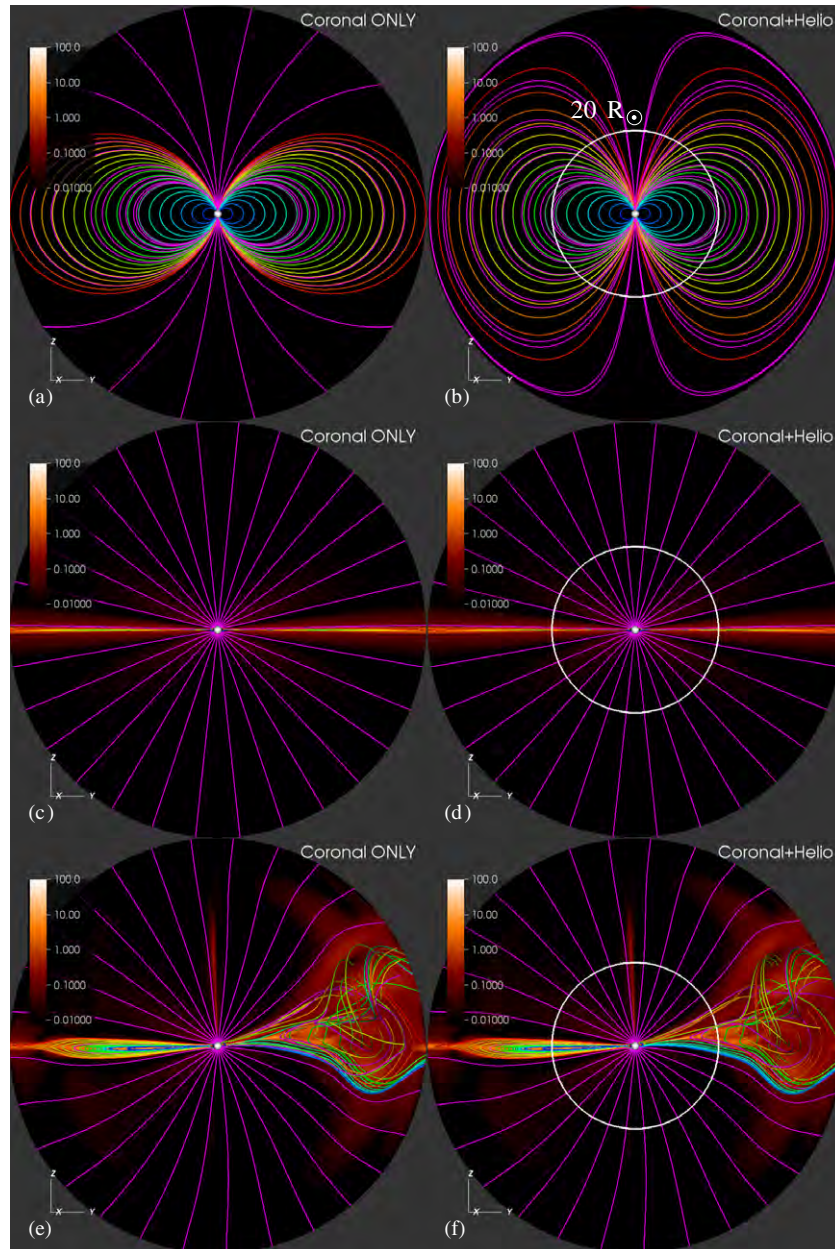


Figure 1. Magnetic field lines and J/B during the relaxation and flux rope eruption, in the coronal and heliospheric calculations without rotation, in a meridional plane (solar north is up). (a) Coronal model ($R_\odot \leq r \leq 50 R_\odot$) at the beginning of the relaxation phase. (b) Coronal model ($R_\odot \leq r < 20 R_\odot$) and the heliospheric model ($20 R_\odot \leq r \leq 50 R_\odot$) at the beginning of the relaxation phase. The boundary between the two models is traced in white. (c) Coronal model at the end of the relaxation phase, just before the flux rope is introduced. (d) Same as (c) for the coronal and heliospheric models combined. (e) Propagation of the flux rope in the coronal model. (f) Same as (e) for the coronal and heliospheric models combined.

(A color version of this figure is available in the online journal.)

volume currents are present in the closed-field region under the helmet streamer (Figure 2(b)). Using the technique described in Section 2.2, we extract from a spherical shell at approximately $20 R_\odot$ the values of the fields corresponding to the initial state of the coronal model and subsequent states at every 10 hr for the entire relaxation period. As an initial condition for the magnetic field of the heliospheric model, we prescribe a potential field extrapolation of the values of B_r at $r = 20 R_\odot$ at $t = 0$ from the coronal model. Likewise, we use the values of v_r , ρ , and T from the $r = 20 R_\odot$ spherical surface in the coronal simulation to prescribe the initial conditions for the plasma properties. While the values of v_r and T from this surface are assigned to each internal point of corresponding latitude and longitude, the

values of ρ are also scaled by a r^{-2} factor. In Figure 1(b), we show magnetic field lines of the initial state of the heliospheric solution in the region $r \geq 20 R_\odot$ and of the initial state of the coronal solution for $r = 20 R_\odot$ (the $r = 20 R_\odot$ circle is marked in white). (It is not surprising that the $r \geq 20 R_\odot$ region differs from the initial state of the coronal model shown in Figure 1(a).) Then, we relax the heliospheric model for 6.7 days, driving it with the sequence extracted from the coronal model. Our heliospheric calculation is also performed in the same inertial frame of reference as the coronal model. As Figure 1(d) shows, at the end of the relaxation phase the heliospheric solution is indistinguishable from that calculated using the coronal model.

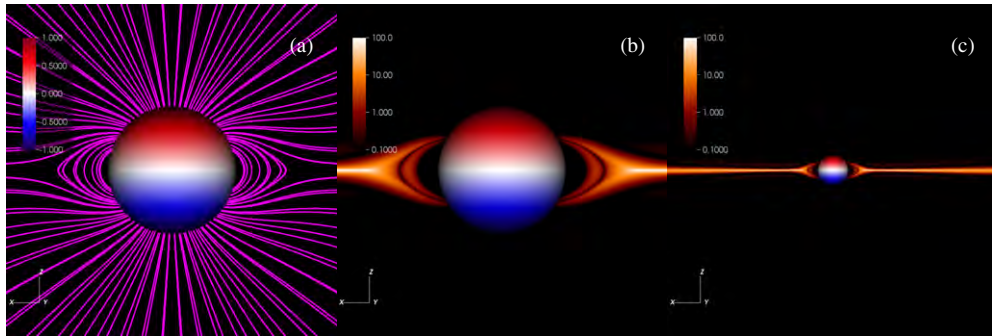


Figure 2. Relaxed state of the coronal calculation without rotation. The solar surface is colored according to the value of B_r . (a) Magnetic field lines outlining the global field structure. (b) J/B near the solar surface showing volume currents in the streamer belt. (c) J/B further out in the corona showing the equatorial current sheet.

(A color version of this figure is available in the online journal.)

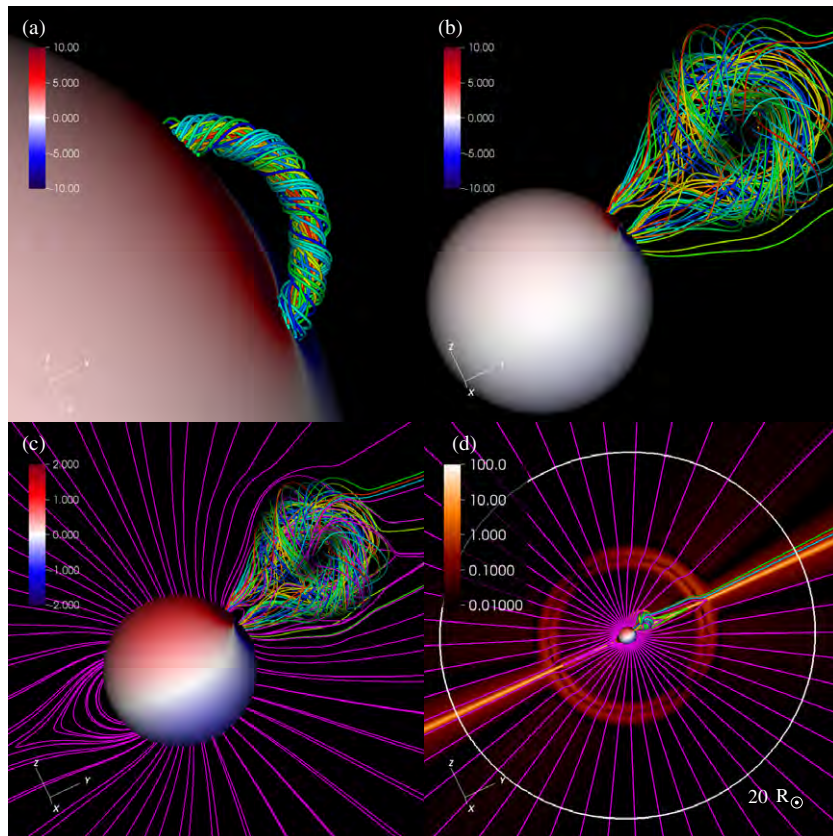


Figure 3. (a) Magnetic field lines of the out-of-equilibrium Titov-Démoulin flux rope introduced in the coronal solution after the relaxation phase. (b) The flux rope immediately erupts. (c) Interaction between the flux rope and the ambient dipole field. (d) J/B at larger heliocentric distances. We truncate the flux rope solution at $\sim 7 R_\odot$, thus causing a disturbance that propagates outward in the solar wind.

(A color version of this figure is available in the online journal.)

Having obtained a virtually identical relaxed state for both models, we introduce a strongly out-of-equilibrium, modified version of the coronal flux rope model of Titov & Démoulin (1999, hereafter TDM) into the coronal calculation. The main difference between the original and the TDM model is that in the latter the stabilizing, analytical magnetic field is replaced with the ambient field of the CME source region into which the flux rope is inserted. Titov-Démoulin flux ropes have been used in recent simulations of observed CMEs (e.g., Tóth et al. 2007; Manchester et al. 2008; Lugaz et al. 2011) In all these cases, the flux rope was inserted out of equilibrium, causing an immediate eruption. Further details of our implementation of the TDM model will be described in a separate publication (V. S.

Titov et al., in preparation), with emphasis placed on obtaining stable, pre-eruption configurations, such as the run described in Section 4. A view of some magnetic field lines of the flux rope, which is inserted at the equator into the relaxed configuration, is presented in Figure 3(a). If we simply added the flux-rope solution to the coronal field, this would instantly modify the magnetic field everywhere in the domain, including the region beyond $r = 20 R_\odot$. This would create a discrepancy with the heliospheric model, for which the evolution for $r > 20 R_\odot$ is solely the result of changes at the $r = 20 R_\odot$ boundary. Therefore, when introducing the flux rope, we truncate the solution at $r = 7 R_\odot$, which is well within the limits of the region bounded by the coronal model, but far enough from the flux rope

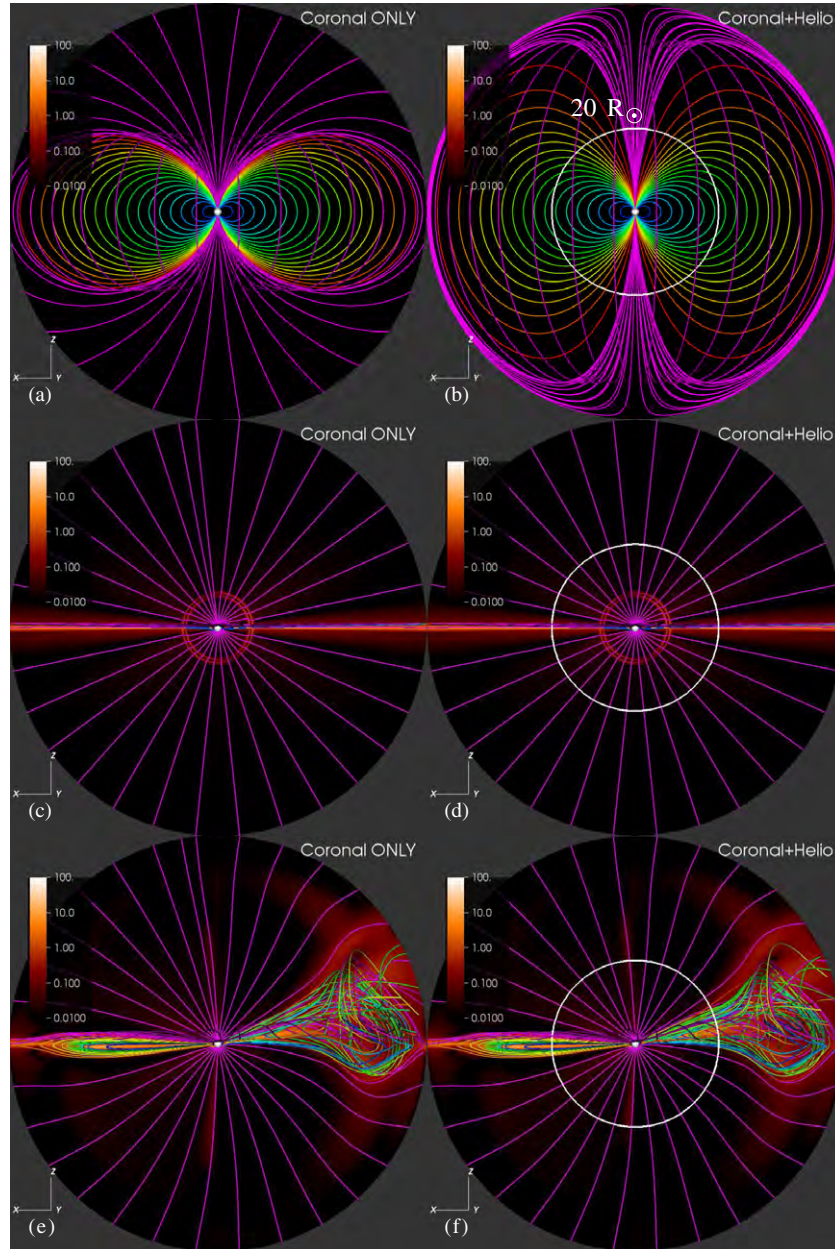


Figure 4. Magnetic field lines and J/B during the relaxation and flux rope eruption, in the coronal and heliospheric calculations with rotation in a meridional plane (solar north is up). (a) Coronal model at the beginning of the relaxation phase. (b) Coronal model and the heliospheric model at the beginning of the relaxation phase. The boundary between the two models at $20 R_{\odot}$ is traced in white. (c) Coronal model at the end of the relaxation phase, just before the flux rope is introduced. (d) Same as (c) for the coronal and heliospheric models combined. (e) Propagation of the flux rope in the coronal model. (f) Same as (e) for the coronal and heliospheric models combined.

(A color version of this figure is available in the online journal.)

itself not to have significant physical consequences. However, this causes a slight deformation of the opposite streamer for $r \leq 7 R_{\odot}$ and the formation of a small perturbation at $r = 7 R_{\odot}$, which is visible in the J/B cut shown in Figure 3(d).² This disturbance travels out of the computational domain when we advance the calculation, further perturbing the opposite streamer as it adjusts to the presence of the inserted magnetic field. The flux rope itself, being out of equilibrium, immediately erupts,

² We note that the field modification is exceptionally strong here because we have inserted a flux rope with a very intense magnetic field. If the flux rope is inserted in equilibrium with the ambient magnetic field, as in the case described in Section 4, these modifications are typically negligible outside the CME source region.

forming a CME (Figures 3(c) and (d)), which propagates and expands in the computational domain. After 20 hr, the ICME has crossed the outer boundary at $50 R_{\odot}$ and we stop the calculation. Figure 1(e), which shows a cut in the meridional plane for this time, illustrates how the flux rope has expanded to an angular width of almost 30° . To model this highly dynamic phase with the heliospheric model, we extract ρ , T , \mathbf{B} , and \mathbf{v} at $r = 20 R_{\odot}$ from the coronal calculation with a higher frequency, namely a frame every 289 s. We drive the heliospheric model for 20 more hours to follow the propagation of the ICME (Figure 1(f)). The coronal and heliospheric calculations, which visually appear to be identical, are actually in agreement to within 1% for ρ , $|\mathbf{v}|$, $|\mathbf{B}|$, and T .

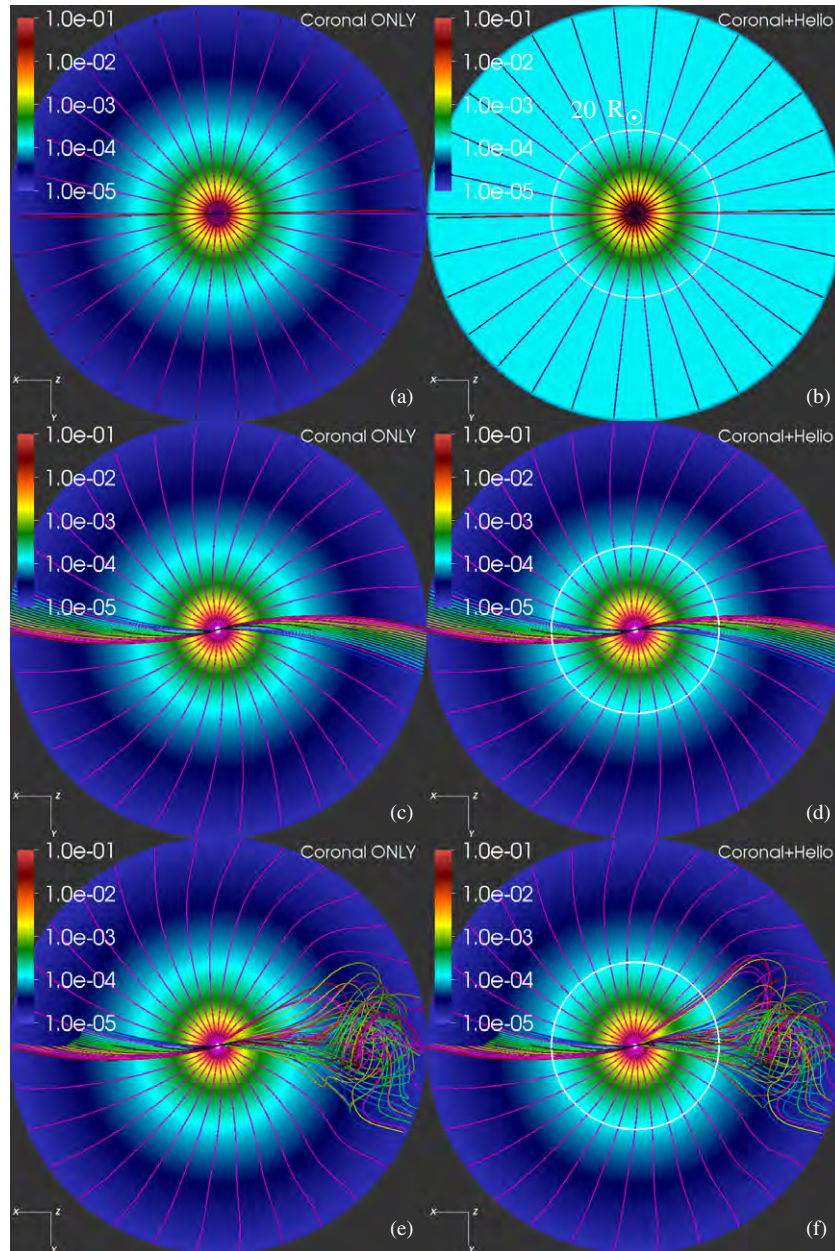


Figure 5. Magnetic field lines and scaled density (ρr^2) during the relaxation and flux rope eruption, in the coronal and heliospheric calculations with rotation in the equatorial plane (viewed from above the Sun’s north pole). (a) Coronal model at the beginning of the relaxation phase. (b) Coronal model and the heliospheric model at the beginning of the relaxation phase. The boundary between the two models at $20 R_{\odot}$ is traced in white. (c) Coronal model at the end of the relaxation phase, just before the flux rope is introduced. The Parker spiral is clearly visible. (d) Same as (c) for the coronal and heliospheric models combined. (e) Propagation of the flux rope in the coronal model. (f) Same as (e) for the coronal and heliospheric models combined.

(A color version of this figure is available in the online journal.)

3.2. Rotating Case

We now repeat the validation described in the previous section for a case where we account for solar rotation. We perform the calculation for the coronal model in the rotating (non-inertial) frame of reference, where Equation (6) contains a non-vanishing fictitious forces term, \mathbf{F}_{fict} . As presented in Figure 4(a), an identical dipole state is prescribed for the initial magnetic field. At $t = 0$, the components of the magnetic field are only radial and latitudinal, as the cut in the equatorial plane of Figure 5(a) shows. Then, we relax the system by again advancing the MHD equations for 6.7 days to obtain a steady state. Figure 4(c), which displays the configuration after this

time, is rather similar to the non-rotating case of Figure 1(c). However, in the present case, a longitudinal component of the magnetic field is introduced because of rotation. The effects of rotation can be appreciated in Figure 5(c), which shows, viewed from above the north pole of the Sun, how a burgeoning Parker spiral develops in the equatorial plane. From this coronal simulation, we extract a sequence of fields at the $r = 20 R_{\odot}$ surface with the same frequency used in the non-rotating case and use a similar sequence of frames to drive the heliospheric model. The heliospheric calculation with rotation is performed in the inertial frame to show how our model is not tied to using the same frame of reference as the coronal simulation. Following the procedure outlined in the previous section, we

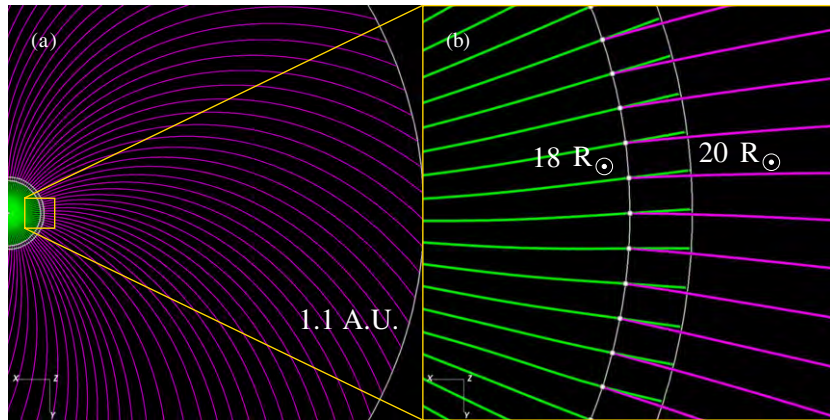


Figure 6. (a) Field lines in the equatorial plane for the combined coronal and heliospheric model of CME/ICME propagation of Section 4. All field lines are traced from $18 R_{\odot}$. (b) Enlargement of a portion of (a). The coronal model (green field lines) was calculated by Török et al. (in preparation) in a non-rotating frame extending from 1 to $20 R_{\odot}$. The heliospheric model (purple field lines) was calculated in an inertial frame with solar rotation included extending from $18 R_{\odot}$ to 1.1 AU.

(A color version of this figure is available in the online journal.)

build the initial condition for the magnetic field through a potential field extrapolation using B_r at the lower boundary and prescribe the solar wind parameters starting from the values on the same surface. Figures 4(b) and 5(b) show magnetic field lines, in the meridional and equatorial plane, respectively. Then, we drive the heliospheric model with the series of boundary conditions extracted from the coronal model until relaxation. While the initial state of the heliospheric model is clearly different from that of the coronal model (compare Figure 4(a) with 4(b) and Figure 5(a) with 5(b)), the final states are for all purposes virtually indistinguishable (compare Figure 4(c) with Figure 4(d) and Figure 5(c) with Figure 5(d)).

Having relaxed the configuration, we insert an out-of-equilibrium TDM flux rope in the coronal model. As was the case in the non-rotating frame (see Figure 3(d)), a ring of current appears at $r \sim 7 R_{\odot}$. The CME, which is formed by the expanding flux rope, propagates similarly outward. The coronal calculation is finally concluded 20 hr after triggering the eruption, resulting in the state shown in Figures 4(e) (meridional view) and 5(e) (equatorial view). As it appears in Figure 4(e), the CME occupies about 30° in the meridional plane, with current densities extending to approximately 60° . In the equatorial plane shown in Figure 5(e), the field lines of the CME appear to extend roughly over the same angle, implying a conical geometry for the whole structure. Then, using a sequence of boundary conditions extracted from the coronal model at intervals of 289 s as a driver at the $r = 20 R_{\odot}$ surface, we advance the heliospheric model for 20 more hours. The injection of the flux rope and the current disturbance associated with it occur well below the $r = 20 R_{\odot}$ boundary, as in the non-rotating case. The CME also propagates seamlessly through the $r = 20 R_{\odot}$ boundary. The final state of the heliospheric model is shown in Figures 4(f) (meridional plane) and 5(f) (equatorial plane), which can be compared with Figures 4(e) and 5(e), respectively. As for the non-rotating case, all quantities calculated with the two models are in agreement to within 1%.

4. PROPAGATION OF A REALISTIC ICME

Having shown how the technique of coupled models successfully reproduces the results of a single domain calculation, we now present an advanced application of the heliospheric model by studying the propagation of an ICME from $18 R_{\odot}$ to 1.1 AU in the inertial frame of reference. To achieve this goal, we use the results calculated by T. Török et al. (in preparation) to drive

our model. Török et al. specified a more realistic plasma environment than that used in Section 3 by employing the full MHD thermodynamic model of Lionello et al. (2009). In a corotating frame of reference that neglected the effect of fictitious forces, Török et al. prescribed a potential, global dipole field together with a quadrupolar active region on the solar surface. After relaxing the configuration for about 60 hr, they inserted a TDM flux rope. Contrary to our simple and less realistic earlier approaches (Sections 3.1 and 3.2), their flux rope was inserted *in equilibrium* into the stabilizing ambient coronal field. Then, it was relaxed for another 13 hour period, during which cold and dense plasma accumulated in the flux rope, resembling the conditions observed in prominences. After that, they introduced converging flows near the polarity inversion line of the active region, which caused the field overlying the flux rope to expand quasi-statically, progressively reducing the magnetic tension. As a consequence, the flux rope rose slowly until a critical height was reached, at which point a loss of equilibrium and eruption occurred. A fast and powerful CME was formed, which rapidly accelerated to a speed of $\sim 3,000 \text{ km s}^{-1}$, driven predominantly by strong reconnection below the erupting flux rope and producing a fast forward shock. The CME then rapidly slowed down to $\lesssim 1,000 \text{ km s}^{-1}$ before it reached $3 R_{\odot}$. The reasons for this significant deceleration are currently under investigation. Most likely they are related to the very strong reconnection flows ($\geq 10,000 \text{ km s}^{-1}$) that temporarily accelerated the flux rope to very large speeds. After the rapid deceleration, the CME slowed down only gradually and reached the outer coronal boundary at $20 R_{\odot}$ with a speed of about $700\text{--}800 \text{ km s}^{-1}$. The simulation was stopped 74 hr after the insertion of the flux rope, enough for the CME to leave the coronal computational domain. Every 6 minutes, we extract from the simulation of Török et al. the magnetic field, velocity, density, and temperature on a spherical surface at $18 R_{\odot}$, which is beyond the critical Alfvén and sonic points. We choose to start our simulation from $18 R_{\odot}$ rather than $20 R_{\odot}$ to allow overlap in the computational domains of the coronal and heliospheric model. Since the physical variables in the $18 R_{\odot} \leq r \leq 20 R_{\odot}$ region are directly calculated in either model, we are able to verify that no boundary effects arise in this more realistic simulation. We also estimate the importance of including rotation in the computation.

Using the first extracted set of fields at $18 R_{\odot}$, we again specify a potential extrapolation as initial conditions for the magnetic field of the heliospheric model. We extrapolate radially

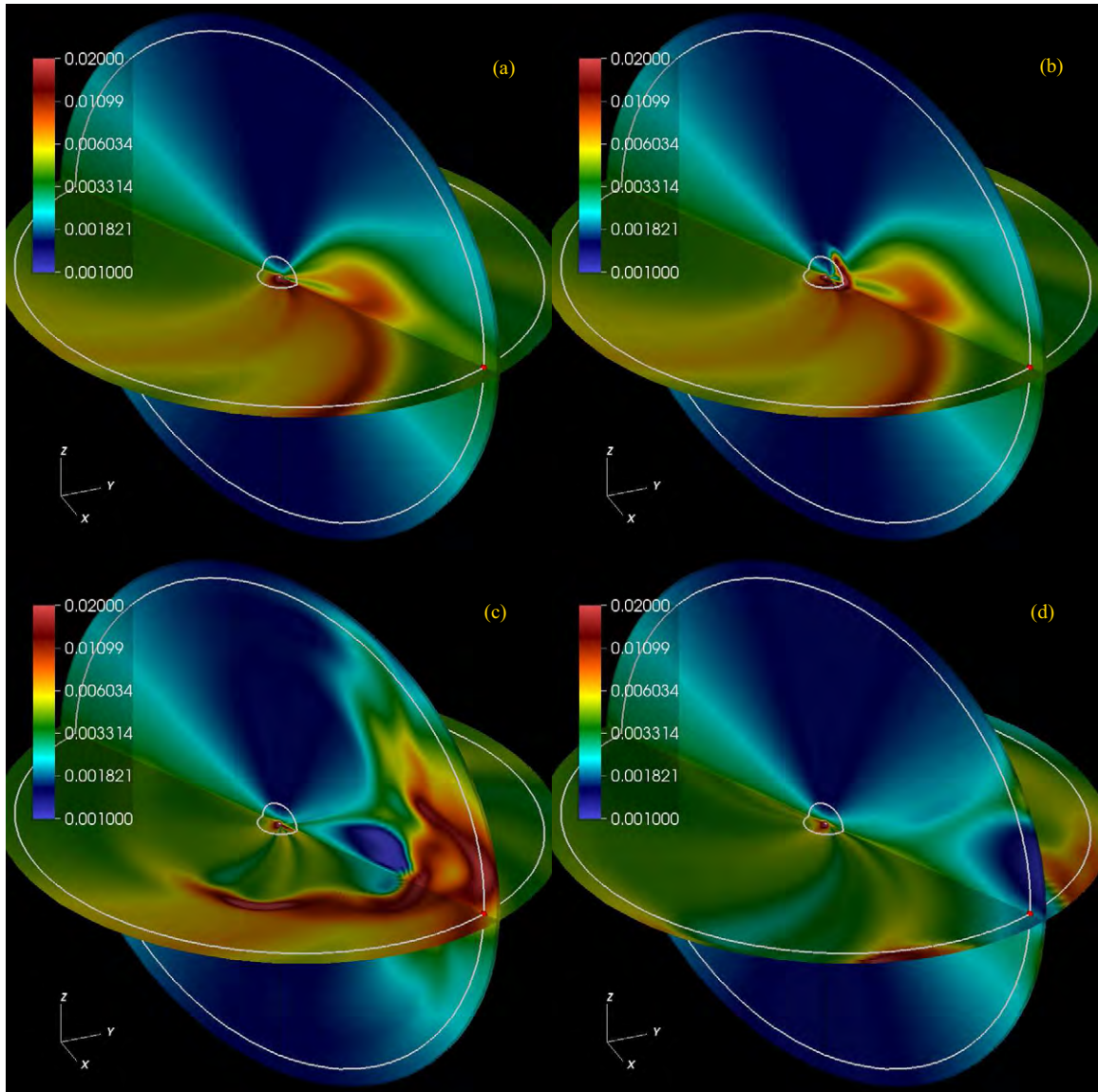


Figure 7. Evolution of the scaled density (ρr^2) in two cut-planes during the propagation of an ICME from Sun to Earth (red dot). The inner white circle lies at $20 R_{\odot}$. The coronal part of the calculation is described in T. Török et al. (in preparation). (a) Configuration in steady state just before the eruption on the solar surface ($t = 402$ hr). (b) CME leaving the computational domain of the coronal model and entering the heliosphere ($t = 408$ hr). (c) ICME as it reaches Earth ($t = 458$ hr). (d) ICME leaving the computational domain of the heliospheric model. End of the calculation ($t = 502$ hr).

(A color version of this figure is available in the online journal.)

the values of v_r , ρ , and T to initialize the plasma properties, as described in the previous section. We then advance the MHD equations with fixed boundary values for 402 hr to ensure that a steady state solution is formed in the heliosphere. While in Török et al. the full thermodynamic treatment of the energy equation was employed, here we use the polytropic approximation, by setting $S = 0$ in Equation (5) and $\gamma = 1.5$ (Totten et al. 1996; Feldman et al. 1998). It has been shown that such an approximation is justified for heliospheric simulations (e.g., Riley et al. 2001a); however, in future simulations, we plan to explore the effect of including collisionless thermal conduction in the energy equation. The relaxed configuration of the magnetic field is shown in Figures 6(a) and (b). Both green (coronal) and purple (heliospheric) field lines are traced from $18 R_{\odot}$. The Parker spiral is fully developed in the heliospheric calculation. Note that in the region between 18 and $20 R_{\odot}$, there is a slight discrepancy between the coronal and heliospheric calculations, since the former neglects the effect of rotation.

In Figure 7(a), we show the distribution of ρr^2 in the heliosphere and corona at the end of the relaxation phase in the equatorial plane and in the meridional plane perpendicular to the Sun-Earth line. In the equatorial plane, streams characterized by higher or lower density are visible, forming the typical Parker spiral. At this point, we continue the simulation for 100 more hours, driving the lower boundary with the series of frames extracted from the simulation of Török et al. When this series is exhausted, we keep the last frame as a fixed boundary condition until $t = 502$ hr. During this second phase of the calculation, we follow the CME as it travels through the heliospheric computational domain and finally leaves through the outer boundary. At $t = 408$ hr, Figure 7(b) shows the CME as it crosses the outer boundary of the calculation of Török et al. A selection of field lines threading the CME are presented in Figure 8(b) and show the flux rope crossing into the heliospheric domain. The ICME continues to propagate in the heliosphere and at $t = 458$ hr arrives in the vicinity of

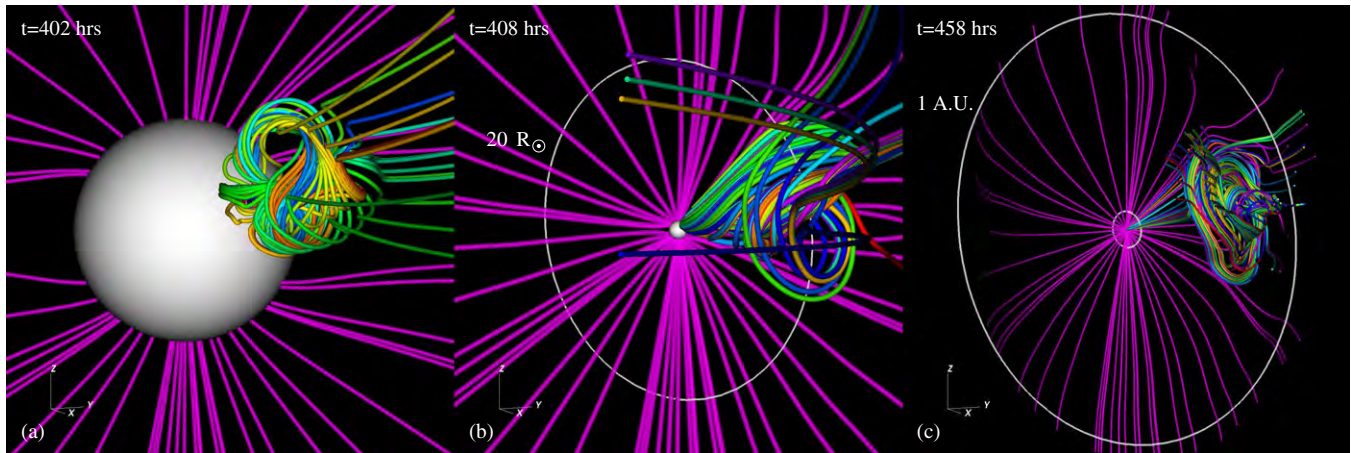


Figure 8. Magnetic field lines showing the propagation of a CME/ICME from Sun to Earth: (a) immediately after the eruption, (b) 6 hr after the eruption, the CME is crossing into the heliospheric domain, (c) 56 hr after the eruption, the ICME is about to reach Earth. The coronal part of the solution (below $20 R_{\odot}$) was calculated by T. Török et al. (in preparation).

(A color version of this figure is available in the online journal.)

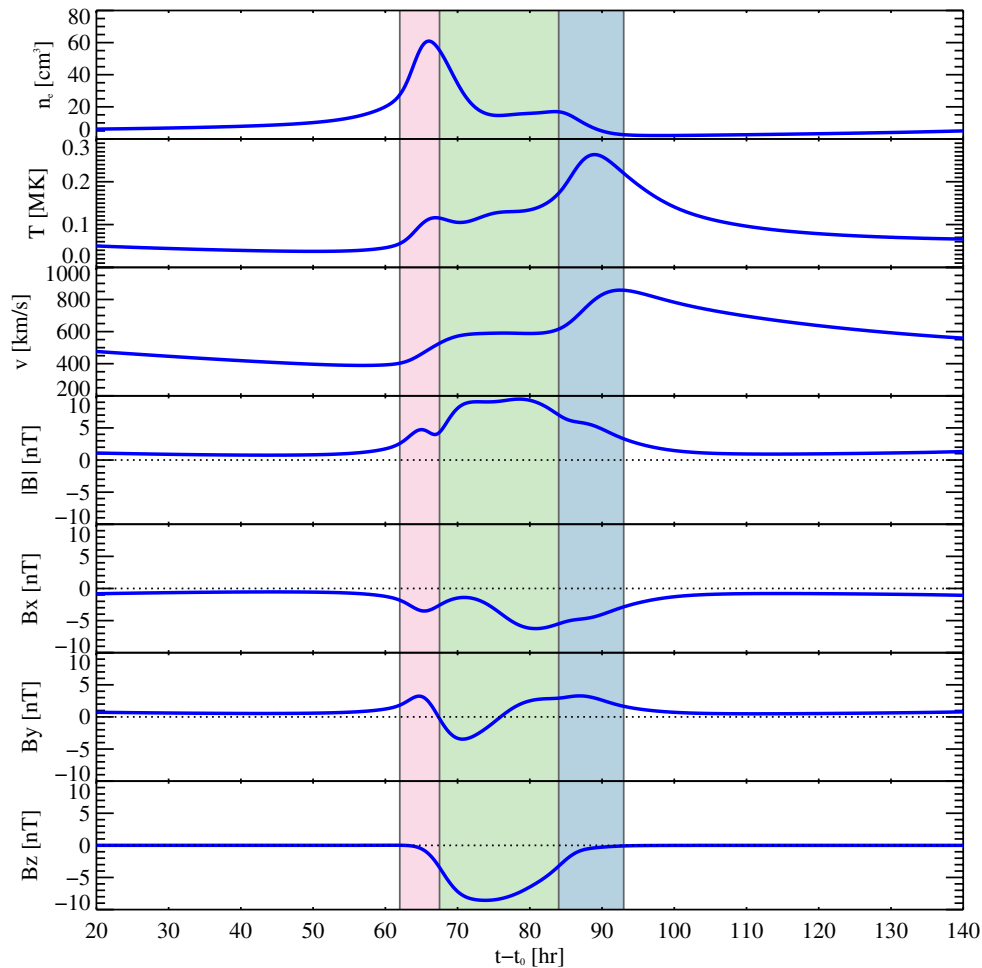


Figure 9. Time history of local plasma variables at 1AU for a point situated in the path of the ICME described in Section 4. The magnetic field vectors have been converted to GSE coordinates. The pink highlighted region indicates the compressed solar wind upstream of the ICME. The green region indicates the flux system of the ICME. The blue region indicates the trailing plasma, which was compressed by a high speed stream behind it. Time is in hours from the insertion of the CME in the calculation of T. Török et al. (in preparation; $t_0 = 402$ hr).

(A color version of this figure is available in the online journal.)

the Earth. Figure 7(c) shows the denser, enlarged structure of the ejecta followed by a depletion region, while Figure 8(c) shows the envelope of some field lines connected to the ICME. After passing by, the ICME crosses over the outer boundary

and leaves the computational domain of the heliospheric model (Figure 7(d)). Since the ICME does not hit Earth directly, in Figure 9 we show the time history of the local plasma variable for an observer situated along its path. The magnetic field

components are expressed in Geocentric Solar Ecliptic (GSE) coordinates (Russell 1971). The low value of B within the ICME can be explained considering that our model active region has a field strength considerably smaller than in the source regions of the most powerful events that produce very fast CMEs ($\lesssim 1000$ G versus $\gtrsim 2000$ G). Thus, it is not surprising that the magnetic field at 1 AU is smaller than for typical fast events. Also, most of the interaction of the flux rope with the ambient magnetic field has already occurred in the coronal solution. Starting from 40 hr after the eruption ($t = 442$ hr), the density of the plasma begins to increase as it is swept by the ICME. The density reaches a maximum of 10 times the base value (the area shaded in pink in Figure 9). Then, the observer is overtaken by the flux system and the magnetic field exhibits a typical pattern of rotation (green area). Finally, trailing the ICME, there is region of fast solar wind that compresses the plasma (blue area). These features, which are beyond the scope of this article, are described in more detail in P. Riley et al. (in preparation).

5. CONCLUSIONS

We have shown how our computational MHD model of the heliosphere is capable of following the propagation of ICMEs from beyond the critical point to Earth. The key feature of our model is its flexibility. It can in principle accept as input at the lower boundary time-dependent results obtained from (1) MHD simulations of the solar corona, (2) Potential-Field Source-Surface (PFSS) models, (3) empirical models, (4) observations, or (5) a combination thereof. Moreover, the frame of reference from which the lower-boundary data are extracted can be either the inertial frame or the corotating frame. If the coronal model is calculated in the corotating frame, the inertial forces can either be included or neglected. The heliospheric computation itself can be either performed in the inertial or in the corotating frame. Particular care has been taken in the interpolation of the input magnetic field at the boundary to avoid the formation of spurious current layers. To demonstrate the capabilities of our model, we have presented three simulations. In the first two, we used our coronal MHD model to simulate a CME eruption from the solar surface to $50 R_{\odot}$, in a fixed and a corotating frame, respectively. From these two simulations, we extracted the data at $r = 20 R_{\odot}$ and used them to drive our model. In either case, the agreement between the coronal and the heliospheric models in the common portion of the computational domain was remarkable. Disturbances propagated smoothly across the lower surface and no boundary layer was formed. We also presented a third, more realistic, simulation driven by data extracted from the coronal model of a CME described by T. Török et al. (in preparation). This is a fast and powerful CME originating from a source region of approximately 3 kG. We have shown that our model is able to follow the propagation of the CME from $18 R_{\odot}$ to 1.1 AU.

Our newly developed heliospheric model is not restricted to event studies of CME eruption and subsequent ICME propagation. It can also be used to model the heliosphere and the solar wind from a variety of inputs. Magnetic flux evolution models are ever more frequently used to create coronal models, either through MHD or PFSS extrapolations (for a review, see Mackay & Yeates 2012). These can be extended to study the structure of the heliosphere or, more easily, they can provide input to our heliospheric model. Computationally, it is less intense to update the boundaries of the heliospheric model when the coronal model is updated, rather than using a single model encompassing both physical regions.

This work was supported by NASA through the LWS, HTP, and SBIR programs, and by NSF through the Center for Integrated Space Weather Modeling (CISM) and Frontiers in Earth System Dynamics (FESD) program. Computational resources were provided by the NSF supported Texas Advanced computing Center (TACC) in Austin and the NASA Advanced Supercomputing Division (NAS) at Ames Research Center.

REFERENCES

- Arge, C. N., & Pizzo, V. J. 2000, *JGR*, **105**, 10465
- Burlaga, L. F., Behannon, K. W., & Klein, L. W. 1987, *JGR*, **92**, 5725
- Burlaga, L. F., Klein, L., Sheeley, N. R., Jr., et al. 1982, *GeoRL*, **9**, 1317
- Feldman, W. C., Barraclough, B. L., Gosling, J. T., et al. 1998, *JGR*, **103**, 14547
- Feng, X., Yang, L., Xiang, C., et al. 2010, *ApJ*, **723**, 300
- Gosling, J. T. 1990, in Washington DC American Geophysical Union Geophysical Monograph Series, Vol. 58, Washington DC American Geophysical Union Geophysical Monograph Series, ed. C. T. Russell, E. R. Priest, & L. C. Lee (Washington, DC: AGU), 343
- Gosling, J. T., McComas, D. J., Phillips, J. L., & Bame, S. J. 1991, *JGR*, **96**, 7831
- Groth, C. P. T., De Zeeuw, D. L., Gombosi, T. I., & Powell, K. G. 2000, *JGR*, **105**, 25053
- Hayashi, K. 2012, *JGRA*, **117**, 8105
- Jeffrey, A. 1966, *Magnetohydrodynamics*, University Mathematical Texts (Edinburgh: Oliver & Boyd)
- Kleimann, J. 2012, *SoPh*, **281**, 353
- Kunow, H., Crooker, N. U., Linker, J. A., Schwenn, R., & von Steiger, R. 2006, *Coronal Mass Ejections* (Berlin: Springer-Verlag)
- Linker, J. A., Mikić, Z., Lionello, R., et al. 2003, *PhPI*, **10**, 1971
- Lionello, R., Linker, J. A., & Mikić, Z. 2009, *ApJ*, **690**, 902
- Lionello, R., Mikić, Z., & Linker, J. A. 1999, *JCoPh*, **152**, 346
- Lionello, R., Mikić, Z., & Schnack, D. D. 1998, *JCoPh*, **140**, 10
- Lugaz, N., Downs, C., Shibata, K., et al. 2011, *ApJ*, **738**, 127
- Lugaz, N., Manchester, W. B., IV, Roussev, I. I., Tóth, G., & Gombosi, T. I. 2007, *ApJ*, **659**, 788
- Mackay, D., & Yeates, A. 2012, *LRSP*, **9**, 6
- Manchester, W. B., Ridley, A. J., Gombosi, T. I., & Dezeew, D. L. 2006, *AdSpR*, **38**, 253
- Manchester, W. B., IV, Vourlidis, A., Tóth, G., et al. 2008, *ApJ*, **684**, 1448
- Merkin, V. G., Lyon, J. G., McGregor, S. L., & Pahud, D. M. 2011, *GeoRL*, **38**, 14107
- Mikić, Z., Linker, J. A., Schnack, D. D., Lionello, R., & Tarditi, A. 1999, *PhPI*, **6**, 2217
- Odstrcil, D., Linker, J. A., Lionello, R., et al. 2002, *JGRA*, **107**, 1493
- Odstrcil, D., Pizzo, V. J., & Arge, C. N. 2005, *JGRA*, **110**, 2106
- Odstrcil, D., Pizzo, V. J., Arge, C. N., et al. 2008, in ASP Conf. Ser. 385, *Numerical Modeling of Space Plasma Flows*, ed. N. V. Pogorelov, E. Audit, & G. P. Zank (San Francisco, CA: ASP), 167
- Odstrcil, D., Riley, P., Linker, J. A., et al. 2003, in ESA Special Publication, Vol. 535, *Solar Variability as an Input to the Earth's Environment*, ed. A. Wilson (Noordwijk: ESA), 541
- Odstrcil, D., Riley, P., & Zhao, X. P. 2004, *JGRA*, **109**, 2116
- Riley, P., Gosling, J. T., & Pizzo, V. J. 2001a, *JGR*, **106**, 8291
- Riley, P., Linker, J. A., & Mikić, Z. 2001b, *JGR*, **106**, 15889
- Riley, P., Linker, J. A., Mikić, Z., et al. 2003, *JGRA*, **108**, 1272
- Riley, P., Schatzman, C., Cane, H. V., Richardson, I. G., & Gopalswamy, N. 2006, *ApJ*, **647**, 648
- Russell, C. T. 1971, *CosEl*, **2**, 184
- Titov, V. S., & Démoulin, P. 1999, *A&A*, **351**, 707
- Tóth, G., de Zeeuw, D. L., Gombosi, T. I., et al. 2007, *SpWea*, **5**, 6003
- Tóth, G., Sokolov, I. V., Gombosi, T. I., et al. 2005, *JGRA*, **110**, 12226
- Tóth, G., van der Holst, B., Sokolov, I. V., et al. 2012, *JCoPh*, **231**, 870
- Totten, T. L., Freeman, J. W., & Arya, S. 1996, *JGR*, **101**, 15629
- Usmanov, A. V., & Dryer, M. 1995, *SoPh*, **159**, 347
- Usmanov, A. V., & Goldstein, M. L. 2006, *JGRA*, **111**, 7101
- Vourlidis, A., Lynch, B. J., Howard, R. A., & Li, Y. 2013, *SoPh*, **284**, 179
- Wang, Y.-M., & Sheeley, N. R. 1995, *ApJL*, **447**, L143
- Wang, Y. M., Wang, S., & Ye, P. Z. 2002, *SoPh*, **211**, 333
- Wang, Y. M., Ye, P. Z., & Wang, S. 2003, *JGRA*, **108**, 1370
- Wu, S. T., Guo, W. P., Michels, D. J., & Burlaga, L. F. 1999, *JGR*, **104**, 14789
- Zhao, X. P., Plunkett, S. P., & Liu, W. 2002, *JGRA*, **107**, 1223

SLOW RISE AND PARTIAL ERUPTION OF A DOUBLE-DECKER FILAMENT. II MODELING BY A DOUBLE FLUX ROPE EQUILIBRIUM

BERNHARD KLIEM^{1,2}, TIBOR TÖRÖK³, VIACHESLAV S. TITOV³, ROBERTO LIONELLO³,
JON A. LINKER³, RUI LIU^{4,5}, CHANG LIU⁴, AND HAIMIN WANG⁴

Draft version: May 14, 2012

ABSTRACT

Force-free equilibria containing two vertically arranged magnetic flux ropes of like chirality and current direction are considered as a model for split filaments or prominences. Such equilibria are constructed analytically through an extension of the methods developed in Titov & Démoulin (1999) and numerically through an evolutionary sequence including shear flows, flux emergence, and flux cancelation in the photospheric boundary. It is demonstrated that the equilibria are stable if an external toroidal (shear) field component of sufficient strength is included. If this component decreases sufficiently below the threshold, both flux ropes turn unstable for conditions typical of solar active regions. Then either both flux ropes erupt upward, or only the upper rope erupts with the lower rope being destroyed by reconnection with the ambient field low in the corona. However, the configuration also admits **partial eruptions** with only the upper flux rope becoming unstable **and the lower one remaining in place. Such an evolution can be triggered**, for example, **by** a transfer of flux and current from the lower to the upper rope, as suggested by the observations of a filament in the companion paper (Liu et al. 2012). **A partial eruption can similarly result from tether-cutting reconnection in the space between the flux ropes, which influences their stability properties in opposite ways.**

Subject headings: Instabilities—Magnetohydrodynamics (MHD)—Sun: coronal mass ejections (CMEs)—Sun: filaments, prominences—Sun: magnetic topology

1. INTRODUCTION

The magnetic structure of solar prominences (filaments if observed on the disk) is one of the major debated subjects in solar physics: a flux rope and a sheared loop arcade are being controversially discussed (e.g., Mackay et al. 2010). An extension of the flux rope concept is suggested to be relevant in some cases by the analysis of a “double-decker” filament in Liu et al. (2012), hereafter Paper I. The filament, located in active region 11093, consisted of two main branches and experienced a partial eruption, ejecting only the upper branch, on 2010 August 7. The clear vertical separation of the filament branches prior to eruption and the stability of the lower branch in the course of the eruption both suggest that the filament may have formed in a double flux rope structure. An alternative explanation in terms of a single flux rope with a hyperbolic flux tube (HFT), i.e., an X-type magnetic structure, at its underside also appears possible. In this case the upper and lower filament branch would be located in the flux rope above and in the arcade below the HFT, respectively. These two configurations are illustrated in Figure 1. The formation of both branches within a single flux rope or within an arcade is far less likely, as it requires two special conditions to be satisfied simultaneously: the injection of the filament material at two clearly separated heights and the formation of the flare current sheet in the course of the eruption at an intermediate height.

A striking phenomenon observed during the slow-rise phase of the upper filament branch prior to its eruption was the transfer of material from the lower to the upper branch, occurring in several episodes. Assuming dominantly horizontal field orientation in the filament, a corresponding transfer of flux is implied. This may have caused the eruption by producing an imbalance between the flux in the upper branch and the ambient flux (e.g., Su et al. 2011) or by lifting the upper branch into the torus-unstable height range (Kliem & Török 2006).

Employing two MHD modeling approaches, the present paper substantiates the suggestion that a double flux rope configuration can be consistent with the long-term stability of the split filament studied in Paper I during its slow rise phase, and with the partial eruption. This also introduces new scenarios for partial filament eruptions. For some events these may be an alternative to the dynamical splitting and partial expulsion of a single, originally purely O-type flux rope whose top part has become unstable while the bottom part remains line-tied in the photosphere (Gibson & Fan 2006). In such a configuration the flux splits only after the main acceleration of the eruption has commenced.

We restrict the consideration to the case that the flux ropes are of like chirality, with the axial field component pointing into the same direction, as suggested by the event in Paper I. This can be expected to be the typical situation in split filaments that form side by side in the same filament channel and have common or close end points. The axial (toroidal) currents in the ropes then point in the same direction implying an attractive force between them.

The existence of a stable double flux rope equilibrium is not trivial if the ropes are relatively close to each other so that the force between them is comparable to or larger than the force exerted by the ambient field. Perturbations will trigger a pinching of the HFT between the ropes into a current sheet, where the subsequent reconnection will start redistributing the

Electronic address: bkliem@uni-potsdam.de

¹Institute of Physics and Astronomy, University of Potsdam, Karl-Liebknecht-Str. 24, 14476 Potsdam, Germany

²Mullard Space Science Laboratory, University College London, Holmbury St. Mary, Dorking, Surrey RH5 6NT, UK

³Predictive Science, Inc., San Diego, CA 92121, USA

⁴Space Weather Research Laboratory, Center for Solar-Terrestrial Research, NJIT, Newark, NJ 07102, USA

⁵CAS Key Laboratory of Geospace Environment, University of Science and Technology of China, Hefei 230026, China

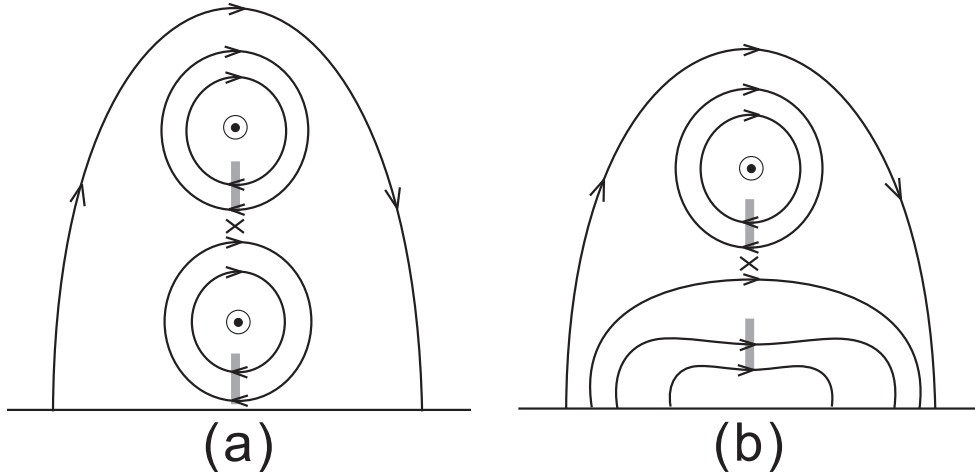


FIG. 1.— Cartoon illustrating the cross section of the two double-decker filament configurations suggested in Paper I: (a) double flux rope equilibrium; (b) flux rope above a sheared arcade. The axial field of both filament branches points in the same direction (out of the plane in the specific case analyzed in Paper I). The HFT is indicated by a small cross. Slabs of grey color indicate the filament body trapped in dipped field line sections.

magnetic flux between the ropes and the ambient field. This may cause the perturbation to grow, eventually merging the ropes or pushing them apart, depending on the properties of the configuration and perturbation.

Using an extension of the Shafranov equilibrium of a single toroidal force-free flux rope (Shafranov 1966; Titov & Démoulin 1999), we first demonstrate the existence, stability, and instability of an equilibrium containing two vertically arranged force-free flux ropes in bipolar external field (Section 2). We find that the external field’s toroidal (shear) component is a key parameter controlling the stability of the configuration if the ropes are relatively close to each other. We also demonstrate that a scenario of current and flux transfer from the lower to the upper rope, which resembles the flux transfer indicated by the observations, leads to instability of the upper flux rope only.

In Section 3 we describe an MHD simulation which exhibits the formation and subsequent splitting of two flux ropes in the slow-rise phase of a modeled filament eruption. Different from the model by Gibson & Fan (2006), this timing corresponds to the observations of the double-decker filament presented in Paper I.

2. STABILITY AND INSTABILITY OF A DOUBLE FLUX ROPE EQUILIBRIUM

2.1. Construction of the Equilibrium

We build on the construction of an approximate analytical equilibrium of a toroidal force-free flux rope in bipolar current-free external field in Titov & Démoulin (1999, hereafter TD99), done in two steps. First, the “external equilibrium” of the rope in a given simple (axisymmetric) external poloidal field B_{ep} is determined by balancing the Lorentz force of the flux rope current in the field B_{ep} with the Lorentz self-force (hoop force) of the current. Then an approximate “internal equilibrium” of the current channel in the core of the rope is constructed by matching the expressions for a straight force-free current channel in each cross section of the toroidal channel to the external field at its surface.

A second flux rope, lying in a concentric arrangement in the same plane as the first rope, can **easily** be added **at a sufficiently large distance, such that** its influence on the external equilibrium of the first rope is negligible. The second rope

can then be constructed in the same way as a single rope, except that the known poloidal field of the first rope must be added to the external poloidal field in determining the external equilibrium of the second rope. Since the equilibrium current decreases with increasing major radius of the torus (see Eq. 6 in TD99), the second rope must always have the larger major radius. This very simple approximation yields equilibria that readily relax to a numerical equilibrium very near to the analytical one as long as the ratio of the major radii is not reduced below ≈ 4 .

In order to find equilibria of two flux ropes with smaller distance, the construction of the external equilibrium in TD99 can straightforwardly be generalized. Doing so also for their construction of the internal equilibrium is a very involved task. However, applying the expressions for the internal equilibrium without modification to each channel individually yields an acceptable approximation down to ratios of the major radii of ≈ 2.5 . Subsequent numerical MHD relaxation quickly adjusts the internal equilibrium of the ropes and, supported by line tying in the photospheric boundary, yields a nearby force-free numerical equilibrium in the stable part of the parameter space.

If the external equilibrium of two current channels is considered, the relevant poloidal field is the superposition of the external poloidal field, B_{ep} , and the poloidal field by the other current channel, B_I , where I is the total toroidal (ring) current of the channel. In TD99 the external poloidal field is due to a pair of auxiliary magnetic charges $\pm q$ on the symmetry axis of the torus at distance $\pm L$ from the torus plane (or simply the field connecting the corresponding “sunspots” in the photospheric plane); we will also refer to this field component as B_q . Using subscripts 1 and 2 to denote quantities of the inner (lower) flux rope FR1 and outer (upper) flux rope FR2, respectively, we have the following dependencies on the flux rope currents: $F_{I_{1,2}} \propto I_{1,2}^2$ for the Lorentz self-force; $F_{q_{1,2}} \propto I_{1,2}$ for the force by the field from the magnetic charges; and $F_{B_{1 \rightarrow 2}} \propto I_1 I_2$ for the force due to the field of the other current channel. The resulting force equations,

$$0 = F_{I_1} + F_{q_1} + F_{B_{2 \rightarrow 1}} = b_1 I_1^2 + c_1 I_1 + e_1 I_1 I_2 \quad (1)$$

$$0 = F_{I_2} + F_{q_2} + F_{B_{1 \rightarrow 2}} = b_2 I_2^2 + c_2 I_2 + e_2 I_1 I_2, \quad (2)$$

can easily be solved for I_1 and I_2 , given the geometry ($R_{1,2}$,

$a_{1,2}, d, L$) and the strength of the field B_q , set by q and L . Here R and a denote major and minor torus radius, respectively, and d is the depth of the torus center below the photospheric plane. The expressions of the coefficients $b_{1,2}$, $c_{1,2}$, and $e_{1,2}$ can be found in TD99 (their Equations 5, 4, and 25, respectively). As in TD99, an axisymmetric external toroidal field B_{et} of arbitrary strength can be superposed. It is provided by an auxiliary line current I_0 running along the symmetry axis of the tori.

The resulting equilibrium is only a very crude approximation of the suggested interpretation of the double-decker filament in Paper I in terms of two flux ropes. Both ropes in the model must have toroidal shape, so that their footpoints are quite separate, different from the observed configuration. Moreover, the use of a line current as the source of the external toroidal field, dictated by the concentric arrangement of the tori, prevents us from realistically modeling an ejective eruption (a CME). Since the resulting B_{et} falls off only linearly with distance from the torus center, it enforces any eruption to remain confined for realistic values of its strength (Roussev et al. 2003; Török & Kliem 2005). On the other hand, the configuration allows us to demonstrate the existence of the suggested equilibrium, the instability of only the upper flux rope for certain parameter settings, and the key role of B_{et} . This can be done for a geometry that matches the observed height relationships between the lower and upper filament branches at the apex points of the two flux ropes.

The double flux rope equilibrium is intrinsically less stable than the equilibrium of a single toroidal flux rope, due to the additional force between the ropes. To attain a stable force-free equilibrium in the absence of an external toroidal field, the ropes must be positioned sufficiently far apart, so that $F_{B_{1 \rightarrow 2}}$ is small compared to $F_{q_{1,2}}$, and B_q must be relatively uniform, i.e., L must be large. The slope of the total poloidal field as a function of R then remains sufficiently small at the positions of both ropes, so that both are stable against vertical displacements (Kliem & Török 2006). Here we have to consider a situation with the flux ropes situated relatively close to each other and the sources of the field B_q also being relatively close (see below). In this case, an external toroidal field is required for stability. If one or both ropes are displaced by a perturbation, the compression of this field component will counteract the perturbation. Thus, the strength of the external toroidal field is a key parameter deciding between stability and instability of the configuration.

This is confirmed in the following subsection by MHD relaxation runs, which also show that a size ratio $R_2/R_1 \gtrsim 2.5$ is required for the analytical equilibrium to be close to a stable numerical one with the HFT lying not too close to the current channel in the lower rope. In the stable domain of parameter space, reconnection at the HFT remains very weak, just redistributing the fluxes to the extent needed to reach the nearby numerical equilibrium.

Prominence material in flux ropes is supposed to be trapped in dips of the field lines, i.e., it can occupy a slab-like volume extending between the bottom flux surface and the magnetic axis of the rope (Figure 1). The height measurements of the two filament branches on 2010 August 7 (Section 2.3 in Paper I) thus suggest apex heights of 12 and 36 Mm for the magnetic axis of FR1 and FR2, respectively, and an apex height of 25 Mm for the HFT (which is the bottom of the upper flux rope on the vertical line through the apex). The first two measurements are met, for example, by the choice $R_1 = 16$ Mm, $R_2 = 40$ Mm, $d = 4$ Mm. The third measurement can be met to

a good approximation by the choice $a_1 = 4$ Mm, $a_2 = 6$ Mm, resulting in an HFT apex height of 23 Mm. We have chosen the current channels to be relatively thin, so that both possess a large aspect ratio, which guarantees relatively high precision in the construction of the equilibrium (TD99). Note that it is the larger cross section of the magnetic structure (the flux rope) which matters for the location of field line dips, not the cross section of the current channel. To have the HFT apex lying exactly at the estimated height of 25 Mm, we would have to choose $a_2 = 2$ Mm, smaller than a_1 , which we consider neither appropriate nor necessary for the purpose of this study. Under the force-free constraint, the relatively small values of the minor radii imply relatively high values of the flux rope twists. Both ropes are stabilized against the helical kink mode by the external toroidal field. We set $L = 8$ Mm, corresponding to the distance of the main photospheric flux concentrations near the middle section of the filament (Figure 2 in Paper I).

2.2. Numerical Simulations

2.2.1. Stable Configuration

The resulting analytical equilibrium is used as initial condition in zero-beta MHD simulations in a cubic Cartesian box more than five times higher than FR2 and resolving the minor diameter of the current channel in FR1 by 35 grid cells. The initial density is specified as $\rho_0(\mathbf{x}) = |\mathbf{B}_0(\mathbf{x})|^{3/2}$, where $\mathbf{B}_0(\mathbf{x})$ is the initial magnetic field, so that the Alfvén velocity decreases slowly with height above the flux rope, as in the solar corona.

To check the equilibrium currents $I_{1,2}$ obtained from Eqs. (1–2), the field B_{et} is first set to a value somewhat below the value that provides stability. After normalizing by the apex height of FR1, $h_1 = R_1 - d$, and by the corresponding Alfvén time $\tau_A = h_1/V_A$, where V_A is the Alfvén velocity at the magnetic axis of FR1, the system is integrated in time for $100 \tau_A$. This reveals both the quality of the equilibrium and its unstable nature. The system first attempts to settle to an exact numerical equilibrium from the approximate analytical one, with velocities rising to the very modest values of only $\approx 0.003 V_A$ in FR1 and only $\approx 0.001 V_A$ in FR2, which already indicates that the analytical equilibrium is nearly perfect. Subsequently, the velocities in both ropes fall very gradually to nonzero values, i.e., the system fails to settle fully to a numerical equilibrium. By slightly modifying one of the currents, a nearly perfect equilibrium is found, with the residual velocities of FR1 falling monotonically to $1.4 \times 10^{-4} V_A$ and the ones of FR2 oscillating very gradually around a value $6 \times 10^{-4} V_A$ by $t = 100 \tau_A$; this requires reducing I_1 by 0.5%.

Next, this configuration is integrated for a range of B_{et} values, with a velocity perturbation applied at the apex of both flux ropes to find the minimum stabilizing external toroidal field. The velocity perturbation is applied for $5 \tau_A$, linearly ramped up to the peak value of $\pm 0.05 V_A$ and then switched off. Marginal stability (the critical value $B_{\text{et, cr}}$) is found for B_{et} slightly below $1.7 B_q$, with B_{et} and B_q taken at the lower flux rope’s magnetic axis. Figure 2 shows field lines of the stable analytical equilibrium with $B_{\text{et}} = 1.7 B_q$ and of the configuration after numerical relaxation, along with height and velocity of the fluid elements at the apex points of the two flux ropes in the relaxation run. This stable numerical equilibrium is very close to the analytical one.

The external toroidal (shear) field strength required for stability is relatively high, exceeding the poloidal component of the external field (perpendicular to the filament). This situation can be realized if the filament ends in the main flux con-

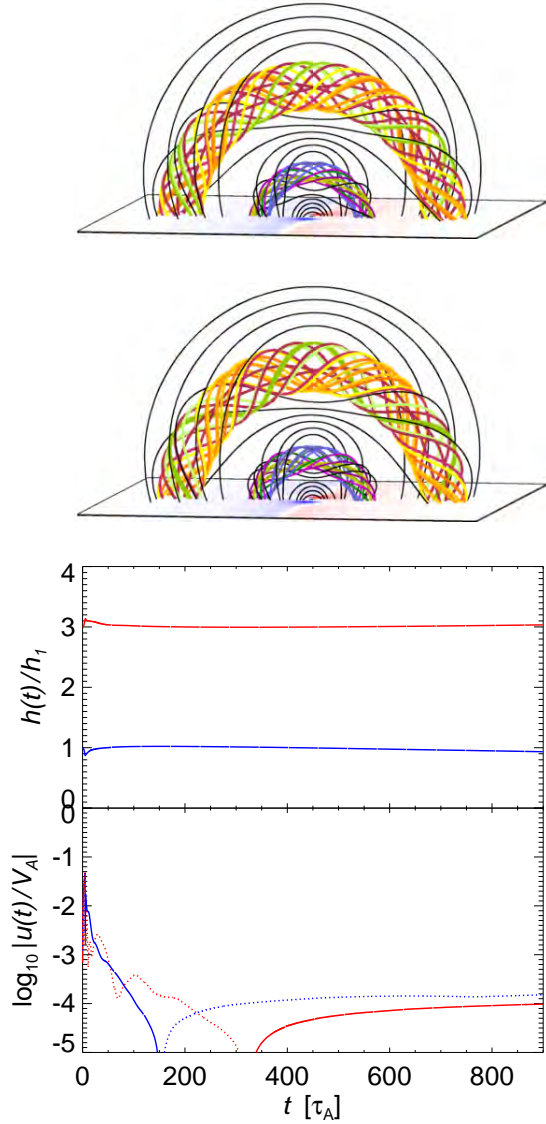


FIG. 2.— Field lines showing the two flux ropes in the stable analytical equilibrium with $B_{\text{et}} = 1.7B_q$, slightly above the marginal stability value of the external toroidal field (top panel) and after numerical relaxation at $t = 645\tau_A$ (middle panel). The field lines lie in flux surfaces near the surface of the current channels (slightly inside the channel for FR1). All black field lines pass through the vertical axis in the middle of the system, illustrating the apex heights of the two HFTs (below the lower rope FR1 and between FR1 and FR2) by the transition between downward and upward concave curvature. The magnetogram, $B_z(x, y, 0, t)$, is displayed in the bottom plane. The bottom panel shows height and velocity of the fluid elements at the apex points of the magnetic axes of the two ropes in the relaxation run. Due to the symmetry of the system, these fluid elements move only vertically. The relaxation run includes an initial velocity perturbation in small spherical volumes centered at the two apex points, applied up to $t = 5\tau_A$. Downward velocities are shown dotted.

centrations of the active region. These sources then provide not only the axial field of the filament, but also give the ambient field a strong component in the direction of the filament. The filament investigated in Paper I did have this configuration.

2.2.2. Unstable Configurations

If the stabilizing external toroidal field strength is slightly reduced below the threshold value $B_{\text{et,cr}} \approx 1.7B_q$, the configuration can no longer be relaxed to a nearby equilibrium (Section 2.2.1). The nature of the instability and the com-

plexity inherent in the configuration become apparent when B_{et} is reduced considerably. In this and the following two paragraphs we refer to simulations with $B_{\text{et}} = B_{\text{et,cr}}/3$ when quoting numbers. Identical qualitative behavior is obtained in the range $0 \leq B_{\text{et}} \lesssim B_{\text{et,cr}}/2$. The simulations confirm that both flux ropes are unstable against vertical displacements (i.e., the torus instability) for the geometrical parameters chosen. The relevant parameter is the “decay index” of the total poloidal field at the position of each rope, $n = -d \ln(B_q + B_l)/d \ln h$, where B_l is the poloidal field from the other rope. Its threshold value lies in the range $n_{\text{cr}} \approx 1.5\text{--}2$ if B_{et} is small (Kliem & Török 2006; Török & Kliem 2007). Our configuration yields $n_1 = 3.1$ and $n_2 = 2.8$, implying a higher growth rate for the instability of the lower flux rope FR1. (Additionally, higher Lorentz forces can be expected to develop in the evolution of the lower rope, since the field strength and current density are higher.) The decay index at the position of the lower flux rope generally has a high value, since the poloidal field of the upper flux rope, B_{l_2} , and the external poloidal field, B_q , are oppositely directed under the upper rope. The decay index at the position of the upper flux rope is largely determined by the field B_q , which has a supercritical decay index at heights exceeding $\sim L$. This condition is clearly met by our choice of geometrical parameters. Obviously, both flux ropes in a double flux rope equilibrium of the type studied in this paper tend to be torus unstable if the external toroidal (shear) field falls below the threshold value $B_{\text{et,cr}}$.

Two different evolutions are enabled by the dominant instability of the lower flux rope. When a small upward perturbation is applied to FR1, it then shows an exponential rise which saturates as the upper rope FR2 is approached. FR2 stays near its initial position in this period. Subsequently, the ropes merge, forming an arch which expands upward with a velocity of order $0.1 V_A$ (Figure 3). The rise is terminated at about four times the initial height of the upper rope, $h_2 = R_2 - d$, by the onset of reconnection between the legs of the strongly writhing rope and the ambient field. The writhing is here primarily due to the presence of B_{et} (Isenberg & Forbes 2007; Kliem et al. 2012), i.e., it does not indicate the development of the helical kink instability. The velocity doubles and the rise continues until the upper boundary of the box is approached if B_{et} is reduced further, below $\sim B_{\text{et,cr}}/10$. This full eruption is clearly driven by the stronger torus instability of the lower flux rope and is very similar to the eruption of a single torus-unstable flux rope.

When a small downward perturbation is applied to FR1, it shows a short, exponentially increasing downward displacement until the bottom boundary of the box (the model photosphere) is hit. FR1 then reconnects with the sunspot field, splitting in two low-lying ropes which come to rest at the bottom of the box. FR2 immediately begins an exponential rise which enters the saturation phase at about $1.5h_2$, followed by an approximately linear rise, again with a velocity of order $0.1 V_A$ (Figure 4). Similar to the case in Figure 3, reconnection between the legs of the writhing rope and the ambient field terminates the rise at $\sim 4h_2$, but a further reduction of B_{et} to $\sim B_{\text{et,cr}}/10$ allows the upper flux rope to double the rise velocity and to escape (i.e., reach the top boundary of the box). Hence, a partial eruption (of only the upper flux rope) occurs, but it is accompanied by a strong change of the lower flux rope.

The scenario of decreasing B_{et} considered here may easily be realized on the Sun as the sources of the external toroidal

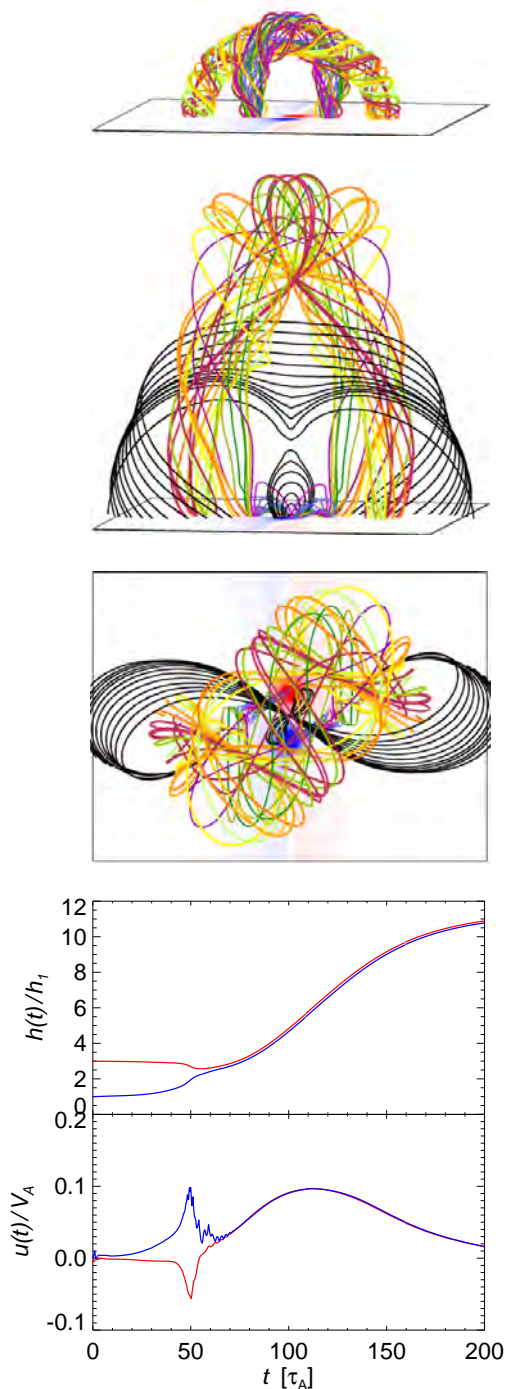


FIG. 3.— Instability and full eruption of the double flux rope equilibrium in the case of sub-critical external toroidal field, $B_{\text{et}} = B_{\text{et,cr}}/3$, and upward motion of the lower rope. Field line plots similar to Figure 2 are shown at $t = 65 \tau_A$ (top panel) and $t = 165 \tau_A$ (second and third panel). The lower flux rope largely merges with the upper one; the other part of its flux reconnects with the ambient flux to join the forming post-eruption arcade. The motion of the fluid elements at the apex points of the flux ropes is displayed in the bottom panel. A small upward initial velocity perturbation is applied at the apex of the lower flux rope.

field weakened by flux dispersal and cancellation. Thus, the eruption of double flux rope equilibria on the Sun will often involve a complete change of the configuration, both for full and partial eruptions. Since B_{et} will typically decrease only very gradually, the instability will set in long before a value

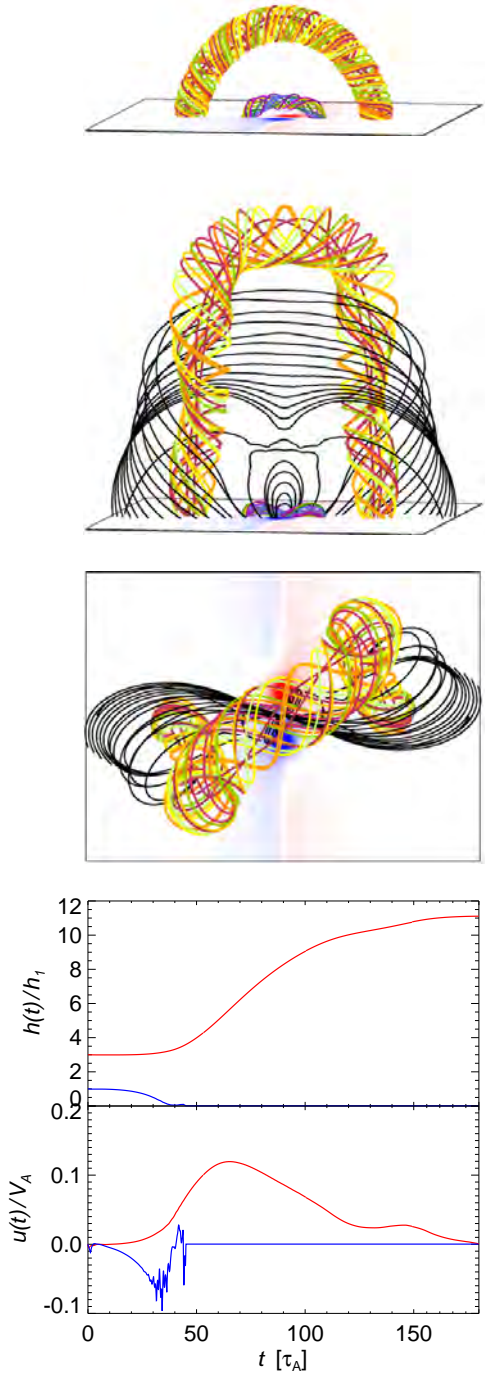


FIG. 4.— Same as Figure 3 for the case of downward moving lower rope (following a small downward velocity perturbation) at $t = 30 \tau_A$ (top panel) and $t = 100 \tau_A$ (second and third panel). Here all of the flux in the lower rope moves downward and reconnects with the ambient flux.

of order $B_{\text{et,cr}}/3$ is reached. Nevertheless, the upward directed velocities in such eruptions can be expected to be similar to or even higher than the values found in the simulations, since the external toroidal field in the corona is expected to fall off with height above the filament much faster than the model field, which is unrealistic in this regard (Section 2.1). The downward directed velocities should remain considerably below the simulated ones, since B_{et} will be much closer to the threshold value in this height range. Thus, in the scenario of eruptions driven by gradually reducing external toroidal field,

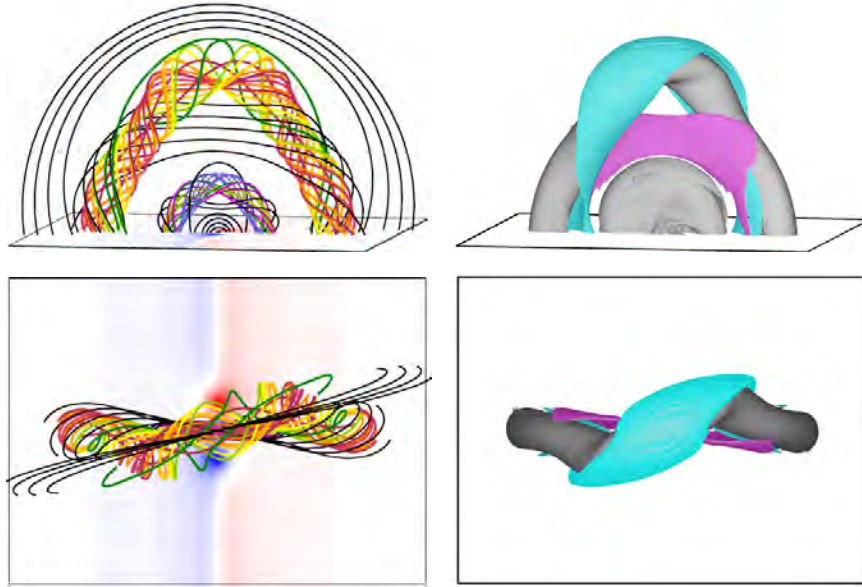


FIG. 5.— Partial eruption of the double flux rope equilibrium due to the instability of the upper rope after flux and current transfer from the lower rope ($\Delta I_2/I_2 = 0.1$) at the marginal stability condition in the absence of flux transfer, $B_{\text{et}} = B_{\text{et,cr}}$. Field lines similar to Figure 2 and current density isosurfaces at $|\mathbf{J}| = 0.07J_{\text{max}}$ show snapshots of the system at $t = 645 \tau_A$. The helical and vertical current sheets are colored in cyan and magenta, respectively. The ensuing reconnection of the unstable rope with the overlying field, which subsequently cuts the whole rope so that it remains confined in spite of the instability, is indicated by the dark green field lines.

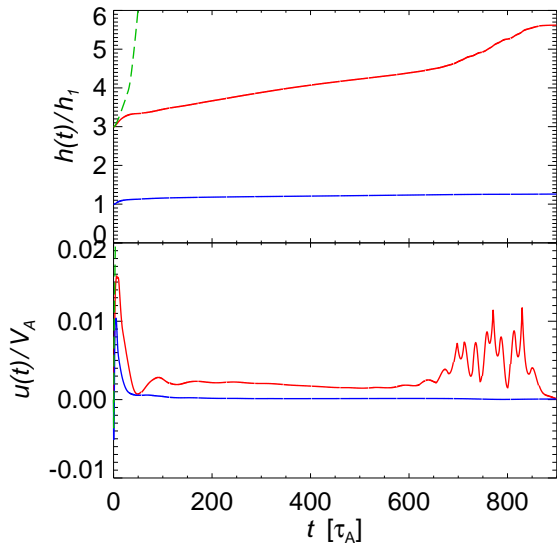


FIG. 6.— Height and velocity of the fluid elements at the apex points of the two ropes in the partial eruption shown in Figure 5, which does not employ any explicit perturbation. The dashed green lines show the rise of the unstable upper flux rope when B_{et} is reduced by a factor 10.

a partial eruption may have a less dramatic effect on the lower flux rope than found in the simulation, but a destruction of the lower flux rope must still be expected. However, partial eruptions involving only the upper flux rope, with the lower flux rope remaining stable at its initial position, are also possible.

Such a partial eruption can result under the same scenario of decreasing B_{et} if the upper flux rope is sufficiently twisted, so that the helical kink instability develops in the upper rope while the lower rope is still stable against the torus instability. We have verified this possibility by reducing the minor radius of the upper rope to $a_2 = 3.5 \text{ Mm}$, which doubles its twist to about 10π , with B_{et} kept at the critical value of $1.7B_q$ of the original configuration. The upper rope then kinks upward,

while the lower rope stays very close to its original position with very small residual velocity for more than $100 \tau_A$, i.e., apparently in a stable state. However, the occurrence of such high twist values is very unlikely and has so far been reported only in a single case (Romano et al. 2003). Therefore, we now consider another scenario for partial eruptions of double flux rope equilibria.

Based on the observation that the most significant change in the energy buildup phase prior to the eruption studied in Paper I consisted in the transfer of material and (necessarily current-carrying) flux from the lower to the upper branch of the filament, we next raise the current I_2 through the upper flux rope and decrease I_1 in the lower rope, keeping the total current $I_1 + I_2$ at the equilibrium value (and also $B_{\text{et}} = 1.7B_q$). This moves the HFT between the ropes a little bit downward, so that the cross sections and the total flux in the ropes experience a change similar to the currents. We have considered changes $\Delta I_2 = 0.05I_2, 0.1I_2,$ and $0.2I_2$, with the corresponding changes of I_1 being close to $-\Delta I_2/2$. Integrating the resulting analytical configurations in time shows nearly identical behavior in all three cases, except that the time scale of the evolution roughly halves with each doubling of ΔI_2 . (The run with $\Delta I_2/I_2 = 0.05$ begins to show signs of numerical diffusion, slightly damping the intrinsic dynamics of the flux ropes in the course of the $> 6 \times 10^5$ time steps performed, but it still clearly shows the dynamics as described here.) The upper rope FR2 first moves relatively quickly upward, to find the equilibrium position corresponding to the increased current $I_2 + \Delta I_2$ in about $30 \tau_A$. From this position, an approximately linear ascent to $\approx (1.5-2)h_2$ commences. In the course of this rise, the left-handed rope writhes into a projected forward S shape, piling up a helical current sheet at its front side, analogous to the runs shown in Figures 3 and 4. Simultaneously, the HFT between the ropes collapses into a vertical current sheet. The upward outflow resulting from the onset of reconnection in this current sheet accelerates FR2 to a rise faster than linear. Since the overlying field resists the rise (primar-

ily due to the relatively strong B_{et}), the top part of the helical current sheet is quickly steepened and reconnection between FR2 and the overlying field commences at the rope apex, cutting the rope in two halves which remain confined. The torus instability of the lower flux rope FR1 is efficiently suppressed by the external toroidal field. FR1 stays near its initial position for more than $10^3 \tau_A$ with velocities remaining smaller than the rise velocity of FR2 by a factor ~ 20 .

Figure 5 shows a snapshot of this evolution for the system with $\Delta I_2/I_2 = 0.1$. Figure 6 characterizes the motion of the fluid elements at the apex points of the two flux ropes. The additional acceleration of FR2 by the upward reconnection outflow is seen at $t \gtrsim 650 \tau_A$. The terminal height of FR2 in this plot is the result of reconnection with the overlying field.

Finally, to demonstrate that the rise of FR2 is driven by an instability, the run with $\Delta I_2/I_2 = 0.1$ is repeated with B_{et} reduced by a factor 10. Now the rise from the equilibrium position is initially relatively close to an exponential function, as expected for an instability developing in a weakly perturbed equilibrium (see Figure 6). (As discussed above, for this low value of B_{et} the lower flux rope FR1 is unstable as well.)

On the Sun, both the long-term stability of the double-decker filament and the ejective eruption of the upper branch into a CME can be allowed by an external toroidal field of the strength required for stability at the position of the filament, but falling off with height above the filament much faster than the model field. Our model field is unrealistic in this regard but the coronal field is generally expected to satisfy this condition.

The transfer of flux from the lower to the upper flux rope is different from flux transfer by reconnection at the HFT between the ropes, e.g., tether-cutting reconnection. Such reconnection would exchange flux in both ropes with ambient flux. It is conceivable that the transfer is enforced by configuration changes of the current in the lower flux rope, which, in turn, can be enforced by changes in the photospheric boundary. It is well known that current-carrying flux rises if it is stressed (sheared or twisted) by photospheric motions (e.g., Mikic & Linker 1994; Török & Kliem 2003). In the considered event, such processes may have acted preferentially in the footpoint areas of the lower flux rope.

3. SPLITTING FLUX BUNDLE IN THE SLOW RISE PHASE OF A CME

The formation and partial eruption of a double flux rope configuration was also found in an MHD simulation that was designed to model the well-known filament eruption and CME on 1997 May 12 (e.g., Thompson et al. 1998; Webb et al. 2000). The details of this simulation will be described elsewhere (Linker et al., in preparation); here we merely summarize its main features and focus on the evolution shortly before the eruption.

The simulation code solves the standard resistive and viscous MHD equations on a spherical grid and incorporates radiative losses, thermal conduction parallel to the magnetic field, and an empirical coronal heating function (see, e.g., Mikić et al. 1999; Lionello et al. 2009). The latter allow the modeling of prominence formation due to plasma condensation. The initial magnetic field in the simulation is obtained from a potential field extrapolation, using a combination of synoptic and real-time line-of-sight magnetograms (for a simplified model of the large-scale magnetic configuration around the time of the eruption, see Titov et al. 2008). After a solar wind MHD solution is obtained by relaxing the system

to a steady state, the CME-producing active region is energized by a combination of photospheric shear flows and transverse field “emergence”, which both keep the radial flux distribution unchanged (e.g., Linker et al. 2001; Bisi et al. 2010). This produces a highly sheared core field with little indications of twist, i.e., of flux rope geometry. Finally, the system is further energized, and an eruption is triggered, via flux cancelation, driven by localized flows converging toward the photospheric polarity inversion line (PIL) (e.g., Linker et al. 2003).

During the energization of the system, a sheet-like, coherent structure of cold and dense plasma forms within the core field (Figure 7(b),(c)). Interestingly, a significant fraction of this plasma is not located in concave-up field line segments, so the common picture of prominence material held against gravity in dipped fields does not seem to fully apply here. The detailed mechanisms by which this “prominence” is formed and maintained in the simulation require further study – it seems that both levitation of chromospheric plasma and condensation of coronal material are involved. For our present purpose, it is sufficient to consider its evolution in the phase leading up to the eruption.

It has been shown that magnetic reconnection associated with flux cancelation successively transforms a sheared arcade into a flux rope, which slowly detaches from the photosphere, leaving behind short arched field lines (e.g., van Ballegooijen & Martens 1989; Amari et al. 2003; Aulanier et al. 2010). A similar process occurs in our simulation during the cancelation phase, although the evolution is more complex (Titov et al., in preparation). As can be inferred from vertical cuts of the so-called squashing factor Q (Titov et al. 2002), the core field consists of several flux bundles before it erupts (Figure 7(d)). The central flux bundle contains two adjacent flux ropes: a highly twisted low-lying one and an arched, less twisted upper one (Figure 7(a)). These two structures start to form relatively early in the cancelation phase, and gradually develop a flux rope geometry as they accumulate twist about their respective axes. However, in contrast to the distinct flux ropes considered in the previous subsection, a clear boundary between them does not develop; rather they remain merged to some extent for most of the cancelation phase. (Interestingly, although the upper flux rope possesses twist, it does not contain dipped field lines below its axis, which is due to its strong curvature.)

In the course of the flux cancelation and associated reconnection, the core field first expands quasi-statically until, after about 3.5 hours, its slow evolution transitions into a fast rise phase, marking the onset of the eruption (Figure 7(e)). In the pre-eruptive phase, the central flux bundle becomes increasingly stretched in the vertical direction. Shortly before the eruption, the splitting into two parts becomes more pronounced (Figure 7(d)), which is associated with tether-cutting reconnection of ambient flux into the core flux at the HFT between the two main flux bundles. The added flux runs under the apex of the upper flux rope and contributes to its twist, thus, it potentially acts destabilizing. For the lower rope, the added flux acts like strengthened overlying flux, thus stabilizing. The increasing separation of the flux ropes is accompanied by a splitting of the plasma sheet (Figure 7(b),(c)). Subsequently, the eruption carries away the upper flux rope and the top part of the plasma sheet, while the lower rope and the bottom part of the sheet remain at low heights.

The origin of the splitting of the central flux bundle must be different from the partial eruption mechanism modeled by

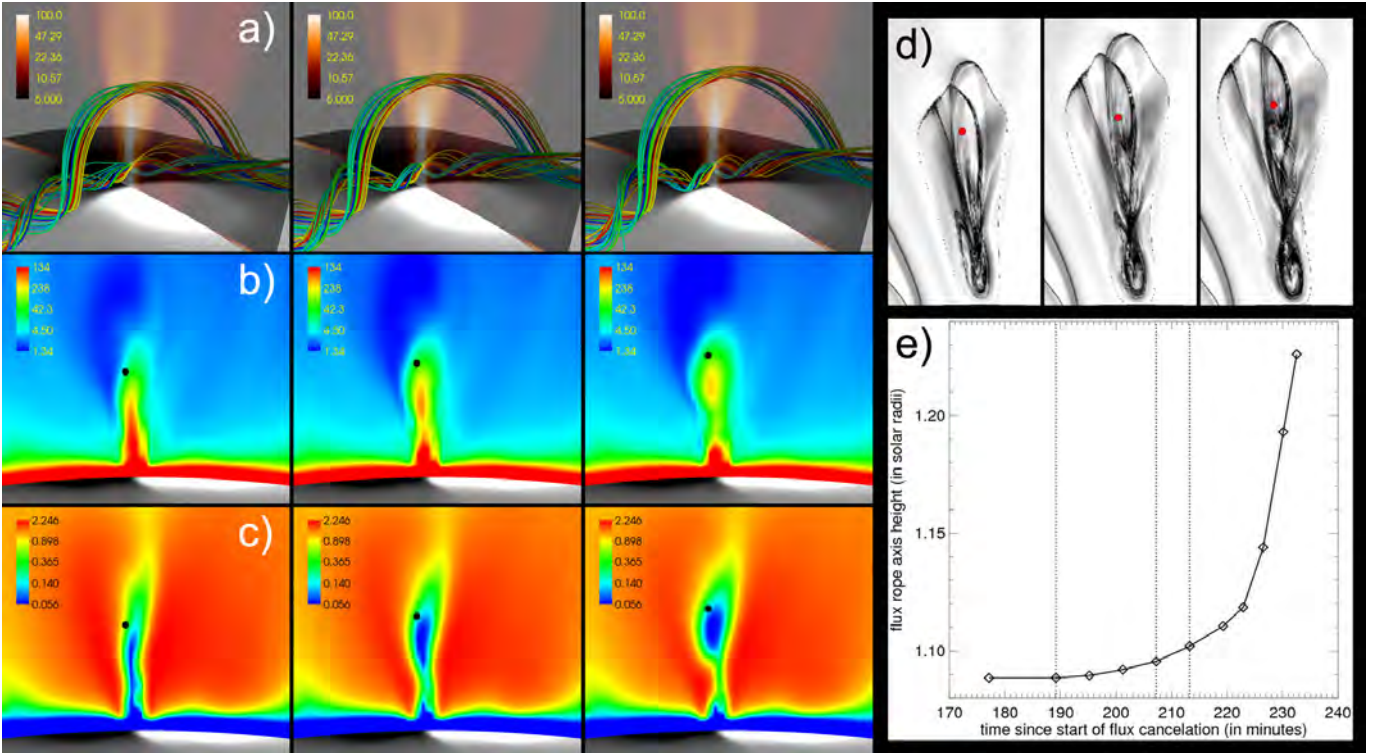


FIG. 7.— Snapshots of the 1997 May 12 simulation during the pre-eruptive phase. Panels (a–d): Vertical cuts perpendicular to the flux rope axis, taken at the apex of the upper rope; the specific times of the sub-panels from left to right are marked by dotted lines in the time–height profile of the upper flux rope axis apex shown in Panel (e). Panel (a) shows the (transparent) logarithmic distribution of the ratio of electric current density and magnetic field strength, j/B (in normalized units), and magnetic field lines that outline the cores of the upper and lower flux rope in an oblique view. Panels (b–d) are views along the upper flux rope axis, showing mass density ρ (in $10^{-16} \text{ g cm}^{-3}$), temperature T (in MK), and the logarithmic distribution of the squashing factor Q (shown in a zoomed-in view), respectively. The dots in panels (b–d) mark the approximative position of the upper flux rope axis apex. The radial magnetic field is shown in panels (a–c) at the photospheric plane, where white (black) colors outline strong positive (negative) flux.

Gibson & Fan (2006). There, the splitting of one coherent flux rope into two parts was associated with reconnection occurring in a current layer that formed in the course of the rope’s eruption, due to a deformation (writhing) of the rope by the helical kink instability. In our case, the splitting occurs already in the pre-eruptive stage, during which no noticeable helical deformation takes place (Figure 7(a)). Moreover, two flux ropes form within the central flux bundle even earlier in the evolution. In a later simulation described in Fan (2010), where the eruption was driven by the torus instability, a current layer formed within the flux rope already in the pre-eruptive phase, and a similar breaking of the magnetic structure as in our simulation was observed (Y. Fan, private communication). Further study is required to fully understand how the splitting of the magnetic flux occurs in our simulation. A number of aspects may play a role, as for example the complexity of the initial potential field, the specific techniques by which the system is driven, gravity in regions of strong density, and reconnection at bald patches in the outer parts of the PIL.

By producing two stacked flux ropes early on in the evolution leading up to an eruption, our simulation supports the conjecture that such a configuration can exist in stable state for long periods in the corona, and it provides indications for their possible formation. Also, the splitting of the plasma sheet corresponds nicely to the observed separation of the two filament branches in the event analyzed in Paper I. However, the plasma splitting occurs only rather shortly before the eruption, different from the 2010 August 7 event (although the separation of the branches was most pronounced shortly

before the eruption of the upper branch; see Figure 4 in Paper I). We did not succeed in producing a stable or longer-lasting configuration with a split plasma sheet by, for instance, switching off the flux cancellation at earlier times in the simulation. It seems that, at least for the specific parameters that were used to control the formation and driving of the core field in our simulation, such a configuration is difficult to obtain. The absence of plasma splitting at an earlier stage of the simulation might be due to the absence of field line dips in the upper flux rope. It remains to be seen whether the formation of (meta-)stable double-decker filament configurations can be modeled by simulations similar to the one presented here, or whether different physical mechanisms (as for example flux emergence) are required.

4. CONCLUSIONS AND DISCUSSION

An approximate analytical equilibrium of two concentric, toroidal, force-free flux ropes can be constructed by a generalization of the methods developed in Titov & Démoulin (1999). The technique **can be used** for ratios of the major torus radii $R_2/R_1 \gtrsim 2.5$ and should be supplemented by numerical MHD relaxation to a nearby numerical equilibrium in the range $R_2/R_1 \lesssim 4$.

The equilibrium is stabilized by an external toroidal field B_{et} of sufficient strength, which can be considerable if the flux ropes are located relatively close to each other. For the geometry studied here, $R_2/R_1 = 2.5$ and the ratio of minor torus radii $a_2/a_1 = 1.5$, we find that $B_{\text{et}} > B_{\text{et,cr}} \approx 1.7B_q$ is required, where B_q is the external poloidal field strength at the position of the inner (lower) flux rope.

The analytical construction of a double flux rope equilibrium with $B_{\text{et}} \neq 0$ in this paper is restricted to the case that a line current at the symmetry axis of the tori is the source of B_{et} . Therefore, B_{et} decreases only weakly with increasing distance R from the symmetry axis, $B_{\text{et}} \propto R^{-1}$. This allows only confined eruptions to be modeled (except in the case that B_{et} is set considerably below $B_{\text{et,cr}}$).

If the external toroidal field strength is reduced, then both flux ropes tend to become torus unstable. Typically the lower (inner) flux rope exhibits the stronger instability. This is due to the facts (i) that the poloidal field by the upper (outer) flux rope is oppositely directed to the external poloidal field at the position of the lower flux rope, giving the total poloidal field at this position a steep decrease with height, and (ii) that field and current are generally stronger in the lower flux rope. If the lower flux rope erupts upward, it pushes the upper rope upward as well. A full eruption of the configuration results which is quite similar to the eruption of a single flux rope. If the lower rope moves downward, it reconnects with the ambient field, splitting and coming to rest low in the box. This is accompanied by the upward eruption of the upper rope. However, it is also possible that only the upper flux rope turns unstable, with the lower rope staying in place without experiencing any significant change. This occurs in a scenario suggested by the observations in Paper I and demonstrated here: transfer of flux and current from the lower to the upper flux rope.

An equilibrium consisting of two force-free flux ropes, arranged vertically above a photospheric boundary, is also numerically obtained through an evolutionary sequence of shear flows, flux emergence, and flux cancellation in the photosphere. The stable double flux rope structure shows a slow rise in the cancellation phase. This evolution gradually transitions into a faster rise involving **tether-cutting reconnection with the ambient field at the HFT between the ropes**. Such reconnection lowers the stability of the upper flux rope and improves the lower rope's stability. Thus, it is a second potential driver for a partial eruption. The simulation indeed yields an eruption of the upper flux rope while the lower rope remains at low heights.

A **third possibility, although less likely**, consists in building supercritical twist for onset of the helical kink instability only in the upper flux rope.

Both the existence of stable double flux rope equilibria and the possibility that only the upper flux rope loses stability support the suggestion that the split, partially erupting filament investigated in Paper I may have formed in such a configuration.

This topology may not be a rare occurrence, since split filaments and prominences are seen quite frequently and since partial eruptions are not uncommon (e.g., Pevtsov 2002). One can expect this also from the fact that the simulation in Section 3 was designed to model another event and yet shows a double flux rope. Moreover, the double flux rope topology may not only be relevant for split filaments and prominences, since one of the flux ropes, especially the upper one, may be void of absorbing material. The existence of two flux ropes is quite likely in an event on 2010 March 30 which exhibits both confined and ejective components in a common eruption

(Koleva et al. 2012). Both main branches of a split prominence were seen to erupt successively in an event on 2010 April 8 (Su et al. 2011), possibly providing an example for the case that the lower rope in a double flux rope equilibrium loses stability first.

The support for the double flux rope configuration given here does not imply that the alternative configuration of a single flux rope situated above a magnetic arcade is less feasible. That configuration actually has advantages in terms of stability (it does not necessarily require a strong external shear field component to suppress instabilities), and it naturally allows partial eruptions that do not strongly perturb the lower part of the flux. However, at present it is unclear whether this configuration can stably exist for extended periods of time in spite of a changing photospheric boundary. Several investigations have suggested that the slow evolution of active regions toward an eruption may typically involve the formation of this configuration (e.g., Titov & Démoulin 1999; Aulanier et al. 2010). Recent studies indicate further that the system may already be close to the eruption when the HFT forms (Su et al. 2011; Savcheva et al. 2012). Typically, flux cancellation is a main driver in this final part of the evolution. Since flux cancellation is a common process, the **quasi-static evolution phase** of the configuration may typically be relatively short. The split filament studied in Paper I existed for a considerable period of at least two days. However, in this case, this is not in conflict with the assumption of a single rope and HFT structure, since the flux cancellation under the filament was observed to remain weak in this period.

Several new scenarios for partial eruptions are suggested by the investigations presented in Paper I and here. The upper part of a split flux system can erupt without strongly perturbing the lower part in the double flux rope configuration when only the upper flux rope is unstable (Figures 5–7), **which can be achieved by flux transfer from the lower to the upper rope and by tether-cutting reconnection with the ambient field in the space between the ropes**. Similar evolutions are possible in the configuration with a single flux rope separated by an HFT from an underlying arcade (Figure 1). The double flux rope configuration also allows the eruption of the upper flux rope accompanied by downward motion and eventual destruction of the lower flux rope if the lower flux rope is unstable. In each of these cases, the flux can be split already during long periods before the eruption starts, in line with the properties of the filament studied in Paper I. This distinguishes them from the well known mechanism of a splitting unstable and lined-tied flux rope in Gibson & Fan (2006) (see also Gilbert et al. 2001), which involves a splitting of the flux only in the course of the eruption.

B.K. acknowledges support by the DFG and the STFC. The contributions of T.T., V.S.T., R. Lionello, and J.A.L. were supported by NASA's HTP, LWS, and SR&T programs, and by CISM (an NSF Science and Technology Center). Computational resources were provided by NSF TACC in Austin and by NASA NAS at Ames Research Center. R. Liu, C.L., and H.W. were supported by NSF grants ATM-0849453 and ATM-0819662.

REFERENCES

- Amari, T., Luciani, J. F., Aly, J. J., Mikic, Z., & Linker, J. 2003, *ApJ*, 585, 1073
 Aulanier, G., Török, T., Démoulin, P., & DeLuca, E. E. 2010, *ApJ*, 708, 314
 Bisi, M. M., Breen, A. R., Jackson, B. V., Fallows, R. A., Walsh, A. P., Mikić, Z., Riley, P., Owen, C. J., Gonzalez-Esparza, A., Aguilar-Rodriguez, E., Morgan, H., Jensen, E. A., Wood, A. G., Owens, M. J., Tokumaru, M., Manoharan, P. K., Chashei, I. V., Giunta, A. S., Linker, J. A., Shishov, V. I., Tyul' Bashev, S. A., Agalya, G., Glubokova, S. K., Hamilton, M. S., Fujiki, K., Hick, P. P., Clover, J. M., & Pintér, B. 2010, *Sol. Phys.*, 265, 49

- Fan, Y. 2010, *ApJ*, 719, 728
- Gibson, S. E., & Fan, Y. 2006, *ApJ*, 637, L65
- Gilbert, H. R., Holzer, T. E., & Burkepile, J. T. 2001, *ApJ*, 549, 1221
- Isenberg, P. A., & Forbes, T. G. 2007, *ApJ*, 670, 1453
- Kliem, B., & Török, T. 2006, *Phys. Rev. Lett.*, 96, 255002
- Kliem, B., Török, T., & Thompson, W. T. 2012, *Sol. Phys.*, in press
- Koleva, K., Madjarska, M. S., Duchlev, P., Schrijver, C. J., Vial, J.-C., Buchlin, E., & Dechev, M. 2012, *A&A*, 540, A127
- Linker, J. A., Lionello, R., Mikić, Z., & Amari, T. 2001, *J. Geophys. Res.*, 106, 25165
- Linker, J. A., Mikić, Z., Lionello, R., Riley, P., Amari, T., & Odstrčil, D. 2003, *Physics of Plasmas*, 10, 1971
- Lionello, R., Linker, J. A., & Mikić, Z. 2009, *ApJ*, 690, 902
- Liu, R., Kliem, B., Török, T., Liu, C., Titov, V. S., Lionello, R., Linker, J. A., & Wang, H. 2012, *ApJ*, submitted (Paper I)
- Mackay, D. H., Karpen, J. T., Ballester, J. L., Schmieder, B., & Aulanier, G. 2010, *Space Sci. Rev.*, 151, 333
- Mikić, Z., & Linker, J. A. 1994, *ApJ*, 430, 898
- Mikić, Z., Linker, J. A., Schnack, D. D., Lionello, R., & Tarditi, A. 1999, *Physics of Plasmas*, 6, 2217
- Pevtsov, A. A. 2002, *Sol. Phys.*, 207, 111
- Romano, P., Contarino, L., & Zuccarello, F. 2003, *Sol. Phys.*, 214, 313
- Roussev, I. I., Forbes, T. G., Gombosi, T. I., Sokolov, I. V., DeZeeuw, D. L., & Birn, J. 2003, *ApJ*, 588, L45
- Savcheva, A., Pariat, E., van Ballegoijen, A., Aulanier, G., & DeLuca, E. 2012, *ApJ*, 750, 15
- Shafranov, V. D. 1966, *Reviews of Plasma Physics*, 2, 103
- Su, Y., Surges, V., van Ballegoijen, A., DeLuca, E., & Golub, L. 2011, *ApJ*, 734, 53
- Thompson, B. J., Plunkett, S. P., Gurman, J. B., Newmark, J. S., St. Cyr, O. C., & Michels, D. J. 1998, *Geophys. Res. Lett.*, 25, 2465
- Titov, V. S., & Démoulin, P. 1999, *A&A*, 351, 707
- Titov, V. S., Hornig, G., & Démoulin, P. 2002, *J. Geophys. Res.*, 107, 1164
- Titov, V. S., Mikić, Z., Linker, J. A., & Lionello, R. 2008, *ApJ*, 675, 1614
- Török, T., & Kliem, B. 2003, *A&A*, 406, 1043
- . 2005, *ApJ*, 630, L97
- . 2007, *Astron. Nachr.*, 328, 743
- van Ballegoijen, A. A., & Martens, P. C. H. 1989, *ApJ*, 343, 971
- Webb, D. F., Lepping, R. P., Burlaga, L. F., DeForest, C. E., Larson, D. E., Martin, S. F., Plunkett, S. P., & Rust, D. M. 2000, *J. Geophys. Res.*, 105, 27251

A MULTI-SPACECRAFT VIEW OF A GIANT FILAMENT ERUPTION DURING 2009 SEPTEMBER 26/27

SANJAY GOSAIN¹, BRIGITTE SCHMIEDER², GUY ARTZNER³, SERGEI BOGACHEV⁴, AND TIBOR TÖRÖK⁵

¹ National Solar Observatory, 950 N. Cherry Avenue, Tucson, AZ 85719, USA

² LESIA, Observatoire de Paris, CNRS, UPMC, Université Paris Diderot, 5 Place Jules Janssen, F-92190 Meudon, France

³ CNRS UMR 8617, Institut d'astrophysique Spatiale (IAS), F-91405 Orsay Cedex, France

⁴ Lebedev Physical Institute of Russian Academy of Science, Leninskij prospekt 53, Moscow 119991, Russia

⁵ Predictive Science, Inc., 9990 Mesa Rim Rd., Suite 170, San Diego, CA 92121, USA

Received 2012 June 25; accepted 2012 October 18; published 2012 November 20

ABSTRACT

We analyze multi-spacecraft observations of a giant filament eruption that occurred during 2009 September 26 and 27. The filament eruption was associated with a relatively slow coronal mass ejection. The filament consisted of a large and a small part, and both parts erupted nearly simultaneously. Here we focus on the eruption associated with the larger part of the filament. The *STEREO* satellites were separated by about 117° during this event, so we additionally used *SoHO*/EIT and CORONAS/TESSIS observations as a third eye (Earth view) to aid our measurements. We measure the plane-of-sky trajectory of the filament as seen from *STEREO-A* and TESSIS viewpoints. Using a simple trigonometric relation, we then use these measurements to estimate the true direction of propagation of the filament which allows us to derive the true R/R_\odot -time profile of the filament apex. Furthermore, we develop a new tomographic method that can potentially provide a more robust three-dimensional (3D) reconstruction by exploiting multiple simultaneous views. We apply this method also to investigate the 3D evolution of the top part of filament. We expect this method to be useful when *SDO* and *STEREO* observations are combined. We then analyze the kinematics of the eruptive filament during its rapid acceleration phase by fitting different functional forms to the height-time data derived from the two methods. We find that for both methods an exponential function fits the rise profile of the filament slightly better than parabolic or cubic functions. Finally, we confront these results with the predictions of theoretical eruption models.

Key words: Sun: activity – Sun: coronal mass ejections (CMEs) – Sun: filaments, prominences

Online-only material: animations, color figures

1. INTRODUCTION

Coronal mass ejections (CMEs) are huge expulsions of plasma and magnetic field from the solar corona into interplanetary space. They are often accompanied by the eruption of a filament or prominence, which becomes visible as the core of the CME in coronagraph observations, and by a flare that occurs almost simultaneously with the eruption. It is now well accepted that these three phenomena are different observational manifestations of a more general process, namely a local disruption of the coronal magnetic field (e.g., Forbes 2000). The detailed mechanisms that trigger and drive such disruptions are, however, still controversial, and a large number of theoretical models have been put forward in the past decades (for recent reviews, see Amari & Aly 2009; Aulanier et al. 2010; Forbes 2010).

Early observations indicated that there are two distinct classes of CMEs, namely fast (or impulsive) ones, originating in active regions and associated with flares, and slow (or gradual) ones, associated with large prominence eruptions outside of active regions and no, or no significant, flaring (MacQueen & Fisher 1983; Sheeley et al. 1999). Consequently, it has been suggested that different eruption mechanisms may be at work in these two types of eruptions. However, the analysis of considerably larger data sets in the *SoHO* era revealed a continuous distribution of CME velocities with a single peak (e.g., Zhang & Dere 2006), indicating that both fast and slow CMEs are driven by the same physical mechanism(s). This is supported by the considerable range of CME kinematics that could be modeled based on a single physical mechanism (Chen & Krall 2003; Török & Kliem

2007), as well as by the fact that large prominence eruptions outside active regions can produce loops and ribbons that are morphologically similar to those seen in flare-related CMEs. The majority of prominence-related CMEs are most likely not associated with flares simply because the magnetic fields in their source regions are too weak to produce significant emission in $H\alpha$ and in EUV wavelengths (see, e.g., Forbes 2000).

Virtually all theoretical models describe CMEs as coronal magnetic flux ropes that are anchored in the dense photosphere (see, e.g., Gibson et al. 2006), although it is debated whether a flux rope is present in the corona prior to an eruption or is formed during the eruption process. The expulsion of a flux rope into interplanetary space as a CME has been explained by, e.g., the continuous increase of poloidal flux in the rope due to flux injection from the convection zone into the corona (e.g., Chen & Krall 2003), by ideal MHD instabilities like the helical kink instability (Fan 2005; Török & Kliem 2005) or the torus instability (Kliem & Török 2006), or by the combination of a “loss of equilibrium” of a flux rope and magnetic reconnection occurring in its wake (e.g., Forbes & Isenberg 1991). Other models invoke reconnection from the beginning of the eruption, as for example the “tether cutting” (e.g., Moore et al. 2001) and “magnetic breakout” (e.g., Antiochos et al. 1999) models.

Using observations to support or reject specific models for a particular eruption is difficult for several reasons. First, many models employ more than one physical mechanism, resulting in a partial overlap between them (see Aulanier et al. 2010). Second, several distinct mechanisms may occur almost simultaneously in an eruption, in particular in complex events, making it difficult to establish which one is the main driver of the

eruption (e.g., Williams et al. 2005). Third, the models predict a very similar evolution for the main phase of an eruption, i.e., for the evolution after the impulsive flare phase and initial rapid acceleration of the ejecta. When looking for clues for possible eruption mechanisms, one therefore often focuses on the early eruption phase, for example, on the morphology and timing of pre-flare H α and EUV brightening (e.g., Chandra et al. 2011). For eruptions associated with large quiescent prominences, as the one studied in this paper, such signatures are, however, often not available.

Another possibility to obtain information about the mechanisms at work in an eruption is to study its kinematic properties, in particular the early rise phase (Schrijver et al. 2008). Eruptions typically start with the slow rise of a filament or prominence and/or overlying loops, at an approximately constant velocity of a few km s⁻¹, which is followed by the rapid acceleration of the ejecta to several 100 km s⁻¹. The acceleration should initially follow some functional dependence, but will then saturate and decrease afterward (see, e.g., Figure 3 in Gallagher et al. 2003). Profiles of the initial acceleration phase, if extractable from measured height-time data with sufficient coverage, can be compared with predictions of theoretical eruption models.

Observed rise profiles of the early phase of filament eruptions and CMEs have been fitted by constant-acceleration curves (e.g., Gilbert et al. 2000; Kundu et al. 2004; Chifor et al. 2006), power-law, $h(t) \propto t^m$, with $3.0 \lesssim m \lesssim 3.7$ (e.g., Alexander et al. 2002; Schrijver et al. 2008; Liu et al. 2009), and exponential functions (Gallagher et al. 2003; Williams et al. 2005). As for theoretical models, the functional dependence of eruption trajectories has not often yet been reported, and systematic investigations of its parameter dependence are quite rare so far. Still, some model predictions can be inferred from the literature. For example, an exponential early rise is naturally expected if an eruption is initially driven by an ideal MHD instability (e.g., Török et al. 2004). A power-law dependence with $m = 2.5$ has been found for the trajectory in a two-dimensional (2D) version of the loss of equilibrium model (Priest & Forbes 2002), and a parabolic rise (i.e., constant acceleration) was reported for a simulation of the breakout model (Lynch et al. 2004). Furthermore, Schrijver et al. (2008) showed that a velocity perturbation at the onset of the rapid acceleration of an eruption can change the resulting functional dependence of the trajectory (from exponential to near-cubic for the case of the torus instability they studied), given that this perturbation is sufficiently large (somewhat larger than typical velocities observed during the initial slow rise phase of an eruption). We refer to Schrijver et al. (2008) for further details.

Prominence eruptions and CMEs have been observed for a long time with various ground- and space-based instrument. For example, the LASCO coronagraphs (Brueckner et al. 1995) on board the *SoHO* spacecraft have been observing thousands of CMEs in white light. However, one of the limitations of LASCO, and of other instruments that are located at or close to Earth, is that they can only obtain 2D observations, projected onto the plane of sky (POS). Height-time data of eruptions are particularly hampered by this, since obtaining the correct radial rise velocities requires the knowledge of the true three-dimensional (3D) trajectories.

The *STEREO* mission (Kaiser et al. 2008) was launched during the solar minimum and therefore initial studies were of quiescent filament eruptions (Gosain et al. 2009; Artzner et al. 2010; Gosain & Schmieder 2010). With *STEREO* 3D reconstructions, it is, in principle, possible to derive the shape

of the prominence, its twist or writhe, and its true trajectory when it erupts. These properties can be useful for comparisons with model predictions (e.g., Török et al. 2010; Kliem et al. 2012; Zuccarello et al. 2012). Other case studies of quiescent filament eruptions observed with *STEREO* are reviewed in Bemporad (2011) and Aschwanden (2011) and those of CMEs in Mierla et al. (2010).

The main difficulty in stereoscopic reconstruction arises when the separation angle between the two *STEREO* satellites is large, because then it becomes difficult to identify the same feature in both views unambiguously (Thompson et al. 2012). In such cases one has to use complementary observations from other instruments, such as *SoHO*/EIT (Delaboudinière et al. 1995), CORONAS/TESSIS (Kuzin et al. 2009), and now *SDO*/AIA (Lemen et al. 2012). The addition of the Earth view to *STEREO* views makes life easier as it provides us (1) more than one stereoscopic pair, and (2) smaller separation angles. Also, in a special circumstance when a structure (filament/prominence) is not visible in one of the *STEREO* satellites (e.g., remains hidden behind the limb during initial rising phases), adding an Earth view to one of the *STEREO* satellites allows us to make stereoscopic reconstruction. Some recent examples where three views have been used are Li et al. (2011) and Feng et al. (2012).

In this paper we will present such an example. We present He II 304 Å observations of a large filament eruption that occurred during 2009 September 26–27. The observations were taken from the twin *STEREO* satellites and were combined with complementary observations from *SoHO*/EIT and CORONAS/TESSIS, giving us a third view, i.e., the Earth view of the event. The filament eruption was seen as a limb event by *STEREO-A*, EIT, and TESSIS, while it was seen as an on-disk event by *STEREO-B*.

Based on these multi-spacecraft data, we derive the R/R_{\odot} or simply height-time profile of the erupting prominence by different methods. First, we independently derive the POS height-time profiles of the prominence top as viewed from *STEREO-A* and TESSIS. Second, we apply a trigonometric relation to simultaneous *STEREO-A* and EIT observation of the prominence and estimate the propagation direction of the filament. Knowing the propagation direction we can derive true height-time profile of the filament top. Finally, we apply a 3D stereoscopic reconstruction method based on Marinus projections to derive the height-time profile, we call this method “tomographic method” as it can use simultaneous multiple views for reconstruction. We then fit these height-time profiles by functional forms, viz., parabolic, exponential, and cubic and compare the results.

The paper is organized as follows. Section 2 summarizes the observations. In Sections 3 and 4 we describe the trigonometric and tomographic methods, respectively, results derived from these methods. Finally, we discuss the results as well as the potential of the newly developed tomographic method.

2. OBSERVATIONS AND METHOD OF DATA ANALYSIS

2.1. He II 304 Å Filament Observations

During 2009 September 26–27 a large filament eruption was observed near the northeast solar limb. The observations were obtained in the He II 304 Å wavelength at a cadence of ten minutes by the SECCHI/EUVI instrument aboard the *STEREO-A* and *B* satellites. Figure 1 (top panel) shows on-disk observations by *STEREO-B* during the early phase of the eruption. Two filaments can be seen, a long one (LF) located

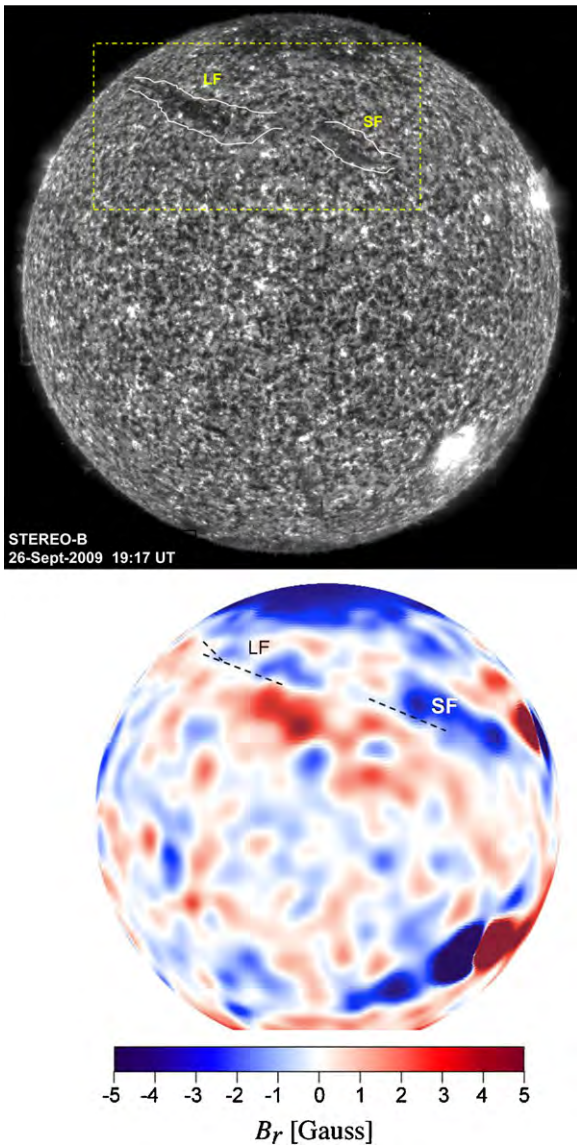


Figure 1. Top panel shows the He 304 \AA filtergram observed from *STEREO-B* at 19:17 UT on 2009 September 26. LF and SF mark the large and the small filament (highlighted inside yellow rectangle, outlined by white line segments for clarity), respectively. The bottom panel shows a map of the radial magnetic field component, reconstructed from a synoptic MDI magnetogram, as *STEREO-B* would have seen it at the same time (courtesy of Z. Mikić). The dashed lines indicate the polarity inversion line above which the filaments are located.

(Animations and color version of this figure are available in the online journal.)

at $23^\circ\text{--}34^\circ \text{ N}$, and a short one (SF) located at $18^\circ\text{--}32^\circ \text{ N}$. The bottom panel shows a reconstruction of the photospheric magnetic field distribution as it would have been seen from *STEREO-B* (at 19:17 UT on 2009 September 26, using $B_0 = 5^\circ 54'$ and $\text{CML} = 164^\circ 4'$, where B_0 and CML are the Carrington coordinates of the disk center in the *STEREO-B* view). It can be seen that both filaments follow the same polarity inversion line (PIL), suggesting that they were both located within an extended filament channel. The magnetic field on either side of the PIL was weak ($\pm 3 \text{ G}$). In the limb view of *STEREO-A*, LF starts to rise earlier than SF (see movie 1), while both eruptions seem to occur simultaneously in the disk view of *STEREO-B* (movie 2). Since LF is much more prominent than SF, in this paper we focus on the evolution of LF and refer to Li et al. (2010) for further

details on the eruption of SF. In the following, “filament” or “prominence” therefore refers only to LF.

During this event, the *STEREO* satellites were separated by about 117° and the main part of the filament was hidden behind the solar limb in the *STEREO-A* viewpoint until about 18:20 UT on 2009 September 26. A 3D stereoscopic reconstruction in combination with *STEREO-A* before 18:20 UT was therefore not possible from either *STEREO-B* or Earth view (EIT and TESIS). He II 304 \AA images from *SoHO*/EIT at a cadence of 6 hr and CORONAS/TESS images at a cadence of ten minutes provide the Earth view, which are used for 3D reconstruction with *STEREO-A* after 18:20 UT September 26 using the tomographic method described in Section 3.3. The He II 304 \AA images of the filament from the four instruments are shown in Figure 2. The Earth–Sun–*STEREO-A* and Earth–Sun–*STEREO-B* angles on 2009 September 26 were 61° and 56° , respectively. The observations of the filament top from two different vantage points (TESIS and *STEREO-A*) allows us to observe the POS evolution in a piecewise continuous manner from TESIS (00:00 to 22:00 UT) and *STEREO-A* (19:10 to 23:10 UT), as shown in Figure 6 (top left panel). A simple trigonometric method, described in Section 3.2, is used to triangulate the true propagation direction of the filament apex. Knowing this angle, the POS height-time profiles are corrected to derive the true height-time profiles as shown in Figure 6 (bottom left panel).

The filament LF (as seen from *STEREO-A*; Figure 3) suggests a sheet-like morphology. The stereoscopic reconstruction by Li et al. (2010, see their Figure 2) also infers a sheet-like structure. We outline its apparent edges by dashed (red) and dotted (yellow) lines in *STEREO-A* and *B* views. A careful inspection of the legs of the prominence in *STEREO-A* images suggests a twisted morphology of the legs. However, a quantification of the twist of the filament sheet is not possible in the present case.

2.2. CME Observations

STEREO-A observed the CME associated with the filament eruption on 2009 September 26/27 with its coronagraphs, COR1 ($1.4\text{--}4 R_\odot$) and COR2 ($2.5\text{--}15 R_\odot$). The CME was not seen by *STEREO-B* since it was directed toward it and was perhaps too faint to be seen as a halo CME. The LASCO/C2 ($1.5\text{--}6 R_\odot$) and C3 ($3.7\text{--}30 R_\odot$) coronagraphs also observed the CME. The time of arrival of CME in C2 was 23:06 UT on September 26, in C3 was 14:18 UT on September 27, and in HI1 was on 21:29 UT on September 27.

The propagation angle of the CME leading edge is derived using the same procedure as described in Section 3.2 and applied to filament apex. The projection correction to the POS height-time profiles of the CME (top right panel of Figure 6) is then applied to derive the true height-time profiles (bottom right panel of Figure 6).

3. HEIGHT-TIME PROFILE OF ERUPTING FILAMENT AND CME

3.1. Plane-of-sky Measurements

We make POS measurements of the filament apex (marked by the “+” symbol in the panels of Figure 2) using TESIS and *STEREO-A* observations. The R_{POS}/R_\odot profile of the filament apex measured from the two views (from *STEREO-A* and TESIS) is plotted in the top left panel of Figure 6. Similarly, the top right panel of Figure 6 shows the R_{POS}/R_\odot profile of the leading edge of the CME measured with *STEREO-A* and LASCO coronagraph observations. The difference in the

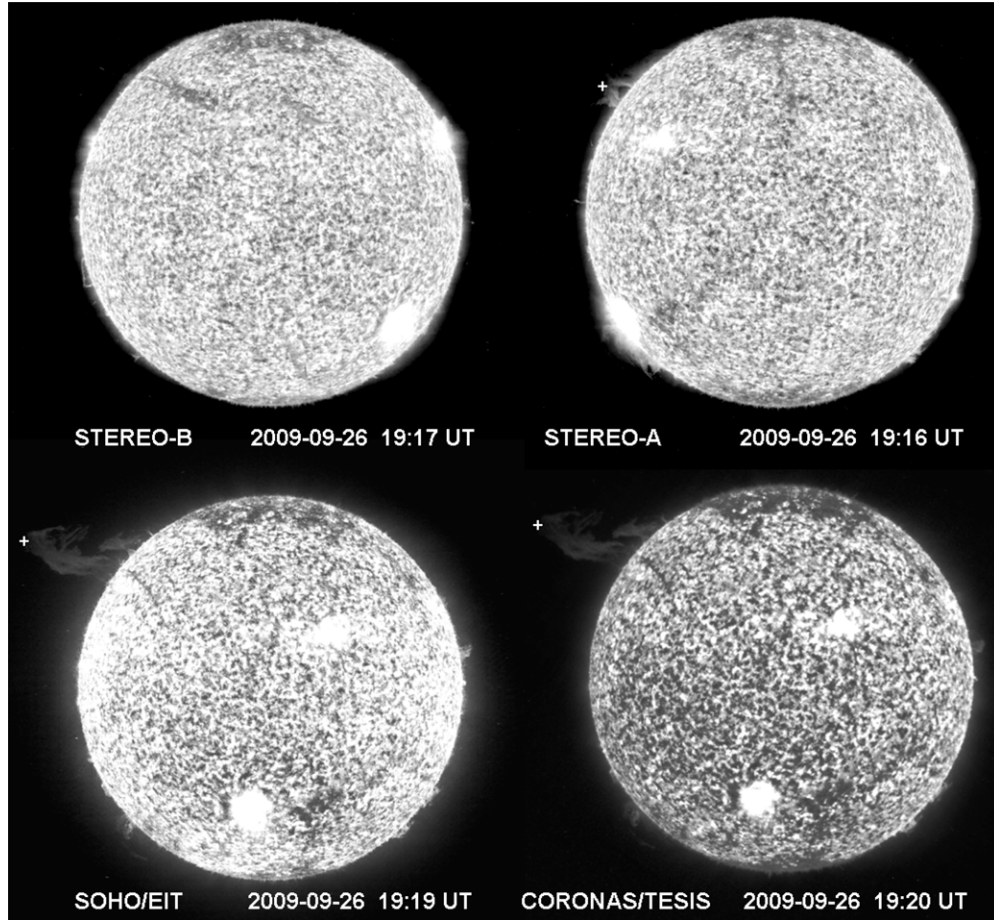


Figure 2. Four different views on the erupting filament in He II 304 Å. The top panel shows the *STEREO-Behind* (left) and *STEREO-Ahead* (right) views. The bottom panel shows the Earth views by *SoHO/EIT* (left) and *CORONAS/TESES* (right).

R_{POS}/R_{\odot} profiles of the filament apex and CME leading edge as seen by different satellites is apparent, since the measurements correspond to two different vantage points.

3.2. Estimation of the True Height-time Profile using Simple Triangulation

The POS measurements, R_{POS}/R_{\odot} , of the filament apex and the CME leading edge, described above, can be corrected for projection effect if we know the angle between the real trajectory of the erupting feature and the POS in the observer's frame of reference. The true R/R_{\odot} profile is related to the R_{POS}/R_{\odot} profile, measured in the POS, by $(R/R_{\odot})\cos\theta = R_{\text{POS}}/R_{\odot}$, where θ is the angle between the real trajectory and the POS, referred to as propagation angle henceforth.

Here we apply a simple trigonometric relation, using image pairs from *STEREO-A* and TESIS/EIT (henceforth, Earth view or EV), to estimate the propagation angle. We then use this information to derive the true R/R_{\odot} profile of the erupting filament and the CME. A simple assumption made here is that the propagation angle remains unchanged during the time of the measurements. We verified this assumption by computing the propagation angle using *STEREO-A* and TESIS pair at later times and found that the angle remains the same (see Table 1).

We explain the trigonometric procedure here briefly. The illustration in Figure 4 shows the geometric setting of the two *STEREO* satellites and the EV with respect to the filament. The projected height of the top part of the filament is h_a and h_b in the POS of *STEREO-A* and EV, respectively. S is the separation

Table 1
Propagation Direction using Simple Triangulation and Marinus Method

TESIS	<i>STEREO-A</i>	$\angle\alpha^a$	$\angle\beta^a$	Latitude ^b	Longitude ^b
20:16 UT	20:16 UT	41°	20°	28°	148°
20:24 UT	20:26 UT	41°	20°	28°	148°
20:48 UT	20:46 UT	41°	20°	27°	149°
20:56 UT	20:56 UT	41°	20°	25°	149°
21:04 UT	21:06 UT	41°	20°	25°	149°
21:59 UT	21:56 UT	40°	21°	21°	152°
22:15 UT	22:16 UT	40°	21°	19°	152°

Notes.

^a Angles α and β measured by simple triangulation method.

^b Carrington latitude and longitude using Marinus method.

angle between *STEREO-A* and EV (61°), and α and β are the angles that the top of the filament apex (trajectory) makes with respect to the POS. We obtain the angles using the relations $S = \alpha + \beta$ and $h_a/h_b = \cos(\alpha)/\cos(S - \alpha)$. Knowing these angles, we can apply corrections to the POS heights h_a and h_b to obtain the true height $h_{\text{True}} = h_a/\cos(\alpha) = h_b/\cos(\beta)$.

Figure 5 shows an example of two stereoscopic image pairs, i.e., *STEREO-A* (left panel) and EIT (right panel), observed almost simultaneously. The two images are in epipolar view. The segments h_a and h_b measure the top part of the filament as viewed from two vantage points. Knowing h_a , h_b , and S , we determine α and β to be 41° and 20°, respectively. Since only one stereoscopic pair is available between *SoHO/EIT* and

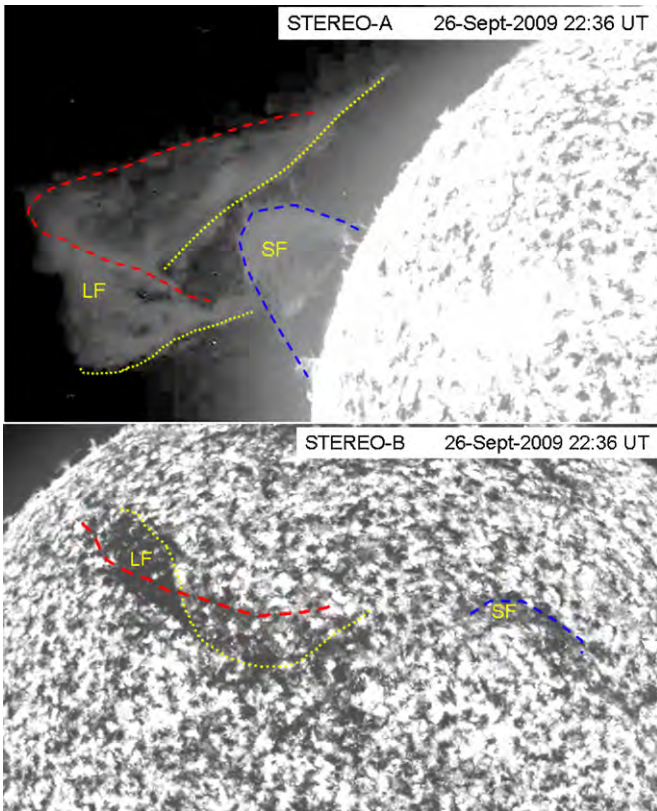


Figure 3. *STEREO-A* (top) and *B* (bottom) images of the eruptive filament (LF and SF) are shown. The edges of the filament sheet (LF) are outlined by dashed (red) and dotted (yellow) lines. The sheet appears to be twisted along its legs. (A color version of this figure is available in the online journal.)

STEREO-A, we make use of TESIS data to make pairs with *STEREO-A*. The observations of *STEREO-A* and TESIS are not synchronized in time and both instruments follow a different time cadence (see Table 1). Assuming that the filament did not evolve significantly within the small time differences, we could make eight near-simultaneous stereoscopic pairs of TESIS and *STEREO-A*. The timings of these pairs and the value of angles α and β deduced using these pairs are given in Table 1. It may be noticed that during the observed time interval the propagation angle does not change and therefore it is possible to correct the observed POS height-time profiles for propagation angle using the single value of α and β . In Section 3.3.3 we show that these values are consistent with other 3D reconstruction methods. The corrected height-time profile of the filament apex is shown in the lower left panel of Figure 6.

Similarly, applying this method to the CME leading edge we deduce angles α and β to be 36° and 25° , respectively. The true height-time profile of CME leading edge after correcting for these angles is shown in the lower right panel of Figure 6. It is interesting to note that the direction of propagation of the filament apex and the CME leading edge differs by about 5° . The filament typically forms a core in the three part CME structure. However, since the CME leading edge is more extended, i.e., the front surface of a tear-drop shaped bubble in which filament forms a trailing part, the difference of 5° is small considering the large angular extent of the filament and the associated CME. Another interesting point about this method is that the two curves merge into one (as seen in the combined curves in lower panels) only for a unique pair of α and β angles, where the sum of the two angles ($S = \alpha + \beta$, in this case equal to separation

between Earth and *STEREO-A*, i.e., $61^\circ 5'$) is well constrained by the known separation angle between the two vantage points. For any other pair of these angles the two curves did not merge into one. Thus, just by knowing the separation angle between two vantage points and the respective POS height-time profiles, one can iteratively adjust the angles (in fact only one of the angles, as the two angles α and β are simply α and $S - \alpha$), until the two curves merge as one. This procedure also gives the same solution for α and β . These true height-time profiles are then used for deriving the velocity and acceleration profiles of the filament and CME, which is described in the following sections.

3.2.1. Estimating the Duration of Rapid Acceleration Phase

In this section, we use the true height-time curves, shown in the lower panels of Figure 6, to derive the velocity, acceleration, and jerk (rate of change of acceleration, following Schrijver et al. 2008) profile of the filament and CME. The latter can then be compared to the predictions of theoretical eruption models described in the Introduction. Since the acceleration and jerk are the higher order time derivative of the trajectory, errors in the measured data amplify strongly, so one is typically forced to smooth the data before calculating acceleration curves, for example, using spline smoothing (Vršnak et al. 2007). Here we will use a different approach: we first fit a fourth-order polynomial of the form $H(t) = a + bt + ct^2 + dt^3 + et^4$ to the height-time data. We then use this smooth curve to obtain the velocity, acceleration, and jerk profiles. These profiles are shown in Figure 7 for the filament and the CME leading edge in the left and right columns, respectively.

It is to be noted that the underlying physical mechanism responsible for the eruption determines the functional form of the height-time profile only initially, i.e., during the phase when acceleration is growing, but not yet saturating. Once the acceleration starts to saturate, the functional form is changing. From Figure 7 we note that the acceleration profiles as estimated from the fourth-order polynomial are quite different for the filament and the CME. While the acceleration of the CME leading edge is higher than that of the filament, the rate of change of acceleration, i.e., the value of jerk for the CME is declining, in contrast to the filament. This suggests that during the time interval of the CME data the increase of the acceleration of the leading edge is slowing down, while the growth of the acceleration of the filament is still increasing. We therefore restrict our fits of different functional forms to the filament only and not to the CME.

3.2.2. Fitting Functional Forms to the Filament Rapid Acceleration Phase

Before we fit the functional forms we make an estimation of the optimum time interval which corresponds to rapid acceleration phase of the filament. To get the first estimation, we took the start time where the acceleration starts to grow from zero and the end time as the last data point. We then fine tune our estimation of the time interval of the rapid acceleration phase by varying their start and end times and observing the resulting quality of the overall fits of all three functional forms. The interval leading to an overall best-fit quality for all functional forms is marked by vertical dashed lines in Figure 7.

Within this rapid acceleration interval we then find the best-fit functional form as described below. We fit the three different functional forms: (1) parabolic, $H(t) = a + bt + ct^2$, (2) exponential, $H(t) = ae^{bt} + c$, and (3) cubic, $H(t) = a + bt + ct^3$ to the height-time profile during the rapid acceleration

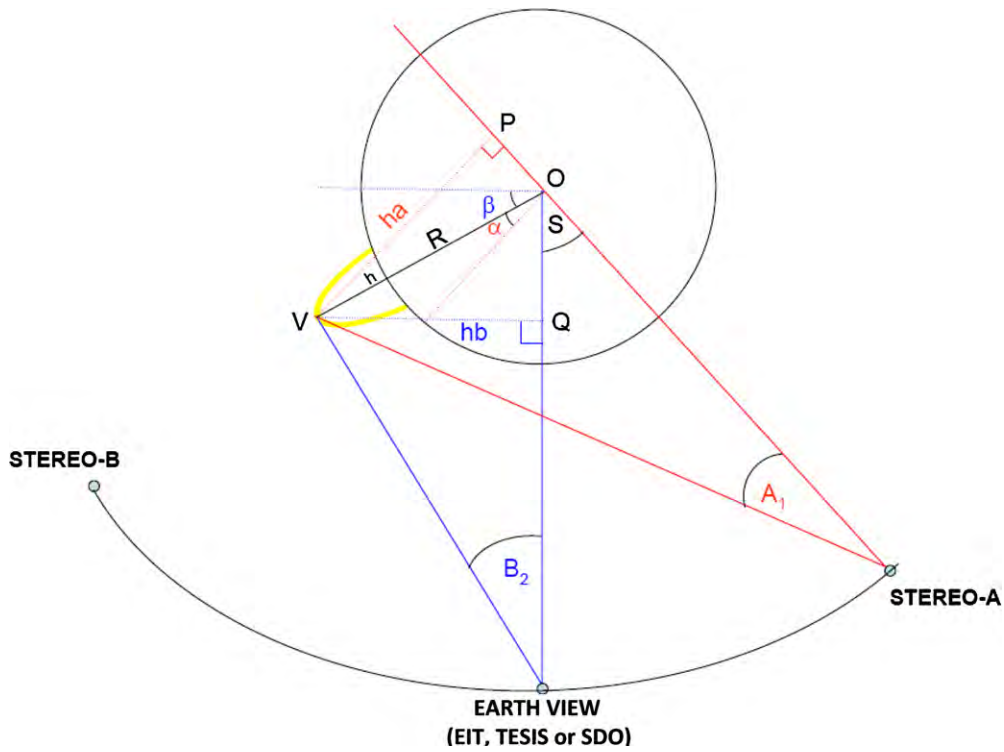


Figure 4. Illustration of the de-projection method. The coronal structure is represented by a yellow loop extending above the solar limb. The top part of this loop is at an angle α (β) to the plane of sky in the reference frame of *STEREO-A* (Earth view, EV). S is the separation angle between *STEREO-A* and EV. The segments ha and hb are the projected distances $(R + h) \cos(\beta)$ and $(R + h) \cos(\alpha)$, respectively. S is related to α and β by $S = \alpha + \beta$ (if the loop is seen in front of the limb in one view and behind the limb in the other) or by $S = |\alpha - \beta|$ (if the loop is seen on the same side of the limb, i.e., either in front of or behind the limb, in both views). If ha , hb , and S are known, α and β can be determined.

(A color version of this figure is available in the online journal.)

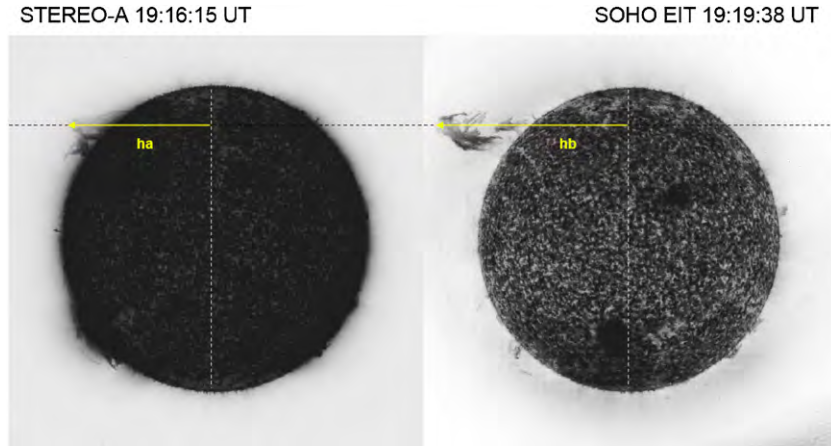


Figure 5. Near-simultaneous *STEREO-A* and *SoHO/EIT* filtergrams in epipolar geometry. The segments h_a and h_b are measured from the apex of the filament. The separation angle between Earth and *STEREO-A* is $S = \alpha + \beta = 61^\circ$.

(A color version of this figure is available in the online journal.)

phase. The left panel of Figure 9 shows these fits. The reduced χ^2 values are shown at the top left corner of each panel. The weights that we apply to the data points for fitting are taken to be $W = 1/\sigma^2$, where σ is the standard deviation of the measurement error. We assume a Gaussian distribution for the latter. The pixel size of *STEREO/EUVI* is about 2 Mm. For the filament (or prominence), which is typically quite diffuse in He II 304 Å images, we consider 3 pixels, i.e., 6 Mm as the 1σ error. The actual errors may be somewhat different. However, while using different values of 1σ will lead to different values of χ_v , the relative values of χ_v between different functional forms will remain the same. The fits of the three functional

forms shown in the left panels of Figure 9 clearly favor an exponential rise of the filament, with a relatively better value of χ_v .

3.3. The 3D Reconstruction by using Marini's Projection

3.3.1. The Method

Here we describe a new tomographic method for the 3D reconstruction. We used simultaneous views of the filament from *STEREO-A* and *B* and *TESIS* in He II 304 Å wavelength. The essence of the method is as follows.

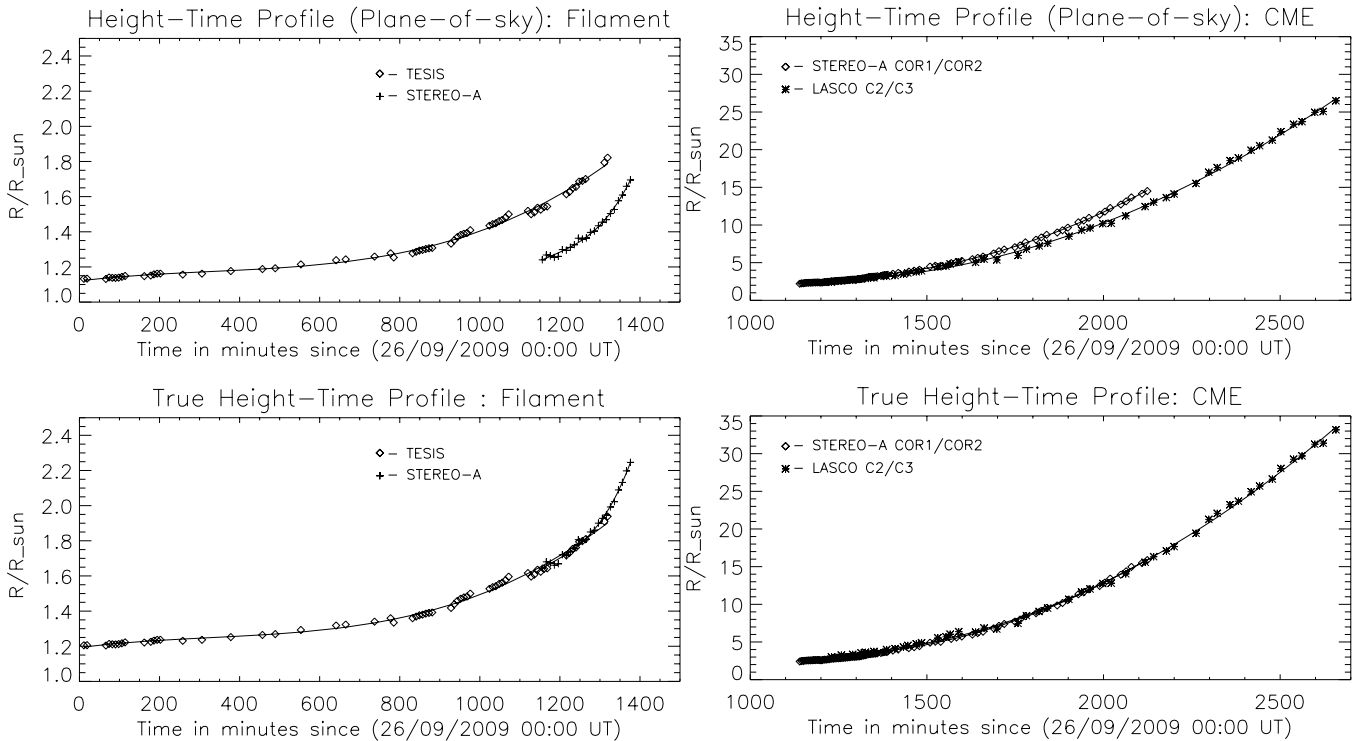


Figure 6. Top panels show the POS height-time profiles of the filament apex (left) and CME leading edge (right) as seen from different viewpoints (see the inset for the observing satellites). The lower panels show the true height-time profiles derived by using the simple trigonometric method (Section 3.2).

A continuum intensity image of the Sun, $I(x, y)$, can be easily projected into heliographic coordinates $I(l, b)$. This projection is also known as equidistant cylindrical or Marinus projection. Since the continuum intensity $I(x, y)$ corresponds to the solar photosphere, each point (x, y) on the intensity image can be associated with heliographic coordinates (l, b) , assuming a spherical Sun with radius, $R = R_{\odot}$. A common feature on the solar disk such as a sunspot should then correspond to the same Carrington latitude–longitude, no matter what the viewing angle of the Sun is. However, for coronal images like in He II 304 Å the intensity features corresponding to filaments, spicules, etc., do not lie on the same sphere but are elevated structures in 3D. Thus, a common feature like a filament or coronal loop will correspond to location (l_1, b_1) and (l_2, b_2) in heliographic projection of the coronal images obtained from different viewing points 1 and 2, respectively (when $R = R_{\odot}$ is assumed). Conversely, if the heliographic projection is attempted assuming the Sun to be a sphere of radius larger than one solar radius and a correct radius of the sphere is assumed (equal to the altitude of the feature), then we should get $l_1 = l_2$ and $b_1 = b_2$ for the common feature.

Thus, generating the generalized Carrington maps for different assumed radii of the spherical grid, using a 5 Mm step from $R = 700$ Mm to $R = 1500$ Mm, and comparing the Carrington coordinates (latitude–longitude) of a recognizable common feature, such as filament apex, in the three Carrington maps (one for each viewing angle) until they all agree gives us a solution for the 3D coordinates of the feature. We found that this step size of 5 Mm gives an optimum choice to arrive at the best agreement for the generalized coordinates of a recognizable feature. Thus the generic accuracy of the method can be assumed to be about 5 Mm.

We geometrically consider both intersections of the line of sight with the reference sphere. When the radius of the reference sphere is equal to the chromospheric radius, we

take into account the single point located physically in front of the POS. When the radius of the reference sphere is greater than the chromospheric radius, we must in principle take into account both intersection points located respectively in front of and behind the POS. That is why in the top panel of Figure 8 the prominence, projected on the far side of the reference sphere, behind the POS of *STEREO-A*, appears as reversed from right to left with respect to the direct view in Figure 2. In addition, the far side of the solar disk appears as a dark, missing disk in the top panel of Figure 8.

3.3.2. Advantages and Limitations of the Method

It is well known that all stereoscopic reconstruction methods are limited by the ambiguity in recognizing a common feature in different views. Further, a common limitation that arises with any 3D stereoscopic reconstruction technique is when the apex point from two viewing angles may be different. Such situations would lead to a systematic error in the reconstructed 3D coordinates. However, we expect such errors to be less severe in our case because (1) the filament studied here has a large extension in longitude which is rising globally as a whole, so height-time profile of several neighboring points along the filament will be similar, and (2) using combination of *STEREO-A* and TESIS (separation angle 61°) as compared to *STEREO-A* and *STEREO-B* (separation angle 117°), we reduce the errors. Although such systematic errors cannot be avoided, the time derivative of measured altitude and hence the derived velocity and acceleration should not be affected severely as long as the systematic error remains similar in magnitude. Therefore, for studying the kinematic evolution of erupting prominence such reconstruction methods may still be applicable, with aforementioned limitations.

Figure 8 shows selected parts of the three generalized Carrington maps corresponding to *STEREO-A*, TESIS, and *STEREO-B* views, generated assuming radii of the spherical grid to be

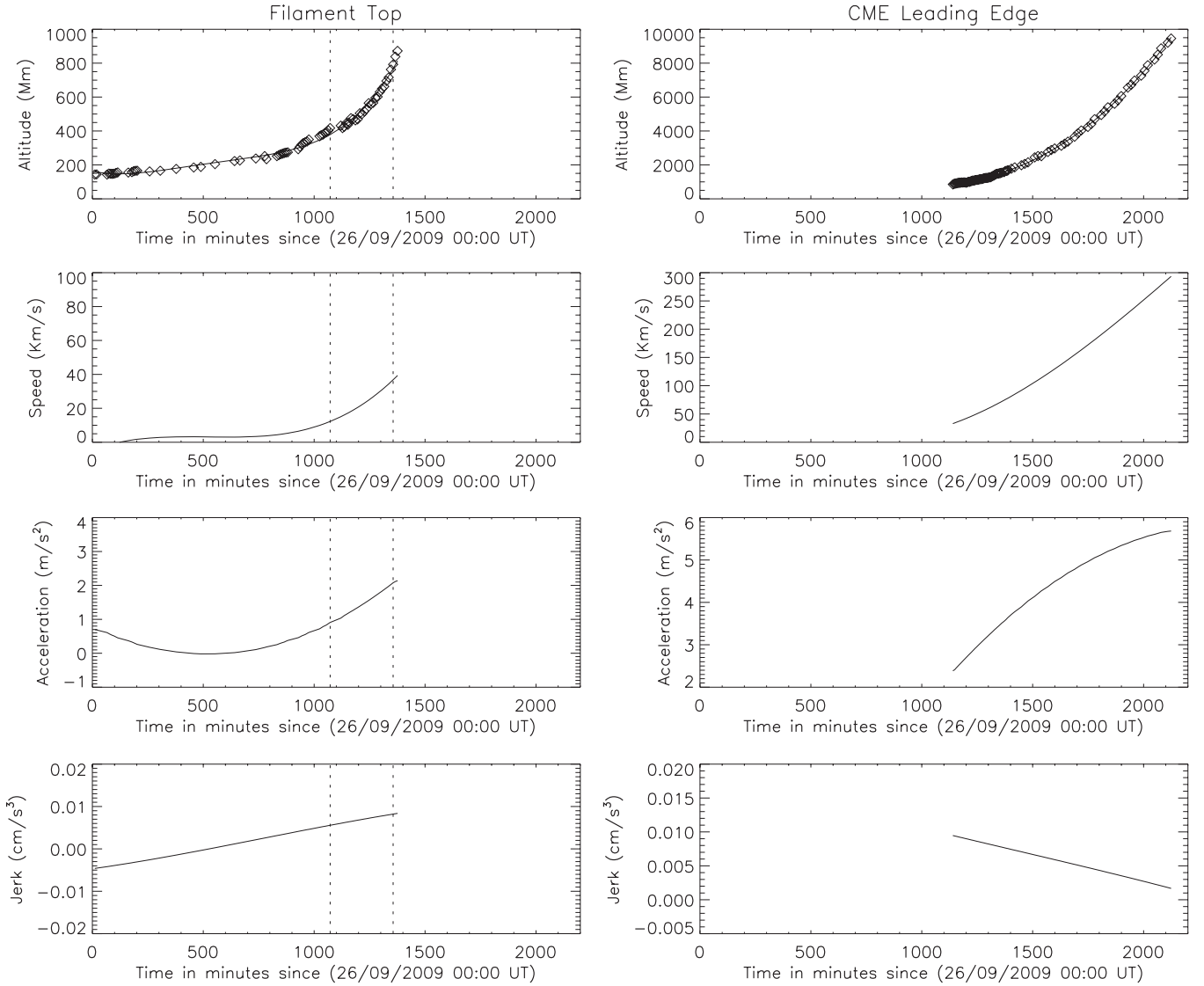


Figure 7. Left (right) panels show, from top to bottom, the height, speed, acceleration, and jerk (rate of change of acceleration) profiles of the filament apex (CME leading edge), respectively. In the top panels, the data points are shown by “+” marks and the solid line corresponds to a fourth-order polynomial fit ($H(t) = a + bt + ct^2 + dt^3 + et^4$) to the data. The fitted profile $H(t)$ is used to derive the speed, acceleration, and jerk curves in the subsequent panels. The two vertical dotted lines in the left panels correspond to the estimated duration of the rapid acceleration phase of the filament, which is fitted with different functional forms in Figure 9.

1245 Mm, i.e., 545 Mm above the solar surface. At the choice of this radius, the common feature, i.e., the filament apex marked by a square box, corresponds to the same Carrington latitude–longitude coordinates in the different views. In principle, two stereoscopic views are sufficient for the application of this method. However, adding more views increases redundancy (for example, in the present case more emphasis is given to TESIS and *STEREO-A* for constraining reconstruction) and therefore may add to its robustness. In the future, we plan to apply this method to the events observed simultaneously by the two *STEREO/EUVI* instruments along with the high-resolution *SDO/AIA* observations.

3.3.3. Comparison with SCC_MEASURE and Simple Triangulation Method

The 3D reconstruction of the filament studied in this paper was also carried out by Li et al. (2010) using SCC_MEASURE procedure (developed by W. Thompson). They used *STEREO-A* and *STEREO-B* pair for their reconstruction. Further, they reconstructed many (12) points along the filament body (their

Figure 5). Their points 6, 7, and 8 correspond to the top of the filament and one can note that the height evolution of these points (their Figure 6(a)) is quite similar to each other (within ± 6 Mm), though the points are separated spatially, this is due to the large-scale uniform evolution of the filament. For comparison, we overlay the altitude data points of location 7, as reconstructed by Li et al. (2010) in our height-time plot shown with red symbols in the top right panel of Figure 9. The reconstruction from two independent methods agrees quite well, considering the general scatter in the reconstructed coordinates.

On the other hand, a poorer match is expected between the true 3D reconstruction methods and the simple triangulation method since the latter only estimates the propagation angle and not the 3D coordinates of the filament. The height derived from simple triangulation method shows a systematic offset with respect to the true height derived from 3D reconstruction methods. Apart from the systematic offset, the profile of the derived speed and acceleration should, however, remain unaffected, as these depend upon the shape of the curve. This is evidenced in a similar fit quality of the height-time profile by both the

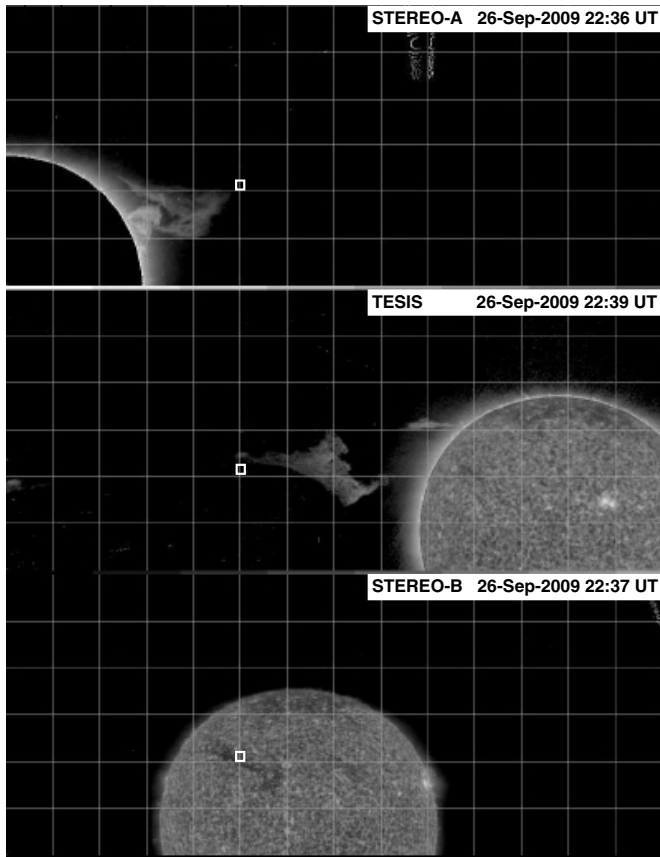


Figure 8. Top, middle, and bottom panels show the three views of the Sun from the *STEREO-A*, *TESIS*, and *STEREO-B*, respectively, in Mariner projection. The top part of the filament is marked by a white box in all images.

methods to different functional forms (see Section 3.3.4). Also, the method is straightforward and relies on tracking a common feature in the images taken from the same vantage point albeit at different times. The natural advantage is that it is easy to track a common feature in time if the time difference between two images is not very large.

Further, it may be noted from Table 1 that the angles α and β are not changing significantly. In the 3D reconstruction by Li et al. (2010, their Figure 4, right panels) it can be seen that a propagation angle of $\sim 20^\circ$ in front of the east solar limb is deduced and is not changing significantly. Also, the Carrington longitude of the filament apex reconstructed using Mariner method (Table 1) shows a small variation in longitude of $\sim 4^\circ$, while the mean value of the longitude, $\sim 150^\circ$, corresponds to an angle of $\sim 20^\circ$ in front of the east solar limb, in agreement with Li et al. (2010) and angle β from simple triangulation method.

3.3.4. Rapid Acceleration Phase and Its Functional Form

We use this tomographic 3D reconstruction method based on Mariner projection to obtain the 3D trajectory of the filament apex. The rise of the altitude of the filament apex is fitted for different functional forms. The time interval of the rapid acceleration phase is taken to be the same as estimated in Section 3.2.1. The height-time curve and the fitted parabolic, exponential, and cubic functions to it are shown in the right panel of Figure 9 from top to bottom, respectively. The reduced χ^2 values are shown at the top left corner of each panel. It is found that an exponential form fits the observations relatively better as compared to the other functions. The exponential

function was also found to fit the rapid acceleration phase relatively better than other functions in Section 3.2.2, where simple triangulation method was used. This is shown in the left panel of Figure 9.

4. DISCUSSION AND CONCLUSIONS

In this paper we analyzed the observations of a large erupting quiescent filament which was observed from three vantage points by *STEREO-A*, *B*, and the *EV (SoHO/EIT and TESIS)*. The filament rose slowly for several hours before accelerating rapidly and erupting in two parts, a large and a small filament. We analyzed the kinematics of the large filament, whose true trajectory was derived by two methods: one simple triangulation method and another newly introduced tomography method. The new tomographic method can potentially take advantage of simultaneous observations from multiple vantage points to constrain the reconstructions better. After deriving the true trajectory by the two methods, we fitted the height-time curves with different functional forms and compared the results with predictions of theoretical eruption models.

The key points in the observational analysis can be summarized as follows.

1. The eruption involved two filaments, a large one and a small one, which were located above the same PIL, suggesting that they were embedded in the same, elongated filament channel. The photospheric magnetic field strengths at the location of the filaments were weak (up to about 3 G). The two filaments erupted almost simultaneously. In the present analysis we focused on the eruption of the more prominent large filament.
2. We used two different approaches to derive the true height-time profile of the filament. First, we used a simple triangulation method to determine the angle which the filament trajectory makes with respect to the POS and applied correction to the POS height-time profile to derive true height-time profile. Second, we used tomographic approach where we make Mariner projections of the three views of the Sun on spheres of radii larger than the solar radii so as to arrive at a common latitude–longitude position of a common feature (filament apex) in all maps. The advantage of the first method is that once we know the propagation angle with respect to POS from triangulation, we can go back and forth in time and correct the POS height-time profile obtained with even one satellite, i.e., durations when only one view is available, e.g., when in one of the stereoscopic pairs the filament is behind the limb or out of the field of view (FOV). However, the method assumes that the propagation angle of the filament with respect to POS does not change substantially over the time of observations.
3. During its early rise phase, the filament exhibits the morphology of a twisted sheet. However, its chirality could not be inferred from the images.
4. We derived the acceleration and jerk (rate of change of acceleration) profiles for the filament and the CME (Figure 7). It is believed that the initial rapid acceleration phase, when acceleration is growing, may be suggestive of the physical mechanism behind the eruption (Schrijver et al. 2008). However, the acceleration curve must be growing and not saturating or slowing down; in other words, the jerk should be increasing. By studying the jerk profiles in Figure 7 for the filament and the CME we decided to fit different functional forms to the filament observations

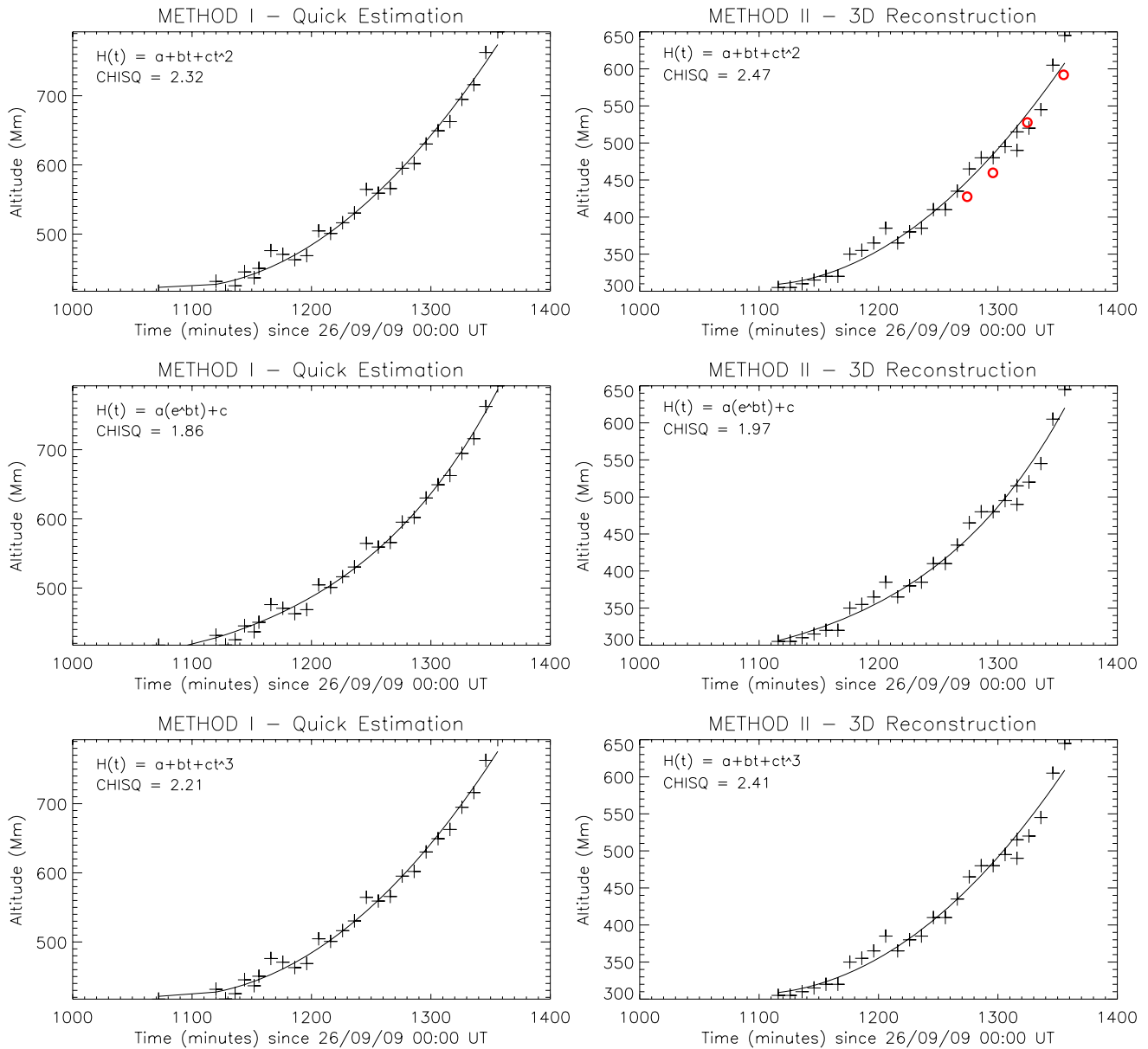


Figure 9. Panels on the left and right show the altitude-time curve for the erupting filament derived from simple triangulation method (Section 3.2) and 3D reconstruction method (Section 3.3). The four data points in red in the top right panel correspond to the altitude reconstructed by using SCC_MEASURE method. The altitude-time curve corresponds to the rapid acceleration phase of the filament eruption and is fitted for three functional forms *viz.* parabolic, exponential, and cubic (from top to bottom). The reduced χ^2 value of the fit is displayed on the top left corner of each panel.

(A color version of this figure is available in the online journal.)

only and not to the CME, because the jerk profile of the CME suggests that its acceleration is already saturating. Since the CME observations are available only when it enters the coronagraph’s FOV, which is much later than the observations of the filament eruption, we missed the initial rapid acceleration phase of the CME.

5. We estimate the rapid acceleration phase of the filament between 17:50 UT and 22:33 UT, using the procedure described in Section 3.2.1. This phase is marked by two dashed lines in the left panel of Figure 7. We fit functional forms of a parabolic, exponential, and cubic function to the true height-time profile of the filament apex during the rapid acceleration phase. The fits to the true height-time curves derived from two independent reconstruction methods described in Sections 3.2 and 3.3, respectively, are shown in Figure 9.

We now compare our analysis of the eruption kinematics with the predictions of theoretical eruption models described in the Introduction. We note that the conclusions obtained from such a comparison should be read with some care and not be understood as a way to strictly confirm or rule out certain models. First, height-time data obtained with current instruments are still not accurate enough and typically do not have sufficient cadence to allow us to clearly pin down the functional forms of rise profiles, which may behave very similar over the relatively short timescales of the initial rapid acceleration in solar eruptions. Also, a clear functional dependence may not be present if several acceleration mechanisms are at work simultaneously in an eruption. Second, for many models, a proper investigation of the functional dependence of the eruption kinematics has not yet been reported, and even for most of those for which it was, there exists no parametric study, which may reveal kinematics

of a different functional dependence than reported for specific settings of the model parameters.

Our data indicate that the rapid acceleration phase already started before the eruption became visible in the coronagraph data, so we restricted our analysis of the early acceleration phase to the filament observations. Our fits suggest that the filament enters an exponential rise phase at about 17:50 UT, which then appears to saturate from around 22:33 UT. Such exponential initial acceleration is in line with many previous studies (see the Introduction) and supports the current picture that both quiescent and active region filament eruptions, and their associated CMEs, are driven by the same mechanisms. It suggests the occurrence of an ideal MHD instability, here most likely the torus instability. We did not find indications of a clear writhing motion of the filament that would suggest the additional occurrence of the helical kink instability, although the twisted appearance of the filament sheet may indicate some untwisting of the magnetic field during the early phase of the eruption.

The exponential acceleration found here is different from the cases studied by Schrijver et al. (2008), where a cubic (or near-cubic) rise was found for two active region filament eruptions. However, using numerical simulations, these authors showed that a relatively large initial velocity of the erupting structure at the onset of its rapid acceleration can change the subsequent rise behavior from exponential to cubic. The slow rise velocity of the filament (estimated from Figure 7, plateau in the filament speed curve before the first vertical dashed line) before the filament enters rapid acceleration phase is relatively small, about $\sim 2.5 \text{ km s}^{-1}$, however, comparable to the case described in Schrijver et al. (2008). The exponential rise also differs from the recent results by Joshi & Srivastava (2011), who found a constant acceleration for both the slow rise and rapid acceleration phases of the two 3D-reconstructed quiescent prominence eruptions. However, these authors apparently did not fit functions other than parabolic, and also the quality of their fits is not reported.

While the data we considered here support the torus instability as the mechanism responsible for the initial rapid acceleration of the filament, they do not provide reasonable clues for the cause for its preceding relatively long slow rise phase. We did not find indications of pre-flare brightening which are often used to draw conclusions. Hence, we do not find support for tether-cutting or magnetic breakout, but we cannot rule out the occurrence of these and other reconnection-related mechanisms, since the magnetic fields in the source region of the eruptions might have been simply too weak to produce detectable brightening. We therefore refrain from speculating on the exact underlying mechanism responsible in the present case. However, more studies using the methods developed in this work and encompassing larger sets of observations, including the high-resolution *SDO/AIA* observations, could provide better clues.

We thank the *SoHO/EIT* and *STEREO/SECCHI* teams for their open data policy. We thank *TESIS/CORONAS* team for providing the data. Financial support by the European

Commission through the FP6 SOLAIRE Network (MTRN-CT-2006-035484) is gratefully acknowledged.

REFERENCES

- Alexander, D., Metcalf, T. R., & Nitta, N. V. 2002, *Geophys. Res. Lett.*, 29, 100000
- Amari, T., & Aly, J. 2009, in *IAU Symp. 257, Universal Heliophysical Processes*, ed. N. Gopalswamy & D. F. Webb (Cambridge: Cambridge Univ. Press), 211
- Antiochos, S. K., DeVore, C. R., & Klimchuk, J. A. 1999, *ApJ*, 510, 485
- Artzner, G., Gosain, S., & Schmieder, B. 2010, *Sol. Phys.*, 262, 437
- Aschwanden, M. J. 2011, *Living Rev. Sol. Phys.*, 8, 5
- Aulanier, G., Török, T., Démoulin, P., & DeLuca, E. E. 2010, *ApJ*, 708, 314
- Bemporad, A. 2011, *J. Atmos. Solar-Terr. Phys.*, 73, 1117
- Broeckner, G. E., Howard, R. A., Koomen, M. J., et al. 1995, *Sol. Phys.*, 162, 357
- Chandra, R., Schmieder, B., Mandrini, C. H., et al. 2011, *Sol. Phys.*, 269, 83
- Chen, J., & Krall, J. 2003, *J. Geophys. Res. (Space Phys.)*, 108, 1410
- Chifor, C., Mason, H. E., Tripathi, D., Isobe, H., & Asai, A. 2006, *A&A*, 458, 965
- Delaboudinière, J., Artzner, G. E., Brunaud, J., et al. 1995, *Sol. Phys.*, 162, 291
- Fan, Y. 2005, *ApJ*, 630, 543
- Feng, L., Inhester, B., Wei, Y., et al. 2012, *ApJ*, 751, 18
- Forbes, T. 2010, in *Models of Coronal Mass Ejections and Flares*, ed. C. J. Schrijver & G. L. Siscoe (Cambridge: Cambridge Univ. Press), 159
- Forbes, T. G. 2000, *J. Geophys. Res.*, 105, 23153
- Forbes, T. G., & Isenberg, P. A. 1991, *ApJ*, 373, 294
- Gallagher, P. T., Lawrence, G. R., & Dennis, B. R. 2003, *ApJ*, 588, L53
- Gibson, S. E., Fan, Y., Török, T., & Kliem, B. 2006, *Space Sci. Rev.*, 124, 131
- Gilbert, H. R., Holzer, T. E., Burckpile, J. T., & Hundhausen, A. J. 2000, *ApJ*, 537, 503
- Gosain, S., & Schmieder, B. 2010, *Ann. Geophys.*, 28, 149
- Gosain, S., Schmieder, B., Venkatakrishnan, P., Chandra, R., & Artzner, G. 2009, *Sol. Phys.*, 259, 13
- Joshi, A. D., & Srivastava, N. 2011, *ApJ*, 739, 8
- Kaiser, M. L., Kucera, T. A., Davila, J. M., et al. 2008, *Space Sci. Rev.*, 136, 5
- Kliem, B., & Török, T. 2006, *Phys. Rev. Lett.*, 96, 255002
- Kliem, B., Török, T., & Thompson, W. T. 2012, *Sol. Phys.*, 281, 137
- Kundu, M. R., White, S. M., Garaimov, V. I., et al. 2004, *ApJ*, 607, 530
- Kuzin, S. V., Bogachev, S. A., Zhitnik, I. A., et al. 2009, *Adv. Space Res.*, 43, 1001
- Lemen, J. R., Title, A. M., Akin, D. J., et al. 2012, *Sol. Phys.*, 275, 17
- Li, T., Zhang, J., Zhang, Y., & Yang, S. 2011, *ApJ*, 739, 43
- Li, T., Zhang, J., Zhao, H., & Yang, S. 2010, *ApJ*, 720, 144
- Liu, R., Alexander, D., & Gilbert, H. R. 2009, *ApJ*, 691, 1079
- Lynch, B. J., Antiochos, S. K., MacNeice, P. J., Zurbuchen, T. H., & Fisk, L. A. 2004, *ApJ*, 617, 589
- MacQueen, R. M., & Fisher, R. R. 1983, *Sol. Phys.*, 89, 89
- Mierla, M., Inhester, B., Antunes, A., et al. 2010, *Ann. Geophys.*, 28, 203
- Moore, R. L., Sterling, A. C., Hudson, H. S., & Lemen, J. R. 2001, *ApJ*, 552, 833
- Priest, E. R., & Forbes, T. G. 2002, *A&AR*, 10, 313
- Schrijver, C. J., Elmore, C., Kliem, B., Török, T., & Title, A. M. 2008, *ApJ*, 674, 586
- Sheeley, N. R., Walters, J. H., Wang, Y., & Howard, R. A. 1999, *J. Geophys. Res.*, 104, 24739
- Thompson, W. T., Kliem, B., & Török, T. 2012, *Sol. Phys.*, 276, 241
- Török, T., Berger, M. A., & Kliem, B. 2010, *A&A*, 516, A49
- Török, T., & Kliem, B. 2005, *ApJ*, 630, L97
- Török, T., & Kliem, B. 2007, *Astron. Nachr.*, 328, 743
- Török, T., Kliem, B., & Titov, V. S. 2004, *A&A*, 413, L27
- Vršnak, B., Maričić, D., Stanger, A. L., et al. 2007, *Sol. Phys.*, 241, 85
- Williams, D. R., Török, T., Démoulin, P., van Driel-Gesztelyi, L., & Kliem, B. 2005, *ApJ*, 628, L163
- Zhang, J., & Dere, K. P. 2006, *ApJ*, 649, 1100
- Zuccarello, F. P., Bemporad, A., Jacobs, C., et al. 2012, *ApJ*, 744, 66

2010 AUGUST 1–2 SYMPATHETIC ERUPTIONS. I. MAGNETIC TOPOLOGY OF THE SOURCE-SURFACE BACKGROUND FIELD

V. S. TITOV¹, Z. MIKIC¹, T. TÖRÖK¹, J. A. LINKER¹, AND O. PANASENCO²

¹ Predictive Science Inc., 9990 Mesa Rim Road, Suite 170, San Diego, CA 92121, USA; titovv@predsci.com

² Helio Research, 5212 Maryland Avenue, La Crescenta, CA 91214, USA

Received 2012 June 18; accepted 2012 September 14; published 2012 October 17

ABSTRACT

A sequence of apparently coupled eruptions was observed on 2010 August 1–2 by *Solar Dynamics Observatory* and *STEREO*. The eruptions were closely synchronized with one another, even though some of them occurred at widely separated locations. In an attempt to identify a plausible reason for such synchronization, we study the large-scale structure of the background magnetic configuration. The coronal field was computed from the photospheric magnetic field observed at the appropriate time period by using the potential field source-surface model. We investigate the resulting field structure by analyzing the so-called squashing factor calculated at the photospheric and source-surface boundaries, as well as at different coronal cross-sections. Using this information as a guide, we determine the underlying structural skeleton of the configuration, including separatrix and quasi-separatrix surfaces. Our analysis reveals, in particular, several pseudo-streamers in the regions where the eruptions occurred. Of special interest to us are the magnetic null points and separators associated with the pseudo-streamers. We propose that magnetic reconnection triggered along these separators by the first eruption likely played a key role in establishing the assumed link between the sequential eruptions. The present work substantiates our recent simplified magnetohydrodynamic model of sympathetic eruptions and provides a guide for further deeper study of these phenomena. Several important implications of our results for the S-web model of the slow solar wind are also addressed.

Key words: magnetic reconnection – solar wind – Sun: coronal mass ejections (CMEs) – Sun: flares – Sun: magnetic topology

Online-only material: color figures

1. INTRODUCTION

Coronal mass ejections (CMEs) are spectacular solar phenomena that have been intensely studied over more than 40 years. Being the main driver of space weather disturbances near the Earth, they are part of a more general eruption process, often including filament eruptions and flares. Although it is now understood that these phenomena are due to a local destabilization of the coronal magnetic field, many basic questions on the physics of CMEs are still under study (e.g., Forbes 2000, 2010). Accordingly, theoretical and numerical investigations of CME initiation and evolution have so far focused mainly on *single* eruptions.

However, there also exist *multiple* eruptions occurring within a relatively short period of time and at different, often widely separated, locations. In the largest events, the respective source regions can cover a full hemisphere (so-called global CMEs; e.g., Zhukov & Veselovsky 2007), so that such events naturally produce large heliospheric disturbances. While it has been argued whether or not the temporal correlation of multiple eruptions is coincidental (e.g., Biesecker & Thompson 2000), both statistical investigations (e.g., Moon et al. 2002; Wheatland & Craig 2006) and detailed case studies (e.g., Wang et al. 2001; Jiang et al. 2011; Yang et al. 2012; Shen et al. 2012) indicate that there are *causal connections* between them.³ We accept this fact as a starting point of our study and will henceforth call such eruptions *sympathetic* or *linked*.

The physical mechanisms of these connections, however, have yet to be unveiled. In earlier works they have been related,

for instance, to destabilization by chromospheric large-scale waves (Ramsey & Smith 1966) or large-scale properties of convective flows (Bumba & Klvana 1993). More recent research suggests that the mechanisms linking sympathetic eruptions act in the corona and involve its magnetic field structure. For example, one proposed mechanism relies on perturbations propagating along field lines between the source regions of eruptions (e.g., Jiang et al. 2008), while another appeals to changes in the background field due to reconnection (Liu et al. 2009; Zuccarello et al. 2009; Jiang et al. 2011; Shen et al. 2012). Yet such explanations were often based on qualitative and sometimes rather speculative considerations.

The high-cadence, full-disk observations by *Solar Dynamics Observatory* (*SDO*), along with studies of the large-scale coronal magnetic field, now provide us the opportunity to substantially increase our understanding of such eruptions. The event under study attracted considerable attention in the solar community and beyond. It involved an entire hemisphere of the Sun, consisted of several flares and six filament eruptions and CMEs, and triggered a geomagnetic storm on August 3 (Harrison et al. 2012). A detailed account of all eruptions and their precursors can be found in Schrijver & Title (2011). Here, we restrict ourselves to the main five eruptions, whose connections we aim to explain in the present study. Using a combination of *SDO* data and analysis of field line connectivity for the 2010 August 1–2 eruptions, Schrijver & Title (2011) found evidence that *all* involved source regions were connected by structural features such as separatrix surfaces, separators, and quasi-separatrix layers (QSLs; Priest & Démoulin 1995; Démoulin et al. 1996; Titov et al. 2002). We have recently performed a simplified magnetohydrodynamic (MHD) simulation of a subset of these eruptions (Török et al. 2011), in which two successive

³ We do not distinguish here between sympathetic flares and sympathetic CMEs, since typically both are part of the same eruption process.

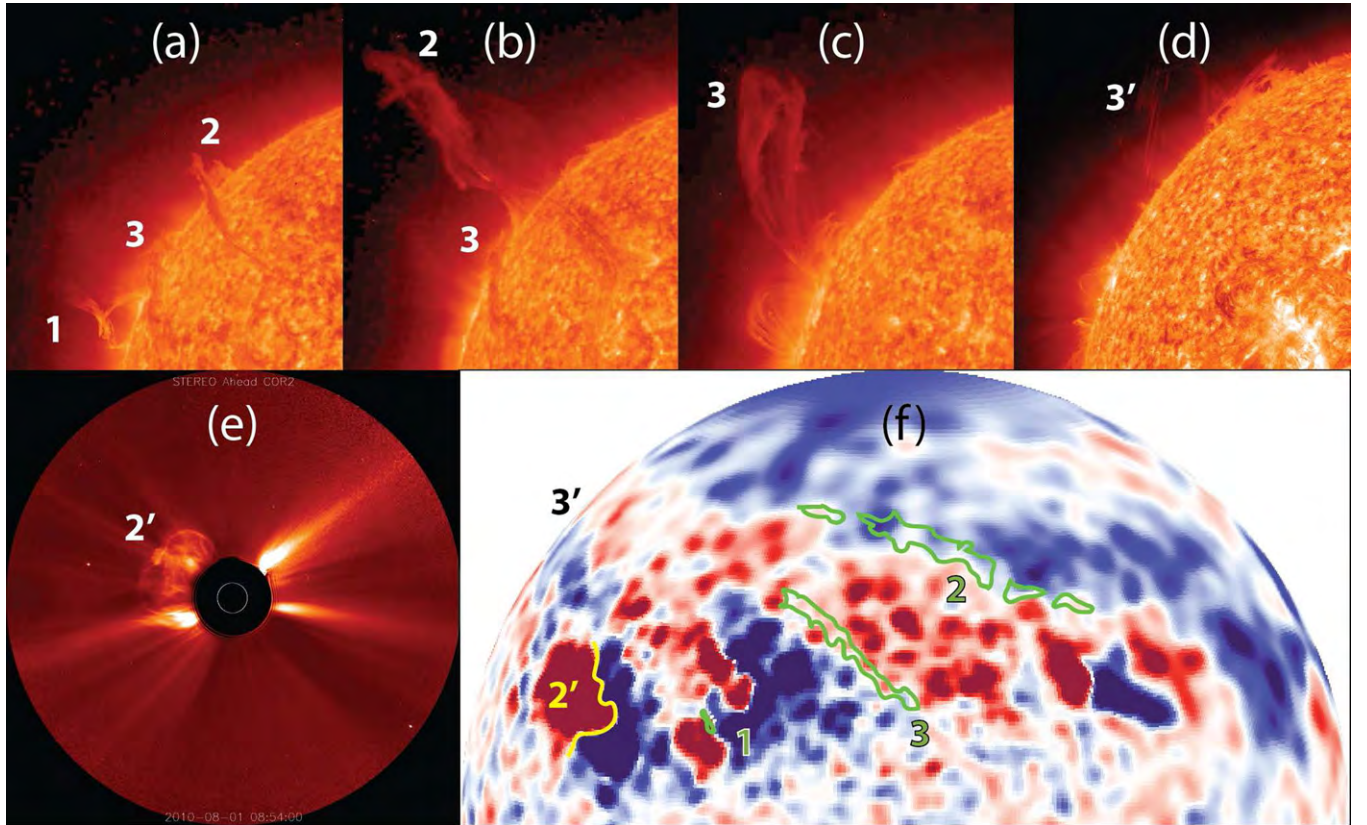


Figure 1. Sympathetic CMEs on 2010 August 1 with the main eruptions numbered in the order of their occurrence, primed numbers indicate near-simultaneous events; (a)–(c) eruptions 1, 2, and 3 as seen by *STEREO-A* 304 Å at 02:56, 09:16, and 22:06 UT (left to right); (d) eruption 3' observed by *SDO/AIA* 304 Å at 21:30 UT; (e) eruption 2' captured by the COR2 coronagraph on board *STEREO-A* at 08:54 UT; (f) synoptic MDI magnetogram and contours (green) of the pre-eruption filaments that were visible in H α , the yellow line indicates the location of the active-region filament 2' prior eruption.

(A color version of this figure is available in the online journal.)

eruptions were initiated by reconnection at a separator high in the corona. Thus, this work strongly supports the idea that the structural features can indeed play a key role in generating linked eruptions.

While these new results are very encouraging, further research is needed. First, our simulation used only a simplified magnetic configuration and addressed just a subset of the complex sequence of CMEs on 2010 August 1–2. Second, the findings by Schrijver & Title (2011), being of a general nature, did not explain the exact role of structural features in connecting individual eruptions. We show here that a comprehensive structural analysis of the magnetic environment in which such eruptions occur allows one to get deeper insights into the relationship between linked eruptions.

Figure 1 shows that the sequence of eruptions started with a CME following the eruption of the small filament 1. About 6 hr later, the large quiescent filament 2 erupted, almost simultaneously with a C-class flare and fast CME originating in active-region NOAA 11092 (whose polarity inversion line is denoted by 2') to the east of filament 1. After another 12 hr, the large quiescent filament 3 erupted, again almost simultaneously with a large filament eruption (denoted by 3') that was observed above the eastern limb. All of the large filament eruptions evolved into separate CMEs. Interestingly, while a filament was present along 2', it did not erupt as part of the CME (Liu et al. 2010).

Our topological analysis of the large-scale background coronal field, which we describe in detail in Section 3, reveals that, first, all of the erupting filaments were located prior to their

eruption below so-called pseudo-streamers (e.g., Hundhausen 1972; Wang et al. 2007). A pseudo-streamer is morphologically similar to a helmet streamer but, in contrast to it, divides coronal holes of the same rather than opposite polarity and contains two lobes of closed magnetic flux below its cusp to produce a ρ -type structure. These structures are quite common in the corona (e.g., Eselevich et al. 1999) and are often observed to harbor filaments in their lobes (Panasenco & Velli 2010). As the latter authors pointed out, an eruption in one lobe of a pseudo-streamer is often followed by an eruption in the other lobe shortly thereafter, indicating that these structures are prone to producing linked eruptions.

Second, as suggested by Török et al. (2011), the eruptions 2 and 3, which originated below one pseudo-streamer, were apparently triggered by eruption 1 that occurred outside the pseudo-streamer. Third, as also suggested in that study, the fact that filament 2 erupted before filament 3, although it was located further from eruption 1 than filament 3, can be explained by the topological properties of the pseudo-streamer.

These three conclusions are strongly supported by our analysis in Sections 3 and 4 and indicate the central role that pseudo-streamers may play in many linked eruptions. We further develop this concept and generalize it in Section 4, arguing that the order of *all* our eruptions, including those of filaments 2' and 3', is not coincidental but causal. It is essentially predetermined by the overall magnetic topology of the ensemble of pseudo-streamers that were involved into the eruptions. We comprehensively investigate this topology in the framework of the potential field source-surface (PFSS; Altschuler & Newkirk 1969;

Schatten et al. 1969) model (Section 2.1), using new techniques for the structural analysis of magnetic fields (Section 2.2).

Being of a general character, our findings on magnetic topology of pseudo-streamers have a broader impact than was initially anticipated for this study. In particular, they also provide important implications for the problem of the origin of the slow solar wind, which was recently addressed in the framework of the so-called S-web model (Antiochos et al. 2007; Antiochos et al. 2011; Linker et al. 2011) and whose aspects have already been discussed in a number of papers (Titov et al. 2011; Wang et al. 2012; Crooker et al. 2012). We address the implications of our new results for the S-web model in Section 5 and summarize our work in Section 6.

Although solar magnetic fields obtained from PFSS and MHD models often qualitatively match each other, at least if the latter are based only on line-of-sight magnetograms (Riley et al. 2006), it remains an open question whether the magnetic field topology, as understood in mathematical terms, is in both cases the same. Section 3.3 makes it clear that this question indeed requires a special study, which is already on the way and will be described in the part II of a series of papers. In that part, we will repeat our analysis of the magnetic structure for the global solar MHD model derived from the same magnetogram as used in the present PFSS model. We will also compare the results of our analysis for both these models and, additionally, extend the discussion of these results, which we start in Section 4, in relation to observations.

2. INVESTIGATION METHODS

2.1. PFSS Model

As a boundary condition for our PFSS model, we used the magnetic data that were derived from a *Solar and Heliospheric Observatory*/MDI synoptic map of the radial field B_r for Carrington rotation 2099 (2010 July 13–August 9) using the Level 1.8.2 calibration. We processed the synoptic map, first, by interpolating it to a uniform latitude–longitude mesh with a resolution of 0.5° . The polar magnetic field was fitted in the new map with a geometrical specification to reduce noise in the poorly observed polar regions. Second, we smoothed the resulting B_r by applying a diffusion operator such that its nonuniform diffusion coefficient was smaller in the active region and larger everywhere else. Finally, we interpolated the obtained B_r distribution from the uniform grid to a nonuniform one that has a higher and lesser resolution, respectively, inside and outside the eruptive region. This region is spread in longitude and latitude approximately from 45° to 180° and from -20° to 65° , respectively, with the resolution ranging from $0.37^\circ \times 0.37^\circ$ in this region to $2.6^\circ \times 1.8^\circ$ outside (see Figure 2(a)).

The spherical source surface, at which the scalar magnetic potential is set to be constant, is chosen at $r = 2.5 R_\odot$, where R_\odot is the solar radius. For such a PFSS model, we have computed the photospheric map of coronal holes on a uniform grid with an angular cell size of 0.125° , which is much smaller than the smallest grid cell for the computed field itself. The result is shown in Figure 2(b) together with the source-surface distribution of the squashing factor Q , which will be discussed below. The three coronal holes of negative polarity that are located in the eruptive region are distinctly disconnected from each other and from the negative northern polar coronal hole. As will become clear later, the presence of these coronal holes in the eruptive region is crucial for understanding both the

underlying magnetic topology and the plausible casual link that this topology sets up between the erupting filaments.

2.2. Techniques for Analyzing Magnetic Structure

Magnetic configurations can generally have both *separatrix surfaces* and *QSLs*. To comprehensively analyze the structure of our configuration, it is necessary to determine all such structural features, whose complete set we call the *structural skeleton* of the configuration. We fulfill this task in two steps: first, we identify the footprints of the corresponding (quasi-)separatrix surfaces at the photosphere and source surface by calculating the distributions of the *squashing factor* Q of elemental magnetic flux tubes (Titov et al. 2002; Titov 2007); these footprints are simply high- Q lines of the calculated distributions. Second, using the found footprints as a guide, we trace a number of field lines that best represent these surfaces.

For the calculation of Q we use its definition in spherical coordinates (Titov 2007; Titov et al. 2008). By construction, the Q factor has the *same* value at the conjugate footprints, so it can be used as a marker for field lines. In other words, despite being originally defined at the boundary surfaces only, the Q factor can be extended into the volume by simply transporting its defined values along the field lines according to the equation

$$\mathbf{B} \cdot \nabla Q = 0,$$

where \mathbf{B} is a given coronal magnetic field and Q is an unknown function of space coordinates. This equation can be solved in many different ways depending on the desirable accuracy and efficiency of the computation. We will describe our methods for extending Q in the volume in a future article together with other techniques for investigating (quasi-)separatrix surfaces, while here we would like to outline a few relevant considerations.

The extension of Q in the volume makes it possible to determine the structural skeleton as a set of high- Q layers. They can intersect each other in a rather complicated way, especially low in the corona. With increasing height, however, the intersections become simpler, which particularly helps our goal of studying the large-scale structure. Determining the Q distribution at a given cut plane, similar as done before in other works (Aulanier et al. 2005; Titov et al. 2008; Pariat & Démoulin 2012; Savcheva et al. 2012a, 2012b), is also helpful for analyzing complex structures. We calculate Q distributions at cut planes, extending the method that Pariat & Démoulin (2012) described for configurations with plane boundaries to the case of spherical boundaries. The high- Q lines in such distributions visualize the cuts of the structural skeleton by those planes. As will be shown below (Figure 9), this kind of visualization becomes particularly useful if the colors corresponding to low values of Q ($\lesssim 10^2$) are chosen to be transparent.

We also find it useful to apply this transparency technique to the photospheric and source-surface Q distributions, particularly if one uses in addition a special color coding that takes into account the local sign of the normal field B_r at the boundary. The function that facilitates this color coding is called *signed log Q* or simply *slog Q* and defined as (Titov et al. 2011)

$$\text{slog } Q \equiv \text{sign}(B_r) \log[Q/2 + (Q^2/4 - 1)^{1/2}]. \quad (1)$$

Using a symmetric blue–white–red palette in combination with the above transparency mask, we make visible in *slog Q* distributions only high- Q lines, colored either in blue or red in negative or positive polarities, respectively. The resulting maps

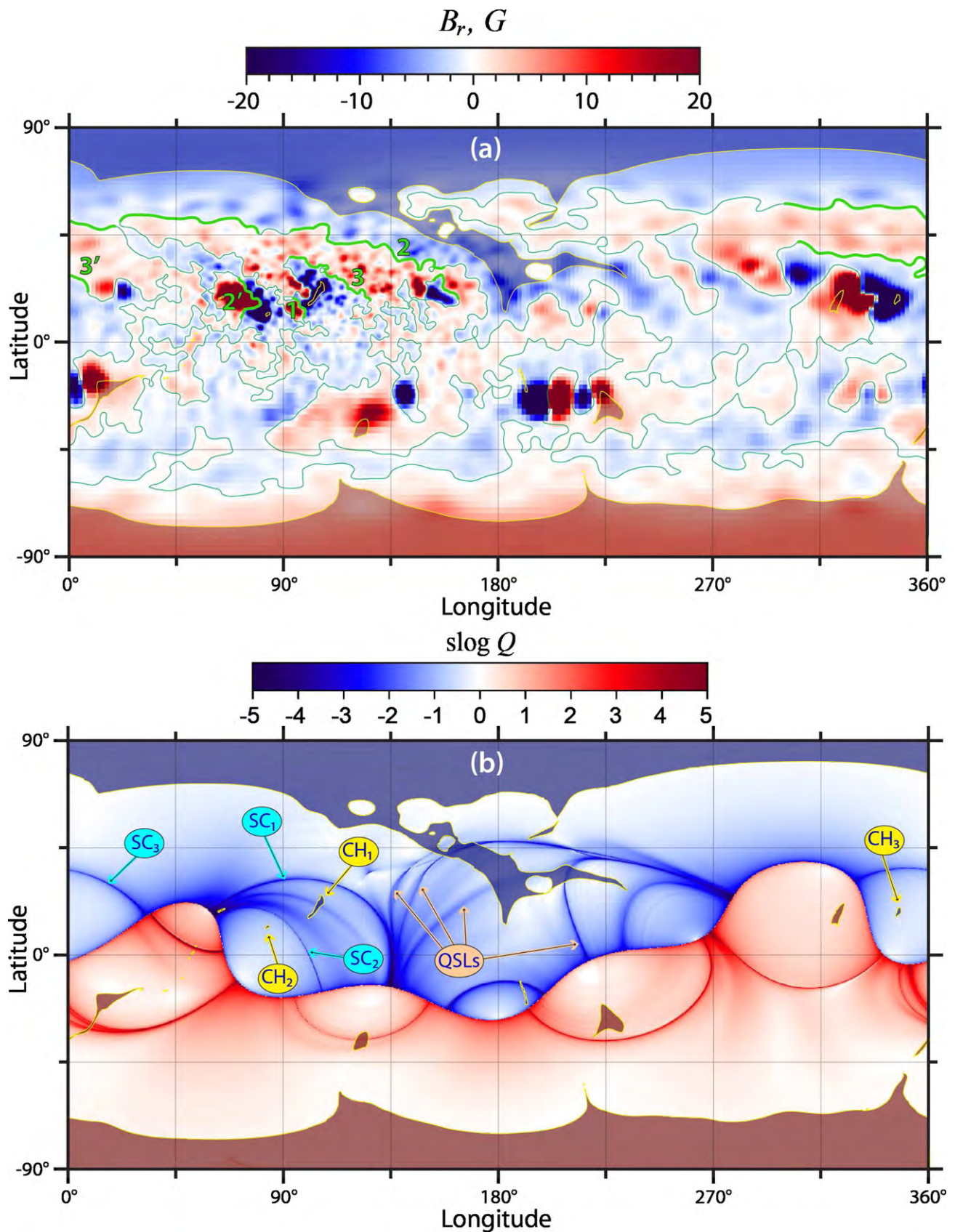


Figure 2. Map of B_r (a) used as a photospheric boundary condition for our PFSS model of the 2010 August 1–2 magnetic field and map of $\text{slog } Q$ for this model at the source surface (b) with superimposed (semi-transparent) photospheric map of coronal holes (shaded either in dark red ($B_r > 0$) or dark blue ($B_r < 0$) and outlined in yellow). Thin (green) lines represent the photospheric polarity inversion line, whose thick segments designate the location of the filaments, part of which are numbered in the order they erupted. Yellow balloons indicate the coronal holes involved in the eruptions; cyan balloons indicate source-surface footprints of the separatrix curtains of these pseudo-streamers.

(A color version of this figure is available in the online journal.)

provide a compact and powerful representation of the structural skeleton at the boundaries, as evident from our illustrations below.

Since our magnetic field is potential, Q acquires high values only in three cases: either the corresponding field lines scatter from localized inhomogeneities of the field nearby its null points or minimum points (Titov et al. 2009) or touch the so-called bald patches (BPs), which are certain segments of the photospheric polarity inversion line (Seehafer 1986; Titov et al. 1993). To make the whole analysis comprehensive, we separately determine the location of all such relevant features and then relate them to the high- Q lines at the boundaries by tracing a number of field lines that pass through these features. The pattern of high- Q lines determined at spherical surfaces of different radii provides us with estimates of the regions in which the magnetic nulls and minima can be present. Using then standard numeric algorithms (see, e.g., Press et al. 2007), both these features are found as local minima of B^2 that is defined between the grid points in these regions by cubic spline interpolation. Calculation of the matrix of magnetic field gradients $[\nabla\mathbf{B}]$ and its eigenvectors at the found nulls and minima allows us to determine the local (quasi-)separatrix structure, which is further used to initialize tracing of the respective (quasi-)separatrix field lines. For tracing generalized (quasi-)separators (see Section 3), which connect a pair of any of the above three features (i.e., nulls, minima, or BP points), we use a technique that is based on similar principles as described earlier for classical null-null separators by Close et al. (2004) and Haynes & Parnell (2010).

3. ANALYSIS OF THE MAGNETIC STRUCTURE

3.1. Coronal Holes versus High- Q Lines at the Boundaries

As mentioned in Section 2.1, the eruptive region contains three coronal holes of negative polarity that are distinctly disconnected at the photospheric level by positive parasitic polarities. With increasing height, however, these coronal holes start to expand and subsequently merge with each other and with the main body of the northern polar coronal hole. Being fully open at the source surface, the magnetic fluxes of these coronal holes still remain separated by the so-called *separatrix curtains* (SCs; Titov et al. 2011). As will become clear below, the SCs are simply vertical separatrix surfaces that originate at null points of the magnetic field low in the corona. At the source surface, their footprints appear as arcs joined at both ends to the null line of the magnetic field, so that the corresponding junction points divide the null line into several segments. Taken in different combinations, such segments and footprints of SCs form several closed contours. The contours encompass the fluxes corresponding to the coronal holes that are disconnected at the photospheric level from each other and from the like-polarity coronal holes at the poles. This fact clearly manifests itself on our source-surface $\text{slog}Q$ map that is superimposed in Figure 2(b) on top of the photospheric coronal holes' map. The figure indicates, in particular, that the high- Q line of the footprint SC₂ (SC₃) and the null-line segment to which the footprint adjoins encompass the CH₂ (CH₃) flux. Similarly, the source-surface footprints SC₁ and SC₂ and two short null-line segments to which the footprints adjoin encompass the CH₁ flux.

It should be noted, however, that some of the source-surface high- Q lines do not represent the footprints of SCs, but rather the footprints of QSLs that stem at the photosphere from narrow open-field corridors connecting spaced parts of otherwise single

coronal holes. The high- Q lines of QSLs usually appear less sharp than those of SC footprints (see Figure 2(b)). The indicated QSL footprints can easily be related to certain open-field corridors in the northern polar coronal hole. If one traces down several field lines from the paths that go across these high- Q lines, the photospheric footprints of these field lines will sweep along the respective open-field corridors, as predicted earlier by Antiochos et al. (2007). However, a similar procedure in the case of the SCs would give a very different result, which becomes clear after analyzing the magnetic topology low in the corona near the indicated coronal holes.

As a first step in this analysis, let us consider the coronal-hole maps and $\text{slog}Q$ distribution, both defined at the photospheric level and superimposed onto each other as shown in Figure 3. The pattern of high- Q lines here is more complicated than at the source surface, as expected. Nevertheless, in the region of interest, it prominently reveals three high- Q lines (red), which are identified after inspection as photospheric footprints of the above-mentioned SCs. They traverse along parasitic polarities and separate the indicated coronal holes in a similar manner as their source-surface counterparts. Note also that these footprints and nearby filaments are locally co-aligned, and at least five of these filaments were eruptive.

Figure 4 shows the described distributions of $\text{slog}Q$ and B_r in three dimensions and a few field lines that produce loop-arcade structures above the filaments. The loops of arcades are rooted with one footpoint at the positive parasitic polarities that disconnect our three coronal holes either from each other (CH₁ from CH₂) or (CH₁ and CH₃) from the northern coronal hole. Thus, these arcades form in pairs the twin magnetic field lobes of the three pseudo-streamers embedded between the indicated coronal holes. We also see here that four of the five filaments (all the numbered ones, except for 2', in Figures 3 and 4) were initially located inside such lobes.

3.2. Separatrix Structure of Pseudo-streamers

Of particular interest to us is the question on how the pseudo-streamer lobes are bounded in our configuration by separatrix surfaces of the magnetic field. It turns out that these surfaces originate either at the null points or at the BPs, both mentioned already in Section 2.2 in connection with high- Q lines. Following Priest & Titov (1996), we will use the terms “fan surface” and “spine line” to designate, respectively, two-dimensional and one-dimensional separatrix structures that are related to a null point. They are defined through the eigenvectors of the matrix of magnetic field gradients at this point in the following way. The fan separatrix surface is woven from the field lines that start at the null point in the plane spanned on the eigenvectors, whose eigenvalues are of the same sign. The spine line is a separatrix field line that reaches the null point along the remaining third eigenvector. For a potential field, the spine line is always perpendicular to the fan surface.

In accordance with the recent analytical model of pseudo-streamers (Titov et al. 2011), the boundaries of our pseudo-streamers are composed of three types of separatrix surfaces, two of which are the fan surfaces of some coronal null points, while the third one is a BP separatrix surface. The fans of the first type have a curtain-like shape, whose field lines emanate from a null point, called henceforth basic one. We have already discussed these surfaces above as SCs in connection with boundary high- Q lines. They contain both closed and open field lines and extend from the photosphere to the source surface, as shown in Figures 5 and 6.

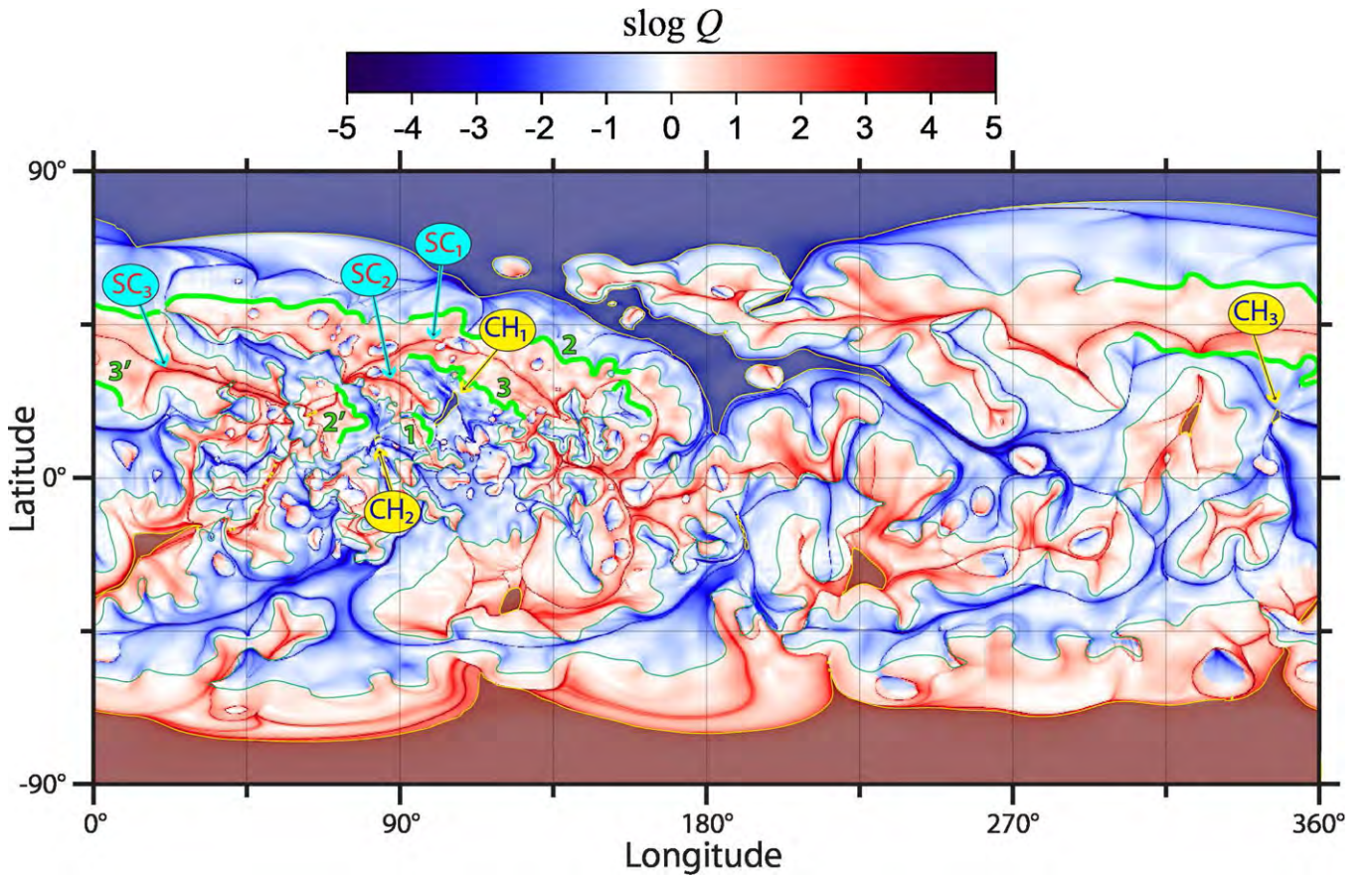


Figure 3. Map of $\text{slog } Q$ for our PFSS model at the photosphere with superimposed (semi-transparent) photospheric map of coronal holes and the photospheric polarity inversion line, both shown in the same way as in Figure 2. Yellow balloons indicate the coronal holes of the pseudo-streamers involved in the eruptions; cyan balloons indicate photospheric footprints of the separatrix curtains of these pseudo-streamers.

(A color version of this figure is available in the online journal.)

The fans of the second type are associated with other nulls and include only closed field lines. Each of these fans bounds the closed flux of the parasitic polarity in a given pseudo-streamer only at one flank and forms a half-dome-like surface, whose edge is located in the middle of the pseudo-streamer and coincides exactly with the spine line of the basic null point (see Figure 7). The second half-dome is formed in all our three pseudo-streamers by the third type of separatrix surfaces that originate in BPs at the opposite flanks of pseudo-streamers. In fact, in our third pseudo-streamer even both separatrix half-domes are due to the presence of BPs (Figure 8).

3.3. Field Line Topology of Separatrix Curtains

Consider now in more detail the field line topology in all our three pseudo-streamers, starting from the two neighboring separatrix curtains SC_1 and SC_2 (see Figures 5 and 6). The field lines in each of these curtains fan out from its own basic null point that is located between two adjacent coronal holes of like polarity and above the respective parasitic polarity. The footprints of SCs, which are discussed in Section 3.1, can be viewed then as photospheric or source-surface images of single null points N_1 and N_2 due to their mapping along closed or open, respectively, field lines.

Within a given SC, such a mapping is continuous everywhere except for few special field lines, called *separators*, where the mapping suffers a jump. This jump takes place whenever a mapping field line hits a null point (like N_{1-2} and N_{1-3} in

Figure 5, or a BP, like BP_1 in both Figures 5 and 6). To distinguish these separators from other field lines, we have plotted them thicker in these and further similar figures.

In addition to the mentioned closed separators, there are also two open ones for each of the curtains. These open separators connect the null N_1 (or N_2) to a pair of null points belonging to the source-surface null line. The latter is simply the helmet streamer cusp, from which the heliospheric current sheet arises. Each of these pairs of nulls also coincides with the end points of the source-surface footprints of SCs.

Note, however, that any null line of the magnetic field is a topologically unstable feature that can exist only under very special conditions. We think, therefore, that the source-surface null line is most likely an artifact inherent only in the employed PFSS model. If passing from PFSS to MHD model, such a null line must turn at radii close to $2.5 R_\odot$ into a feature that has a substantially different magnetic topology. Thus, the indicated topological linkages have yet to be refined, using a more realistic than PFSS model of the solar corona. We will do that in our next paper II, while here we proceed the analysis, assuming that our findings on open separators are approximately correct.

3.4. Field Line Topology of Separatrix Half-domes

Consider now in more detail the topology of separatrix domes (Figure 7), starting from the pseudo-streamers that are embedded between CH_1 , CH_2 , and the northern polar coronal

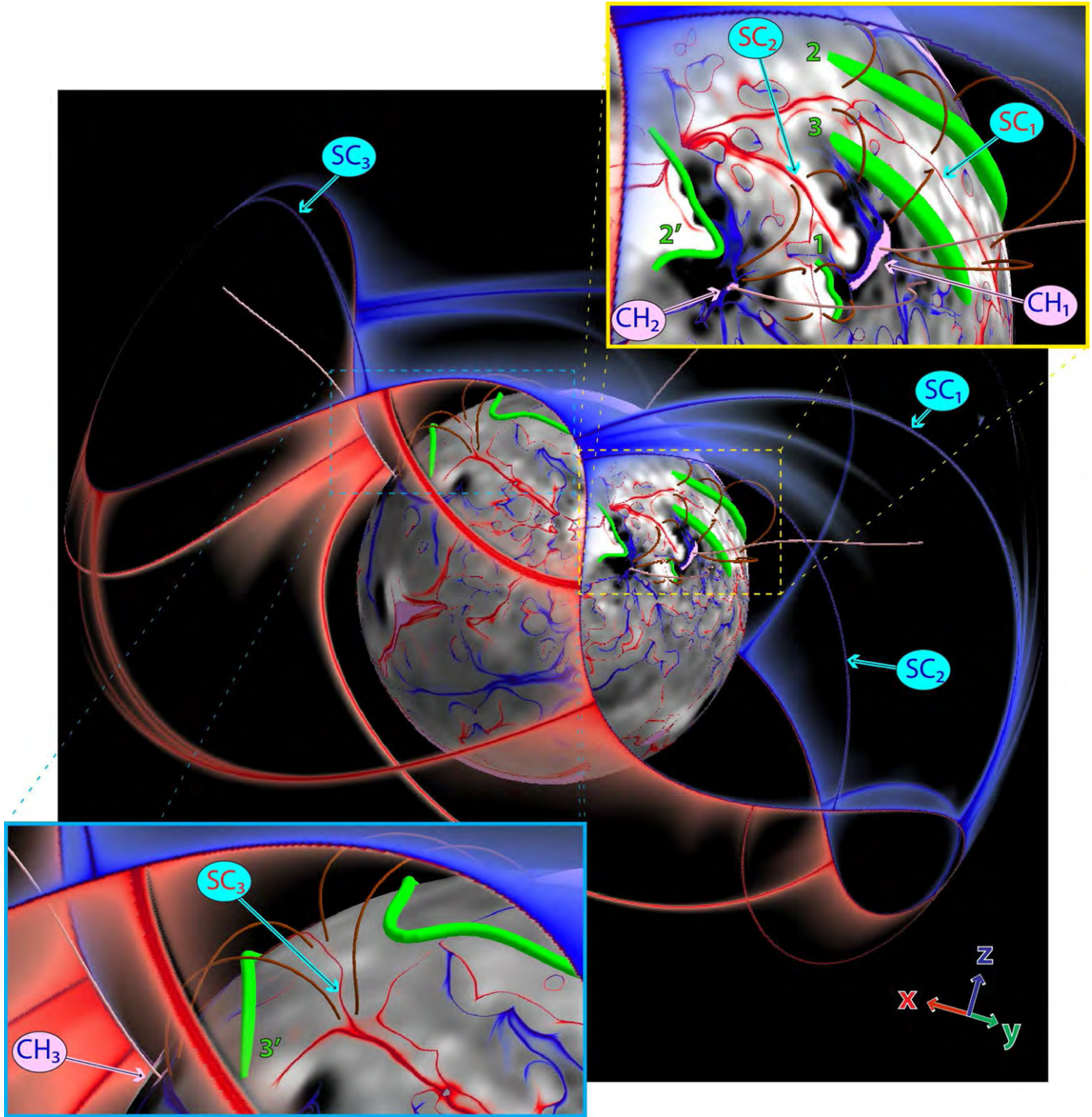


Figure 4. $\text{slog}Q$ distributions are mapped on the photospheric and source-surface globes with a varying opacity such that the low- Q areas ($Q \lesssim 300$) appear to be fully transparent. The photospheric $\text{slog}Q$ map is superimposed on the respective gray-scale B_r distribution with the coronal holes shaded in light magenta. Green tubes depict the major filaments prior to the onset of sympathetic eruptions and several field lines (brown) indicate the pseudo-streamer lobes enclosing these filaments. Open field lines (colored in pink) start in the middle of the coronal holes closest to the pseudo-streamers. The vector triad in the lower right-hand corner indicates the angle orientation of the Cartesian system that is rigidly bound to the Sun center with the z -axis directed to the north pole.
(A color version of this figure is available in the online journal.)

hole. The eastern half-domes (on the left) are combined in one simply connected surface, because they originate in one small bald patch BP_1 located at the border of an active region near the filament $2'$. Spreading out from BP_1 , the field lines extremely diverge within this surface at the nulls N_1 and N_2 and hit the photosphere near the indicated coronal holes. Two of these field lines (red and thick), however, go instead straight to N_1 and N_2 and so, as discussed above, are *generalized separators* belonging to SC_1 and SC_2 , respectively.

In contrast to the eastern half-domes, the western ones (on the right) do not merge with each other and have different originations. The half-dome covering filaments 2 and 3 is simply a fan surface of an extra null point N_{1-2} that is located far to the west from the basic null N_1 . These two nulls are connected by an ordinary separator, which belongs to both this half-dome and the curtain SC_1 .

It is somewhat surprising, but the half-dome covering filament 1 appears to be a quasi-separatrix surface that originates at

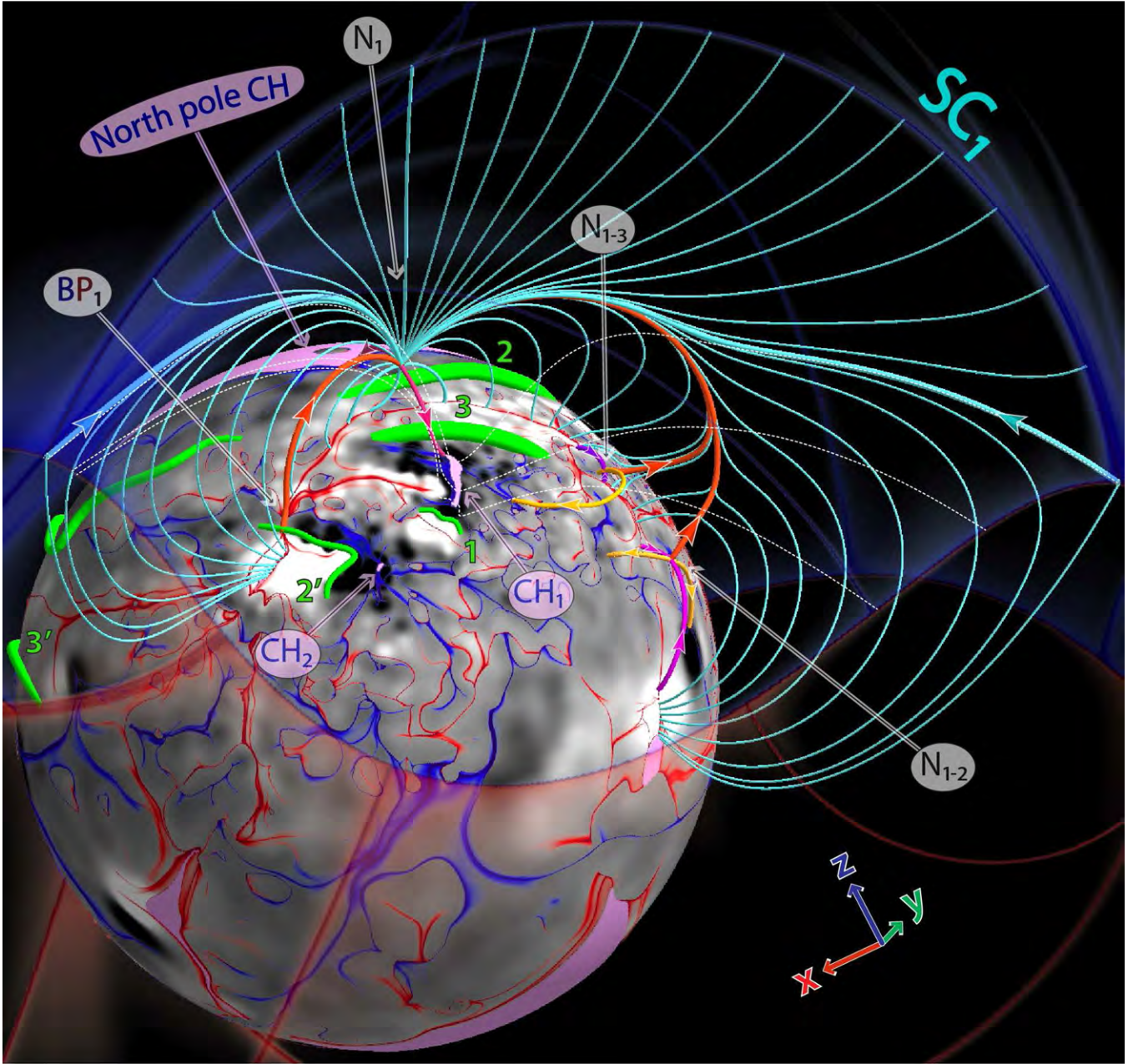


Figure 5. Field line topology of the separatrix curtain SC_1 of pseudo-streamer 1 (embedded between the northern polar coronal hole and CH_1). The thickest lines represent separators, of which the red ones are closed field lines connecting the null point N_1 either to the bald patch BP_1 or another nulls N_{1-2} or N_{1-3} , while the cyan ones are open field lines connecting N_1 to the null line of the source surface. Magenta lines are the spine field lines of the nulls; the yellow lines are the separatrix field lines that emanate from the nulls N_{1-2} and N_{1-3} along the fan eigenvectors that are complementary to the separator ones; several field lines (white dashed) belonging to the boundary of CH_1 are also shown. The maps at the photosphere and source surface and their color coding are the same as in Figure 4.

(A color version of this figure is available in the online journal.)

a magnetic minimum point M_{2-1} lying very close to the photosphere. The field line (red and thick) that passes through and connect M_{2-1} to the basic null N_2 is a *quasi-separator*. The field direction remains unchanged after passing this line through the minimum M_{2-1} , as opposed to a genuine null point, where the field direction would change to the opposite. A similar behavior of the field at M_{2-1} would also occur if it were a degenerate null point, whose one eigenvalue identically equals zero (Titov et al. 2011). We regard this possibility as highly unlikely here, but we cannot fully exclude it, relying only on our numerical study as an approximation of nature.

The existence of the null N_{1-3} in the first of the two discussed pseudo-streamers brings an extra complexity into the structure.

Figures 5 and 7 show that, similarly to N_{1-2} , the null N_{1-3} is connected via an additional separator to the basic null N_1 . This implies that the fan surface of N_{1-3} is also a half-dome such that its edge coincides with the spine line of the null N_1 . We did not plot this half-dome in Figure 7 to avoid cluttering the image with too many lines, but it is very similar to the plotted half-dome that originates in the null N_{1-2} .

The third pseudo-streamer, which is embedded between CH_3 and the northern polar coronal hole, has the topology as analogous as the one of the two others considered above (see Figure 8). The main difference is only that both half-domes originate here at bald patches BP_2 and BP_3 , which are located at the opposite flanks of the pseudo-streamer. In this respect,

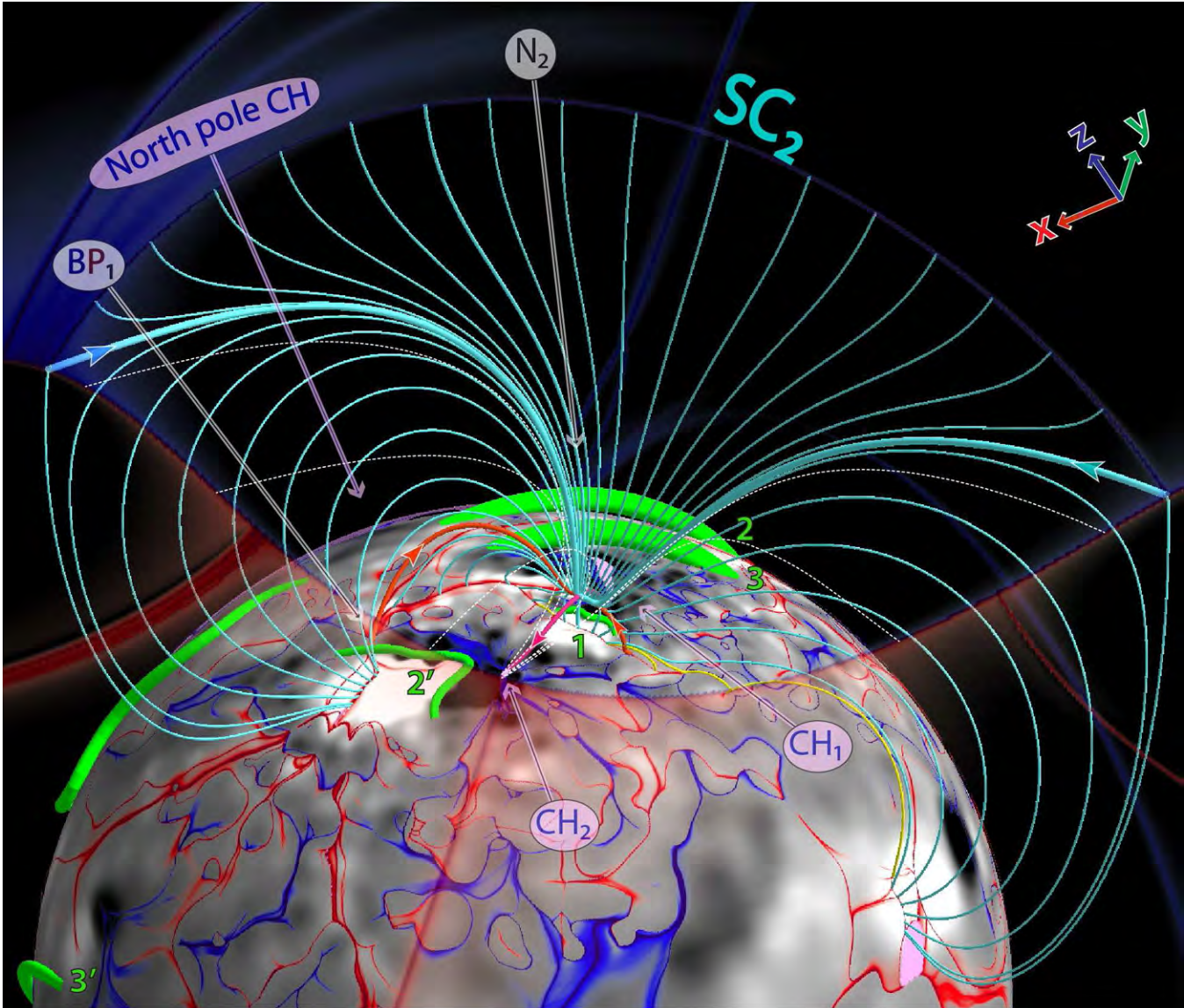


Figure 6. Field line topology of the separatrix curtain SC_2 of pseudo-streamer 2 (embedded between the coronal holes CH_1 and CH_2). The field line styles are the same as in Figure 5, except that the thin yellow lines represent separatrix field lines associated with small-scale photospheric polarity regions. The maps at the photosphere and source surface and their color coding are the same as in Figure 4.

(A color version of this figure is available in the online journal.)

the structure is the same as the one used before for initializing our MHD model of sympathetic eruptions (Török et al. 2011). It is important that these simulations have demonstrated that the generalized separators connecting such BPs and null points are physically similar to the ordinary separators. They both appear to be preferred sites for the formation of current sheets and reconnection of magnetic fluxes.

3.5. Field Line Topology versus High- Q Lines in the Cut Planes

A complementary way to study the structure of a pseudo-streamer is to consider its cross-sectional Q distributions and analyze their variation in response to changing location of the cut plane. As one can anticipate from the above analysis, the simplest pattern of high- Q lines appears to occur in the cut plane across the very middle of pseudo-streamers, where the basic null point is located. The corresponding high- Q lines form there a \cap -type intersection such that the vertical line and arc in the symbol \cap represent, respectively, the discussed SCs and domes.

The shape of separatrix domes at this place essentially follows the path of the spine line associated with the respective basic null point. Above such a dome, the SC separates the open fields of two adjacent coronal holes and observationally corresponds to the stalk of the pseudo-streamer.

However, with shifting the cut plane from the middle to the flanks of pseudo-streamers, the pattern of high- Q lines gets more complicated. In particular, the above high- Q arc can split into several lines, each of which corresponds to a separate half-dome, except for the uppermost line. The latter asymmetrically rises on one side from the curtain up to the source surface and, touching it, forms a cusp. This line determines the border between closed and open fields, since it is nothing else than an intersection line of the cut plane with the separatrix surface of the helmet streamer. Figure 9 illustrates such a structure in a particular cut plane; it also shows schematically how the cross-sectional pattern varies along the pseudo-streamer. Only three cases where the cut plane passes at the photospheric level outside CH_1 and CH_2 are shown in this figure, while the

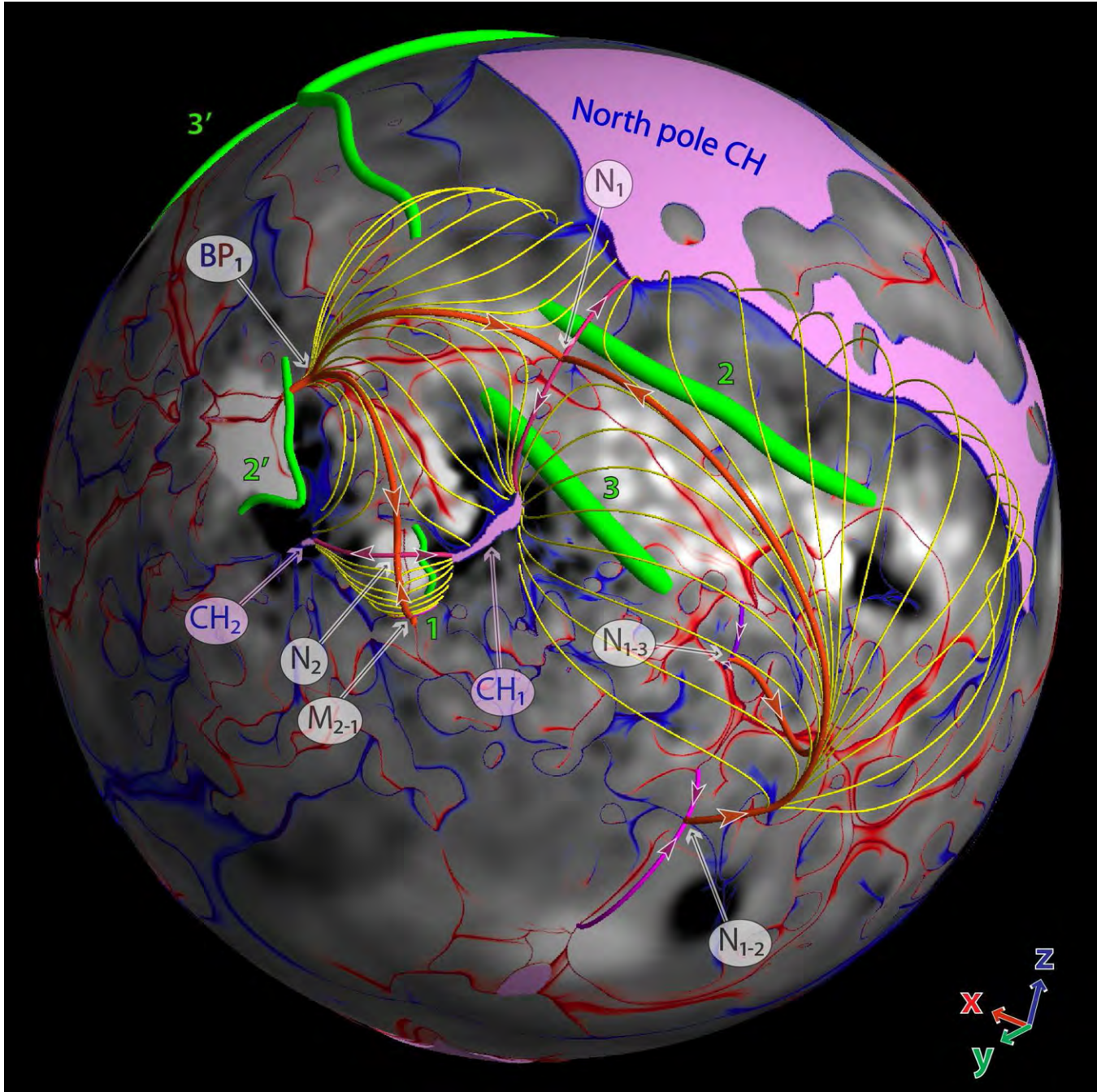


Figure 7. Field line topology of the separatrix domes of pseudo-streamers 1 and 2, one of which is embedded between the northern polar coronal hole and CH_1 and the other between the coronal holes CH_1 and CH_2 . The field line styles are the same as in Figures 5 and 6, except that the thin yellow lines represent separatrix field lines starting either at the bald patch BP_1 or in the fan plane of the null point N_{1-2} ; a similar separatrix dome associated with the null N_{1-3} is not shown. The same style is used for the field lines of the quasi-separatrix surface originated at the magnetic minimum point M_{2-1} . The maps at the photosphere and source surface and their color coding are the same as in Figures 4–6.

(A color version of this figure is available in the online journal.)

remaining cases can be reproduced analogously from the above analysis.

3.6. Concluding Remarks

So far, we have only fully described the structural skeleton of the first pseudo-streamer, including the separatrix curtain SC_1 and respective half-domes with their separators. As concerned with the other two pseudo-streamers, we still have not touched on several separators depicted in Figures 6 and 8 with yellow

and orange thin lines. These separators are due to “scattering” of the SC field lines on small photospheric flux concentrations of negative polarity. Such scattering occurs at BPs or null points to yield additional half-domes, whose edges coincide with the spine lines of the basic nulls N_2 or N_3 . The existence of these features, however, can vary depending on the resolution and smoothing of the used magnetic data, so we ignore them in our study, focusing only on stable structural features that are due to large-scale properties of the configuration.

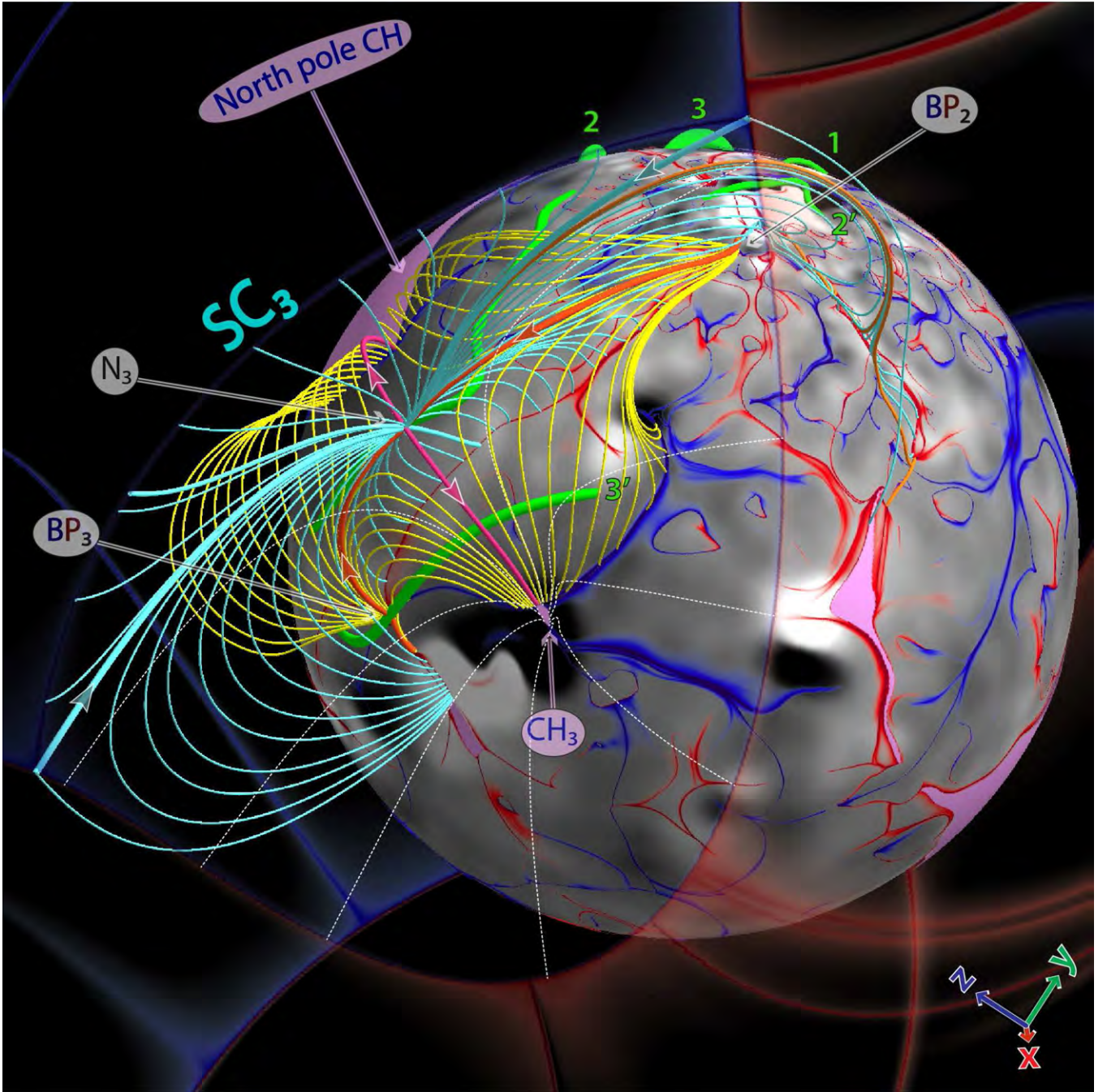


Figure 8. Field line topology of the separatrix curtain (cyan) and dome (yellow) of pseudo-streamer 3 (embedded between the northern polar CH and CH_3). The field line styles are the same as in Figures 5–7, except that the thin orange lines represent the separatrix field lines that are associated with the bald patches and null points of small-scale photospheric polarity regions. The maps at the photosphere and source surface and their color coding are the same as in Figures 4–7.

(A color version of this figure is available in the online journal.)

One also has to remember that the described structure might be distorted in reality by the field of filaments whenever they are present inside pseudo-streamer lobes. Note, however, that such filaments reside prior to eruption in the middle of the lobes along photospheric polarity inversion lines. So possible intense currents of the filaments are located relatively far from the found separatrix domes and curtains and hence the contribution of such currents to the total field must be small at these places compared to the background potential field. Therefore, we think that at large length scales our PFSS model is accurate enough to describe the structure of the real pseudo-streamers with the filaments inside the lobes.

4. MAGNETIC TOPOLOGY AS A CAUSAL LINK IN SYMPATHETIC CMEs

We have studied in Section 3 how SCs and half-domes originate in a given pseudo-streamer at magnetic null points and/or BPs and how they intersect each other along separator field lines. These results are of importance for unveiling a causal link in the sequential eruption of filaments, in which the magnetic topology and reconnection likely played a key role. Indeed, according to the present state of knowledge (Priest & Forbes 2000), a perturbation in the neighborhood of a separator line generally creates along it a current sheet, across which

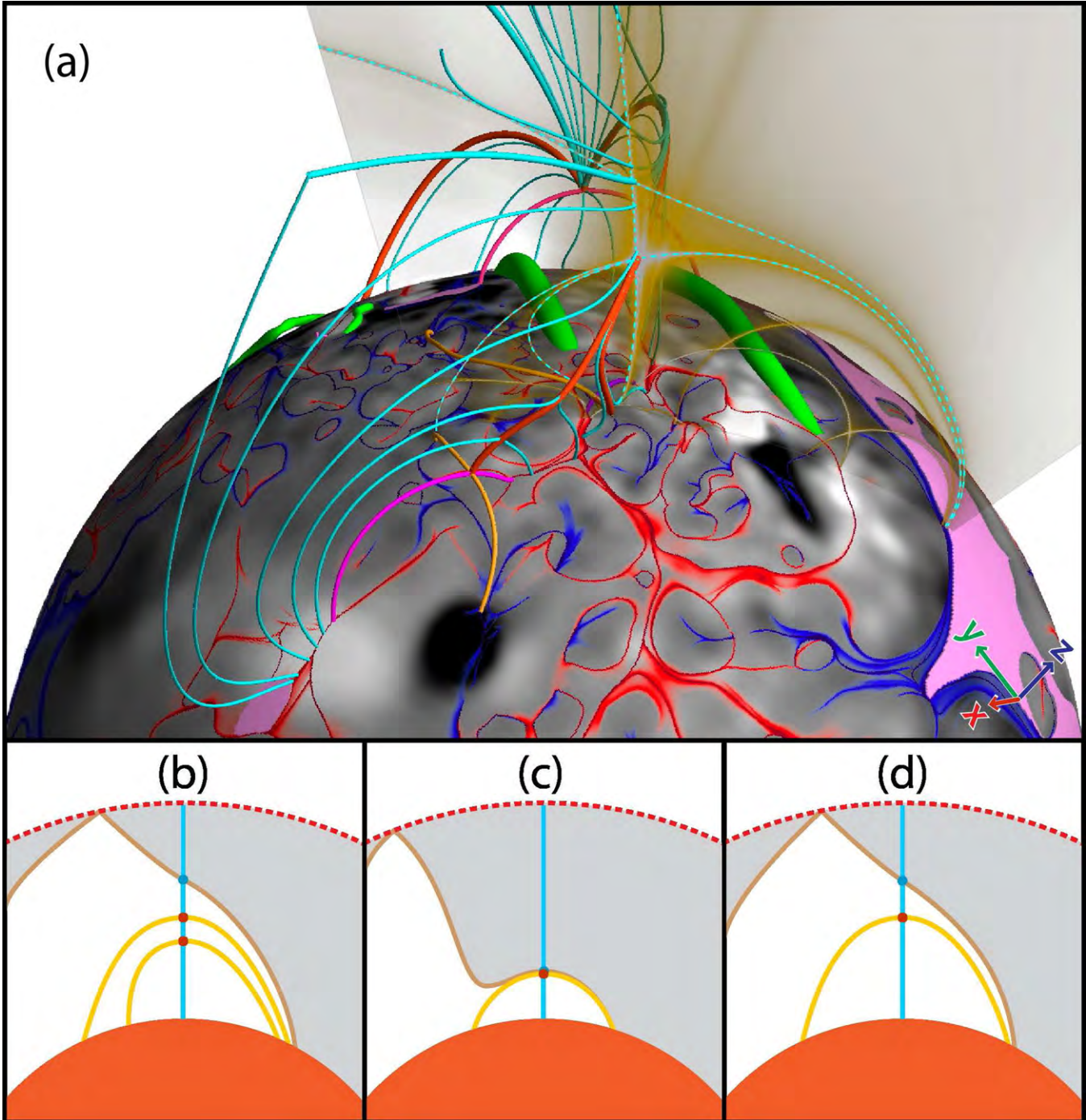


Figure 9. Field line topology of the separatrix curtain SC_1 in relation to the $\log Q$ distribution in a cut plane across the pseudo-streamer 1 (a). This distribution is plotted by using a yellow palette, whose opacity linearly decreases with $\log Q$ in the range from 2.5 to 0.3 down to a complete transparency; the maps at the photosphere, their color coding, and the field line styles are the same as in Figure 5. Dashed (cyan) curves highlight the high- Q lines that represent the intersection lines of the cut plane with SC_1 , helmet-streamer separatrix surface, and two separatrix domes. Such a structure is shown also schematically for this cut and two others in panels (b)–(d), respectively, where the open-field regions are shaded in gray; the extra two cuts are made successively further eastward from the middle of the pseudo-streamer. (A color version of this figure is available in the online journal.)

magnetic fluxes subsequently reconnect in an amount depending on the form and strength of the perturbation. As demonstrated above, each of our pseudo-streamers contains several separators, all of which are connected to a basic null point. A perturbation in its neighborhood is expected then to cause reconnection along each of these separators, resulting ultimately in a flux redistribution between adjacent topological regions.

It follows from our analysis that these regions are simply the volumes bounded by various parts of the SC, half-domes, and

separatrix surface of the helmet streamer. Unfortunately, such a complex topological partition of the volume makes it difficult to foresee all the details of the response of our pseudo-streamers to different MHD perturbations. It is clear, however, that eventually such perturbations will change the magnetic fluxes in the lobes and consequently the stability conditions for the filaments within them. The latter in turn can influence the order of eruption of the filaments, which was recently demonstrated in our simple MHD model of sympathetic eruptions (Török et al. 2011).

In this model, a pseudo-streamer similar to the one that stems from the basic null N_1 played a key role in guiding the eruptions of the magnetic flux ropes, analogous to our filaments 2 and 3. Thus, our present topological analysis of the potential background field further substantiates the model.

Let us put now the results of that model into the context of our present analysis in order to explain the observed sequence of the 2010 August 1–2 CMEs. For simplicity, we restrict our consideration to the reconnection processes that occur in the vicinity of the basic nulls of the pseudo-streamers, where we expect the greatest perturbation to occur during the onset of eruptions. As shown above, all separatrix half-domes merge there and form together with the SC a simple ρ -type intersection. Such a separatrix structure implies that, irrespective of the form of the external perturbation, the reconnection triggered there will be of the interchange type (e.g., Fisk 2005). It will exchange the fluxes between the lobes and coronal holes in such a way that the sum of the fluxes in both the two lobes and the two coronal holes remains unchanged. In other words, the diagonally opposite lobes and coronal holes form conjugate pairs, so that the flux in one pair increases by the same amount that it decreases in the other pair.

To facilitate further discussion, we label the pseudo-streamers by the numeric label of their basic null; similarly, we label the lobes by the label of their embedded filament. Note, first, that erupting filament 1 resides initially in pseudo-streamer 2, which is located south of pseudo-streamer 1 (see Figure 7). Therefore, the rise of filament 1 perturbs the southern side of pseudo-streamer 1 and eventually triggers interchange reconnection between the fluxes of coronal hole CH_1 and lobe 2. This reconnection reduces the flux in lobe 2, thereby removing the field lines that overlie and stabilize filament 2, eventually causing it to erupt (i.e., the second eruption). On the other hand, this same interchange reconnection causes the flux in lobe 3 to increase, adding field lines that overlie filament 3, thus further stabilizing it. However, later in time, after erupting filament 2 has risen to a sufficient height, a vertical current sheet forms in its wake, providing a site for interchange reconnection between the fluxes of lobe 3 and the northern polar coronal hole. This second reconnection eventually reduces the flux in lobe 3, removing field lines that overlie and stabilize filament 3, eventually causing filament 3 to erupt (i.e., the third eruption).

This scenario is consistent with that proposed for the sequential eruption of filaments 1–3 in our idealized model (Török et al. 2011). There is one difference though: our present PFSS model reveals that filament 1 was also located inside a pseudo-streamer, which is pseudo-streamer 2 in our notation. The presence of this pseudo-streamer, however, merely facilitates the eruption of filament 1, because its overlying field becomes open at a very low height. So this new feature fits nicely with our earlier proposed mechanism.

The present analysis suggests possible explanations also for the eruptions 2' and 3'. According to Figures 5–7, filament 2' passes above bald patch BP_1 , which is connected by two separators to the basic null points N_1 and N_2 . As discussed above, the rise of filaments 1 and 2 is expected to activate these separators, forming current sheets along them, and subsequently triggering reconnection. Around the location of BP_1 , this reconnection may have been of the tether-cutting type (Moore et al. 2001), reducing the confinement of the active-region core field and eventually unleashing its eruption. This explanation is in agreement with the fact that *SDO/AIA* observed several brightenings in the active region before the CME occurred. There was

a particularly strong brightening at $\sim 06:36$ UT below and above filament 2', very close to the bald patch BP_1 (see the inset in Figure 10). This brightening occurred after filament 2 had already started to rise, implying the above activation of the separator and subsequent reconnection in the vicinity of bald patch BP_1 . We note that Liu et al. (2010) also associated the pre-eruption brightening at $\sim 06:36$ UT to tether-cutting reconnection, triggered, however, by photospheric converging flows rather than separator activation. It appears indeed possible that both processes played a role. We will make a more detailed comparison of our topological analysis with observations in Paper II.

The location of pseudo-streamers 1 and 3 indicates that the eruptions 2 and 2' should produce a significant perturbation of the northern side of pseudo-streamer 3. This should lead to interchange reconnection between lobe 3' and the northern polar coronal hole, reducing the magnetic flux in this lobe and eventually causing filament 3' to erupt, in a similar way as described for filament 2. Note also that filament 3' rises above bald patch BP_3 , which is connected by a separator to the basic null N_3 (see Figure 8). As discussed above for eruption 2', resulting tether-cutting reconnection may trigger the destabilization of filament 3', in tandem with the indicated flux reduction in the lobe 3' caused by interchange reconnection.

This concludes the extended scenario for the sympathetic eruptions under study. Figure 10 summarizes it, presenting all the topological features that are relevant for this scenario. In particular, it depicts the closed separators (red thick lines) that form a long chain that traverses through all three pseudo-streamers. As described above, such a separator chain likely sets up a global coupling between eruptions occurring at widely separated locations. Figuratively speaking, this separator chain plays the role of a “safety fuse” in which a single eruption at one end of the chain triggers along it a sequence of the observed electromagnetic explosions.

Additional global coupling between pseudo-streamers and eruptions might also be provided by the open separators (thick cyan lines in Figure 10), which connect the basic nulls of the pseudo-streamers to the cusp of the helmet streamer. This coupling, however, has yet to be verified. It requires a more advanced model than the PFSS model used in the present study. We plan to use an MHD model for this purpose in the next step of our study.

The proposed explanation of the assumed causal link in the observed sympathetic eruptions is of substantial heuristic value. It is particularly useful as a guide for setting up and analyzing further numerical studies of these eruptions. In combination with our structural analysis, more detailed numerical simulations of CMEs in this configuration are needed to prove the existence of such a link and to deepen its understanding.

5. IMPLICATIONS FOR THE S-WEB MODEL

The structural analysis of pseudo-streamers that we have described has important implications not only for sympathetic CMEs but also for the slow solar wind. The recent S-web model (Antiochos et al. 2011; Linker et al. 2011) has sparked substantial interest in the community (Crooker et al. 2012; Wang et al. 2012). Unfortunately, several important issues related to this model are not well understood. Since the results obtained above relate to the S-web model, we will use this opportunity to clarify these issues.

The first issue relates to the concept of coronal-hole connectivity. Some confusion has arisen because the connectivity

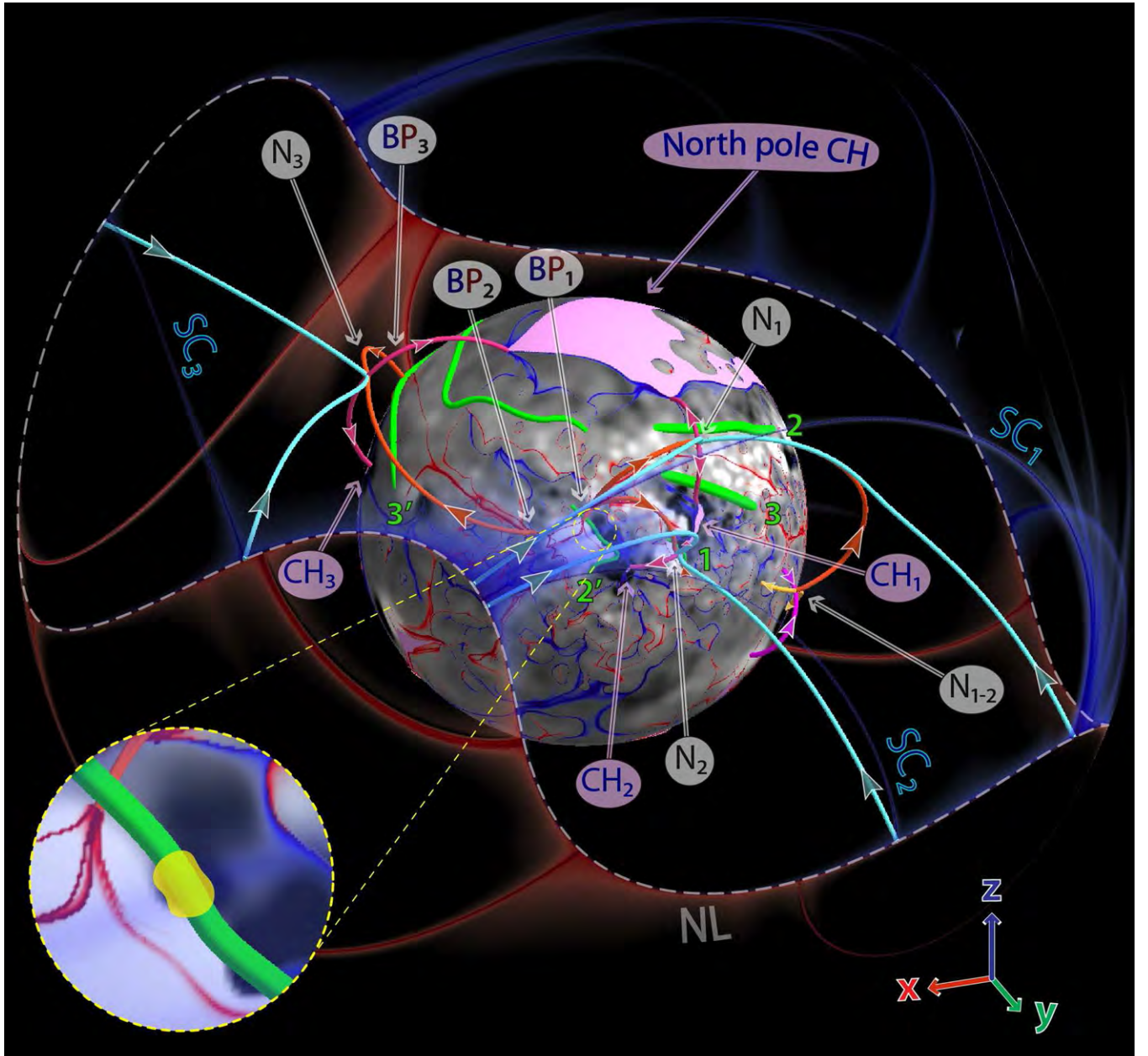


Figure 10. Chain of separators and spine lines in all three pseudo-streamers that were involved in the 2010 August 1–2 sympathetic CMEs. The white dashed line is the null magnetic field line of the source surface—together with the open separator field lines (cyan), it provides a global coupling between all three null points of the pseudo-streamer separatrix curtains. The inset shows a zoomed region near BP_1 , where a strong pre-flare brightening (indicated by yellow blob) was observed by *SDO/AIA* at $\sim 06:36$ UT shortly after which eruption 2' started.

(A color version of this figure is available in the online journal.)

of coronal holes has been interpreted in two different senses. We can consider coronal holes either as two-dimensional regions at the photosphere or as three-dimensional regions in the corona. Though coronal holes of like polarity are always connected when considered as three-dimensional regions, it is important to note that they *can be disconnected* in the photosphere when considered as two-dimensional regions (Titov et al. 2011). In this case, they merge at some height in the corona via a field line separatrix structure that observationally manifests itself as a pseudo-streamer.

The pseudo-streamers we described above (see Figures 5–8) illustrate this fact conclusively. All these cases were characterized by disconnected coronal holes CH_1 , CH_2 , and CH_3 (Figure 2), each of which merges with an adjacent coronal

hole at the height of the basic null point of the corresponding pseudo-streamer. At heights where the magnetic field becomes completely open, the corresponding separatrix curtains SC_1 , SC_2 , and SC_3 serve as interfaces between the holes. Note also that their footprints appear at the source surface as very sharp high- Q lines, whose ends are joined to the null line of the magnetic field (Section 3.1).

Of course, this does not exclude the possibility for different parts of photospheric open-field regions to be connected with each other through narrow corridors. Several examples of such corridors are also seen in our northern polar coronal hole (Figure 2). They imply the appearance of QSLs in the open field, as proposed first by Antiochos et al. (2007), and whose transformation into SCs and back to QSLs has been described

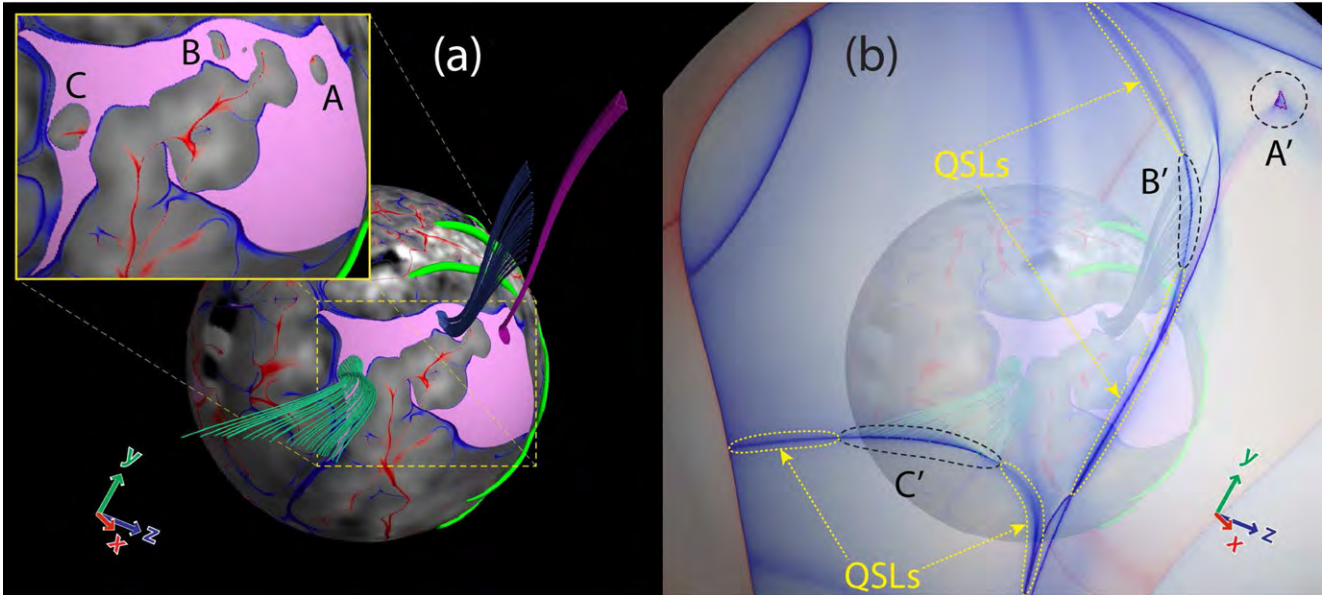


Figure 11. Structure of magnetic field lines near parasitic polarity regions A, B, and C embedded into the northern coronal hole (a) and location of their footprints A', B', and C' at the source surface (b), where a (semi-transparent) $\text{slog} Q$ distribution is also displayed. The high- Q lines encircled by dashed (yellow) lines correspond to the footprints of QSLs that originate in the photospheric open-field corridors adjacent to these polarities.

(A color version of this figure is available in the online journal.)

at length by Titov et al. (2011). As already pointed out in Section 3.1, such QSLs appear at the source surface as high- Q lines with a smooth distribution of Q across their widths (Figure 2(b)). Just as in the case of SCs, these high- Q lines are joined at both ends to the null line of the magnetic field.

Thus, in both the case of truly disconnected and connected coronal holes, interpreted as two-dimensional photospheric regions, their mapping to the source surface connects to the null line of the helmet streamer. This is in contrast to the interpretation of Crooker et al. (2012), who regarded this property of the field line mapping as evidence of the connectivity of coronal holes at the photospheric level. Moreover, we think that the V-shaped coronal hole they interpreted as connected in the photosphere is actually disconnected, as our earlier study of the same case indicates in the framework of the global MHD model (Titov et al. 2011). This particular example shows that when coronal holes are connected in three dimensions it does not necessarily imply that they are connected in the photosphere too.

It remains to be studied how numerous the above open-field QSLs are, compared to SCs, in magnetic configurations with a realistically high resolution. Note that by definition they both belong to the S-web. In the $\text{slog} Q$ -distribution at the source surface, the S-web appears as a network of high- Q arcs connected to the null line of the helmet streamer (Figure 2(b)). The width in latitude of the S-web at this surface is a well-defined quantity, because its value is uniquely related to the open photospheric flux that is (nearly) disconnected from the main bodies of the polar coronal holes. It is unlikely that this flux, and hence the width of the corresponding S-web, will significantly change if one further increases the resolution of the input magnetic data and the corresponding PFSS model.

This conclusion is in contrast with the statement of Wang et al. (2012) that the S-web will extend to the polar region if one resolves its small parasitic polarities. Each such polarity will, indeed, bring additional (quasi-)separatrix structures into the open-field regions. However, in contrast to the SCs of pseudo-streamers, these structures will, first, have a much smaller angular size and, second, will not criss-cross the S-web, but

rather stay mostly isolated from it. Since the quasi-separatrix structures arising from parasitic polarities in polar coronal holes have different geometrical sizes and structural properties, their physical properties are also likely to be different. Therefore, they have not been included into the definition of the S-web (Antiochos et al. 2011), regardless of the fact that the polar plumes associated with these parasitic polarities might appear similar to pseudo-streamers observationally.

To clearly make this point, Figure 11 shows what happens around three small parasitic polarities (A, B, and C) embedded into the northern coronal hole. Panel (a) depicts three sets of open field lines that start very close to the oval high- Q lines bordering the closed magnetic flux of these polarities. Panel (b) shows their source-surface footprints A', B', and C', indicating that such field lines hit the boundary far away from the null line. Thus, their behavior indeed differs from that of the field lines belonging to the SCs we described previously.

In particular, as stated above, for polarities that are far from the main border of their surrounding coronal hole, such as A, their signature at the source surface A' is completely isolated from the S-web. Polarities B and C, however, are much closer to the coronal-hole border; they are detached from it by only a relatively narrow open-field corridor. As expected, the field lines starting in these corridors form QSLs whose footprints at the source surface adjoin on each side of their respective footprints B' and C' (as shown in Figure 2(b)). The high- Q lines resulting from these merged QSLs would appear, at first sight, to form arcs whose ends join the null line of the helmet streamer. However, we would argue that these “arcs” do not genuinely belong to the S-web because these segments have rather low values of $\log Q$ ($\lesssim 1.5$). In summary, we have argued that the addition of small parasitic polarities in polar coronal holes would not contribute to the S-web significantly, if at all. We intend to test this conjecture in future work by explicitly calculating the contribution of parasitic polarities in high-resolution PFSS models.

These considerations help us to predict how our S-web will change with increasing resolution of the input magnetic data

and the corresponding PFSS model. First, increased resolution will cause additional fragmentation of the disconnected coronal holes, while leaving their total magnetic flux approximately unchanged. Our analysis suggests that this will increase the number of cells and high- Q lines in the S-web, but will not substantially increase its width in latitude at the source surface.

Depending on the strength of the parasitic polarities introduced when going to higher resolution, and their positions in coronal holes, the separatrix structure enclosing these polarities can be of two types. First, it can be just a single BP separatrix surface, as in our examples shown in Figure 11. This structure contains no null points in the corona, but nevertheless it completely separates the closed flux of the parasitic polarity from the surrounding magnetic field (Bungey et al. 1996; Müller & Antiochos 2008). Second, it can also be a more familiar structure with a dome-like fan surface and spine line across both coming out from a single null point and surrounded by QSLs (Masson et al. 2009).

These two types of separatrix structures are similar in that their (quasi)-separatrix field lines do not fan out in the open-field region as much as they do in pseudo-streamers. The perturbation of such a structure due to local flux emergence or photospheric motion causes formation of a current sheet and reconnection, both localized in a small region near the corresponding BPs or null points. This process can be considered as a mechanism for producing coronal plumes or “anemone” jets in polar coronal holes (Moreno-Insertis et al. 2008; Müller & Antiochos 2008; Pariat et al. 2010).

The pseudo-streamers are structurally very different. As shown above, they contain several separators, two of which are open, while the others are closed. An emergence, submergence, and/or displacement of photospheric flux concentrations in the lobes of pseudo-streamers, and in their surrounding, must lead to the formation of current sheets along the separators closest to the source of the perturbations. Since current sheets form along the entire length of separators, the related reconnection processes proceed similarly (Parnell et al. 2010). This indicates that reconnection in pseudo-streamers and coronal plumes might have quite different characteristics, which additionally substantiates the original definition of the S-web.

The open separators are lines at which the open and closed magnetic fields become in contact with each other. They appear to be the longest separators in the pseudo-streamers, so most of the interchange reconnection must occur along them. How does it proceed in the presence of multiple closed separators, all connected together with the basic nulls of the pseudo-streamers? This question is of particular importance for understanding the physics of pseudo-streamers and has never been investigated before, because their topological structure was unknown. The answer to this fundamental question is crucial to determine if the S-web model can explain the origin of the slow solar wind. Therefore, it ought to be the focus of the future studies, with special emphasis on the processes that occur both at open separators and the QSLs associated with open-field corridors.

The plasma sheets of pseudo-streamers, as observed in the white-light corona, are composed of fine ray-like structures that are presumed to be formed by interchange reconnection at the streamer cusp (Wang et al. 2012). Such an explanation is consistent with our discussion of open separators, except that in our scenario reconnection occurs along the entire length of these separators rather than just at the mentioned cusp points (which are the footpoints of our open separators at the source surface). In light of our present analysis, the observed ray-like structures are

likely a part of the S-web. For structural features (like separators) to be visible, they have to not only be present, but also perturbed sufficiently (e.g., by waves or photospheric motions). Therefore, at any moment in time, only a small fraction of the S-web might be visible in white light.

It should also be emphasized that the S-web model does not assume a priori that reconnection in pseudo-streamers generates the slow wind in the form of plasma blobs, as it does in helmet streamers (Wang et al. 2012). In fact, we expect that this process must be so different here that it will directly affect the observational properties of the pseudo-streamers. Indeed, in contrast to the helmet streamers, the reconnection in the pseudo-streamers has to occur not in the plasma sheet itself but rather at its edges, where the above open separators are located. Consequently, the pseudo-streamer material must be replenished, at least in part, by the plasma that flows out from those edges. This process has likely to occur in a sporadic fashion, namely, each time when the interchange reconnection takes place between open and closed fields. As a result, the respective reconnection outflows have to be modulated accordingly to produce in the pseudo-streamers the mentioned above ray-like rather than blob-like structures. This consideration shows that, irrespective of its relevance to the problem of the origin of the slow solar wind, the question on how the interchange reconnection modifies the properties of the wind flow in the pseudo-streamers deserves very close attention in the future studies.

6. SUMMARY

We have studied the large-scale topology of the coronal magnetic field determined in the framework of a PFSS model for the time period 2010 August 1–2, when a sequence of sympathetic CMEs occurred. First, this model was computed from the observed data of the photospheric magnetic field. Second, we have calculated high-resolution distributions of the squashing factor Q at the photospheric and source-surface boundaries and at several cut planes across the regions where the CMEs started. Third, we have developed a special technique for tracing (quasi)-separatrix field lines that pass through the high- Q lines of such distributions. These tools allowed us to fulfill a comprehensive analysis of the magnetic field structure.

Of particular interest to us were large-scale separatrix surfaces that divide the coronal volume into topologically distinct regions in which the erupting filaments originated. We have found that four of these five filaments were initially located in the lobes of three pseudo-streamers. Such lobes are obtained as a result of intersection of curtain-like and dome-like separatrix surfaces of the coronal magnetic field. The SC is a fan separatrix surface associated with a null point that is called basic one and located at a certain height in the corona between two adjacent coronal holes of like polarity. Such a curtain is formed by open and closed field lines fanning out from the basic null point. The dome separatrix surfaces are made of two half-domes joined with each other along the spine line of this null point. The half-domes are formed by the field lines that also fan out either from a BP or another null point, which both are located at the flanks of the pseudo-streamer.

In the middle cross-section passing through the basic null of a pseudo-streamer, these separatrix surfaces intersect to produce a \cap -type shape in which the vertical line and arc represent the SC and adjoint half-domes, respectively. Above the half-domes in this cross-section, the curtain separates adjacent coronal holes of like polarity and observationally corresponds to the stalk of

pseudo-streamers. At heights below the basic null of the pseudo-streamer, the coronal holes become disconnected by closed magnetic fields rooted in parasitic polarities and separated by the distance equal to the local width of the separatrix half-domes.

The separatrix surfaces of the pseudo-streamers in the August 1–2 events are located relatively far from the pre-eruption positions of the filaments, so that their contributions to the total field and hence their influence on these surfaces must be small. Therefore, our source-surface model should be sufficiently accurate to reproduce the large-scale structure of real pseudo-streamers with filaments inside.

The indicated SCs intersect half-domes along closed separator field lines, or simply separators, that pass through the null points or BPs at the flanks of the pseudo-streamers. In addition, these curtains intersect the helmet-streamer separatrix surface twice along open separator field lines, which connect the basic nulls of the pseudo-streamers to streamer-cusp points. Invoking our recent MHD model of sympathetic eruptions (Török et al. 2011), we argue that magnetic reconnection at both these types of separators is likely a key process in sympathetic eruptions, because it controls how magnetic fluxes are redistributed between the lobes of pseudo-streamers during eruptions. It has been demonstrated here that the configuration which harbored the first three erupting filaments had a similar magnetic topology as was assumed in that model. Thus, the present topological analysis of the PFSS background field substantiates the previous assumptions on the initial configuration in Török et al. (2011).

Here, we proceeded with a generalization of this earlier proposed scenario, by noticing, first, that the indicated separators in our configuration form a huge chain that traverses through all three pseudo-streamers involved in the eruptions. We have qualitatively explained how a single eruption at one end of such a separator chain can trigger a whole sequence of eruptions.

We have also discussed the implications of our obtained results for the S-web model of the slow solar wind by emphasizing those issues that have not been well understood so far. First, we have demonstrated how the pseudo-streamer structure accommodates disconnection and merging of two coronal holes, respectively, below and above the basic nulls of the pseudo-streamers. Second, we have explained the differences in magnetic topology between pseudo-streamers and separatrix structures enclosing small parasitic polarities in the polar coronal holes and discussed why such structures were not included in the original definition of the S-web. Third, we have emphasized that the sources of the slow solar wind most likely reside both at the separators of pseudo-streamers and QSLs originated in narrow photospheric corridors of the open magnetic field.

The contribution of V.S.T., Z.M., T.T., and J.A.L. was supported by NASA's HTP, LWS, and SR&T programs, SHINE under NSF Grant AGS-1156119, CISM (an NSF Science and Technology Center), and a contract from Lockheed-Martin to Predictive Science, Inc.; O.P. was supported by NSF Grant ATM-0837519 and NASA Grant NNX09AG27G.

REFERENCES

- Altschuler, M. D., & Newkirk, G. 1969, *Sol. Phys.*, **9**, 131
- Antiochos, S. K., DeVore, C. R., Karpen, J. T., & Mikić, Z. 2007, *ApJ*, **671**, 936
- Antiochos, S. K., Mikić, Z., Titov, V. S., Lionello, R., & Linker, J. A. 2011, *ApJ*, **731**, 112
- Aulanier, G., Parlat, E., & Démoulin, P. 2005, *A&A*, **444**, 961
- Biesecker, D. A., & Thompson, B. J. 2000, *J. Atmos. Sol.–Terr. Phys.*, **62**, 1449
- Bumba, V., & Klivana, M. 1993, *Ap&SS*, **199**, 45
- Bungey, T. N., Titov, V. S., & Priest, E. R. 1996, *A&A*, **308**, 233
- Close, R. M., Parnell, C. E., & Priest, E. R. 2004, *Sol. Phys.*, **225**, 21
- Crooker, N. U., Antiochos, S. K., Zhao, X., & Neugebauer, M. 2012, *J. Geophys. Res.*, **117**, 4104
- Démoulin, P., Henoux, J. C., Priest, E. R., & Mandrini, C. H. 1996, *A&A*, **308**, 643
- Eselevich, V. G., Fainshtein, V. G., & Rudenko, G. V. 1999, *Sol. Phys.*, **188**, 277
- Fisk, L. A. 2005, *ApJ*, **626**, 563
- Forbes, T. 2010, in *Models of Coronal Mass Ejections and Flares*, ed. C. J. Schrijver & G. L. Siscoe (Cambridge: Cambridge Univ. Press), 159
- Forbes, T. G. 2000, *J. Geophys. Res.*, **105**, 23153
- Harrison, R. A., Davies, J. A., Möstl, C., et al. 2012, *ApJ*, **750**, 45
- Haynes, A. L., & Parnell, C. E. 2010, *Phys. Plasmas*, **17**, 092903
- Hundhausen, A. J. (ed.) 1972, *Coronal Expansion and Solar Wind* (Berlin: Springer)
- Jiang, Y., Shen, Y., Yi, B., Yang, J., & Wang, J. 2008, *ApJ*, **677**, 699
- Jiang, Y., Yang, J., Hong, J., Bi, Y., & Zheng, R. 2011, *ApJ*, **738**, 179
- Linker, J. A., Lionello, R., Mikić, Z., Titov, V. S., & Antiochos, S. K. 2011, *ApJ*, **731**, 110
- Liu, C., Lee, J., Karlický, M., et al. 2009, *ApJ*, **703**, 757
- Liu, R., Liu, C., Wang, S., Deng, N., & Wang, H. 2010, *ApJ*, **725**, L84
- Masson, S., Parlat, E., Aulanier, G., & Schrijver, C. J. 2009, *ApJ*, **700**, 559
- Moon, Y.-J., Choe, G. S., Park, Y. D., et al. 2002, *ApJ*, **574**, 434
- Moore, R. L., Sterling, A. C., Hudson, H. S., & Lemen, J. R. 2001, *ApJ*, **552**, 833
- Moreno-Insertis, F., Galsgaard, K., & Ugarte-Urra, I. 2008, *ApJ*, **673**, L211
- Müller, D. A. N., & Antiochos, S. K. 2008, *Ann. Geophys.*, **26**, 2967
- Panasenco, O., & Velli, M. M. 2010, *Magnetic Structure of Twin Filaments Inside Pseudostreamers*, AGU Fall Meeting Abstracts, A1663
- Parlat, E., Antiochos, S. K., & DeVore, C. R. 2010, *ApJ*, **714**, 1762
- Parlat, E., & Démoulin, P. 2012, *A&A*, **541**, A78
- Parnell, C. E., Haynes, A. L., & Galsgaard, K. 2010, *J. Geophys. Res.*, **115**, A02102
- Press, W. H., Teukolsky, S. A., Vetterling, W. T., & Flannery, B. P. 2007, *Numerical Recipes: The Art of Scientific Computing* (3rd ed.; Cambridge, NY: Cambridge Univ. Press)
- Priest, E. R., & Démoulin, P. 1995, *J. Geophys. Res.*, **100**, 23443
- Priest, E. R., & Forbes, T. G. 2000, *Magnetic Reconnection: MHD Theory and Applications* (Cambridge: Cambridge Univ. Press), 612
- Priest, E. R., & Titov, V. S. 1996, *Phil. Trans. R. Soc. A*, **354**, 2951
- Ramsey, H. E., & Smith, S. F. 1966, *AJ*, **71**, 197
- Riley, P., Linker, J. A., Mikić, Z., et al. 2006, *ApJ*, **653**, 1510
- Savcheva, A., Parlat, E., van Ballegoijen, A., Aulanier, G., & DeLuca, E. 2012a, *ApJ*, **750**, 15
- Savcheva, A. S., van Ballegoijen, A. A., & DeLuca, E. E. 2012b, *ApJ*, **744**, 78
- Schatten, K. H., Wilcox, J. M., & Ness, N. F. 1969, *Sol. Phys.*, **6**, 442
- Schrijver, C. J., & Title, A. M. 2011, *J. Geophys. Res.*, **116**, A04108
- Seehafer, N. 1986, *Sol. Phys.*, **105**, 223
- Shen, Y., Liu, Y., & Su, J. 2012, *ApJ*, **750**, 12
- Titov, V. S. 2007, *ApJ*, **660**, 863
- Titov, V. S., Forbes, T. G., Priest, E. R., Mikić, Z., & Linker, J. A. 2009, *ApJ*, **693**, 1029
- Titov, V. S., Hornig, G., & Démoulin, P. 2002, *J. Geophys. Res.*, **107**, 1164
- Titov, V. S., Mikić, Z., Linker, J. A., & Lionello, R. 2008, *ApJ*, **675**, 1614
- Titov, V. S., Mikić, Z., Linker, J. A., Lionello, R., & Antiochos, S. K. 2011, *ApJ*, **731**, 111
- Titov, V. S., Priest, E. R., & Démoulin, P. 1993, *A&A*, **276**, 564
- Török, T., Panasenco, O., Titov, V. S., et al. 2011, *ApJ*, **739**, L63
- Wang, H., Chae, J., Yurchyshyn, V., et al. 2001, *ApJ*, **559**, 1171
- Wang, Y.-M., Grappin, R., Robbrecht, E., & Sheeley, N. R., Jr. 2012, *ApJ*, **749**, 182
- Wang, Y.-M., Sheeley, N. R., Jr., & Rich, N. B. 2007, *ApJ*, **658**, 1340
- Wheatland, M. S., & Craig, I. J. D. 2006, *Sol. Phys.*, **238**, 73
- Yang, J., Jiang, Y., Zheng, R., et al. 2012, *ApJ*, **745**, 9
- Zhukov, A. N., & Veselovsky, I. S. 2007, *ApJ*, **664**, L131
- Zuccarello, F., Romano, P., Farnik, F., et al. 2009, *A&A*, **493**, 629

Initiation of Coronal Mass Ejections by Sunspot Rotation

T. Török · M. Temmer · G. Valori · A.M. Veronig ·
L. van Driel-Gesztelyi · B. Vršnak

Received: 28 July 2012 / Accepted: 6 March 2013
© Springer Science+Business Media Dordrecht 2013

Abstract We study a filament eruption, two-ribbon flare, and coronal mass ejection (CME) that occurred in NOAA Active Region 10898 on 6 July 2006. The filament was located South of a strong sunspot that dominated the region. In the evolution leading up to the eruption, and for some time after it, a counter-clockwise rotation of the sunspot of about 30 degrees was observed. We suggest that the rotation triggered the eruption by progressively expanding the magnetic field above the filament. To test this scenario, we study the effect of twisting the initially potential field overlying a pre-existing flux-rope, using three-dimensional zero- β MHD simulations. We first consider a relatively simple and symmetric system, and

Electronic supplementary material The online version of this article (doi:[10.1007/s11207-013-0269-9](https://doi.org/10.1007/s11207-013-0269-9)) contains supplementary material, which is available to authorized users.

T. Török (✉)
Predictive Science, Inc., 9990 Mesa Rim Rd., Suite 170, San Diego, CA 92121, USA
e-mail: tibor@predsci.com

M. Temmer · A.M. Veronig
IGAM/Kanzelhöhe Observatory, Institute of Physics, Universität Graz, Universitätsplatz 5, 8010 Graz, Austria

M. Temmer
Space Research Institute, Austrian Academy of Sciences, Schmiedlstrasse 6, 8042 Graz, Austria

G. Valori · L. van Driel-Gesztelyi
LESIA, Observatoire de Paris, CNRS, UPMC, Université Paris Diderot, 5 place Jules Janssen, 92190 Meudon, France

L. van Driel-Gesztelyi
Mullard Space Science Laboratory, University College London, Holmbury St. Mary, Dorking, Surrey RH5 6NT, UK

L. van Driel-Gesztelyi
Konkoly Observatory, Hungarian Academy of Sciences, Budapest, Hungary

B. Vršnak
Hvar Observatory, Faculty of Geodesy, University of Zagreb, Kačićeva 26, 10000 Zagreb, Croatia

then study a more complex and asymmetric magnetic configuration, whose photospheric-flux distribution and coronal structure are guided by the observations and a potential field extrapolation. In both cases, we find that the twisting leads to the expansion of the overlying field. As a consequence of the progressively reduced magnetic tension, the flux-rope quasi-statically adapts to the changed environmental field, rising slowly. Once the tension is sufficiently reduced, a distinct second phase of evolution occurs where the flux-rope enters an unstable regime characterised by a strong acceleration. Our simulations thus suggest a new mechanism for the triggering of eruptions in the vicinity of rotating sunspots.

Keywords Magnetic fields, corona · Active regions, models · Coronal mass ejections, initiation and propagation · Sunspots, velocity

1. Introduction

Filament (or prominence) eruptions, flares, and coronal mass ejections (CMEs) are the three large-scale eruptive events on the Sun. It has become clear in recent years that they are not independent phenomena, but different observational manifestations of a more general process, namely the sudden and violent disruption and dynamic reconfiguration of a localised volume of the coronal magnetic field (*e.g.* Forbes, 2000). Whether or not all three phenomena occur together appears to depend mainly on the properties of the pre-eruptive configuration. For example, CMEs can occur without a filament eruption (if no filament has formed in the source region of the erupting flux prior to its eruption) and without significant flaring (if the magnetic field in the source region is too weak; *e.g.* Zirin, 1998) or, in extreme cases, even without any low-coronal or chromospheric signature (Robbrecht, Patsourakos, and Vourlidas, 2009). On the other hand, both flares and filament eruptions are not always accompanied by a CME (if, for instance, the magnetic field above the source region is too strong; see, *e.g.*, Moore *et al.*, 2001; Nindos and Andrews, 2004; Török and Kliem, 2005). In large events such as the one studied in this article, however, all three phenomena are observed almost always. Such events typically start with the slow rise of a filament and/or overlying loops (*e.g.* Maričić *et al.*, 2004; Schrijver *et al.*, 2008; Maričić, Vršnak, and Roša, 2009), which is often accompanied by weak pre-flare signatures in EUV or X-rays (*e.g.* Maričić *et al.*, 2004; Chifor *et al.*, 2007). The slow rise is followed by a rapid acceleration and a huge expansion of the eruptive structure, which is then observed as a CME. The rapid acceleration has been found in most cases to be very closely correlated with the flare impulsive phase (*e.g.* Kahler *et al.*, 1988; Zhang *et al.*, 2001; Maričić *et al.*, 2007; Temmer *et al.*, 2008).

Although it is now widely accepted that solar eruptions are magnetically driven, the detailed physical mechanisms that initiate and drive eruptions are still controversial. Accordingly, a large number of theoretical models have been proposed in the past decades (for a recent review see, *e.g.*, Forbes, 2010). Virtually all of these models consider as pre-eruptive configuration a sheared or twisted core field low in the corona, which stores the free magnetic energy required for eruption and is stabilised by the ambient coronal field. The choice of such a configuration is supported by observations of active regions, which often display sheared structures (filaments and soft X-ray sigmoids) surrounded by less sheared, tall loops. An eruption is triggered if the force balance between the core field and the ambient field is destroyed, either by increasing the shear or twist in the core field or by weakening the stabilizing restoring force of the ambient field (see, *e.g.*, Aulanier *et al.*, 2010).

One of the many mechanisms that has been suggested to trigger eruptions is the rotation of sunspots. The idea was put forward by Stenflo (1969), who showed that the order of

magnitude of the energy deposition into coronal structures by sunspot rotations is sufficient to produce flaring activity (see also Kazachenko *et al.*, 2009).

Sunspot rotations have been known for a long time – the first evidence, based on spectral observations, was presented one century ago by Evershed (1910) – and since then they have been the subject of numerous analyses. Still, measurements of sunspot rotation are not straightforward, and, depending on the method employed, can give quite different results (see, *e.g.*, Min and Chae, 2009). Meticulous case studies (*e.g.* Zhang, Li, and Song, 2007; Min and Chae, 2009; Yan *et al.*, 2009), as well as detailed statistical analyses (*e.g.* Brown *et al.*, 2003; Yan and Qu, 2007; Zhang, Liu, and Zhang, 2008; Li and Zhang, 2009; Suryanarayana, 2010) showed that sunspots can rotate significantly, up to several hundreds of degrees over a period of a few days. Interestingly, sunspots do not necessarily rotate as a rigid body: Brown *et al.* (2003) and Yan and Qu (2007) showed that the rotation rate often changes with the distance from the sunspot centre. The rotation of sunspots is commonly interpreted as an observational signature of the emergence of a flux-rope through the photosphere (*e.g.* Gibson *et al.*, 2004) or, more generally, as the transport of helicity from the convection zone into the corona (see, *e.g.*, Longcope and Welsch, 2000; Tian and Alexander, 2006; Tian, Alexander, and Nightingale, 2008; Fan, 2009). On the other hand, observations of strong sunspot rotation without signs of significant flux emergence have been reported (*e.g.* Tian and Alexander, 2006, and references therein), suggesting that intrinsic sunspot rotation of sub-photospheric origin exists. In such cases the rotation rate tends to be smaller than for sunspot rotations associated with flux emergence (*e.g.* Zhu, Alexander, and Tian, 2012).

A number of studies have shown a direct cause–consequence relationship between higher-than-average sunspot rotation and enhanced eruptive activity. For example, Brown *et al.* (2003), Hiremath and Suryanarayana (2003), Hiremath, Lovely, and Kariyappa (2006), Tian and Alexander (2006), Yan and Qu (2007), Zhang, Liu, and Zhang (2008), Li and Zhang (2009), Yan *et al.* (2009, 2012), and Suryanarayana (2010) reported an apparent connection between rotating sunspots (with total rotation angles of up to 200° and more) and eruptive events. In particular, Yan and Qu (2007) attributed eruptive activity in an active region to different rotation speeds in different parts of a sunspot, whereas Yan, Qu, and Kong (2008) found indications that active regions with sunspots rotating opposite to the differential-rotation shear are characterised by high X-class-flare productivity. Romano, Contarino, and Zuccarello (2005) reported a filament eruption that was apparently triggered by photospheric vortex motions at both footpoints of the filament, without any sign of significant flux emergence.

Besides purely observational studies of the relationship between sunspot rotation and eruptive activity, some authors presented a combination of observations and modelling. For example, Régnier and Canfield (2006) utilised multi-wavelength observations and modelling of the coronal magnetic field of the highly flare-productive NOAA Active Region 8210 to show that slow sunspot rotations enabled flaring, whereas fast motions associated with emerging flux did not result in any detectable flaring activity. Moreover, they also showed that the deposition of magnetic energy by photospheric motions is correlated with the energy storage in the corona, which is then released by flaring. Similarly, Kazachenko *et al.* (2009) analysed detailed observations of an M8 flare–CME event and the associated rotating sunspot, and combined them in a minimum-current-corona model. They found that the observed rotation of 34° over 40 hours led to a triplication of the energy content and flux-rope self-helicity, sufficient to power the M8 flare.

Numerical MHD investigations of the relationship between sunspot rotation and eruptive activity started with Barnes and Sturrock (1972), who modelled the coronal magnetic field of

a rotating sunspot surrounded by a region of opposite polarity. They found that the rotation causes an inflation of the magnetic field, and that its energy increases with the rotation angle until, when the rotation angle exceeds $\approx 180^\circ$, it becomes larger than that of the open-field configuration with the same boundary conditions, presumably leading to an eruption.

MHD simulations of the formation and evolution of flux-ropes by twisting line-tied potential fields have been widely performed since then. Calculations were done by either twisting uniform fields in straight, cylindrically symmetric configurations (*e.g.* Mikic, Schnack, and van Hoven, 1990; Galsgaard and Nordlund, 1997; Gerrard, Arber, and Hood, 2002; Gerrard *et al.*, 2003) or by twisting bipolar potential fields; the latter yielding arched flux-ropes anchored at both ends in the same plane (*e.g.* Amari and Luciani, 1999; Gerrard, Hood, and Brown, 2004). Most of these simulations focused on the helical kink instability and its possible role in producing compact flares and confined eruptions. Klimchuk, Antiochos, and Norton (2000) studied the twisting of a bipole with emphasis on the apparently uniform cross-section of coronal loops. Very recently, Santos, Büchner, and Otto (2011) simulated the energy storage for the active region that was studied earlier by Régnier and Canfield (2006). They imposed photospheric flows on an extrapolated potential field and found the formation of pronounced electric currents at the locations of the observed flare sites. The authors concluded that the main flare activity in the active region was caused by the slow rotation of the sunspot that dominated the region.

However, none of the above studies were directly related to CMEs. Amari *et al.* (1996) were the first to show that the formation and continuous twisting of an arched flux-rope in a bipolar potential field can lead to a strong dynamic expansion of the rope, resembling what is observed in CMEs. Later, Török and Kliem (2003) and Aulanier, Démoulin, and Grappin (2005) extended this work by studying in detail the stability properties and dynamic evolution of such a system. The underlying idea of these simulations is that slow photospheric vortex motions can twist the core magnetic field in an active region up to the point where equilibrium cannot be longer maintained, and the twisted core field, *i.e.* a flux-rope, erupts (for the role of increasing twist in triggering a flux-rope eruption see also Chen, 1989; Vršnak, 1990; Fan and Gibson, 2003; Isenberg and Forbes, 2007). What has not been studied yet is whether a twisting of the field *overlying an existing flux-rope* can lead to the eruption of the rope.

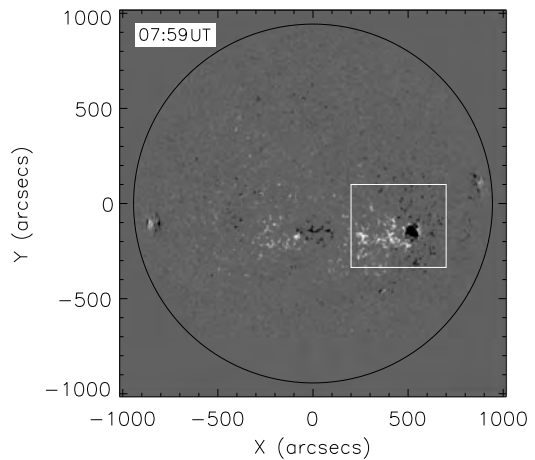
In this article, we present observations of a large solar eruption that took place in the vicinity of a rotating sunspot. We suggest that the continuous rotation of the spot triggered the eruption by successively weakening the stabilizing coronal field until the low-lying core field erupted. We support our suggestion by MHD simulations that qualitatively model this scenario.

The remaining part of this article is organised as follows: In Section 2 we describe the observations, focusing on the initial evolution of the eruption and on the rotation of the sunspot. In Section 3 we describe the numerical simulations, the results of which are presented in Section 4. We finally discuss our results in Section 5.

2. Observations

The eruption on 6 July 2006 in NOAA Active Region 10898 was a textbook two-ribbon flare accompanied by a filament eruption and a halo CME, the latter being most prominent in the southwest quadrant and reaching a linear plane-of-sky velocity of $\approx 900 \text{ km s}^{-1}$ (Temmer *et al.*, 2008). The event was associated with an EIT wave, a type II burst, and very distinct coronal dimming regions. The flare was of class M2.5/2N, located at the heliographic position S9°, W34°. It was observed in soft X-rays (SXR) by GOES (peak time at $\approx 08:37 \text{ UT}$)

Figure 1 Full-disk line-of-sight SOHO/MDI magnetogram recorded on 6 July 2006, 07:59 UT. The active region under study is marked by the white box.

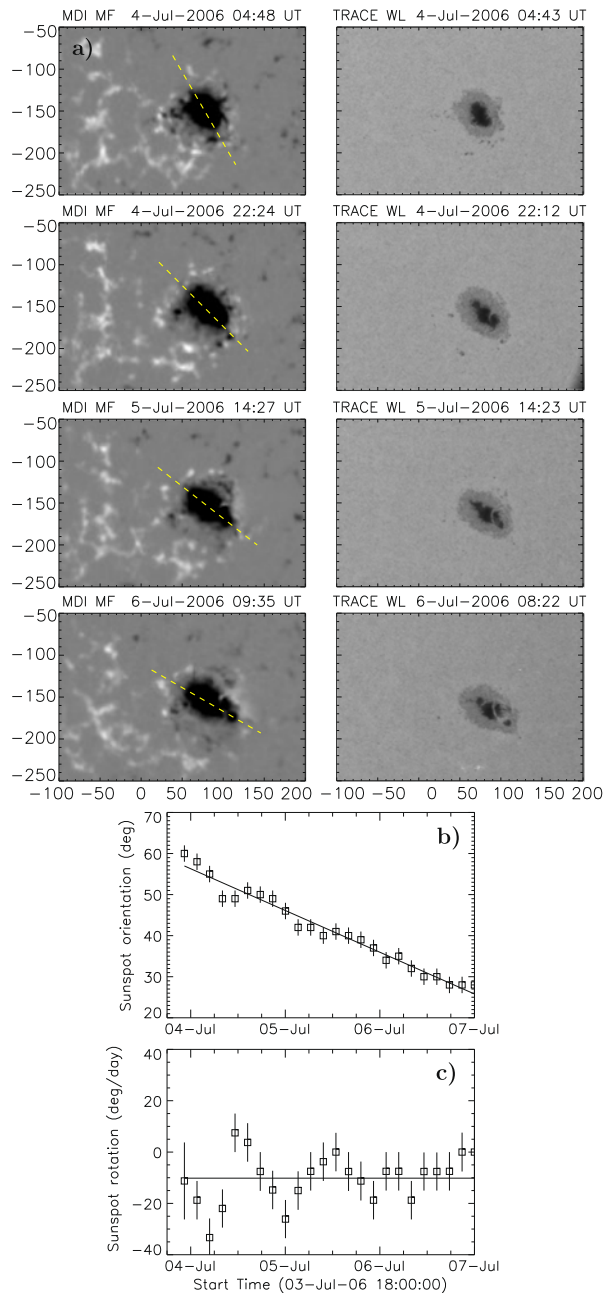


as well as in hard-X rays (HXR) with RHESSI, with the two highest peaks of nonthermal HXR emission occurring during 08:20–08:24 UT.

The evolution of the active region in the days preceding the eruption, and in particular the rotation of the leading sunspot, can be studied using its photospheric signatures. Photospheric line-of-sight magnetograms of the region were obtained by the MDI instrument (Scherrer *et al.*, 1995) onboard the *Solar and Heliospheric Observatory* (SOHO). The active region was a bipolar region of Hale type β , consisting of a compact negative polarity (the sunspot) that was surrounded by a dispersed positive polarity, most of which was extending eastwards (see Figure 1). The maximum of the magnetic-field flux density in the sunspot was about nine times larger than in the dispersed positive polarity. The two polarities were surrounded by a large, “inverse C-shaped” area of dispersed negative flux to the west of the region.

We measured the magnetic flux of the concentrated leading (negative) and dispersed following (positive) polarities using a (re-calibrated) SOHO/MDI synoptic map, which preserves the resolution of the original observation. The map includes magnetic features close to the time of their central meridian passage, when projection effects of the line-of-sight magnetic fields are at minimum. The total magnetic flux (half of the total unsigned flux) was found to be $(2.1 \pm 0.2) \times 10^{22}$ Mx, with the two polarities nearly balanced [$(2.0 \pm 0.2) \times 10^{22}$ and $(-2.2 \pm 0.2) \times 10^{22}$ Mx for the positive and negative flux, respectively]. The error estimates reflect the uncertainty in determining how much of the dispersed positive and negative polarities belonged to the active region. The leading spot, including the penumbral area, had a mean magnetic-field strength (magnetic-flux density over 2340 pixels) of 390 G, reaching 1820 G when a smaller, purely umbral, area was considered (240 pixels). However, since the MDI response becomes non-linear in such a strong, and therefore dark, umbra, the core field strength there was probably higher (≥ 2000 G) (see, *e.g.*, Green *et al.*, 2003). The positive dispersed plage had a much lower mean magnetic-field strength of 50 ± 10 G, depending on the extent of dispersed positive field measured (magnetic-flux density over 13 060–24 600 pixels). Positive flux concentrations (measured over 600 pixels) within the plage had a characteristic field strength of 220 ± 20 G. In summary, magnetic-flux measurements indicate a mere 5 % negative surplus flux in this major bipolar active region of 2.1×10^{22} Mx total flux and maximum-field strengths (negative : positive) in a roughly 10 : 1 ratio.

Figure 2 (a) Representative images of the sunspot evolution during 4–6 July 2006: MDI longitudinal magnetic-field maps (left column); TRACE white-light images (right column). The TRACE image in the bottom panels corresponds to the time of the M2 flare (starting in soft X-rays at 8:20 UT). The dashed yellow line outlines the major axis of the sunspot that was used to measure the sunspot rotation. The corresponding [SOHO/MDI movie](#) is available in the electronic version of the article. (b) Sunspot rotation determined from the MDI magnetic-field maps over the period 3 July 2006, 22:00 UT, to 7 July 2006, 8:00 UT, showing the orientation of the sunspot's major axis, measured clockwise from solar East. (c) Sunspot rotation rate in degrees per day.



In Figure 2(a) we show snapshots of the sunspot evolution as observed by MDI and the *Transition Region and Coronal Explorer* (TRACE: Handy *et al.*, 1999), ranging from two days before the eruption to one day after it. The images are all differentially rotated to the first image of the series, when the sunspot was closer to disk centre. The sequence shows that the sunspot is rotating counter-clockwise during the considered period (see the

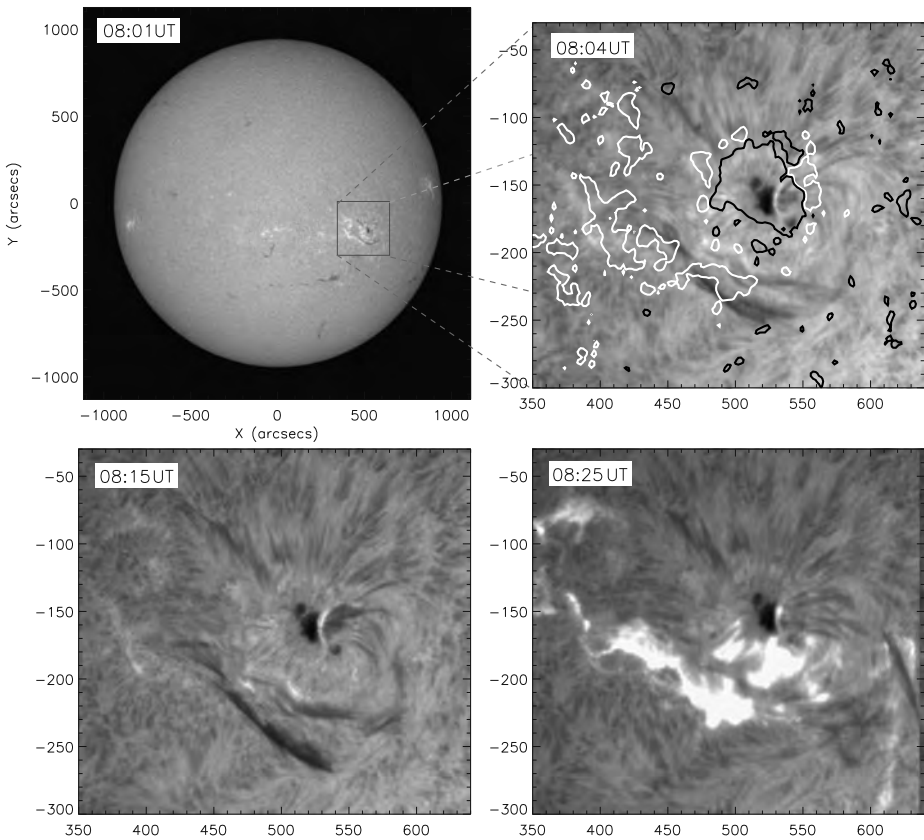


Figure 3 $H\alpha$ filtergram sequence observed before and during the flare on 6 July 2006 by the Kanzelhöhe (full disk) and Hvar (active region area) Observatories. An apparent double structure of the filament is visible South of the sunspot. Contour levels of 100 G from an MDI magnetogram taken at 07:59 UT are added in the top right panel, with white (black) lines corresponding to positive (negative) values.

[Electronic Supplementary Material](#)). From the evolution of the MDI magnetic-field maps, we geometrically determined the major axis of the sunspot and followed its evolution in time. In Figure 2(b) we plot the sunspot's rotation angle over the period 3 July 2006, 22:00 UT, to 7 July 2006, 8:00 UT. The total rotation observed over these three days is about 30° . The sunspot's rotation rate, determined as the temporal derivative of the rotation measurements, yields a mean value of about $10^\circ \text{ day}^{-1}$ during the considered time span (Figure 2(c)). For comparison, we determined the rotation also from the TRACE white-light images and found no significant differences.

The flare and the filament eruption were observed in full-disk $H\alpha$ filtergrams by the Kanzelhöhe Observatory and, over a smaller field-of-view around the active region, by the Hvar Observatory (Figure 3). These observations reveal that the filament consisted of a double structure before and during the eruption (for a similar case of such a double-structured filament, see Liu *et al.*, 2012). Significant rising motions of the filament could be seen from about 08:23 UT on. The $H\alpha$ flare started by the appearance of very weak double-footpoint brightening at 08:15 UT.

Figure 4 (a) TRACE 171 Å running-difference image showing the erupting filament and the overlying CME front. Distances are measured at crossings of the respective leading edges (red solid lines) with the dashed line, starting from the point marked by [x]. (b) Distance–time plot showing the kinematics of the filament and the CME front for the entire distance range. (c) Distance–time plot for the distance range up to $1.8 R_{\odot}$. The distance between [x] and the disk centre is added to all TRACE and EIT data points. (d) Velocity–time plot over the distance range up to $1.8 R_{\odot}$. See text for further details.

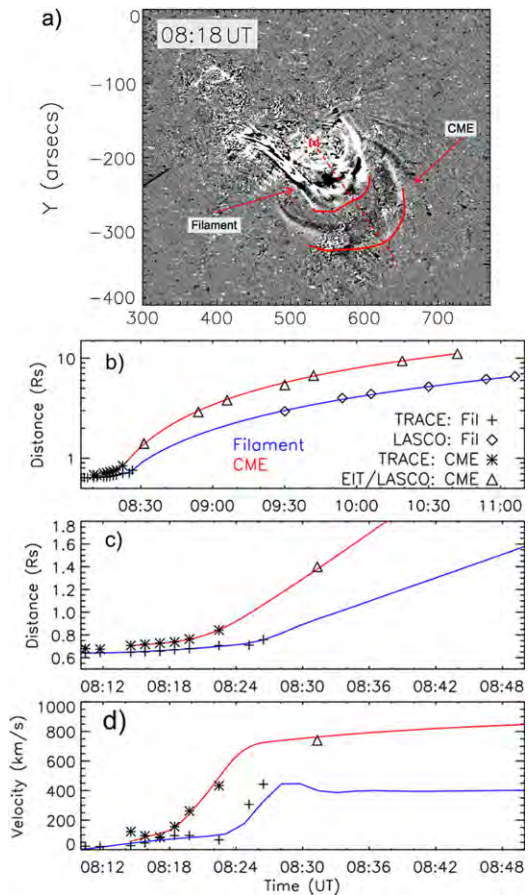


Figure 4(a) shows a running-difference image from TRACE 171 Å in which the erupting filament (the CME core) and the preceding CME front can be identified. From a time sequence of similar images by TRACE, EIT, and LASCO C2/C3 we estimated the kinematics of the filament and the CME front, which are shown in Figure 4(b), (c). The distances were measured in the plane of the sky, from disk centre in the LASCO images and from the midpoint of the line connecting the pre-eruption filament footpoints in the TRACE and EIT images. In order to approximately compensate for this discrepancy, we added to the TRACE and EIT measurements the distance between this point and the disk centre, which corresponds to ≈ 400 Mm. The resulting distances are plotted in Figure 4(b), (c), together with spline-smoothed curves. We did not correct for foreshortening effects, as projection effects only result in a multiplication factor and do not alter the profile of the derived kinematical curves (see, *e.g.*, Vršnak *et al.*, 2007). Additionally, Figure 4(d) gives the velocity profiles for the filament and the CME front, as derived from the first derivative of the distance–time measurements and spline-smoothed curves. From these plots we obtain the result that the coronal loops overlying the filament started their slow rising phase at 08:15 UT, *i.e.* about five–ten minutes before the filament. Similarly, the CME front reached its final, almost constant, velocity a few minutes before the filament.

Various other aspects of the event (flare, CME, EIT wave, dimming) were studied by Jiang *et al.* (2007), McIntosh *et al.* (2007), Attrill *et al.* (2008), Temmer *et al.* (2008), Miklenic, Veronig, and Vršnak (2009), Veronig *et al.* (2010), and Guo *et al.* (2010a). We refer to this work for further details as regards the eruption. Guo *et al.* (2010a) suggested that the eruption was triggered by recurrent chromospheric mass injection in the form of surges or jets into the filament channel. Here we propose a different mechanism, assuming that the filament was suspended in the corona by a magnetic flux-rope, a picture that is supported by various magnetic-field models of active regions containing filaments (*e.g.* Lionello *et al.*, 2002; van Ballegoijen, 2004; Guo *et al.*, 2010b; Canou and Amari, 2010). We suggest that the continuous rotation of the sunspot led to a slow expansion of the arcade-like magnetic field overlying the filament (*i.e.* to a continuous weakening of its stabilizing tension), until a critical point was reached at which equilibrium could not be maintained and the flux-rope erupted. We note that we do not claim that the eruption was triggered *exclusively* by this mechanism. Filaments are often observed to spiral into the periphery of sunspots (*e.g.* Green *et al.*, 2007), and also in our case an inspection of the TRACE and H α images during the early phase of the eruption suggests a possible magnetic connection between the western extension of the filament-carrying core field and the sunspot area. Thus, the sunspot rotation may have added stress to this field, thereby possibly contributing to drive it towards eruption. On the other hand, for an injection of twist as suggested by the simulations mentioned above to occur, the core field must be rooted in the centre of the sunspot, not just in its periphery, which is difficult to establish from observations. It appears reasonable to assume that a clear connection between core field and sunspot centre is not always present, and that the stressing of the overlying ambient field by sunspot rotation may be more relevant for the destabilisation of the system in such cases. In order to test this scenario, we perform a series of three-dimensional (3D) MHD simulations, which are described in the following sections.

3. Numerical Simulations

The purpose of the numerical simulations presented in this article is to show that the rotation of photospheric-flux concentrations can trigger the eruption of an initially stable flux-rope that is embedded in their fields. Differently from previous work (*e.g.* Amari *et al.*, 1996; Török and Kliem, 2003; Aulanier, Démoulin, and Grappin, 2005), the photospheric vortex motions do not directly affect the flux-rope in our simulations, but solely the field surrounding it.

The first simulation (hereafter run 1) involves a relatively simple magnetic configuration, consisting of a flux-rope embedded in a bipolar potential field (see Figure 5(c)). The initially potential field gets twisted at its photospheric-flux concentrations on both sides of the flux-rope in the same manner. This simulation is very idealised with respect to the observations presented in Section 2, in particular because both the initial magnetic configuration and the imposed driving possess a high degree of symmetry.

We then consider a more complex initial magnetic field (hereafter run 2), which is chosen such that it resembles the magnetic-field structure prior to the eruption described in Section 2 (see Figure 5(d)). As in run 1, this configuration contains a flux-rope embedded in a potential field, but the latter is now constructed by a significantly larger number of sub-photospheric sources, in order to mimic the main features of the observed photospheric flux distribution and the extrapolated coronal magnetic field (see Figure 5(c)). Differently from run 1, only one flux concentration is twisted in this case, as suggested by the observations. The purpose of run 2 is to verify that the mechanism studied in run 1 also works in a highly asymmetric

configuration. We do not attempt here to model the full eruption and evolution of the CME, for reasons that are specified below.

To construct our magnetic configurations, we employ the coronal flux-rope model of Titov and Démoulin (1999, hereafter TD). Its main ingredient is a current ring of major radius $[R]$ and minor radius $[a]$ that is placed such that its symmetry axis is located at a depth $[d]$ below a photospheric plane. The outward-directed Lorentz self-force (or “hoop force”) of the ring is balanced by a potential field created by a pair of sub-photospheric point sources $[\pm q]$ that are placed at the symmetry axis, at distances $\pm L$ from the ring centre. The resulting coronal field consists of an arched and line-tied flux-rope embedded in an arcade-like potential field. In order to create a shear component of the ambient field, TD added a sub-photospheric line current to the system. Since the latter is not required for equilibrium, we do not use it for our configurations (see also Rousev *et al.*, 2003; Török and Kliem, 2007).

Previous simulations (*e.g.* Török and Kliem, 2005; Schrijver *et al.*, 2008) and analytical calculations (Isenberg and Forbes, 2007) have shown that the TD flux-rope can be subject to the ideal-MHD helical kink and torus instabilities. Therefore, we adjust the model parameters such that the flux-rope twist stays below the typical threshold of the kink instability for the TD flux-rope (see Török, Kliem, and Titov, 2004). To inhibit the occurrence of the torus instability in the initial configurations, we further adjust the locations and magnitude of the potential field sources such that the field drops sufficiently slowly with height above the flux-rope (see Kliem and Török, 2006; Török and Kliem, 2007; Fan and Gibson, 2007; Aulanier *et al.*, 2010). While this is a relatively easy task for the standard TD configuration used in run 1, an extended parameter search was required for the complex configuration used in run 2, until an appropriate numerical equilibrium to start with could be found.

3.1. Numerical Setup

As in our previous simulations of the TD model (*e.g.* Török, Kliem, and Titov, 2004; Kliem, Titov, and Török, 2004), we integrate the $\beta = 0$ compressible ideal-MHD equations:

$$\partial_t \rho = -\nabla \cdot (\rho \mathbf{u}), \quad (1)$$

$$\rho \partial_t \mathbf{u} = -\rho (\mathbf{u} \cdot \nabla) \mathbf{u} + \mathbf{j} \times \mathbf{B} + \nabla \cdot \mathcal{T}, \quad (2)$$

$$\partial_t \mathbf{B} = \nabla \times (\mathbf{u} \times \mathbf{B}), \quad (3)$$

where \mathbf{B} , \mathbf{u} , and ρ are the magnetic field, velocity, and mass density, respectively. The current density is given by $\mathbf{j} = \mu_0^{-1} \nabla \times \mathbf{B}$. \mathcal{T} denotes the viscous stress tensor, included to improve numerical stability (Török and Kliem, 2003). We neglect thermal pressure and gravity, which is justified for the low corona where the Lorentz force dominates.

The MHD equations are normalised by quantities derived from a characteristic length $[l]$ taken here to be the initial apex height of the axis of the TD current ring above the photospheric plane $[l = R - d]$, the maximum magnetic-field strength in the domain $[B_{0\max}]$, and the Alfvén velocity $[v_{a0}]$. The Alfvén time is given by $[\tau_a = l/v_{a0}]$. We use a Cartesian grid of size $[-40, 40] \times [-40, 40] \times [0, 80]$ for run 1 and $[-40, 40] \times [-30, 30] \times [0, 60]$ for run 2, resolved by $247 \times 247 \times 146$ and $307 \times 257 \times 156$ grid points, respectively. The grids are non-uniform in all directions, with an almost uniform resolution $\Delta = 0.04$ (run 1) and $\Delta = 0.05$ (run 2) in the box centre, where the TD flux-rope and the main polarities are located. The plane $z = 0$ corresponds to the photosphere. The TD flux-rope is oriented along the y -direction in all runs, with its positive-polarity footpoint rooted in the half-plane $y < 0$. We employ a modified two-step Lax–Wendroff method for the integration, and we

additionally stabilise the calculation by artificial smoothing of all integration variables (Sato and Hayashi, 1979; Török and Kliem, 2003).

The boundary conditions are implemented in the ghost layers. The top and lateral boundaries are closed, which is justified given the large size of the simulation box. Below the photospheric plane, the tangential velocities are imposed as described in Section 3.3. The vertical velocities are zero there at all times, and the mass density is fixed at its initial values. The latter condition is not consistent with the imposed vortex flows, but is chosen to ensure numerical stability (see Török and Kliem, 2003). Since we use the $\beta = 0$ approximation, and since the evolution is driven quasi-statically at the bottom plane, fixing the density in $z = -\Delta z$ is tolerable. The tangential components of the magnetic field $[B_{x,y}]$ are extrapolated from the integration domain, and the normal component $[B_z]$ is set such that $\nabla \cdot \mathbf{B} = 0$ in $z = 0$ at all times (see Török and Kliem, 2003). Since our code does not ensure $\nabla \cdot \mathbf{B} = 0$ to rounding error in the rest of the domain, we use a diffusive $\nabla \cdot \mathbf{B}$ cleaner (Keppens *et al.*, 2003), as well as Powell's source-term method (Gombosi, Powell, and de Zeeuw, 1994), to minimise unphysical effects resulting from $\nabla \cdot \mathbf{B}$ errors.

3.2. Initial Conditions

The parameters of the TD equilibrium employed in run 1 are (in normalised units): $R = 2.2$, $a = 0.7$, $d = 1.2$, $L = 1.2$, and $q = 1.27$. The magnetic axis of the TD flux-rope (which is located above the geometrical axis of the current ring, see Valori *et al.*, 2010) has an apex height $z = 1.09$. The potential field connects two fully symmetric flux concentrations and runs essentially perpendicular above the TD flux-rope. The apex of the central field line, *i.e.* the field line connecting the centres of the potential-field polarities, is located at $z = 3.40$. After the initial relaxation of the system (see below), these heights become $z = 1.22$ and $z = 3.62$, respectively. Figures 5(c) and 6(a) show the configuration after the relaxation.

The magnetic configuration used in run 2 is a step towards a more realistic modelling of the coronal field during the 6 July 2006 eruption. Figure 5(b) shows a coronal potential-field source-surface (PFSS) model (Schatten, Wilcox, and Ness, 1969), obtained from a synoptic MDI magnetogram for Carrington Rotation 2045, using the SolarSoft package *pfss* provided by LMSAL (<http://www.lmsal.com/~derosa/pfsspack/>). It can be seen that the field lines rooted in the main polarity (the sunspot) form a fan-like structure, which partly overlies the filament. We again consider a standard TD flux-rope, with $R = 2.75$, $a = 0.8$, and $d = 1.75$, but now we use an ensemble of ten sub-photospheric sources (five point sources, and five vertically oriented dipoles like the ones used by Török and Kliem, 2003) for the construction of the ambient field, in order to resemble the main properties of the observed photospheric flux distribution and the corresponding PFSS field. By adjusting the positions and strengths of the sources, we tried to mimic the approximate flux balance between the concentrated leading negative polarity and the dispersed following positive polarity, the ratio of approximately 10:1 between the peak field strengths in the leading polarity and the following polarity, the size ratio between these polarities, the presence of an "inverse C-shaped" area of dispersed negative flux to the West of the leading polarity (see Section 2), as well as the fan-like shape of the coronal field rooted in the leading polarity. The position of the flux-rope within the ambient field is guided by the observed location of the filament (Figure 5(b)). Since the model is still relatively idealised, all of these features can be matched only approximately. The resulting configuration (after initial relaxation) is shown in Figure 5(d) and in Figure 8(a) below. It can be seen that the TD flux-rope is stabilised by flux rooted towards the southern edge of the main polarity. The rope is inclined with respect to the vertical, which is due to the asymmetry of the potential field surrounding it.

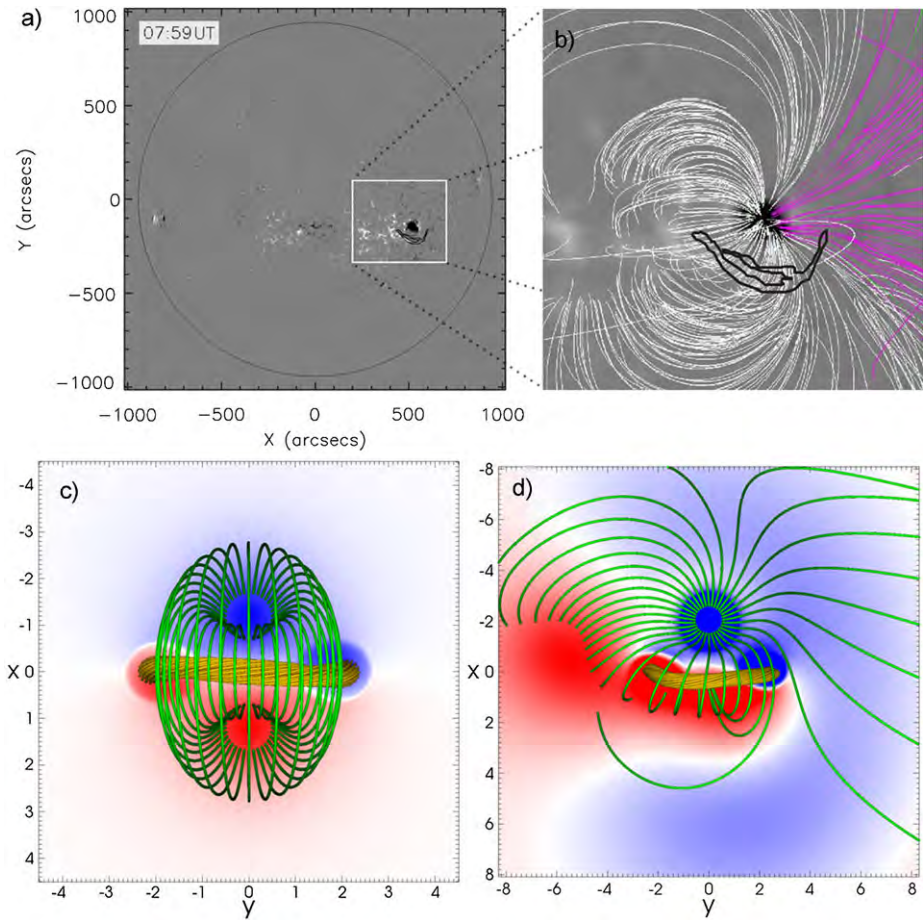


Figure 5 (a) Same as Figure 1. (b) Magnetic-field lines in the active-region area (marked by the white square in panel a) from a potential field source surface (PFSS) model that was calculated for 6 July 2006, 06:04 UT, overlaid on a synoptic MDI magnetogram for the corresponding Carrington Rotation 2045. The model corona is a spherical shell extending from 1.0 to 2.5 R_{\odot} . Pink (white) field lines depict open (closed) fields. The outer contours of the filament, based on $H\alpha$ data taken at 07:59 UT on 6 July 2006, are outlined with black lines. For better illustration, the area is rotated to disk centre. (c), (d): Top view on the magnetic configurations used in runs 1 and 2, respectively, after the initial relaxation of the system (see Section 3 for details). The core of the TD flux-rope is shown by orange field lines, green field lines depict the ambient potential field. B_z is shown in the bottom plane, where red (blue) colours corresponds to positive (negative) values. The colour scale in panel d) is saturated at about 4 % of the maximum B_z , in order to depict also weaker flux distributions.

In contrast to the configuration used in run 1, the magnetic field in run 2 is dominated by one main polarity. Rather than closing down to an equally strong polarity of opposite sign, the flux emanating from the main polarity now spreads out in all directions, resembling a so-called fan–spine configuration (*e.g.* Pariat, Antiochos, and DeVore, 2009; Masson *et al.*, 2009; Török *et al.*, 2009). Note that this flux does not contain fully open field lines, as was presumably the case during the 6 July 2006 eruption (see Figure 5(b)). This is due to the fact that the flux distribution shown in Figure 5(d) is fully surrounded by weak positive flux in the model (imposed to mimic the isolated “inverse C-shaped” weak negative polarity to the

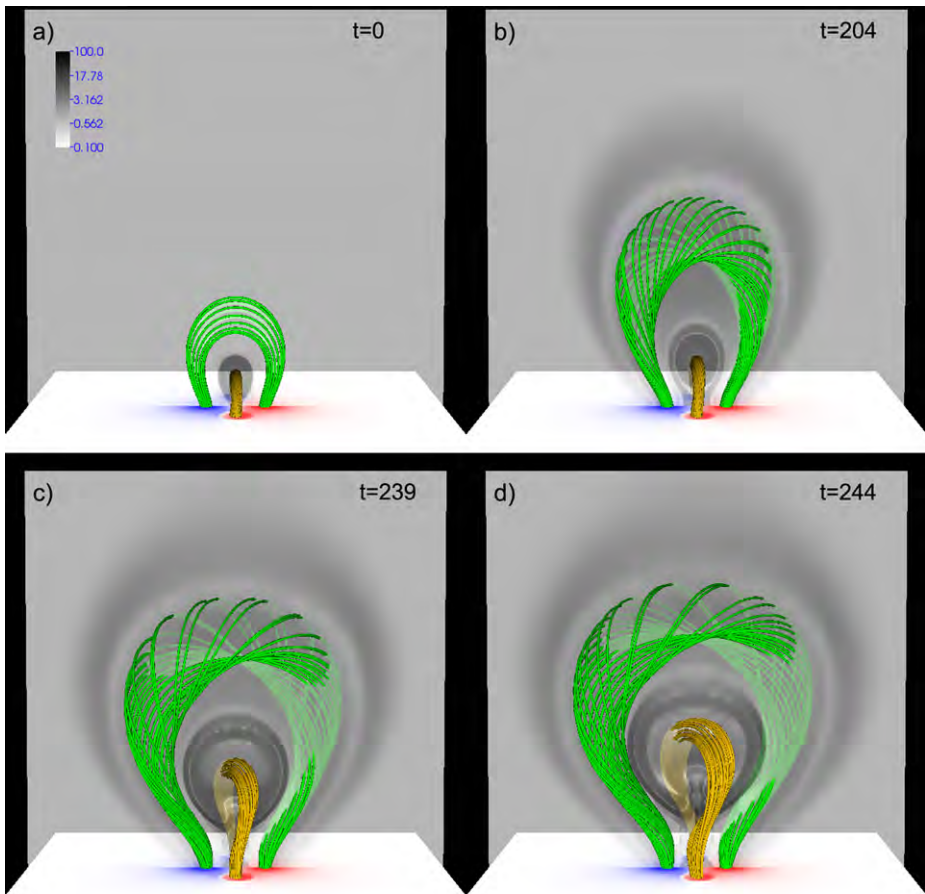


Figure 6 Magnetic-field lines outlining the evolution of the TD flux-rope (orange) and the twisted overlying field (green) for run 1, at $t = 0, 204, 239, 244\tau_A$, respectively; panel (a) shows the system after the initial numerical relaxation. The normal component of the magnetic field $[B_z]$ is shown at the bottom plane $z = 0$, with red (blue) corresponding to positive (negative) values. The transparent grey-scale shows the logarithmic distribution of the current densities divided by the magnetic field strength $[|\mathbf{J}|/|\mathbf{B}|]$ in the plane $x = 0$. The sub-volume $[-8.5, 8.5] \times [-8, 8] \times [0, 16]$ is shown in all panels. An animation of this figure is available in the [electronic version](#) of this article.

West of the main polarity), so that the positive flux in the total simulation domain exceeds the negative flux shown in Figure 5(b). Note that this “total” flux ratio shall not be confused with the flux ratio between the main polarity and the dispersed positive polarity to its East, which is approximately balanced in the model, in line with the observations.

As in Amari *et al.* (1996), Török and Kliem (2003) and Aulanier, Démoulin, and Grappin (2005), we use an initial density distribution $\rho_0(\mathbf{x}) = |\mathbf{B}_0(\mathbf{x})|^2$ corresponding to a uniform initial Alfvén velocity. For the configuration used in run 2 we also ran a calculation with $\rho_0(\mathbf{x}) = |\mathbf{B}_0(\mathbf{x})|^{3/2}$, *i.e.* with a more realistic Alfvén velocity that decreases with distance from the flux concentrations. We found that the evolution was qualitatively equivalent, but somewhat less dynamic.

In order to obtain a numerical equilibrium as a starting point of the twisting phase, we first performed a numerical relaxation of the two configurations used. This is done for $54\tau_a$ for the system used in run 1, and for $75\tau_a$ for the system used in run 2, after which the time is reset to zero in both cases.

3.3. Photospheric Driving

The velocity field used to twist the potential fields is prescribed in the plane $z = -\Delta z$ and located at their main flux concentrations. It produces a horizontal counter-clockwise rotation, chosen such that the velocity vectors always point along the contours of $B_z(x, y, 0, t = 0)$, which ensures that the distribution of $B_z(x, y, 0, t)$ is conserved to a very good approximation. The flows are given by

$$u_{x,y}(x, y, -\Delta z, t) = v_0 f(t) \nabla^\perp \left\{ \zeta [B_{0z}(x, y, 0, 0)] \right\}, \quad (4)$$

$$u_z(x, y, -\Delta z, t) = 0, \quad (5)$$

with $\nabla^\perp := (\partial_y, -\partial_x)$. A smooth function

$$\zeta = B_z^2 \exp\left(\frac{(B_z^2 - B_{z_{\max}}^2)}{\delta B^2}\right), \quad (6)$$

chosen as by Amari *et al.* (1996), defines the vortex profile. The parameter δB determines the vortex width (see Figure 3 in Aulanier, Démoulin, and Grappin, 2005). We use $\delta B = 0.7$ for run 1 and $\delta B = 2$ for run 2. The parameter v_0 determines the maximum driving velocity. We choose $v_0 = 0.005v_A$ for both runs to ensure that the driving is slow compared to the Alfvén velocity. The velocities are zero at the polarity centre and decrease towards its edge from their maximum value to zero (see Figure 2 in Török and Kliem, 2003). The twist injected by such motions is nearly uniform close to the polarity centre and decreases monotonically towards its edge (see Figure 10 below and Figure 9 in Török and Kliem, 2003). The polarity centres are located at $(\pm 1.2, 0, 0)$ for the configuration used in run 1 and the vortex flows are applied at both flux concentrations. In run 2, we twist the potential field only in the main negative polarity, the centre of which is located at $(-2, 0, 0)$. The function $f(t)$ describes the temporal profile of the imposed twisting. The twisting phase starts with a linear ramp ($0 \leq t \leq t_r$) from $f(0) = 0$ to $f(t_r) = 1$, which is then held fixed. If a final relaxation phase is added, $f(t)$ is analogously linearly reduced to zero and held fixed. In all simulations in this article $t_r = 10\tau_a$.

In contrast to the symmetric configuration used in run 1, where most of the flux emanating from the main polarities arches over the flux-rope, the flux that initially stabilises the rope in run 2 is concentrated towards the southern edge of the polarity, where the imposed vortex velocities are relatively small. In order to obtain the eruption of the TD rope within a reasonable computational time in run 2, we therefore use a δB that is larger than in run 1.

4. Simulation Results

4.1. Run 1

We first consider the more idealised and symmetric case, in which the vortices are applied at both photospheric polarities of the potential field. As a result of the imposed motions, the field lines rooted in the polarities become increasingly twisted and a relatively wide twisted flux-tube is formed, which expands and rises with increasing velocity (Figure 6).

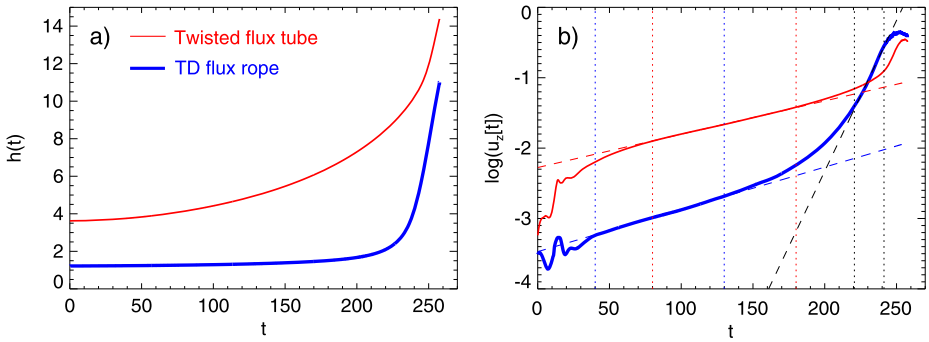


Figure 7 Kinematics of the TD flux-rope (thick blue lines) and of the overlying twisted flux-tube (solid red lines) during the twisting phase in run 1. (a) Height of the axis apex as a function of time. The initial heights are 1.22 for the TD rope and 3.62 for the twisted flux-tube. (b) Logarithmic presentation of the corresponding vertical velocities. The dashed lines show linear fits, obtained within the time periods marked by the vertical dotted lines of the same colour.

Detailed descriptions on the evolution of such twisted fields have been given by Amari *et al.* (1996), Török and Kliem (2003), and Aulanier, Démoulin, and Grappin (2005). Since here we are merely interested in how the rising flux affects the stability of the TD flux-rope, we only note that the rise follows the exponential behaviour found in this earlier work. This is shown in Figure 7, where the kinematics of the two flux systems (the twisted flux-tube and the TD flux-rope) are followed in time by tracking the position of the respective central field-line apex. The exponential rise phase of the twisted flux-tube, preceded by a slower transition, can be clearly seen between $t \approx 80\tau_a$ and $t \approx 180\tau_a$.

The slow rise of the flux-tube successively weakens the stabilizing magnetic tension on the TD rope, so that the latter starts to ascend as well. As can be seen in Figure 7(b), the rise of the TD rope also follows an exponential behaviour up to $t \approx 130\tau_a$. While its growth rate is slightly larger than for the twisted flux-tube, its velocity remains about one order of magnitude smaller. In order to check that this slow exponential rise of the TD rope is indeed an adaptation to the changing ambient field, rather than a slowly growing instability, we performed a relaxation run by ramping down the photospheric driving velocities to zero between $t = 100\tau_a$ and $t = 110\tau_a$ and following the evolution of the system until $t = 181\tau_a$. Both the twisted flux-tube and the TD rope relax towards a numerical equilibrium in this run, without any indication of instability or eruption. Hence, during its slow rise phase until $t \approx 130\tau_a$, the TD rope experiences a quasi-static evolution along a sequence of approximately force-free equilibria, generated by the slowly changing boundary conditions (in particular, the changing tangential components of the magnetic field at the bottom plane).

Starting at $t \approx 130\tau_a$, the TD rope undergoes a successively growing acceleration which ends in a rapid exponential acceleration phase between $t \approx 220\tau_a$ and $t \approx 250\tau_a$ that is characterised by a growth rate significantly larger than during the quasi-static phase (see also the bottom panels of Figure 6). The rope finally reaches a maximum velocity of $0.45v_{a0}$ at $t = 252\tau_a$, after which it starts to decelerate. Such a slow rise phase, followed by a rapid acceleration, is a well-observed property of many filament eruptions in the early evolution of CMEs (see, *e.g.*, Schrijver *et al.*, 2008, and references therein), and is also seen for the event studied in this article (see Figure 4(d)). The evolution of the TD rope after $t \approx 130\tau_a$ can be associated with the development of the torus instability (Bateman, 1978; Kliem and Török, 2006; Démoulin and Aulanier, 2010), as has been shown under similar conditions in

various simulations of erupting flux-ropes (Török and Kliem, 2007; Fan and Gibson, 2007; Schrijver *et al.*, 2008; Aulanier *et al.*, 2010; Török *et al.*, 2011).

During the transition of the TD rope to the torus-unstable regime, the overlying twisted flux-tube continues its slow exponential rise at almost the same growth rate for about 100 Alfvén times, which excludes the possibility that the additional acceleration of the TD rope after $t \approx 130\tau_a$ is due to an adaptation to the evolving environment field. At $t \approx 230\tau_a$, however, the rise speed of the TD rope begins to exceed the rise speed of the flux-tube, and the latter gets significantly accelerated from below by the strongly expanding rope. The overtaking of the twisted flux-tube by the faster TD rope, and the resulting interaction between the two, is reminiscent of the so-called CME cannibalism phenomenon (*e.g.* Gopalswamy *et al.*, 2001; Lugaz, Manchester, and Gombosi, 2005). The investigation of this interaction is, however, beyond the scope of the present article, so that we stopped the simulation at this point.

Run 1 shows that the rotation of the footpoints of a flux system overlying a stable flux-rope can lead to the eruption of the rope, by progressively lowering the threshold for the torus instability. We suggest that this mechanism may have been at the origin of the CME event described in Section 2.

The numerical experiment presented here has a high degree of symmetry, with respect to both the initial magnetic-field configuration and the driving photospheric motions. A practically identical result is obtained if only one of the polarities of the overlying field is twisted, as long as the driving velocity is clearly sub-Alfvénic. In particular, we found that twisting only one flux concentration does not significantly affect the rise direction of the TD rope, indicating that slow asymmetric twisting does not necessarily lead to a non-radial rise of the erupting flux-rope if the overlying field is symmetric. A more general case, which exhibits a strongly non-radial rise, is presented in the following section.

4.2. Run 2

We now consider a much less symmetric initial condition for the magnetic field, together with a driving that is applied to one polarity only. The configuration is still idealised, but closer to the observations (see Sections 2 and 3.2). The purpose of run 2 is to verify that the CME initiation mechanism suggested in Section 4.1 can work also in a more realistic and general setting.

The fan-like structure of the ambient field makes it difficult to follow its evolution during the twisting phase using a single point as a tracer of the whole three-dimensional structure, as was done for run 1. We therefore follow here only the apex of the TD rope axis in time. The inclination of the rope makes it complicated to find the exact position of the axis apex, so we determined it only approximately. Consequently, the trajectories presented in Figure 9 below are somewhat less precise than for run 1.

Figure 8(a) shows that electric currents are formed in the ambient field volume during the initial relaxation of the system. The strongest current concentrations are located in the front of the flux-rope and exhibit an X-shaped pattern in the vertical cut shown. This pattern outlines the locations of quasi-separatrix layers (QSLs: *e.g.* Priest and Forbes, 1992; Démoulin *et al.*, 1996) that separate different flux systems. The QSLs are present in the configuration from the very beginning and arise from the complexity of the potential field (see Section 3.2). Their presence is evident also in the left panel of Figure 8(a): the green field lines show strong connectivity gradients in the northern part of the main polarity and in the vicinity of the western flux-rope footpoint. It has been demonstrated that current concentrations form preferably at the locations of QSLs and other structural

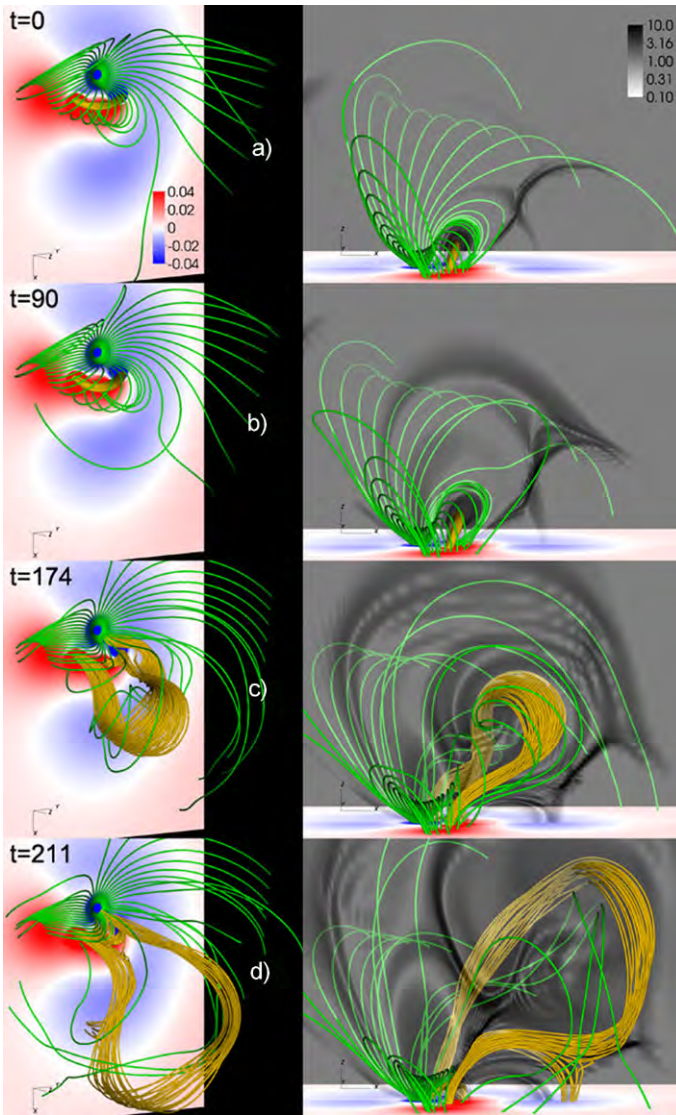


Figure 8 Snapshots of run 2 at times $t = 0, 90, 174, 211\tau_a$, respectively, showing the same features as in Figure 5(d). The system is shown after the initial relaxation (a), during the slow rise phase (b), at the time of the peak flux-rope velocity (c), and during the deceleration of the flux-rope (d). The left panels use a view similar to the observations presented in Section 2, the right panels show a side view. The transparent grey-scale in the right panels depicts the logarithmic distribution of $|j|/|B|$ in the plane $x = 0$, outlining the locations of strong current concentrations. The sub-volume $[-10, 16] \times [-11, 11] \times [0, 18]$ is used for all panels. An animation of this figure is available in the [electronic version](#) of this article.

features like null points, separatrix surfaces, and separators, if a system containing such structures is dynamically perturbed (e.g. Baum and Bratenahl, 1980; Lau and Finn, 1990; Aulanier, Pariat, and Démoulin, 2005). In our case the perturbation results from the – relatively modest – dynamics during the initial relaxation of the system.

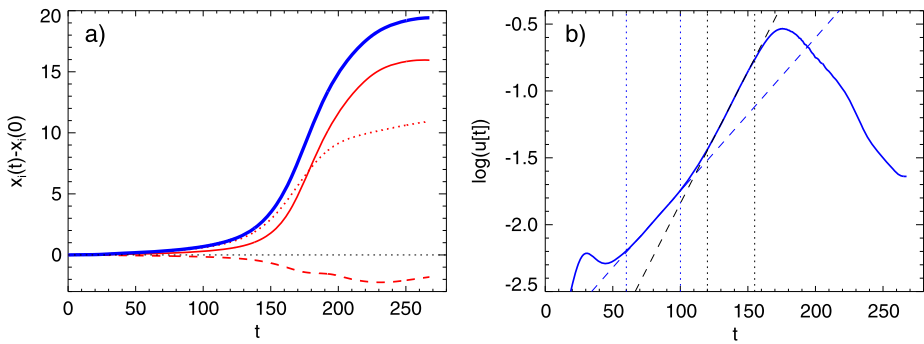


Figure 9 Kinematics of the TD flux-rope in run 2. (a) Red lines show the distances of the axis apex from its initial position, $(x_0, y_0, z_0) = (0.075, 0, 1.076)$, for all three spatial dimensions as a function of time. The solid line shows $x - x_0$, the dashed one $y - y_0$, and the dotted one $z - z_0$. The thick blue line shows the total deviation from the initial position. (b) Logarithmic presentation of the total velocity of the axis apex as a function of time (solid blue line). As in Figure 7, the dashed lines show linear fits obtained for the time periods marked by dotted lines of the same colour.

After the relaxation, at $t = 0$, we start twisting the main negative polarity. Due to the pronounced fan-structure of the field rooted in the main polarity, the photospheric twisting does not lead to the formation of a single twisted flux tube that rises exactly in vertical direction above the TD rope, as was the case in run 1. Rather, the twisting leads to a slow, global expansion of the fan-shaped field lines (see Figure 8 and the corresponding online animations). Since we are mainly interested in the destabilisation of the flux-rope, we did not study the detailed evolution of the large-scale field. We expect it to be very similar to the one described by Santos, Büchner, and Otto (2011), since the active region those authors simulated was also dominated by one main polarity (sunspot), and the field rooted therein had a very similar fan-shaped structure (compare, for example, our Figure 8 with their Figure 1).

Important for our purpose is the evolution of the arcade-like part of the initial potential field that directly overlies the TD flux-rope. Those field lines are directly affected only by a fraction of the boundary flows and therefore get merely sheared (rather than twisted), which still leads to their slow expansion. As was the case for run 1, the TD rope starts to expand as well, adapting to the successively decreasing magnetic tension of the overlying field. This initial phase of the evolution is depicted in Figure 8b. Note that some of the flux at the front of the expanding arcade reconnects at the QSL current layer (see the online animation), which can be expected to aid the arcade expansion to some degree. As in run 1, the TD rope rises, after some initial adjustment, exponentially during this slow initial phase (Figure 9).

As the twisting continues, a transition to a rapid acceleration takes place, which can be seen in Figure 9b after $t \approx 100\tau_a$, when the rise curve leaves the quasi-static regime. After the transition phase, the TD rope again rises exponentially, but now with a significantly larger growth rate than during the slow rise phase. As for run 1, we attribute this transition and rapid acceleration to the occurrence of the torus instability.

The right panels in Figure 8 show that the trajectory of the flux-rope is far from being vertical. As can be seen in Figure 9, the rope axis has reached an inclination of about 45 degrees at the time of its peak rise velocity. Such lateral eruptions have been reported frequently in both observations and simulations (Williams *et al.*, 2005; Aulanier *et al.*, 2010; Bi *et al.*, 2011; Panasenco *et al.*, 2011; Zuccarello *et al.*, 2012; Yang *et al.*, 2012, and references therein), and are usually attributed to an asymmetric

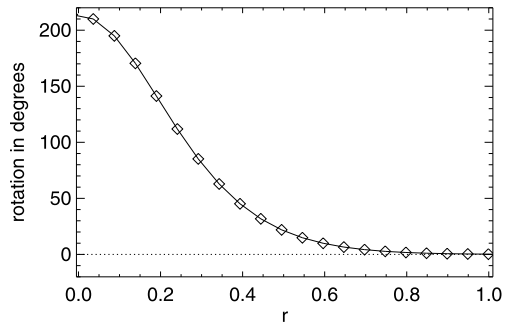
structure of the field overlying the erupting core flux. We believe that this causes the lateral rise also in our case, in particular since we found that asymmetric twisting of a symmetric configuration does not lead to a non-vertical trajectory of the flux-rope (see Section 4.1). We note that such a lateral rise during the very early phase of a CME is different from the often observed deflection of CMEs at coronal holes, where the ejecta is channelled by the structure of the coronal field at larger heights (Kahler, Akiyama, and Gopalswamy, 2012, and references therein). As the eruption continues, the trajectory of the flux-rope becomes increasingly horizontal, resembling the so-called “roll effect” (e.g. Panasenco *et al.*, 2011) and indicating that the rope cannot overcome the tension of the large-scale overlying field. Moreover, as a consequence of its increasing expansion, the flux-rope strongly pushes against the QSL current layer, which results in reconnection between the front of the rope and the ambient field. Eventually, the rope splits into two parts, similar to what has been found in simulations of confined eruptions (Amari and Luciani, 1999; Török and Kliem, 2005). These two effects – which both are not present in run 1 – slow down the rise of the rope after $t \approx 175\tau_a$ and inhibit its full eruption (*i.e.* the development of a CME) in our simulation.

Since QSLs can affect the evolution of an eruption, but are not expected to play a significant role for its initiation, we did not investigate in detail whether or not QSLs were present in the pre-eruption configuration of the 6 July 2006 event. The PFSS extrapolation indicates their presence to the North and the West of the main polarity (see the field-line connectivities in Figure 5(b), but less clearly so to its South. The possible absence of a QSL in front of the erupting core field in the real event is in line with the “smooth” evolution of the observed CME, while in our simulation the coherence of the flux-rope is destroyed before it can evolve into a full eruption. Also, the real large-scale field was probably less confining than our model field: the PFSS extrapolation indicates the presence of open field lines, which are fully absent in our simulation. Since, as stated earlier, we merely aim to model the initiation of the eruption rather than its full evolution into a CME, we refrained from further improving our model to obtain a configuration without a strong QSL in front of the flux-rope and with more open flux.

As for run 1, we check how the system evolves when the twisting is stopped before the flux-rope erupts. When the vortex flows are ramped down to zero during $t = (35-45)\tau_a$ – corresponding to an effective twisting time of $35\tau_a$ – no eruptive behaviour is seen in the subsequent evolution for almost $300\tau_a$, after which we stopped the calculation. However, the system does not fully relax to a numerical equilibrium as it was the case for the simpler configuration (see Section 4.1). Rather, the flux-rope continues to rise very slowly, with velocities smaller than $10^{-3}v_{a0}$. This indicates that the system has entered a meta-stable state, which is possibly supported by continuous slow reconnection at the QSL current layer due to numerical diffusion, so that it can be expected that the rope would finally erupt if the integration were continued sufficiently long. When somewhat more twisting is applied, the system behaves as in the continuously driven configuration, *i.e.* a phase of slow rise is followed by a transition to rapid acceleration and the final eruption of the flux-rope, except that the evolution leading up to the eruption takes the longer the less twist is imposed. For example, for an effective twisting period of $45\tau_a$, the rapid acceleration of the rope sets in at $\approx 265\tau_a$, significantly later than in the continuously driven system.

While it is tempting to quantitatively compare the amount of rotation in the simulation with the observed sunspot rotation, we think that such a comparison can be misleading, since the amount of rotation required for eruption will depend on parameters that have not been studied here and are not available from the observations (see Section 5: Summary and Discussion). Moreover, a quantitative comparison is not straightforward, since the model

Figure 10 Rotation profile for run 2 as a function of distance from the vortex centre; shown at $t = 100\tau_a$, approximately when the transition from slow to fast rise sets in (see Figure 9(b)).



rotation is highly non-uniform (Figure 10), while in the observed case a rigid rotation of the spot was measured (Figure 2). For example, at $t \approx 100\tau_a$, when the transition from slow to fast rise starts in the continuously driven simulation, the field lines rooted very close to the main polarity centre have rotated by about 200° . However, those field lines do not overlie the TD flux-rope directly, rather they connect to the positive polarity region located to the East of the rope (see Figures 5d and 8) and should therefore not significantly influence the rope's stability. On the other hand, the arcade-like field lines that are located directly above the rope are rooted at a distance of $r \approx 0.4$ from the polarity centre, towards its southern edge. As can be seen in Figure 10, the flux surface containing these field lines is rotated by a much smaller amount, about 40° at $t = 100\tau_a$. For the run with an effective twisting time of $t = 45\tau_a$ mentioned above, the imposed total rotation at this flux surface is even smaller, slightly below 20° . These values are similar to the observed sunspot rotation, but, in addition to the reasons given above, such a comparison should be taken with care. While the expansion of the field lines located directly above the TD flux-rope presumably depends mainly on the driving imposed at their footpoints, it is also influenced to some degree by the expansion of higher-lying fields which, in turn, depends on the (significantly larger) amount of rotation closer to the polarity centre. Moreover, the values obtained from the model refer to an overlying field that is initially potential (except for the QSL-related current layers), while the real overlying field may have already contained some stress at the onset of detectable rotational motions. Finally, as discussed at the end of the Introduction, the sunspot rotation may have injected stress also directly into the filament. In both cases, presumably less rotation as suggested by the model would have been required to trigger the eruption.

In summary, the simulation successfully models the early phases of the eruption (the slow rise and the initial rapid acceleration of the flux-rope) in a setting that is qualitatively similar to the observed configuration of the active region around the time of the CME described in Section 2. Hence, the CME-initiation mechanism described in run 1 can work also in more complex and less symmetric configurations.

5. Summary and Discussion

We analyse a filament eruption, two-ribbon flare, and CME that occurred in NOAA Active Region 10898 on 6 July 2006. The filament was located South of a strong sunspot that dominated the region. In the evolution leading up to the eruption, and for some time after it, a counter-clockwise rotation of the sunspot of about 30° was observed. Similar events, which occurred close to a dominant rotating sunspot, were presented by, *e.g.*, Tian and Alexander (2006) and Régnier and Canfield (2006). The triggering of such eruptions is commonly

attributed to the injection of twist (or helicity) beyond a certain threshold by the sunspot rotation (e.g. Török and Kliem, 2003). However, while filaments are frequently observed to spiral into the periphery of main sunspots, the erupting core flux may not always be rooted in the spot itself. Here we suggest that the continuous expansion due to sunspot rotation of the magnetic field that stabilises the current-carrying core flux, *i.e.* the successive decrease of magnetic tension, can also lead to filament eruptions and CMEs in such configurations.

We support this scenario by MHD simulations, in which a potential field overlying and stabilizing a pre-existing flux-rope is slowly twisted at its photospheric-flux concentration(s). The flux-rope is not anchored in these concentrations and is therefore not twisted. In a first configuration, the rope is initially kept in equilibrium by a field rooted in two “sunspots” of opposite polarity that are located at opposite sides of the rope. The twisting of the flux concentrations reproduces the known behaviour of twisted bipolar fields (see, e.g., Amari *et al.*, 1996): a twisted flux tube is generated that expands and rises at an exponentially increasing rate. As a consequence, the magnetic tension of the field above the pre-existing flux-rope is successively weakened. The rope undergoes a quasi-static adaptation to the changing surrounding field, which is manifested in a slow rise phase. As the weakening of the overlying field reaches an appropriate level, the torus instability sets in and rapidly accelerates the rope upwards, leading to a second, fast rise phase and eruption. This evolution in two phases resembles the often-observed slow rise phase and subsequent strong acceleration of filaments in the course of their eruption (see Figure 4, as well as Schrijver *et al.*, 2008, and references therein). Eventually, since the flux-rope erupts faster than the twisted flux-tube rises, the rope catches up and starts to interact with the flux-tube, at which point we stop the simulation.

As a step towards more realistic configurations, we consider a second setup in which the initial ambient field surrounding the flux-rope is created by an ensemble of sub-photospheric sources that qualitatively reproduce the photospheric flux distribution and magnetic-field structure of the active region around the time of the 6 July 2006 event. In particular, the highly asymmetric flux density and the resulting overall fan shape of the active-region field are recovered, while the approximative flux balance of the region is kept. The rotation of the dominant negative polarity (mimicking the observed sunspot rotation) leads to the same qualitative behaviour as in the much more symmetric configuration: after a slow rise phase resembling the quasi-static adaptation of the flux-rope to the expanding ambient field, the rope undergoes a second, strong acceleration phase. In this case, the asymmetry of the ambient field leads to a markedly lateral eruption. However, in contrast to the first configuration, the presence of a QSL-related current layer in the front of the erupting flux-rope leads to reconnection which eventually splits the rope before it can evolve into a CME. Although we are not able to follow the expansion of the flux-rope beyond this phase, we can assert the effectiveness of the proposed mechanism in triggering an eruption also in this more realistic case.

The proposed mechanism requires the presence of a flux-rope in the corona prior to the onset of the twisting motions, which is in line with the relatively small observed rotation of about 30° in our event. Far larger rotations appear to be required to produce a flux-rope that can be driven beyond the threshold of instability by such small additional rotation (e.g. Török and Kliem, 2003; Aulanier, Démoulin, and Grappin, 2005; Yan *et al.*, 2012). It can be expected that the amount of rotation required to initiate the eruption of a pre-existing flux-rope by rotating its overlying field depends on two main parameters: i) the “distance” of the flux-rope from an unstable state and ii) the “effectiveness” of the rotation in reducing the stabilisation by the overlying field. For example, it will take a longer time for a low-lying flux-rope to slowly rise to the critical height required for the onset of the torus instability

than it does for a rope that is already close to this height. Also, the required rotation will be larger if mostly high-arching field lines, rather than field lines located directly above the rope, are twisted. Thus, the amount of rotation required for eruption appears to depend strongly on the details of the configuration. A proper assessment of this question demands an extensive parametric study that is beyond the scope of this article. Here we merely aim to provide proof-of-concept simulations that illustrate the physical mechanism.

In summary, the main result of our study is that the rotation of sunspots can substantially weaken the magnetic tension of the field in active regions, in particular in cases where the sunspot dominates the region. This can lead to the triggering of eruptions in the vicinity of the spot, even if the erupting core flux (the filament) is not anchored in it. The mechanism that we suggest provides an alternative to the common scenario in which eruptions in the vicinity of rotating sunspots are triggered by the direct injection of twist into the erupting core flux.

Acknowledgements We thank the anonymous referee for constructive comments that helped to improve the content of the article. We acknowledge the use of data provided by the SOHO/MDI consortium. SOHO/EIT was funded by CNES, NASA, and the Belgian SPPS. The SOHO/LASCO data used here are produced by a consortium of the Naval Research Laboratory(USA), Max-Planck-Institut für Aeronomie (Germany), Laboratoire d'Astrophysique de Marseille (France), and the University of Birmingham (UK). SOHO is a mission of international cooperation between ESA and NASA. The *Transition Region and Coronal Explorer* (TRACE) is a mission of the Stanford-Lockheed Institute for Space Research, and part of the NASA Small Explorer program. H α data were provided by the Kanzelhöhe Observatory, University of Graz, Austria, and by the Hvar Observatory, University of Zagreb, Croatia. The research leading to these results has received funding from the European Commission's Seventh Framework Programme (FP7/2007–2013) under the grant agreements No. 218816 (SOTERIA project, www.soteria-space.eu) and No. 284461 (eHEROES, <http://soteria-space.eu/eheroes/html>). TT was partially supported by NASA's HTP, LWS, and SR&T programs. LvDG acknowledges funding through the Hungarian Science Foundation grant OTKA K81421.

References

- Amari, T., Luciani, J.F.: 1999, *Astrophys. J. Lett.* **515**, L81. doi:[10.1086/311971](https://doi.org/10.1086/311971).
- Amari, T., Luciani, J.F., Aly, J.J., Tagger, M.: 1996, *Astrophys. J. Lett.* **466**, L39. doi:[10.1086/310158](https://doi.org/10.1086/310158).
- Attrill, G.D.R., van Driel-Gesztelyi, L., Démoulin, P., Zhukov, A.N., Steed, K., Harra, L.K., Mandrini, C.H., Linker, J.: 2008, *Solar Phys.* **252**, 349. doi:[10.1007/s11207-008-9255-z](https://doi.org/10.1007/s11207-008-9255-z).
- Aulanier, G., Démoulin, P., Grappin, R.: 2005, *Astron. Astrophys.* **430**, 1067. doi:[10.1051/0004-6361:20041519](https://doi.org/10.1051/0004-6361:20041519).
- Aulanier, G., Pariat, E., Démoulin, P.: 2005, *Astron. Astrophys.* **444**, 961. doi:[10.1051/0004-6361:20053600](https://doi.org/10.1051/0004-6361:20053600).
- Aulanier, G., Török, T., Démoulin, P., DeLuca, E.E.: 2010, *Astrophys. J.* **708**, 314. doi:[10.1088/0004-637X/708/1/314](https://doi.org/10.1088/0004-637X/708/1/314).
- Barnes, C.W., Sturrock, P.A.: 1972, *Astrophys. J.* **174**, 659. doi:[10.1086/151527](https://doi.org/10.1086/151527).
- Bateman, G.: 1978, *MHD Instabilities*, MIT Press, Cambridge.
- Baum, P.J., Bratenahl, A.: 1980, *Solar Phys.* **67**, 245. doi:[10.1007/BF00149805](https://doi.org/10.1007/BF00149805).
- Bi, Y., Jiang, Y.C., Yang, L.H., Zheng, R.S.: 2011, *New Astron.* **16**, 276. doi:[10.1016/j.newast.2010.11.009](https://doi.org/10.1016/j.newast.2010.11.009).
- Brown, D.S., Nightingale, R.W., Alexander, D., Schrijver, C.J., Metcalf, T.R., Shine, R.A., Title, A.M., Wolfson, C.J.: 2003, *Solar Phys.* **216**, 79. doi:[10.1023/A:1026138413791](https://doi.org/10.1023/A:1026138413791).
- Canou, A., Amari, T.: 2010, *Astrophys. J.* **715**, 1566. doi:[10.1088/0004-637X/715/2/1566](https://doi.org/10.1088/0004-637X/715/2/1566).
- Chen, J.: 1989, *Astrophys. J.* **338**, 453. doi:[10.1086/167211](https://doi.org/10.1086/167211).
- Chifor, C., Tripathi, D., Mason, H.E., Dennis, B.R.: 2007, *Astron. Astrophys.* **472**, 967. doi:[10.1051/0004-6361:20077771](https://doi.org/10.1051/0004-6361:20077771).
- Démoulin, P., Aulanier, G.: 2010, *Astrophys. J.* **718**, 1388. doi:[10.1088/0004-637X/718/2/1388](https://doi.org/10.1088/0004-637X/718/2/1388).
- Démoulin, P., Henoux, J.C., Priest, E.R., Mandrini, C.H.: 1996, *Astron. Astrophys.* **308**, 643.
- Evershed, J.: 1910, *Mon. Not. Roy. Astron. Soc.* **70**, 217.
- Fan, Y.: 2009, *Astrophys. J.* **697**, 1529. doi:[10.1088/0004-637X/697/2/1529](https://doi.org/10.1088/0004-637X/697/2/1529).
- Fan, Y., Gibson, S.E.: 2003, *Astrophys. J. Lett.* **589**, L105. doi:[10.1086/375834](https://doi.org/10.1086/375834).
- Fan, Y., Gibson, S.E.: 2007, *Astrophys. J.* **668**, 1232. doi:[10.1086/521335](https://doi.org/10.1086/521335).

- Forbes, T.: 2010, In: Schrijver, C.J., Siscoe, G.L. (eds.) *Heliophysics: Space Storms and Radiation: Causes and Effects*, Cambridge University Press, Cambridge, 159.
- Forbes, T.G.: 2000, *J. Geophys. Res.* **105**, 23153. doi:[10.1029/2000JA000005](https://doi.org/10.1029/2000JA000005).
- Galsgaard, K., Nordlund, Å.: 1997, *J. Geophys. Res.* **102**, 219. doi:[10.1029/96JA01462](https://doi.org/10.1029/96JA01462).
- Gerrard, C.L., Arber, T.D., Hood, A.W.: 2002, *Astron. Astrophys.* **387**, 687. doi:[10.1051/0004-6361:20020491](https://doi.org/10.1051/0004-6361:20020491).
- Gerrard, C.L., Hood, A.W., Brown, D.S.: 2004, *Solar Phys.* **222**, 79. doi:[10.1023/B:SOLA.0000036877.20077.42](https://doi.org/10.1023/B:SOLA.0000036877.20077.42).
- Gerrard, C.L., Brown, D.S., Mellor, C., Arber, T.D., Hood, A.W.: 2003, *Solar Phys.* **213**, 39. doi:[10.1023/A:1023281624037](https://doi.org/10.1023/A:1023281624037).
- Gibson, S.E., Fan, Y., Mandrini, C., Fisher, G., Demoulin, P.: 2004, *Astrophys. J.* **617**, 600. doi:[10.1086/425294](https://doi.org/10.1086/425294).
- Gombosi, T.I., Powell, K.G., de Zeeuw, D.L.: 1994, *J. Geophys. Res.* **99**, 21525.
- Gopalswamy, N., Yashiro, S., Kaiser, M.L., Howard, R.A., Bougeret, J.-L.: 2001, *Astrophys. J. Lett.* **548**, L91. doi:[10.1086/318939](https://doi.org/10.1086/318939).
- Green, L.M., Démoulin, P., Mandrini, C.H., Van Driel-Gesztelyi, L.: 2003, *Solar Phys.* **215**, 307. doi:[10.1023/A:1025678917086](https://doi.org/10.1023/A:1025678917086).
- Green, L.M., Kliem, B., Török, T., van Driel-Gesztelyi, L., Attrill, G.D.R.: 2007, *Solar Phys.* **246**, 365. doi:[10.1007/s11207-007-9061-z](https://doi.org/10.1007/s11207-007-9061-z).
- Guo, J., Liu, Y., Zhang, H., Deng, Y., Lin, J., Su, J.: 2010a, *Astrophys. J.* **711**, 1057. doi:[10.1088/0004-637X/711/2/1057](https://doi.org/10.1088/0004-637X/711/2/1057).
- Guo, Y., Schmieder, B., Démoulin, P., Wiegmann, T., Aulanier, G., Török, T., Bommier, V.: 2010b, *Astrophys. J.* **714**, 343. doi:[10.1088/0004-637X/714/1/343](https://doi.org/10.1088/0004-637X/714/1/343).
- Handy, B.N., Acton, L.W., Kankelborg, C.C., Wolfson, C.J., Akin, D.J., Bruner, M.E., Carvalho, R., Catura, R.C., Chevalier, R., Duncan, D.W., Edwards, C.G., Feinstein, C.N., Freeland, S.L., Friedlaender, F.M., Hoffmann, C.H., Hurlburt, N.E., Jurevich, B.K., Katz, N.L., Kelly, G.A., Lemen, J.R., Levay, M., Lindgren, R.W., Mathur, D.P., Meyer, S.B., Morrison, S.J., Morrison, M.D., Nightingale, R.W., Pope, T.P., Rehse, R.A., Schrijver, C.J., Shine, R.A., Shing, L., Strong, K.T., Tarbell, T.D., Title, A.M., Torgerson, D.D., Golub, L., Bookbinder, J.A., Caldwell, D., Cheimets, P.N., Davis, W.N., Deluca, E.E., McMullen, R.A., Warren, H.P., Amato, D., Fisher, R., Maldonado, H., Parkinson, C.: 1999, *Solar Phys.* **187**, 229. doi:[10.1023/A:1005166902804](https://doi.org/10.1023/A:1005166902804).
- Hiremath, K.M., Suryanarayana, G.S.: 2003, *Astron. Astrophys.* **411**, L497. doi:[10.1051/0004-6361:20031618](https://doi.org/10.1051/0004-6361:20031618).
- Hiremath, K.M., Lovely, M.R., Kariyappa, R.: 2006, *J. Astrophys. Astron.* **27**, 333. doi:[10.1007/BF02702538](https://doi.org/10.1007/BF02702538).
- Isenberg, P.A., Forbes, T.G.: 2007, *Astrophys. J.* **670**, 1453. doi:[10.1086/522025](https://doi.org/10.1086/522025).
- Jiang, Y., Yang, L., Li, K., Ren, D.: 2007, *Astrophys. J. Lett.* **662**, L131. doi:[10.1086/519490](https://doi.org/10.1086/519490).
- Kahler, S.W., Akiyama, S., Gopalswamy, N.: 2012, *Astrophys. J.* **754**, 100. doi:[10.1088/0004-637X/754/2/100](https://doi.org/10.1088/0004-637X/754/2/100).
- Kahler, S.W., Moore, R.L., Kane, S.R., Zirin, H.: 1988, *Astrophys. J.* **328**, 824. doi:[10.1086/166340](https://doi.org/10.1086/166340).
- Kazachenko, M.D., Canfield, R.C., Longcope, D.W., Qiu, J., Des Jardins, A., Nightingale, R.W.: 2009, *Astrophys. J.* **704**, 1146. doi:[10.1088/0004-637X/704/2/1146](https://doi.org/10.1088/0004-637X/704/2/1146).
- Keppens, R., Nool, M., Tóth, G., Goedbloed, J.P.: 2003, *Comput. Phys. Commun.* **153**, 317. doi:[10.1016/S0010-4655\(03\)00139-5](https://doi.org/10.1016/S0010-4655(03)00139-5).
- Kliem, B., Török, T.: 2006, *Phys. Rev. Lett.* **96**(25), 255002. doi:[10.1103/PhysRevLett.96.255002](https://doi.org/10.1103/PhysRevLett.96.255002).
- Kliem, B., Titov, V.S., Török, T.: 2004, *Astron. Astrophys.* **413**, L23. doi:[10.1051/0004-6361:20031690](https://doi.org/10.1051/0004-6361:20031690).
- Klimchuk, J.A., Antiochos, S.K., Norton, D.: 2000, *Astrophys. J.* **542**, 504. doi:[10.1086/309527](https://doi.org/10.1086/309527).
- Lau, Y.-T., Finn, J.M.: 1990, *Astrophys. J.* **350**, 672. doi:[10.1086/168419](https://doi.org/10.1086/168419).
- Li, L., Zhang, J.: 2009, *Astrophys. J. Lett.* **706**, L17. doi:[10.1088/0004-637X/706/1/L17](https://doi.org/10.1088/0004-637X/706/1/L17).
- Lionello, R., Mikić, Z., Linker, J.A., Amari, T.: 2002, *Astrophys. J.* **581**, 718. doi:[10.1086/344222](https://doi.org/10.1086/344222).
- Liu, R., Kliem, B., Török, T., Liu, C., Titov, V.S., Lionello, R., Linker, J.A., Wang, H.: 2012, *Astrophys. J.* **756**, 59. doi:[10.1088/0004-637X/756/1/59](https://doi.org/10.1088/0004-637X/756/1/59).
- Longcope, D.W., Welsch, B.T.: 2000, *Astrophys. J.* **545**, 1089. doi:[10.1086/317846](https://doi.org/10.1086/317846).
- Lugaz, N., Manchester, W.B. IV, Gombosi, T.I.: 2005, *Astrophys. J.* **634**, 651. doi:[10.1086/491782](https://doi.org/10.1086/491782).
- Maričić, D., Vršnak, B., Roša, D.: 2009, *Solar Phys.* **260**, 177. doi:[10.1007/s11207-009-9421-y](https://doi.org/10.1007/s11207-009-9421-y).
- Maričić, D., Vršnak, B., Stanger, A.L., Veronig, A.: 2004, *Solar Phys.* **225**, 337. doi:[10.1007/s11207-004-3748-1](https://doi.org/10.1007/s11207-004-3748-1).
- Maričić, D., Vršnak, B., Stanger, A.L., Veronig, A.M., Temmer, M., Roša, D.: 2007, *Solar Phys.* **241**, 99. doi:[10.1007/s11207-007-0291-x](https://doi.org/10.1007/s11207-007-0291-x).
- Masson, S., Pariat, E., Aulanier, G., Schrijver, C.J.: 2009, *Astrophys. J.* **700**, 559. doi:[10.1088/0004-637X/700/1/559](https://doi.org/10.1088/0004-637X/700/1/559).

- McIntosh, S.W., Leamon, R.J., Davey, A.R., Wills-Davey, M.J.: 2007, *Astrophys. J.* **660**, 1653. doi:[10.1086/512665](https://doi.org/10.1086/512665).
- Mikic, Z., Schnack, D.D., van Hoven, G.: 1990, *Astrophys. J.* **361**, 690. doi:[10.1086/169232](https://doi.org/10.1086/169232).
- Miklenic, C.H., Veronig, A.M., Vršnak, B.: 2009, *Astron. Astrophys.* **499**, 893. doi:[10.1051/0004-6361/200810947](https://doi.org/10.1051/0004-6361/200810947).
- Min, S., Chae, J.: 2009, *Solar Phys.* **258**, 203. doi:[10.1007/s11207-009-9425-7](https://doi.org/10.1007/s11207-009-9425-7).
- Moore, R.L., Sterling, A.C., Hudson, H.S., Lemen, J.R.: 2001, *Astrophys. J.* **552**, 833. doi:[10.1086/320559](https://doi.org/10.1086/320559).
- Nindos, A., Andrews, M.D.: 2004, *Astrophys. J. Lett.* **616**, L175. doi:[10.1086/426861](https://doi.org/10.1086/426861).
- Panasenco, O., Martin, S., Joshi, A.D., Srivastava, N.: 2011, *J. Atmos. Solar-Terr. Phys.* **73**, 1129. doi:[10.1016/j.jastp.2010.09.010](https://doi.org/10.1016/j.jastp.2010.09.010).
- Pariat, E., Antiochos, S.K., DeVore, C.R.: 2009, *Astrophys. J.* **691**, 61. doi:[10.1088/0004-637X/691/1/61](https://doi.org/10.1088/0004-637X/691/1/61).
- Priest, E.R., Forbes, T.G.: 1992, *J. Geophys. Res.* **97**, 1521. doi:[10.1029/91JA02435](https://doi.org/10.1029/91JA02435).
- Régnier, S., Canfield, R.C.: 2006, *Astron. Astrophys.* **451**, 319. doi:[10.1051/0004-6361:20054171](https://doi.org/10.1051/0004-6361:20054171).
- Robbrecht, E., Patsourakos, S., Vourlidias, A.: 2009, *Astrophys. J.* **701**, 283. doi:[10.1088/0004-637X/701/1/283](https://doi.org/10.1088/0004-637X/701/1/283).
- Romano, P., Contarino, L., Zuccarello, F.: 2005, *Astron. Astrophys.* **433**, 683. doi:[10.1051/0004-6361:20041807](https://doi.org/10.1051/0004-6361:20041807).
- Roussev, I.I., Forbes, T.G., Gombosi, T.I., Sokolov, I.V., DeZeeuw, D.L., Birn, J.: 2003, *Astrophys. J. Lett.* **588**, L45. doi:[10.1086/375442](https://doi.org/10.1086/375442).
- Santos, J.C., Büchner, J., Otto, A.: 2011, *Astron. Astrophys.* **535**, A111. doi:[10.1051/0004-6361/201116792](https://doi.org/10.1051/0004-6361/201116792).
- Sato, T., Hayashi, T.: 1979, *Phys. Fluids* **22**, 1189. doi:[10.1063/1.862721](https://doi.org/10.1063/1.862721).
- Schatten, K.H., Wilcox, J.M., Ness, N.F.: 1969, *Solar Phys.* **6**, 442. doi:[10.1007/BF00146478](https://doi.org/10.1007/BF00146478).
- Scherrer, P.H., Bogart, R.S., Bush, R.I., Hoeksema, J.T., Kosovichev, A.G., Schou, J., Rosenberg, W., Springer, L., Tarbell, T.D., Title, A., Wolfson, C.J., Zayer, I., MDI Engineering Team: 1995, *Solar Phys.* **162**, 129. doi:[10.1007/BF00733429](https://doi.org/10.1007/BF00733429).
- Schrijver, C.J., Elmore, C., Kliem, B., Török, T., Title, A.M.: 2008, *Astrophys. J.* **674**, 586. doi:[10.1086/524294](https://doi.org/10.1086/524294).
- Stenflo, J.O.: 1969, *Solar Phys.* **8**, 115. doi:[10.1007/BF00150662](https://doi.org/10.1007/BF00150662).
- Suryanarayana, G.S.: 2010, *New Astron.* **15**, 313. doi:[10.1016/j.newast.2009.09.004](https://doi.org/10.1016/j.newast.2009.09.004).
- Temmer, M., Veronig, A.M., Vršnak, B., Rybák, J., Gömöry, P., Stoiser, S., Maričić, D.: 2008, *Astrophys. J. Lett.* **673**, L95. doi:[10.1086/527414](https://doi.org/10.1086/527414).
- Tian, L., Alexander, D.: 2006, *Solar Phys.* **233**, 29. doi:[10.1007/s11207-006-2505-z](https://doi.org/10.1007/s11207-006-2505-z).
- Tian, L., Alexander, D., Nightingale, R.: 2008, *Astrophys. J.* **684**, 747. doi:[10.1086/589492](https://doi.org/10.1086/589492).
- Titov, V.S., Démoulin, P.: 1999, *Astron. Astrophys.* **351**, 707.
- Török, T., Kliem, B.: 2003, *Astron. Astrophys.* **406**, 1043. doi:[10.1051/0004-6361:20030692](https://doi.org/10.1051/0004-6361:20030692).
- Török, T., Kliem, B.: 2005, *Astrophys. J. Lett.* **630**, L97. doi:[10.1086/462412](https://doi.org/10.1086/462412).
- Török, T., Kliem, B.: 2007, *Astron. Nachr.* **328**, 743. doi:[10.1002/asna.200710795](https://doi.org/10.1002/asna.200710795).
- Török, T., Kliem, B., Titov, V.S.: 2004, *Astron. Astrophys.* **413**, L27. doi:[10.1051/0004-6361:20031691](https://doi.org/10.1051/0004-6361:20031691).
- Török, T., Aulanier, G., Schmieder, B., Reeves, K.K., Golub, L.: 2009, *Astrophys. J.* **704**, 485. doi:[10.1088/0004-637X/704/1/485](https://doi.org/10.1088/0004-637X/704/1/485).
- Török, T., Panasenco, O., Titov, V.S., Mikić, Z., Reeves, K.K., Velli, M., Linker, J.A., De Toma, G.: 2011, *Astrophys. J. Lett.* **739**, L63. doi:[10.1088/2041-8205/739/2/L63](https://doi.org/10.1088/2041-8205/739/2/L63).
- Valori, G., Kliem, B., Török, T., Titov, V.S.: 2010, *Astron. Astrophys.* **519**, A44. doi:[10.1051/0004-6361/201014416](https://doi.org/10.1051/0004-6361/201014416).
- van Ballegoijen, A.A.: 2004, *Astrophys. J.* **612**, 519. doi:[10.1086/422512](https://doi.org/10.1086/422512).
- Veronig, A.M., Rybak, J., Gömöry, P., Berkebile-Stoiser, S., Temmer, M., Otruba, W., Vrsnak, B., Pötzi, W., Baumgartner, D.: 2010, *Astrophys. J.* **719**, 655. doi:[10.1088/0004-637X/719/1/655](https://doi.org/10.1088/0004-637X/719/1/655).
- Vršnak, B.: 1990, *Solar Phys.* **129**, 295. doi:[10.1007/BF00159042](https://doi.org/10.1007/BF00159042).
- Vršnak, B., Sudar, D., Ruždjak, D., Žic, T.: 2007, *Astron. Astrophys.* **469**, 339. doi:[10.1051/0004-6361:20077175](https://doi.org/10.1051/0004-6361:20077175).
- Williams, D.R., Török, T., Démoulin, P., van Driel-Gesztelyi, L., Kliem, B.: 2005, *Astrophys. J. Lett.* **628**, L163. doi:[10.1086/432910](https://doi.org/10.1086/432910).
- Yan, X.L., Qu, Z.Q.: 2007, *Astron. Astrophys.* **468**, 1083. doi:[10.1051/0004-6361:20077064](https://doi.org/10.1051/0004-6361:20077064).
- Yan, X.L., Qu, Z.Q., Kong, D.F.: 2008, *Mon. Not. Roy. Astron. Soc.* **391**, 1887. doi:[10.1111/j.1365-2966.2008.14002.x](https://doi.org/10.1111/j.1365-2966.2008.14002.x).
- Yan, X.L., Qu, Z.Q., Xu, C.L., Xue, Z.K., Kong, D.F.: 2009, *Res. Astron. Astrophys.* **9**, 596. doi:[10.1088/1674-4527/9/5/010](https://doi.org/10.1088/1674-4527/9/5/010).
- Yan, X.L., Qu, Z.Q., Kong, D.-F., Xu, C.L.: 2012, *Astrophys. J.* **754**, 16. doi:[10.1088/0004-637X/754/1/16](https://doi.org/10.1088/0004-637X/754/1/16).
- Yang, J., Jiang, Y., Yang, B., Zheng, R., Yang, D., Hong, J., Li, H., Bi, Y.: 2012, *Solar Phys.* **279**, 115. doi:[10.1007/s11207-012-0002-0](https://doi.org/10.1007/s11207-012-0002-0).
- Zhang, J., Li, L., Song, Q.: 2007, *Astrophys. J. Lett.* **662**, L35. doi:[10.1086/519280](https://doi.org/10.1086/519280).

- Zhang, J., Dere, K.P., Howard, R.A., Kundu, M.R., White, S.M.: 2001, *Astrophys. J.* **559**, 452. doi:[10.1086/322405](https://doi.org/10.1086/322405).
- Zhang, Y., Liu, J., Zhang, H.: 2008, *Solar Phys.* **247**, 39. doi:[10.1007/s11207-007-9089-0](https://doi.org/10.1007/s11207-007-9089-0).
- Zhu, C., Alexander, D., Tian, L.: 2012, *Solar Phys.* **278**, 121. doi:[10.1007/s11207-011-9923-2](https://doi.org/10.1007/s11207-011-9923-2).
- Zirin, H.: 1998, *The Astrophysics of the Sun*, Cambridge University Press, Cambridge.
- Zuccarello, F.P., Bemporad, A., Jacobs, C., Mierla, M., Poedts, S., Zuccarello, F.: 2012, *Astrophys. J.* **744**, 66. doi:[10.1088/0004-637X/744/1/66](https://doi.org/10.1088/0004-637X/744/1/66).



The challenge in making models of fast CMEs

Zoran Miki, Tibor Török, Viacheslav Titov, Jon A. Linker, Roberto Lionello, Cooper Downs, and Pete Riley

Citation: [AIP Conference Proceedings](#) **1539**, 42 (2013); doi: 10.1063/1.4810985

View online: <http://dx.doi.org/10.1063/1.4810985>

View Table of Contents: <http://scitation.aip.org/content/aip/proceeding/aipcp/1539?ver=pdfcov>

Published by the [AIP Publishing](#)

The Challenge in Making Models of Fast CMEs

Zoran Mikić, Tibor Török, Viacheslav Titov, Jon A. Linker, Roberto Lionello,
Cooper Downs and Pete Riley

Predictive Science, Inc., 9990 Mesa Rim Road, San Diego, CA 92121

Abstract. It has been a challenge to explain theoretically how fast CMEs (exceeding $\sim 1,000$ km/s) occur. Our numerical models suggest that it is not easy to release enough magnetic energy impulsively from an active region. We have been studying CME models that are constrained by observed magnetic fields, with realistic coronal plasma density and temperature profiles, as derived from thermodynamic models of the corona. We find that to get fast CMEs, the important parameters are the magnetic energy density, the magnetic field drop-off index, and the Alfvén speed profile in active regions. We describe how we energize active regions, and how we subsequently initiate CMEs via flux cancellation. We contrast CMEs from idealized zero-beta models with more sophisticated models based on thermodynamic solutions.

Keywords: Coronal Mass Ejections, Solar Corona, Magnetohydrodynamics (MHD)

PACS: 96.60.P-, 96.60.ph, 96.60.qf, 95.30.Qd

INTRODUCTION

It has been difficult to develop successful models of fast coronal mass ejections (CMEs). By fast CMEs we mean those whose speed significantly exceeds the ambient solar wind speed (i.e., exceeding $\sim 1,000$ km/s). In order to explain fast CMEs, we need to demonstrate that a significant fraction of the magnetic energy in an active region can be converted into kinetic energy to accelerate the CME, produce a shock wave low in the corona, open overlying closed magnetic field lines, and accelerate energetic particles. Our numerical models suggest that it is not easy to release enough magnetic energy impulsively for these purposes. This has to be done using realistic parameters (magnetic field strength, coronal density, active region size, solar wind, and global field model). It is desirable to use self-consistent CME initiation mechanisms (e.g., photospheric shearing flows, flux cancellation, flux emergence), rather than starting from configurations that are initially out of equilibrium.

To understand CMEs theoretically it is helpful to idealize the problem to the simplest possible configuration that retains the essential characteristics of CMEs. This is a difficult task, since this simplification might compromise the very goal of getting a fast CME. The photospheric magnetic field that is used in models is typically smoothed because simulations with large Alfvén speed and high-resolution meshes are computationally challenging. This smoothing tends to reduce the size of the photospheric field. In our experience, models with overly smoothed fields do not tend to produce fast CMEs. The smoothing process reduces the magnetic energy density in the active region and the magnitude of the Alfvén speed in the corona, and it is likely that these reductions may lower the speed of CMEs.

The plasma density can also affect the speed of CMEs (presumably via the Alfvén speed). Therefore, the models need to have a realistic density profile, requiring an accurate energy equation in the model, and a reasonable coronal heating model. With a sophisticated energy equation [1], we are able to model the cold, dense prominences that frequently erupt together with the CME. As we describe below, the mass trapped in the prominence may affect the speed of the CME, requiring an accurate model of the lower corona and chromosphere.

Finally, the magnetic field overlying the active region may affect how the CME is confined and the nature of the eruption. Since this field arises from distant magnetic field sources, a global model whose scale is much larger than the source active region may be required to properly model the CME.

It is apparent that all these aforementioned considerations make the modeling of fast CMEs difficult. This may be the reason that models have generally not been able to produce fast CMEs.

AN IDEALIZED MODEL

We illustrate our methodology by developing an idealized model of a CME that was observed on 12 May 1997. We have studied this event for many years. Even though this CME occurred in the SOHO era, it is still relevant today, simply because it is not very well understood yet. The halo CME originated in a “simple” small bipolar active region (AR 8038) at $N21^{\circ}W08^{\circ}$, and was accompanied by a C1.3 flare at 04:42 UT. The projected CME speed was ~ 250 km/s; the estimated actual CME speed was ~ 600 km/s. This CME has been described by Plunkett et al. [2] (LASCO); Thompson et al. [3] (EIT waves); Webb et al. [4] (interplanetary magnetic cloud);

Solar Wind 13

AIP Conf. Proc. 1539, 42-45 (2013); doi: 10.1063/1.4810985
© 2013 AIP Publishing LLC 978-0-7354-1163-0/\$30.00

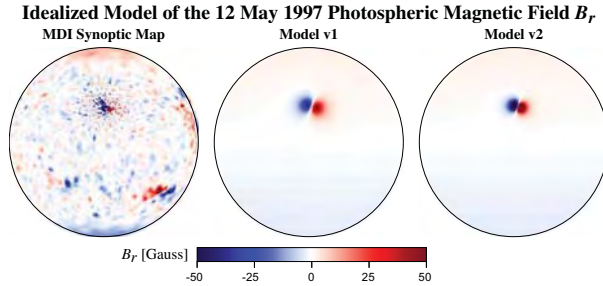


FIGURE 1. The two idealized models of the 12 May 1997 photospheric magnetic field, compared to the SOHO/MDI magnetogram.

Ambastha and Mathew [5] (flux cancellation); Gopalswamy and Kaiser [6] (Type II radio); Attrill et al. [7] (coronal dimmings); and Crooker and Webb [8] (interchange reconnection).

Despite the fact that this was not a fast CME, it is an excellent case to study for the following reason. Our simulations of the pre-eruption corona with a thermodynamic model reproduce several characteristics of the observations, including signatures in EUV and X-ray emission (coronal hole morphology, quiet Sun and active region emission, sigmoid). Furthermore, our simulated eruptions also match the observations, including prominence formation, dimming regions in EUV and X-rays, post-flare loops, and EIT waves. Nevertheless, all our attempts to simulate this CME produce an eruption that is less energetic than the observed CME.

A procedure for developing a simplified model using a global sun-centered dipole and a sub-surface bipole to represent the active region (AR) was described by Titov et al. [9]. We adopt a similar procedure, matching the observed AR flux ($\sim 5 \times 10^{21}$ Mx) and the total global flux ($\sim 4.3 \times 10^{22}$ Mx). The resulting global dipole has $B_r = 2.8$ G at the poles.

We are studying two versions of the model: v1 has a smoother version of the magnetogram with $B_r(\text{max}) = 50$ G in the AR; v2 has less smoothing with $B_r(\text{max}) = 180$ G. The idea is to determine if the reduction of photospheric magnetic field by smoothing reduces the speed of the CME. Both models match the observed AR magnetic flux. Figure 1 shows the models compared to the photospheric field observed with the SOHO/MDI magnetogram.

The simulations are performed with our spherical 3D resistive MHD code, using a semi-implicit technique to overcome the time step limit imposed by the Alfvén speed, and a fully implicit scheme to advance the resistive, viscous, and thermal conduction terms [10, 11]. In the transverse direction, the smallest cells (in the AR) have a size of 2,300 km (690 km) for a medium (high) resolution mesh. In the vertical direction, for the thermodynamic model, the smallest cells have a size of 220 km (60 km) for a medium (high) resolution mesh. The resis-

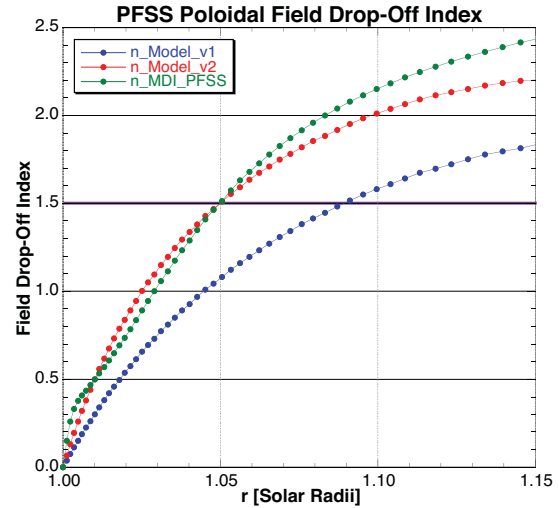


FIGURE 2. The field drop-off index (vertically above the neutral line) for the high-resolution MDI data and for Models v1 and v2.

tivity is chosen to be uniform, with a Lundquist number $S = 10^6$.

Kliem and Török [12] have described how the drop-off of the poloidal component of the potential field that confines a flux rope affects its stability. Assuming that locally $B_{\text{pol}} = B_0(h/h_0)^{-n}$, where $h = r - R_\odot$ is the height above the photosphere, the local drop-off index is $n = -d(\ln B_{\text{pol}})/d(\ln h)$. A heuristic condition for stability is: when $n \gtrsim 1.5$ above the flux rope, the rope erupts more easily; when $n \lesssim 1.5$, the rope tends to be stable [12]. Démoulin and Aulanier [13] consider the critical value to be closer to 1.1–1.3. Török and Kliem [14] have investigated the effect of n on the speed of CMEs. Fields that fall off rapidly with height (larger n) are easier to disrupt, and may produce faster CMEs. An example is a quadrupolar configuration, as exemplified by the Breakout Model [15]. Figure 2 compares n for the high-resolution MDI magnetogram, and for Models v1 and v2 (using a PFSS model). It can be seen that Model v2 matches n of the high-resolution data, whereas Model v1 has a lower n . This is an indication that Model v1 may have been smoothed too much and may have difficulty producing fast CMEs, consistent with our preliminary results. Full confirmation will require a detailed comparison of models v1 and v2 (work in progress).

ACTIVE REGION ENERGIZATION AND CME TRIGGERING

We briefly describe how we typically energize the active region in our model, and how we trigger the eruption. We start with a potential field, and energize the AR by emerging transverse magnetic field along the polarity inversion line (PIL), specified via a boundary condition at $r = R_\odot$ on the transverse electric field, $\mathbf{E}_t = \nabla_t \Phi$.

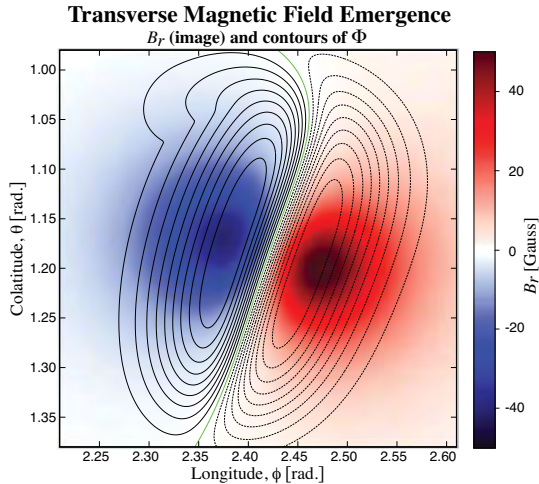


FIGURE 3. The potential Φ used to energize the AR by emerging transverse magnetic field along the PIL (green).

The potential Φ is chosen to change sign across the PIL; see Fig. 3. Since \mathbf{E}_t is the gradient of a scalar, this electric field does not change B_r in the photosphere. We find that the transverse magnetic field emerged by this process introduces shear at the neutral line. The magnetic energy in the active region is raised significantly above the potential field energy.

After the energization is complete, the eruption is triggered by applying flux cancellation at the PIL. There is evidence that flux cancellation preceded the 12 May 1997 CME [5], and may have been its trigger. MDI magnetograms show clear evidence of cancellation of flux at the PIL. This flux cancellation is specified by imposing converging flows at $r = R_\odot$, together with photospheric diffusion [e.g., 16, 17, 18]. Figure 4 shows a typical example of the flow used. In its early stages, flux cancellation converts the highly sheared field along the PIL into a filament. We have found these techniques to be a very flexible way to energize and trigger CMEs.

ZERO BETA AND THERMODYNAMIC MODELS

The full thermodynamic model with an improved energy equation is very costly to run, since it requires high-resolution meshes and small time steps. A “zero-beta” model, in which gravity and pressure forces are neglected, is a useful approximation. In this model, the energy equation is not solved (since $p = 0$). The zero-beta model is numerically more efficient, and is frequently used for the rapid investigation of stability. It is important to note that the coronal density profile $\rho(\mathbf{x})$ can be chosen freely in this model. This choice affects the Alfvén speed profile. In general, it is difficult to choose a realistic ρ profile, especially when the magnetic field varies over a large range (as is the case for global simulations

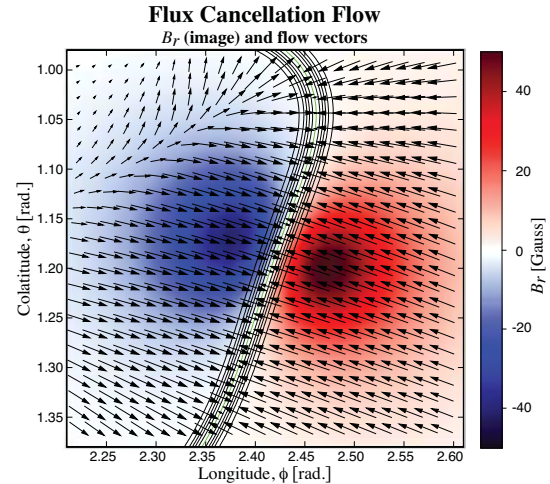


FIGURE 4. Flow applied at $r = R_\odot$ that converges towards the PIL (green), resulting in cancellation of flux. This frequently triggers the initiation of a CME. The contours show the photospheric resistivity.

with high resolution in active regions). That is a primary reason to use a thermodynamic model in which ρ is determined self-consistently. We have found that the choice of $\rho(\mathbf{x})$ can dramatically influence the assessment of a fast CME model.

We studied the energization and eruption of Model v1 using the zero-beta and thermodynamic models. We found that when an arbitrary, though reasonable, density profile was specified in the zero-beta model, the CME reached a certain speed. When we repeated this case using a density profile that was derived from the thermodynamic model (which is more realistic), the CME speed was significantly different. The case with the “fake” density profile was appreciably more energetic. (It turned out to have a higher coronal Alfvén speed.) This ought to be a cautionary tale for users of zero-beta models.

Furthermore, we noticed that the thermodynamic model generally gave less energetic eruptions for the same conditions (energization and flux cancellation), as illustrated in Fig. 5. The thermodynamic model has a smaller burst of kinetic energy, and a correspondingly more gradual release of magnetic energy, than the zero-beta model. (In this case the zero-beta model used the ρ profile from the thermodynamic model to make the comparison as similar as possible.) In the thermodynamic model, the lower field lines in the erupting filament appear to be trapped by the dense plasma in the chromosphere/low corona, in contrast to the zero-beta model, as seen in Figure 6. The thermodynamic model shows the self-consistent formation of a prominence (cool, dense material) in the filament channel, an exciting development in its own right. Since the physics in the thermodynamic model is more accurate, conclusions about the speed of CMEs based on the zero-beta model need to be

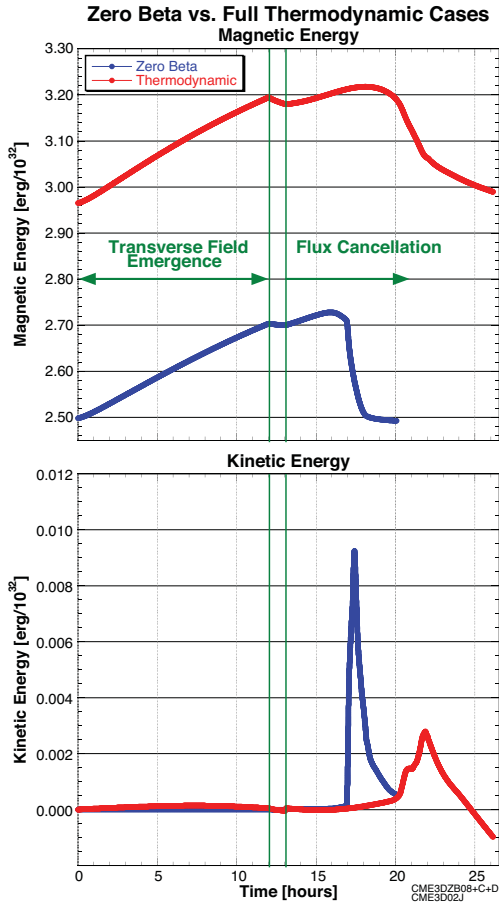


FIGURE 5. The magnetic and kinetic energy for zero-beta and a full thermodynamic simulations. The kinetic energy for the thermodynamic case is that above the initial value.

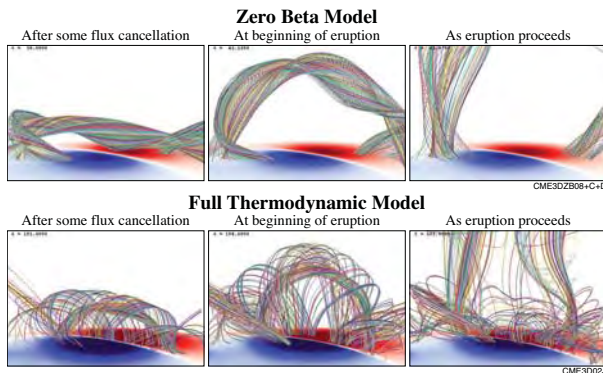


FIGURE 6. The evolution of selected field lines for zero-beta and full thermodynamic simulations.

made carefully.

CONCLUSIONS

It is apparent that models of fast CMEs do not come easily. Although our analysis is not complete, there are strong indications that magnetograms of active regions

used in models must not be smoothed too much, to maximize the chances of getting a fast CME. It appears to be necessary for the models to maintain high Alfvén speeds. The presence of a large field drop-off index low in the corona also helps. Zero-beta models are very useful, but need to be used carefully when making conclusions about the speed of CMEs. Full thermodynamic models offer promise to model the formation of prominences and their eruption within CMEs.

ACKNOWLEDGMENTS

This work was supported by NASA's LWS & Helio-physics Theory Programs, by a subcontract from Lockheed Martin (NASA prime contract NNG04EA00C in support of SDO/AIA), and by NSF via the CISM and FESD Centers.

REFERENCES

1. R. Lionello, J. A. Linker, and Z. Mikić, *ApJ* **690**, 902–912 (2009).
2. S. P. Plunkett, B. J. Thompson, R. A. Howard, D. J. Michels, O. C. St. Cyr, S. J. Tappin, R. Schwenn, and P. L. Lamy, *Geophys. Res. Lett.* **25**, 2477–2480 (1998).
3. B. J. Thompson, S. P. Plunkett, J. B. Gurman, J. S. Newmark, O. C. St. Cyr, and D. J. Michels, *Geophys. Res. Lett.* **25**, 2465–2468 (1998).
4. D. F. Webb, R. P. Lepping, L. F. Burlaga, C. E. DeForest, D. E. Larson, S. F. Martin, S. P. Plunkett, and D. M. Rust, *J. Geophys. Res.* **105**, 27251–27260 (2000).
5. A. Ambastha, and S. K. Mathew, in *Advanced Solar Polarimetry*, edited by M. Sigwarth, 2001, vol. 236 of *ASP Conf. Series*, p. 313.
6. N. Gopalswamy, and M. L. Kaiser, *Adv. Sp. Res.* **29**, 307–312 (2002).
7. G. Attrill, M. S. Nakwacki, L. K. Harra, L. van Driel-Gesztelyi, C. H. Mandrini, S. Dasso, and J. Wang, *Sol. Phys.* **238**, 117–139 (2006).
8. N. U. Crooker, and D. F. Webb, *J. Geophys. Res. (Space Physics)* **111**, 8108 (2006).
9. V. S. Titov, Z. Mikić, J. A. Linker, and R. Lionello, *ApJ* **675**, 1614–1628 (2008).
10. Z. Mikić, D. C. Barnes, and D. D. Schnack, *ApJ* **328**, 830–847 (1988).
11. Z. Mikić, J. A. Linker, D. D. Schnack, R. Lionello, and A. Tarditi, *Physics of Plasmas* **6**, 2217–2224 (1999).
12. B. Kliem, and T. Török, *Phys. Rev. Lett.* **96**, 255002 (2006).
13. P. Démoulin, and G. Aulanier, *ApJ* **718**, 1388–1399 (2010).
14. T. Török, and B. Kliem, *Astron. Nachr.* **328**, 743 (2007).
15. S. K. Antiochos, C. R. DeVore, and J. A. Klimchuk, *ApJ* **510**, 485–493 (1999).
16. T. Amari, J. F. Luciani, J. J. Aly, Z. Mikić, and J. Linker, *ApJ* **585**, 1073–1086 (2003).
17. T. Amari, J.-J. Aly, Z. Mikić, and J. Linker, *ApJ* **717**, L26–L30 (2010).
18. T. Amari, J.-J. Aly, J.-F. Luciani, Z. Mikić, and J. Linker, *ApJ* **742**, L27 (2011).